Spring 1-1-2010

Plasticity Modeling and Coupled Finite Element Analysis for Partially-Saturated Soils

Jaehong Kim
University of Colorado at Boulder, jaehong@colorado.edu

Plasticity modeling and coupled finite element analysis for partially-saturated soils

by

Jaehong Kim

B.A., Chonbuk National University, 1999

M.S., Yonsei University, 2002

A thesis submitted to the

Faculty of the Graduate School of the

University of Colorado in partial fulfillment

of the requirements for the degree of

Doctor of Philosophy

Department of Civil, Environmental, and Architectural Engineering

2010

This thesis entitled:
Plasticity modeling and coupled finite element analysis for partially-saturated soils
written by Jaehong Kim
has been approved for the Department of Civil, Environmental, and Architectural Engineering

Richard A. Regueiro

Prof. Seung-Rae Lee

Prof. Ning Lu

Prof. Ronald Y.S. Pak

Prof. Stein Sture

Prof. Dobroslav Znidarcic

Date

The final copy of this thesis has been examined by the signatories, and we find that both the content and the form meet acceptable presentation standards of scholarly work in the above mentioned discipline.

Kim, Jaehong (Ph.D., Civil Engineering)

Plasticity modeling and coupled finite element analysis for partially-saturated soils

Thesis directed by Prof. Richard A. Regueiro

The objective of the research is to compare various features of partially-saturated soil models within a coupled small strain triphasic mixture finite element implementation to determine an appropriate constitutive modeling framework for partially-saturated soils. To achieve the objective, specific research tasks include: (1) formulating and implementing a small strain nonlinear triphasic mixture finite element in a Matlab code; (2) verifying the triphasic mixture element in Matlab code to partially-saturated water flow simulated by commercial codes and a closed-form solution; (3) formulating and implementing a small strain partially-saturated soil hyperelasto-plasticity model in the Matlab code; (4) using constitutive parameters from experimental data available in the literature; and (5) conducting plane strain finite element analysis of rainfall infiltration into slope surfaces with gravity loading.

Dedication

To Wife and Jaiden.

For your love and encouragement.

Acknowledgements

My earnest thanks go to Professors Seung-Rae Lee, Ning Lu, Ronald Y.S. Pak, Stein Sture, Dobroslav Znidarcic and my advisor, Richard A. Regueiro, for serving on my committee.

I would like to express my sincerest gratitude to my academic advisor, Professor Richard Regueiro. Dr. Regueiro has gradually guided me towards becoming a critical thinker and an independent researcher. My dissertation is the product of his guidance and encouragement. I am grateful to Dr. Znidarcic and Dr. Lu for their constructive criticism of this work and for their advice on academic matters, and I am grateful to Dr. Sture and Dr. Pak for their friendship and help and suggestions provided throughout my PhD program. Dr. Lee has been a member of the reading committee and continued to encourage me, though usually from a distance.

Finally, my dearest wife Yeujin Kim has been my ideal companion for seven years. She is my dearest friend, confidant, partner and advisor. Now as parents, we share the blessing of having a wonderful son, Jaiden Wonbin Kim. It is to Jaiden that I dedicate this dissertation.

Contents

Chapter

Tables

Table

Figures

Figure

Chapter 1

Introduction

1.1 Background

For finite element analysis of partially saturated soils, commercial software analyzing coupled seepage and deformation analyses of soil, such as SEEP/W–SIGMA/W[40], PlaxFlow–Plaxis[74, 73], Abaqus[1], and so on, are usually used. Some commercial software for geotechnical problems, for example UNSAT-H[89], SEEP/W and PlaxFlow, are formulated for conditions of constant net normal stress ($p = \sigma - p_a$; excess of mean stress σ over air pressure p_a) and non-deformable soil media. UNSAT-H and SEEP/W software for 1-Dimensional flow process in partially saturated soil is verified against the Srivastava and Yeh[81] analytical solution, and compared to a partially saturated flow simulation (rigid soil) using a triphasic mixture finite element implemented in a Matlab code. The coupled flow and deformation software is used to compare the coupled FE implementation in a Matlab code, and to better understand the assumptions made in coupling the soil skeleton deformation with pore liquid and gas flow (via the effective stress equation for partially saturated soil).

The seepage and flow processes in a deformable soil are influenced by soil solid skeleton deformations. Pore water pressure change due to seepage will lead to changes in effective stress and to deformation of a soil. Similarly, effective stress changes will modify the seepage process since soil hydraulic properties such as porosity, permeability and water storage capacity are affected by the changes in effective stress. Hence, a monolithically coupled hydromechanical model is preferred to analyze the behavior and stability of a partially saturated soil subjected to external

loads, especially rainfall. As a result, the seepage and stress-deformation problems should be linked simultaneously[97].

The main objective of this research is to develop a monolithically coupled nonlinear finite element model for a deformable partially saturated soil based on the modified Cam-clay model, to make Matlab coding and comparison to commercial FE programs (SEEP/W–SIGMA/W, PlaxFlow–Plaxis, and ABAQUS), to find material parameter fitted with experimental data in the literature, and to illustrate their implementation to study various features, such as yield surface, soil-water characteristic curve (SWCC), and effective stress equations, of a proposed hyperelasto-plastic Cam-clay model for partially-saturated soil in the literature. Issues for investigation to meet the main objective,

(1) various effective stress equations

(2) a hyperelasto-plastic critical-state Cam-clay-like plasticity model implemented in a biphasic and triphasic nonlinear coupled FE Matlab code

(3) and, effect of including pore air pressure ($p_a \neq 0$) versus not ($p_a \approx 0$)

1.2 Motivation

Partially saturated (also called unsaturated) soil mechanics has been closely connected with the history of hydrology, soil mechanics, and soil physics. Engineering problems in partially saturated soil mechanics can be found in many countries in the world, such as construction of dam, natural slopes subjected to environmental changes, stability of excavations, lateral earth pressures on retaining walls, bearing capacity for shallow foundations, collapsing soil structures due to expansive soils, and pavement subgrade and so on. These examples show that there are many practical situations involving partially saturated soils that require an understanding of the seepage, volume change, and shear strength characteristics. Common to all partially saturated soil situations are the negative pressures in the pore-water-air interface (capillarity). The problems involving negative pore-water pressures, which has received the most attention, are that of swelling or expansive

clays[32]. The financial damages associated with expansive soils are about $10 billion each year in the United States and more than twice the complex natural disasters from floods, hurricanes, tornadoes, and earthquakes[48, 55].

With the development of theories and techniques in partially saturated soil mechanics, it requires that many principles of soil mechanics and hydraulics should approach the flow and deformation phenomena of partially saturated soil, and that the results obtained through numerical simulation agree fairly well with field measurements for the various geotechnical engineering problems involving partially saturated soil. However, it should be needed for understanding the processing of these problems, such as setting up boundaries and initial conditions among different geotechnical problems. The majority of practical engineering problems generally involve these two phenomena simultaneously. An effective theory describing the water infiltration and deformation behavior in expansive soil, such as clayey soil, appropriate for application of the principles of stress, strain, and flow in highly deformable soil[65].

Moore[71] is one of the first researchers to recognize the importance of soil suction to the mechanical behavior of a partially saturated soil. He studied soil suction and water flow due to infiltration through experimental tests. Many researchers have referred and begun with the fundamental works of Bishop and Donald[10], Coleman[22], Matyas and Radhakrishna[69] and Fredlund and Morgenstern[31], and these are the basis of suitable stress frameworks to describe the stress-strain-strength behavior of partially saturated soils. In the expression of three stress states, $(\sigma_{ij} - u_a\delta_{ij})$; $(\sigma_{ij} - u_w\delta_{ij})$ and $(u_a - u_w)\delta_{ij}$ where, σ_{ij} is the total stress, u_a and u_w are pore air and water pressure and δ_{ij} is Kronecker delta. Under conditions of partial saturation, the term $u_a - u_w$ is a positive quantity and will be denoted as the suction term s[6].

Alonso et al.[6] suggested a constitutive model for describing the stress-strain behavior of partially saturated soils. This model is formulated within the framework of hardening plasticity using two independent sets of stress variables: the excess of total stress over water and air pressure and the suction. Borja[12] presented a mathematical framework for three-phase deformation and strain localization analyses of partially saturated porous media using conservation laws and a

modified Cam-clay constitutive model formulation.

1.3 Literature Review

1.3.1 Three *vs.* two field finite element analysis of partially saturated soil

When taking into account the solid-water-gas interaction to present the features of the hydro-mechanical behavior of multiphase porous media, the soil model has two kinds of constituent volume fraction. One is that the air phase is considered active in the voids of a three phase soil as a gas phase, and tho other is to treat the gas phase as vacuum in a soil mixture. In the soil mechanics, 'saturated' just means the mixture of soil particles and water, but other fields, such as Earth Science and Multi-phase media literature, define the mixture concept unlike the soil mechanics as shown in Figure 1.1.

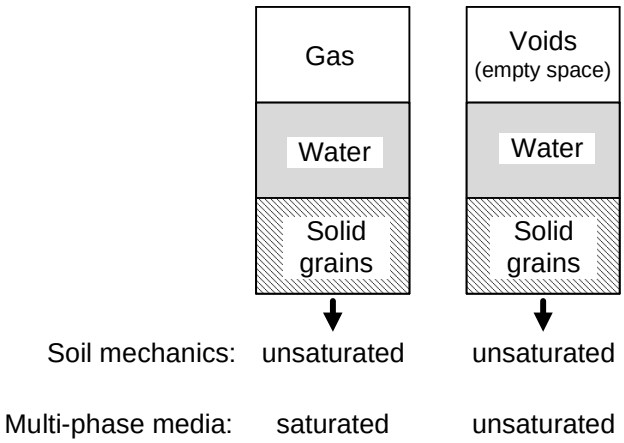

Figure 1.1: Schematic description for three phase mixture[57]

According to the role of the air phase, the soil has either the continuous air or the occluded air bubbles. The former concept like water phase is concerned by mathematical formulation developed in this study, but the latter concept is related to calculate the water compressibility.

On the other hand, the role of the air phase in the hydro-mechanical behavior of deformable soil is treated by the air-water interface or contractile skin to recognize a partially saturated soil as a four phase system[32]. When performing a stress analysis on an element, they assumed the

partially saturated soil can be visualized as a mixture with soil particles and contractile skin that approach to equilibrium under applied stress gradients and air and water phases that flow under applied stress gradients. The reason is why the contractile skin acts like a thin rubber membrane, pulling the particles together when the pore water pressure gradually changes into the negative value during the shrinkage-type experiment involving the drying of a small soil specimen as it is exposed to the atmosphere.

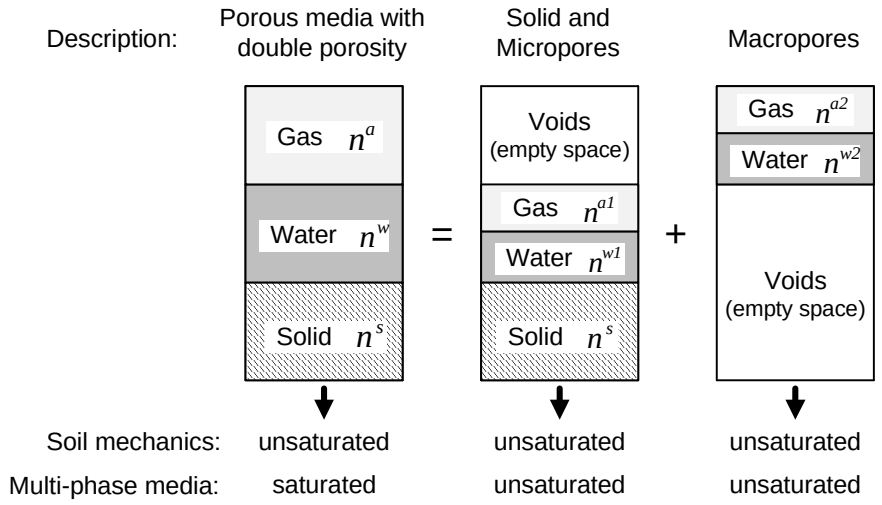

Figure 1.2: Schematic description of a mixture with double porosity[14]

Recently, in order to observe the coupled solid-water-air phenomenon in detail Gray and Schrefler[41, 42], Khalili et al.[51, 52], and Borja[14] formulated conservation equations for a three-phase system consisting of a solid and two immiscible fluids, liquid and gas. They also derived expressions for the effective stress tensor in multi-phase porous media exhibiting two porosity scales, micro- and macroporosity during the course of loading. Figure 1.2 shows to describe the concept of partially saturated porous media with double porosity. The three-phase mixture is composed of porous media consisting of solid and fluids within the micropores and macropores consisting of only fluid constituents, liquid and gas, in the macropores as shown in Figure 1.2.

Developments presented in the literature regarding a mixture of solid, liquid, and gas have recently been proposed as the constitutive framework of the coupled model to simulate water and

air flow in deformable soil. Finite element analysis for partially saturated soil is generally treated as biphasic (i.e., two field phases) mixture state in geotechnical engineering.

While a finite element method for saturated constitutive models have been well studied, research on finite element method for evaluating constitutive models of partially saturated soil is more limited. In order to implement a partially saturated soil model in a finite element code, the stresses are updated by integrating the stress-strain relations with a strain increment and also an updated suction s_{n+1}. For solving this numerical simulation, the methods appropriate for calculating this algorithm can be classified generally into two categories. They are implicit and explicit schemes. Explicit method calculate the state of a soil at a later time from the state of the soil at the current time, while implicit method find a solution by solving an equation involving simultaneously both the current and the later state of the soil. The former is computationally stable, and can be unstable for large time increments (large increments of strain and suction). On the other hand, implicit method is unconditionally stable (accuracy controlled by time increment), but is difficult to implement since it requires consistent tangents (global for balance equations, and local for material models). An explicit scheme with error control has been used to integrate the global differential equations derived in terms of displacement and pore water pressure in partially saturated soils[77, 78]. Implicit method which has been presented by many researchers is used to solve nonlinear constitutive equations by iteration in partially saturated soils[91, 76, 12, 21].

Although a number of constitutive equation for partially saturated soil have been developed based on experimental observations and plasticity theory, a finite element analysis in partially saturated soils is mainly treated by a constitutive model of Cam-clay elastoplasticity based on the model of Alonso et al.[6] and the well-known soil plasticity model, Mohr-Coulomb elastoplasticity. Loret and Khalii[62] proposed a constitutive model based on Cam-clay model involving their effective stress concept, and Griffiths and Lu[43] presented elastoplastic finite element analysis based on Mohr-Coulomb model in conjunction with the suction stress concept for slope stability analysis. Cho and Lee[21] proposed a 2D finite element flow-deformation coupled analysis program for calculating the safety factor for a partially saturated slope. They adopted the modified Mohr-Coulomb

failure criterion to consider variations in strength due to the presence of matric suction.

In this study, a mechanical constitutive model adopted for the partially saturated soil is Cam-clay plasticity model, based on so-called critical state soil mechanics. During the past decade, various aspects of the constitutive model for partially saturated soil have been developed and discussed; Cam-clay model will be studied based on experimental observations and plasticity theory.

1.3.2 Engineering implications of partially saturated finite element analysis

In order to discuss the practical application of finite element analysis for partially saturated soils, many parameters and initial and boundary conditions for numerical simulation must be selected. Unlike classical limit equilibrium methods, the partially saturated finite element approach to flow-deformation simulation of embankment and slope failure problems allow users to make the deformed shape or location of the critical failure surface. The behavior of clay appropriate to critical state concept should be estimated for partially saturated finite element analysis, but, for ease of application, Mohr-Coulomb failure criterion is often used to formulate the shear strength of the soil in conjunction with matric suction[21].

$$\tau = c' + (\sigma_n - p_a)\tan\phi' + (p_a - p_w)\tan\phi^b \tag{1.1}$$

where σ_n is normal stress and ϕ^b is an angle defining the increase in shear strength for an increase in matric suction. The critical failure mechanism develops by calculating the shear stress generated by gravity loading, rainfall infiltration or external loading. The two-dimensional computation of diverse partially saturated finite element analysis composed of biphasic and triphasic mixture can be carried out for coupled behavior of the water and air flow with the solid deformation ranging from very small strains to shear band localizations.

In particular, the investigation of embankment stability problems is a crucial issue and has to be investigated very carefully. Instabilities of embankment are usually initiated by the localization of plastic deformations in shear band driven by gravity load and local saturation. The onset of localizations can appear on both sides of the embankment, for example the water side and the

air side. The environmental problems of embankment which water table is rapidly increased or decreased trigger these localization and local saturation. Because the geometries and technical layouts of embankments are very sensitive to reach a stationary state, two further boundary-value problems have been computed for an embankment. One is a sudden decrease of the water table at the water side and the other is high water level at the water side can leak from slope at the air side of the embankment. Ehlers et al.[29] presented that the air phase in a partially saturated soil is not generally negligible for embankment problem. Their numerical simulation demonstrated the wide range of useful applications of the coupled solid-fluid behavior in the framework of the triphasic mixture formulation.

1.3.3 Experimental data and elastoplasticity

1.3.3.1 Effective stress and stress-strain state variables

Many researchers have presented the effective stress (stress state variable) for partially saturated soils since Terzaghi[86] proposed effective stress to describe the stress state of saturated soils. The effective stress σ' controls behavior of saturated soils and can be expressed as a function of total normal stress and pore-water pressure:

$$\sigma' = \sigma - p_w \tag{1.2}$$

where, σ' is effective stress, σ is total stress, and p_w is pore-water pressure.

Croney et al.[25] and Bishop[8], respectively, defined equations for the effective stress of partially saturated soils as follows:

$$\sigma' = \sigma - \beta' p_w \tag{1.3}$$

$$\sigma' = (\sigma - p_a) + \chi(p_a - p_w) \tag{1.4}$$

where, β' is bonding factor, p_a is pore-air pressure, χ is a parameter related to the degree of saturation of the soil, and $(p_a - p_w)$ is matric suction. Bishop proposed that the weighting parameter

χ parameter should be equal to one for saturated soils and zero for dry soils, but depends on factors such as soil structure, drying and wetting cycles, and stress history. The relationship between χ and degree of saturation S was obtained experimentally. Note that via thermodynamics, Borja[12] obtained $\sigma' = \sigma - Sp_w - (1-S)p_a$ (this was originally obtained by Lewis and Schrefler[58]).

Because of the importance of the effective stress in soil skeleton behavior, the validity of Bishop's equation has been criticized by many researchers. It was found that the equation could be used more accurately for shear strength behavior than for volume change[9]. Several other effective stress equations have been proposed for partially saturated soils[2, 3, 46, 58, 49, 12]. In consequence, the Bishop[8] equation has a more general form and referenced the total stress and pore-water pressure when reviewing many researchers' papers. However, in order to satisfy fundamental consideration of continuum mechanics, variables used for the description of a stress state should be independent of material properties. Using the Bishop's parameter χ violates this principle of continuum mechanics[31].

For the stress state variables, Coleman[22] suggested the use of net normal stress $(\sigma - p_a)$ and matric suction $(p_a - p_w)$ to describe stress-strain relations for partially saturated soil. Further work by Bishop and Blight[9] illustrated some advantages of using net normal stress and matrix suction as stress state variables. Fredlund and Morgenstern[31] studied the approach from both experimental and theoretical standpoints and formally proposed the use of two independent stress state variables, i.e., $(\sigma - p_a)$ and $(p_a - p_w)$. The use of these two independent stress state variables can explain the formulations of shear strength and volume change problems for partially saturated soils[6, 95, 84, 12].

Recently, there have been numerous researchers that make use of stress state variables incorporating soil properties in the constitutive modeling of partially saturated soils[54, 47, 35, 94, 83, 50]. In most of the models proposed, the degree of saturation is assumed to be independent of net mean stress. Kohgo et al.[54] defined the following empirical effective stress equations according to the

experimental results for partially saturated soils:

$$\begin{aligned} \sigma' &= \sigma - p_{w(e)} \\ p_{w(e)} &= \begin{cases} p_a - s & \text{for} \quad s > s_{ae} \\ p_a - \left[s_{ae} + \dfrac{s_c - s_{ae}}{(s - s_{ae}) + a_e}(s - s_{ae}) \right] & \text{for} \quad s \leq s_{ae} \end{cases} \end{aligned} \tag{1.5}$$

where, σ' is effective stress for partially saturated soils, $p_{w(e)}$ is the so called equivalent pore pressure, s is soil suction, a_e is material parameter, s_c is critical soil suction which means the maximum value within elastic regime, and s_{ae} is air entry value of the soil changed with net mean stress. The Kohgo et al.[53, 54] equation is not continuous and contains a soil property a_e.

With equations of Bishop and Kohgo et al. like equation (1.4) and (1.5), respectively, Jommi[47] proposed a stress variable for partially saturated soil, denoted by $\hat{\sigma}_{ij}$, which can be called *average soil skeleton stress*. This stress variable is modified by the Bishop's effective stress when the parameter χ of the Bishop's equation is equal to the degree of saturation S.

$$\begin{aligned} \hat{\sigma}_{ij} &= \sigma_{ij} - \Big[S p_w + (1 - S) p_a \Big] \delta_{ij} \\ &= (\sigma_{ij} - p_a \delta_{ij}) + S(p_a - p_w)\, \delta_{ij} \end{aligned} \tag{1.6}$$

where, σ_{ij} is the total stress, δ_{ij} is the Kronecker delta, and p_a is pore air pressure. This stress variable means the difference between the total stress and the mean value of the pore water pressure regarding the degree of saturation S.

Wheeler et al.[94] employed two kinds of stress state variables in his proposed framework. The first stress variable σ^*_{ij} is the stress tensor which has been used by Jommi[47]. The second stress variable s^* is the function of porosity and suction of the soil as follows:

$$\begin{aligned} \sigma^*_{ij} &= \sigma_{ij} - \Big[S p_w + (1 - S) p_a \Big] \delta_{ij} \\ s^* &= n s = n(p_a - p_w) \end{aligned} \tag{1.7}$$

where, n is the porosity, and $s = (p_a - p_w)$ is the suction.

Lu et al.[66, 63] suggested suction stress σ^s, denotes as effective degree of saturation S_e times matric suction $(p_a - p_w)$, as the extension of Terzaghi's effective stress σ' (positive in tension) in

saturated condition,

$$\begin{aligned} \sigma' &= (\sigma + p_a) + \sigma^s, \quad \sigma^s = -S_e\,(p_a - p_w) \\ S_e &= \frac{S - S_r}{1 - S_r} = \left[1 + (\alpha s)^{\mathrm{n}}\right]^{-\mathrm{m}} \end{aligned} \tag{1.8}$$

where s is matric suction, and α, n, m are curve fitting parameters of van Genuchten[90]'s SWCC equation. The effective stress (equation (1.8)) is defined as a closed-form expression for suction stress for the full range of matric suction,

$$\begin{cases} \sigma^s = -(p_a - p_w) & ;\, p_a - p_w \le 0 \\ \sigma^s = -\dfrac{p_a - p_w}{\left[1 + (\alpha s)^{\mathrm{n}}\right]^{\mathrm{m}}} & ;\, p_a - p_w \ge 0 \end{cases} \tag{1.9}$$

The behavior of suction stress can be effectively described using Suction Stress Characteristic Curve (SSCC) because the effective stress was treated as a function of both matric suction and the degree of saturation as referred in Section 3.3.2.

Furthermore, there are material properties regarding intrinsic volume change in soil phase for the stress-strain behavior of partially saturated soils. These soil properties described the overall volume and the amount of water of a soil are as follows:

- porosity denoted as n,
- void ratio denoted as e,
- specific volume denoted as ν,
- gravimetric water content denoted as w,
- degree of saturation denoted as S,
- volumetric water content denoted as θ (or n^w, volume fraction of water).

Especially, void ratio e is generally used in classical soil mechanics, and specific volume $\nu(= 1 + e)$ is used in critical state soil mechanics. The degree of saturation and volumetric water content requires the measurement of both the gravimetric water content and the volume of the soil at various soil suction in partially saturated soils.

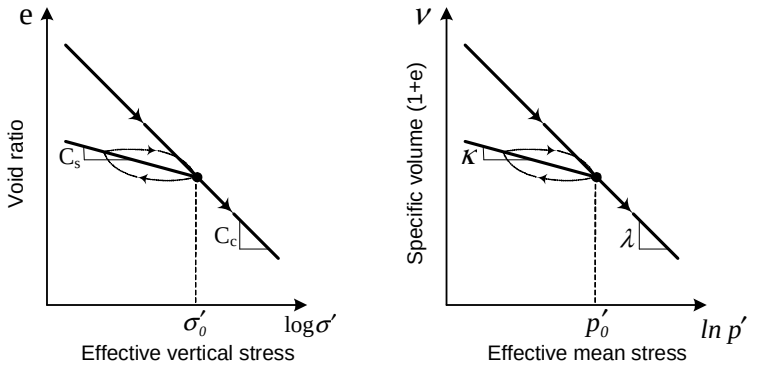

Figure 1.3: Compression curves with the two conventional stress-strain axes systems (Wood, 1990)

When soil suction is equal to zero, the soil is assumed to be saturated. Typical shapes of the curves for the relationships between void ratio and mean effective stress (or vertical effective stress) of a saturated soil are shown in Figure 1.3[96]. The compression curve for presenting the stress-strain constitutive relations of a soil can be found in the theory for critical state saturated soil mechanics, where the Cam-clay model is an example[96]. The compression curve of a soil is approximated by two straight lines on the natural logarithmic effective stress scale. The slopes of the unloading-reloading and virgin compression curves are denoted as elastic parameter κ and plastic parameter λ, respectively.

Under the K_0 loading condition (i.e., one-dimensional uniaxial strain loading condition), void ratio of a soil at any vertical effective stress can be shown in the left side of Figure 1.3. Traditionally, the slope of the unloading-reloading lines and virgin compression line plotted on 10 based log scale are called *unloading-reloading index* C_s, and *virgin compression index* C_c. The value of the effective stress at the intersection of the two lines is classically referred to as the pre-consolidation stress (i.e., one-dimensional loading). On the other hand, the right side of Figure 1.3 shows the compression curve on the natural log scale. The slopes of the unloading-reloading and virgin compression curves are $\kappa\,(= C_s/\ln 10)$ and $\lambda\,(= C_c/\ln 10)$, respectively. It is referred to as the yield stress (i.e., three-dimensional loading). Soils behave elastically approximately if the effective stress is less than the yield stress. Once the effective stress is higher than the pre-consolidation stress (or yield stress),

the soil exhibits both elastic and plastic volume changes[96, 32].

1.3.3.2 Stress-strain relations considering soil suction

Numerous experimental data presenting the relationship between void ratio and net mean stress of a soil at constant soil suctions can be found in the literature. Figure 1.4 shows the stress paths, plotted as suction s against net mean stress p, for compression with decrease in suction. Note that in the literature the net mean stress often denotes as p because the pore air pressure p_a is assumed as zero, so net mean stress $(\sigma - p_a)$ is equal to mean stress σ. In the triaxial cell each sample, the initial point A with a large negative value of pore water pressure (a high value of suction) and zero net mean stress is produced by the compaction process. On the application of the increments of cell pressure, air back-pressure and water back-pressure, compaction tests were conducted from point B_0 and point B corresponding to the suction value. During the subsequent equalization stage, the soil state moved to point C_0, C_1, C_2 or C_3, with suction s falling while net mean stress p remained constant. Then, during compression, p increases while s is held constant.

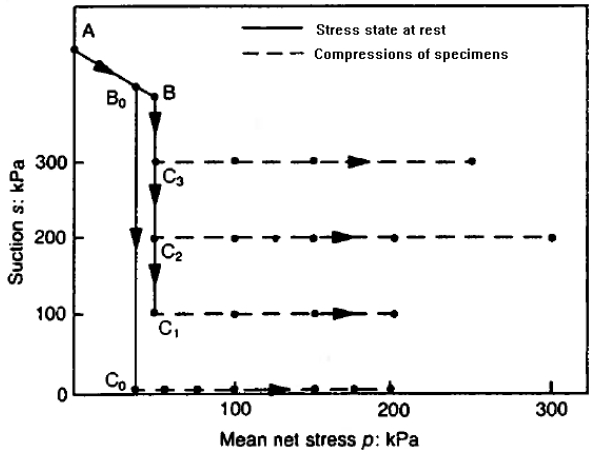

Figure 1.4: Stress paths implemented on partially saturated soils, kaolin (Wheeler and Sivakumar 1995)

Most studies focused on compacted soils that usually collapse during the first wetting process.

The studies followed similar stress paths and are described in Figures 1.5 and 1.6 show experimental data for compression curves on several partially saturated soils at various constant soil suctions and under different loading conditions (i.e., K_0 and isotropic). It has been experimentally shown that soil suction contributes to the stiffness and strength of a soil against the external load[6, 61]. In other words, the yield stress with respect to the net mean stress of a soil increases as the soil suction increases.

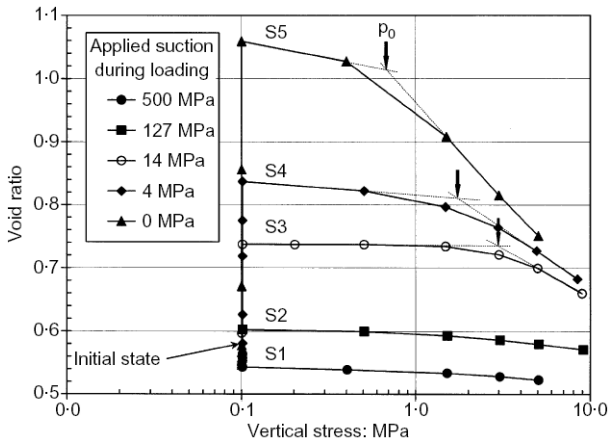

Figure 1.5: Variation of void ratio with suction at initial stage of loading, bentonite (Lloret et al., 2003)

Alonso et al.[6] proposed the similarity between compression curves of a partially saturated soil and a saturated soil. It is a likeness of the compression curve of a soil at a constant soil suction and at the saturated condition. The compression curve of a partially saturated soil at a constant soil suction can be approximated by two straight lines, which are distinguished by the yield stress of the soil as shown in Figure 1.7. The authors also assumed that the slopes of the unloading-reloading line are constant with soil suction, (i.e., $\kappa(0) = \kappa(s)$), while the slope of the virgin compression lines are assumed to be a function of soil suction, $\lambda(s)$.

In the $\nu - s$ graph of Figure 1.7, for the axis of specific volume versus soil suction, Alonso et al.[6] assumed that the compression curve with respect to soil suction at a constant net mean stress can be approximated as two straight lines with an intersection at the yield suction. The

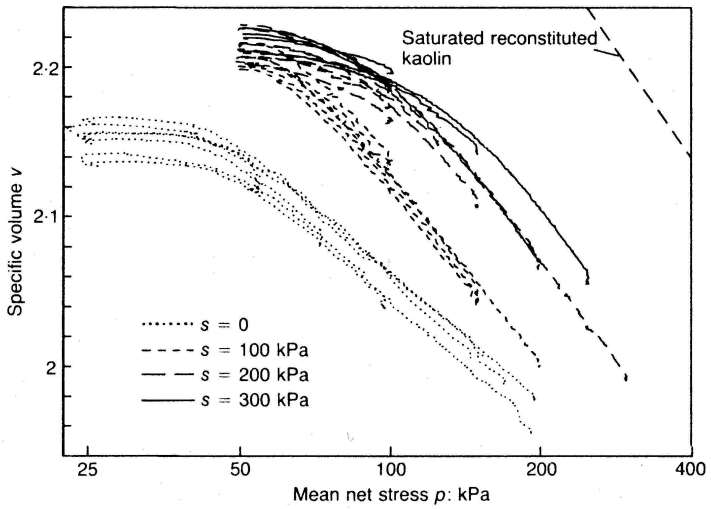

Figure 1.6: Variation of specific volume with net mean stress (Wheeler and Sivakumar, 1995)

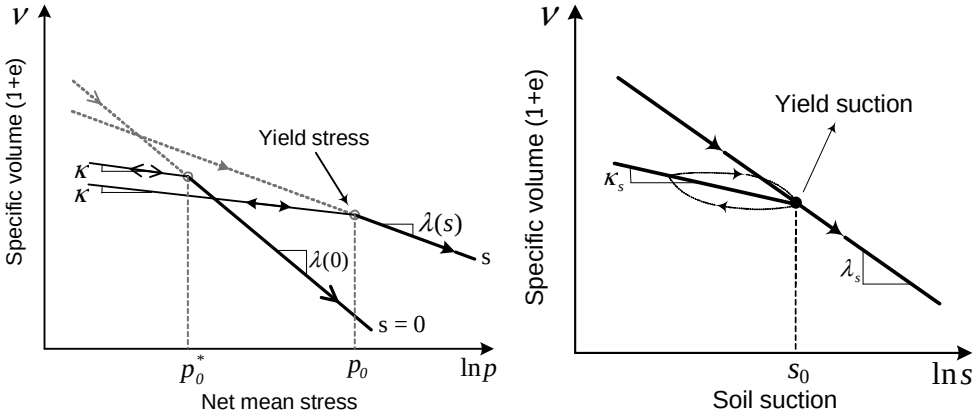

Figure 1.7: Variation of specific volume with net mean stress and soil suction, kaolin and sandy soil (Alonso et al., 1990)

slopes of the unloading-reloading and virgin compression lines with respect to the soil suction are κ_s and λ_s, respectively. It was assumed that the two slopes are independent of net mean stress. The proposed relationships are valid within a low range of soil suction less than the air entry value of the soil which is the matric suction value that must be exceeded before air recedes into the soil pores. The air entry value is also referred to as the *bubbling pressure* in ceramics engineering[32].

However, there is disagreement in the relationship between $\lambda(s)$ and s provided by two models as shown in Figures 1.5 and 1.6. Alonso et al.[6] assumed that the slope of the virgin compression curve of a soil is getting a gentle gradient with an increment of soil suction, while it was assumed to be getting a steep gradient with the increment of soil suction by Wheeler and Sivakumar[95]. The results are different in tendency (gentle versus step). Many experimental results supporting both assumptions can be found from research literatures[6, 95, 84, 11, 20, 61, 83].

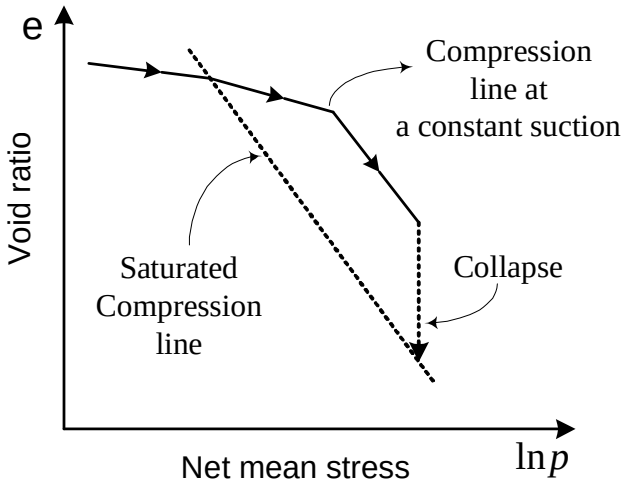

Figure 1.8: Compression curve of Alonso's LC_{mc} model (1993)

Also, it can be observed from numerous experimental results in the literature that the compression curve at a constant soil suction is concave for a wide range of the net mean stress as shown in Figure 1.8. Therefore, the approximation of the compression curve of a soil at a constant soil suction as two straight lines is not always valid and the yield stress is not easy to define[11].

Some researchers have suggested that under an extremely high net mean stress, the void ratios of a soil at saturation and at a certain soil suction must be the same[4, 95, 34]. In other words, the compression curve of a soil at a constant soil suction must meet the compression curve of the soil at saturated conditions (i.e., zero soil suction) at a relative high net mean stress. After the loading-collapse (LC) yield curve proposed by Alonso et al.[6, 4] presented a "new" model called LC_{mc} which is capable of expressing the compression curve of a soil at a constant soil suction as shown in Figure 1.8. Alonso[4]'s LC_{mc} model is extended from the original Barcelona Basic Model (BBM[6]).

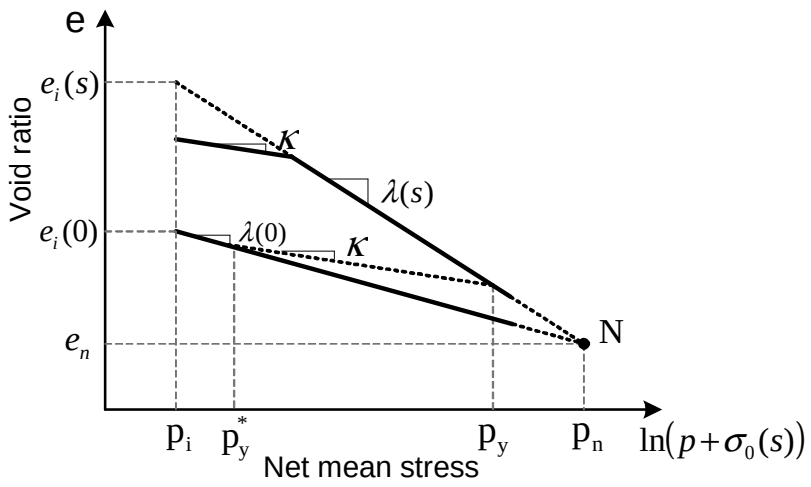

Figure 1.9: Compression curves of saturated and partially saturated soils, kaolin (Sun et al., 2000)

Sun et al.[82] assumed that the compression curve of a partially saturated soil with respect to net mean stress at a constant soil suction is a concave curve (Figure 1.9). Futai et al.[34] proposed a model for the compression curve of a partially saturated soil as shown in Figure 1.10. Silva et al.[79] presented a critical state soil model used for the analysis of partially saturated soils. They proposed some changes in the model of Wheeler and Sivakumar[95] by reducing the number of parameters. Figure 1.11 shows isotropic compression curves to prevent the inconsistency which is possible to cross these lines for high stresses when using the $\lambda(s)$ values directly from tests and extending the

isotropic consolidation lines to different suction values.

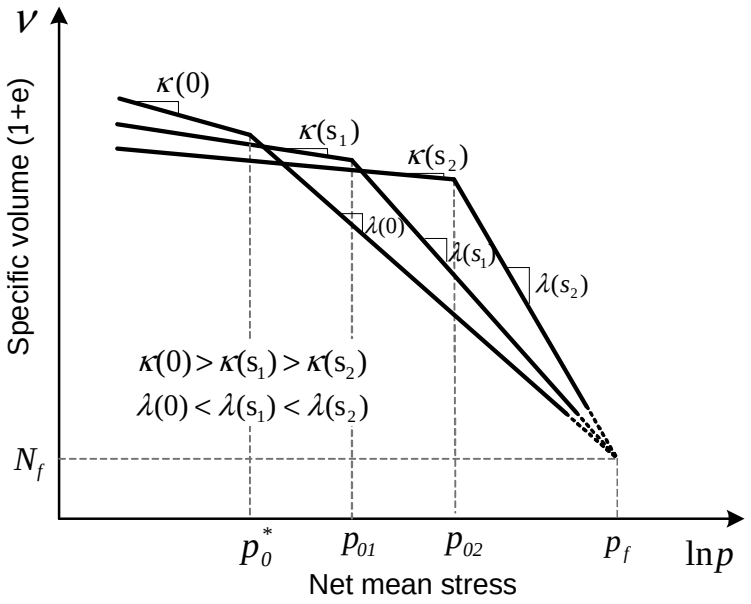

Figure 1.10: Compression curves of partially saturated soils, reddish clay (Futai et al., 2002)

Fredlund and Rahardjo[32] presented the relationship among the four coefficients from a consolidation test as shown in Figure 1.12. Curve A remains saturated during the consolidation process. This represents the relationship between the void ratio and net normal stress $(\sigma - p_a)$ as well as the water content (wG_s) and net normal stress.

For test of the same soil, when increasing suction, the volume change is the same at saturation condition. Once the soil start to desaturate, curve B represents to be less volume change than curve A due to the increasing suction. This means that a suction increase is more effective than a net normal stress increase in removing water from the soil. Curve C is the relationship between the water content versus the suction. The difference between curve B and C is due to the decreasing degree of saturation as the suction increases, that is, the ratio of vertical axis for curve B and C indicates the degree of saturation $(S = wG_s/e)$. On the other hand, for curve $A(S = 1)$, it means that $wG_s = e$.

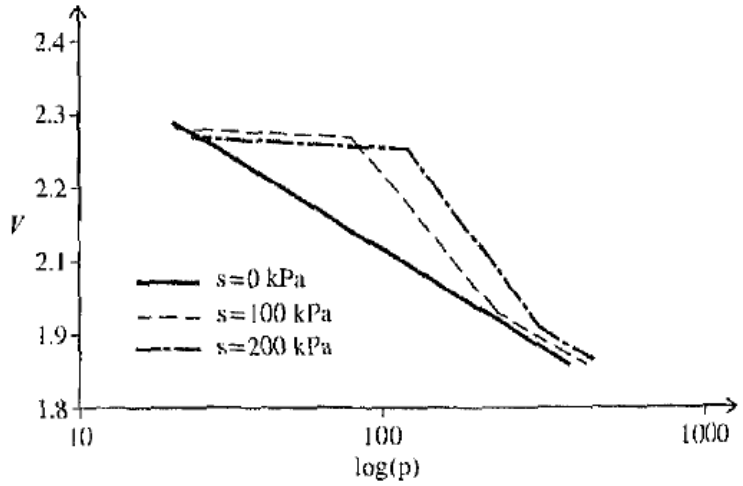

Figure 1.11: Compression curves of partially saturated soils, clay (Silva et al., 2002)

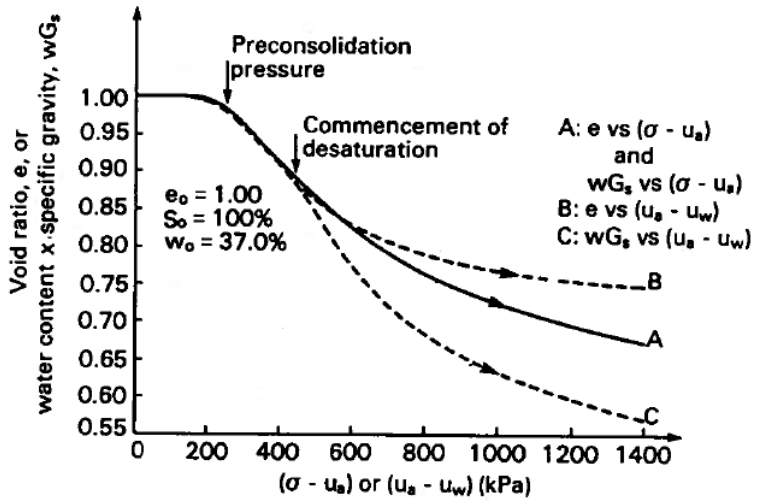

Figure 1.12: Comparison between compression curves with net mean stress and soil suction (Fredlund and Rahardjo, 1993)

Therefore, experimental data performed from researchers show that there is a similarity between the compression curve of specific volume versus a soil suction and that of specific volume versus a net mean stress[6, 32], and the net mean stress increases as the soil suction increases in a ν-p space[95, 82, 79, 34, 61].

1.3.3.3 Soil-water characteristic curve

The relationship between water content (or degree of saturation) and soil suction is defined as the soil-water characteristic curve (SWCC) of the soil. The SWCC which has been studied in the literature reflects material properties including pore size distribution, grain size distribution, density, organic material content, clay content, and mineralogy on the pore water retention behavior. The SWCC plays an important role in understanding the behavior of partially saturated soils. Soil-water characteristic curves have been used to estimate the hydraulic conductivity, shear strength, volume change and aqueous diffusion functions of partially saturated soils[65, 32].

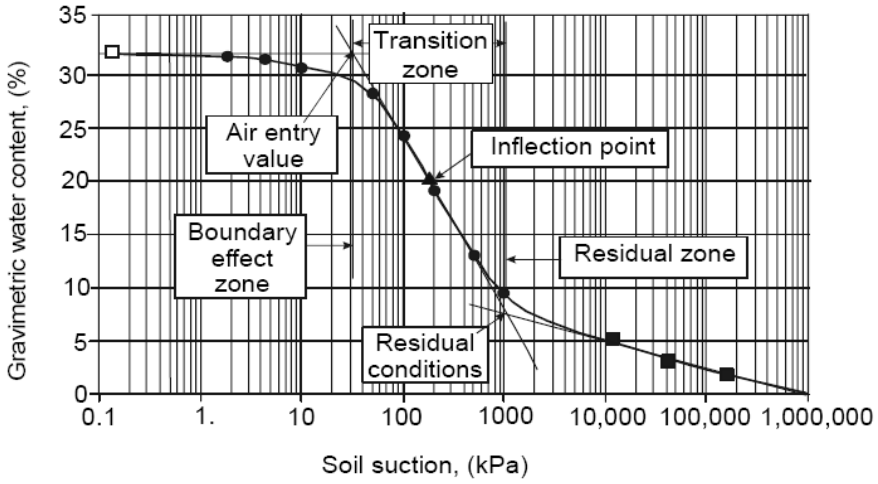

Figure 1.13: Typical soil-water characteristic curve (SWCC) of soil (Fredlund and Rahardjo, 1993)

There are a number of methods for measuring and estimating the SWCC of a soil such as: laboratory measurements, field measurements, estimations using several other soil properties,

and selection from a soil database. On the logarithmic soil suction scale, the SWCC has an S-shape. Based on the S-shape of the soil-water characteristic curve, it is possible to distinguish characteristics of a soil as shown in Figure 1.13. The soil-water characteristic curve of a soil can be divided into three zones; namely, the boundary effect zone, transition zone, and residual zone. There are four key parameters of a SWCC that can be graphically estimated from the SWCC plot: (i) water content at approximately zero soil suction; (ii) air entry value of the soil; (iii) soil suction at the residual condition; and (iv) water content at the residual condition. These parameters provide the necessary information for estimating partially saturated soil functions such as the hydraulic conductivity and the shear strength functions[32, 65].

There are three different types of the SWCC. The first type is gravimetric water content ($w = M_w/M_s$) versus soil suction; the second type is volumetric water content (or the volume fraction of water, $n^w = V_w/V$) versus soil suction; and the third type is the degree of saturation ($S = V_w/V_v$) versus soil suction. The first type is the easiest to measure. The curve requires the measurement of gravimetric water content of the soil at different values of soil suction. But, the second and third types require the measurement of both water content and volume change of the soil at various applied soil suctions.

1.3.3.4 Elasto-plastic models for partially saturated soils

The elasto-plastic constitutive models for partially saturated soils can be classified into two groups; namely, (i) models that make use of the two stress variables, that is, net mean stress ($\sigma - p_a$) and a soil suction ($p_a - p_w$); and (ii) constitutive models incorporating a soil property, including hydraulic hysteresis (Table. 1.1). Most models using two independent stress variables are able to represent the stiffness changes of the soil induced by suction changes and reproduce the irreversible behavior of the soil due to two stress variables. But, because each constitutive model is based on data for a particular soil, the model always has its own limitation[6, 95, 84, 12].

On the other hand, early works of the constitutive models incorporating soil properties is not continuous for transition between saturated and partially saturated conditions[53, 54], however

Table 1.1: Classification of elasto-plastic models by variables in use

$(\sigma - p_a)$ and $(p_a - p_w)$ variables	*Stress variables + Soil properties*
Fredlund and Morgenstern, 1977	Kohgo et al., 1993
Alonso et al., 1990	Dangla et al.,1998
Gens and Alonso, 1992	Jommi, 2000
Wheeler and Sivarkumar, 1995	Romero and Vaunat, 2000
Tang and Graham, 2002	Wheeler et al., 2003
Blatz and Graham, 2003	Galipolli et al., 2003
Chiu and Ng, 2003	Tamagnini, 2004
Borja, 2004	

recent works can describe the irreversibility of the soil against stress and suction reversals and also represent the transition without discontinuity[94, 36, 35, 83].

Most elasto-plastic models for partially saturated soils that make use of two stress variables have assumptions and yield curves on $p - s$ plane that are similar to the Alonso et al.[6] model. These models have been successful in the prediction of stress-strain behavior over certain ranges of net mean stress and soil suction for certain types of soils, particularly compacted soils.

An elasto-plastic framework for partially saturated soils was first introduced by Alonso et al.[5]. The model has been then developed to a complete elasto-plastic model for partially saturated soil by Alonso et al.[6]. This model, called "Barcelona Basic Model," has become the most widely accepted and the basic elasto-plastic model for partially saturated soils. The model makes use of the two independent stress variables, such as net mean stress $\sigma - p_a$ and soil suction $s = p_a - p_w$.

On the space of specific volume versus net mean stress, Alonso et al.[6] assumed that the compression curve of a soil at a constant soil suction can be approximated by two straight lines with an intersection at the yield stress (Figure 1.14).

For an elasto-plastic model, it is important to specify the yield surface of the soil at any stress state. When soil suction increases, the mean yield stress p_0 of the soil is also increased. Alonso et al.[6] defined the LC (Loading-Collapse) yield curve as a curve representing the yielding net mean

stress with respect to the soil suction (Figure 1.16). The LC yield curve can be mathematically presented as follow:

$$\frac{p_0}{p^c} = \left(\frac{p_0^*}{p^c}\right)^{\frac{[\lambda(0)-\kappa]}{[\lambda(s)-\kappa]}} \tag{1.10}$$

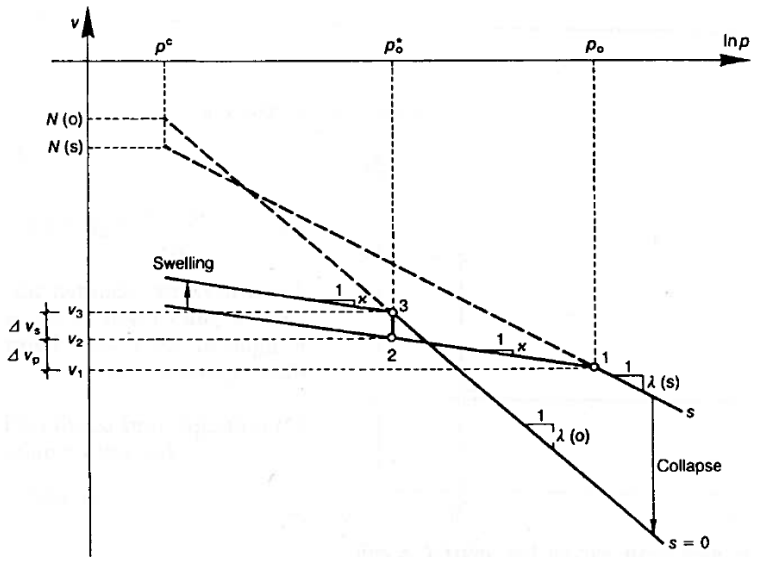

Figure 1.14: Compression curves of a soil at saturated condition and at a constant soil suction (Alonso et al. 1990)

Figure 1.14 shows the response to isotropic loading of two different types of soil. One is saturated condition ($s = 0$), the other is partially saturated condition with a suction (s). p^c, p_0^* and p_0 are the initial net mean stress, the saturated preconsolidation stress and partially saturated preconsolidation stress, respectively. The sample with a suction will yield at a larger isotropic stress p_0. And initial specific volumes are $N(0)$ and $N(s)$ with a suction. $\lambda(s)$ is slope of the normal compression line at a suction of s, and κ is slope of the unloading-reloading line. κ is the same but $\lambda(0)$ is different from $\lambda(s)$ due to a suction. At partially saturated preconsolidation stress of point 1, it proceeds an initially unloading at constant suction and a subsequent reduction in suction, from s to zero, at constant stress (p_0), the sample follows the path 1-2-3.

The slope of the normal compression line of the soil at a constant soil suction of s can be

calculated as follow:

$$\lambda(s) = \lambda(0)\Big[(1-r)\,\exp(-\beta\, s) + r\Big] \tag{1.11}$$

where β and r are curve fitting parameters and $\lambda(0)$ is slope of the normal consolidation line at saturated state.

Wheeler et al.[95] presented a more general form for the LC yield curve, equation (1.10). Their LC yield curve has a shape similar to the Alonso's LC model[4] as shown in Figure 1.16.

$$\Big(\lambda(s)-\kappa\Big)\ln\left(\frac{p_0}{p_{at}}\right) = \Big(\lambda(0)-\kappa\Big)\ln\left(\frac{p_0^*}{p_{at}}\right) + N(s) - N(0) + \kappa_s \ln\left(\frac{s+p_{at}}{p_{at}}\right) \tag{1.12}$$

where, p_{at} is atmospheric pressure (i.e., $\approx$ 100 kPa)

1.3.3.5 Elasto-plastic framework for partially saturated soils

Alonso el al.[6] proposed a critical state framework for partially saturated soil involving four state variables, such as net mean stress $\sigma - p_a$, deviatoric stress q, suction s and specific volume ν. Their critical state framework is an isotropic normal compression hyperline, representing soil states when isotropically loaded to virgin conditions. The term hyperline is used here to describe a locus of state defined within a four-dimensional mathematical space by two independent equations (q, ν).

A critical state hyperline represents soil states when sheared to critical conditions defined by another two independent equations. A section of state boundary hypersurface, joining the critical state and normal compression hyperlines, can be postulated. This state boundary hypersurface would be defined by a single equation relating the four state variables[95],

$$\nu = f(p, q, s) \tag{1.13}$$

The critical state framework is an elasto-plastic form of constitutive model with elastic behavior when the soil state lies inside the state boundary hypersurface and with starting plastic strains when the state boundary hypersurface is reached. As shown in Figure 1.15, the general shape of the yield surface enables several important features of partially saturated soil behavior to

be modelled, for instance, an increase of strength with suction and the possibility of collapse due to reduction of suction.

Figure 1.15 shows that initial state of soil A inside the current position of the yield surface can be started to yield into three different ways. Isotropic loading path ABC can be produced by an increase of p, Shearing path ADE can be produced by an increase of q, and wetting path AFG can be produced by a reduction of s. Also any nonlinear path can be produced by changing p, q and s simultaneously. A yield curve in $p-s$ space generally produced by isotropic loading is called a yield locus to distinguish between yielding in $p-s$ and $p-q$, and the yield locus is shearing in $p-q-s$ space will produce a yield envelope.

The yield surface in saturated soils is represented by a yield envelope in $q-p$ space and a corresponding coupled trace in $p-\nu$ space. For yielding of partially saturated soils, yield surface should be defined in $p-s$ space for isotropic loading. Thus many researchers suggest their yield loci to define the relation between net mean stress and suction as shown in Figure 1.16. It was noticed that collapse of the soil occurred during both drying and wetting processes[6, 39, 95]. Figure 1.16 shows that the compression curve with respect to soil suction can also be approximated by two straight lines. Two horizontal lines are used to describe the yielding boundary of the soil suction, that is suction increment boundary denoted as SI; and suction decrement boundary denoted as SD.

Also, the yield boundary at a certain stress state for partially saturated soils proposed by Alonso et al.[6] is not continuous. Delage and Graham[28] suggested that the yield boundary should be a continuous curve. Tang and Graham[84] suggested a new yield curve called the Loading-collapse and Suction increase Yield (LSY) curve. And, a schematic illustration of the state surface predicted using the Blatz and Graham[11] model is shown in Figure 1.17.

The above series of models[6, 95, 11] require measurements of a few soil parameters to calibrate the models. Alonso et al.[6] suggested two series of tests to obtain the data for calibration; namely, (i) tests that involve isotropic drained compression (loading and unloading) at several constant suction values to provide parameters, such as p^c, p_0^*, $\lambda(0)$, κ, r, and β; and (ii) tests that

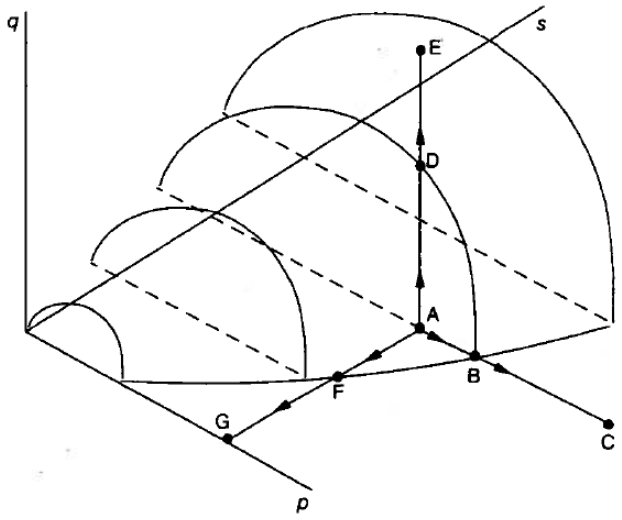

Figure 1.15: Yield surface for partially saturated soil (Wheeler and Sivakumar, 1995)

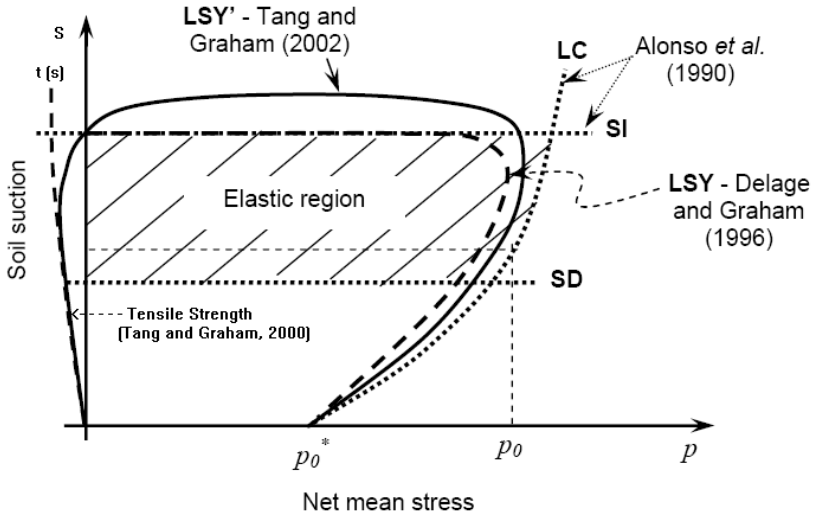

Figure 1.16: Yield boundaries of a partially saturated soil proposed by researchers (Tang and Graham, 2002)

involve drying-wetting cycles at a given net mean stress to provide parameters: s_0, λ_s, κ_s.

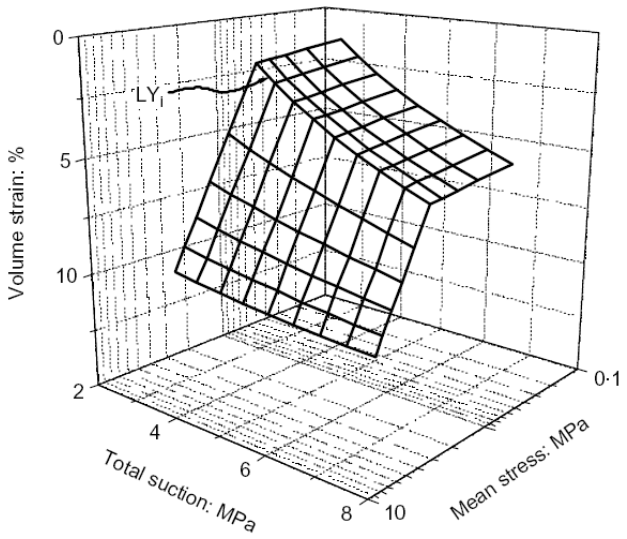

Figure 1.17: 3-dimensional p-s-ϵ_v state surface (Blatz and Graham, 2003)

Figure 1.18 shows the stress-strain behavior by considering the micro and macro structure of soils. Mechanical behaviors of the micro and macro structures were modeled separately. The authors assumed that the deformation for the micro structure is independent of that of the macro structure; but the deformation of the macro structure depends on that of the micro structure[39]. The model provides a good explanation for the mechanical and physical behavior of partially saturated soils; however, the relationship between the deformation of the macro structure and the micro structure is empirical and extremely difficult to verify. Hence, the model did not receive much attention due to its complexity.

Most of the recently proposed elasto-plastic models for a partially saturated soil make use of stress state variables incorporating a soil property[47, 91, 94, 83]. The development of this series of models is similar to that of the Alonso et al.[6] model but the net mean stress was replaced by a stress variable that incorporates one or more soil properties. They assume in their models that the degree of saturation is dependent on the net mean stress, but the assumption might be not valid

due to experimental data of Vu and Fredlund[92] and Huat et al.[44].

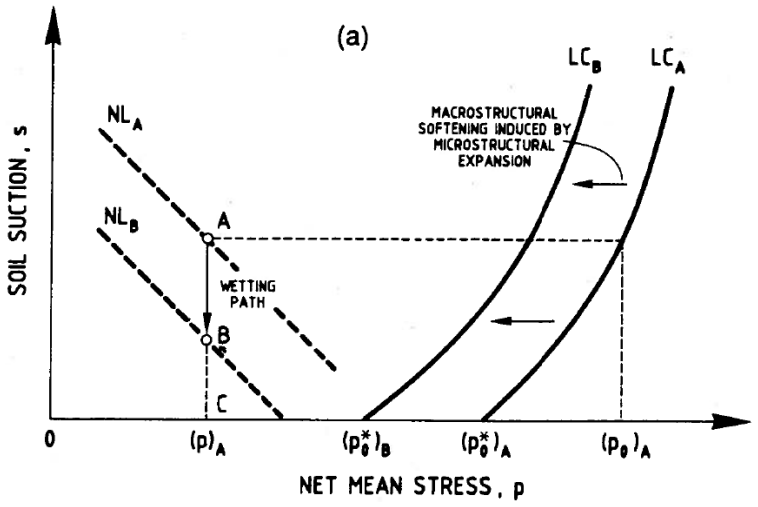

Figure 1.18: Schematic illustration of the yield curves of double structures of a soil (Gens and Alonso, 1992)

Figure 1.19 shows the difference of the relationship between the saturation rate and net mean stress. Vu and Fredlund[92] provides the proof that the saturation rate does not affect net mean stress in Regina clay. On the contrary, Huat et al.[44] performed a laboratory test that showed there is difference between water content and saturation rate for net mean stress at a constant suction.

Hence, a significant improvement in the development of the stress-strain constitutive models for partially saturated soils is to take into account the effect of hydraulic hysteresis. Two models that are more appropriate in this area are the Wheeler et al.[94] and the Tamagnini[83] models. Figure 1.20 shows the hysteresis model for the SWCC incorporated in the Wheeler et al.[94] model, and the good agreement between numerical results (solid line) and experimental data (dots) in the right figure. It marked an important point in the historical development for describing the transition between saturated and partially saturated response, irreversible compression during the drying stages of wetting–drying cycles, and the influence of a wetting–drying cycle on subsequent

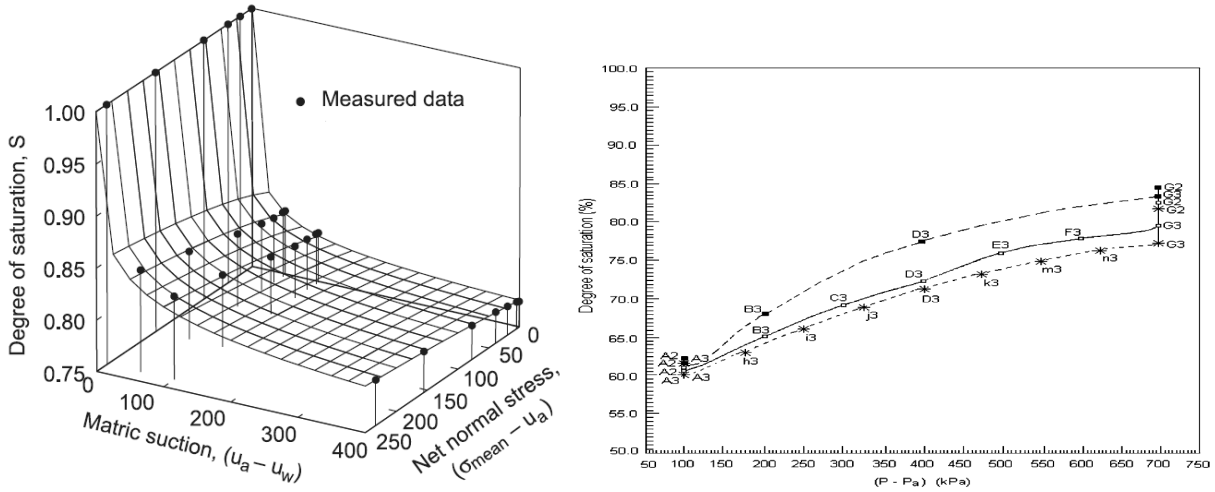

Figure 1.19: Difference between saturation rate and net mean stress (Vu and Fredlund, 2006; Huat et al., 2006)

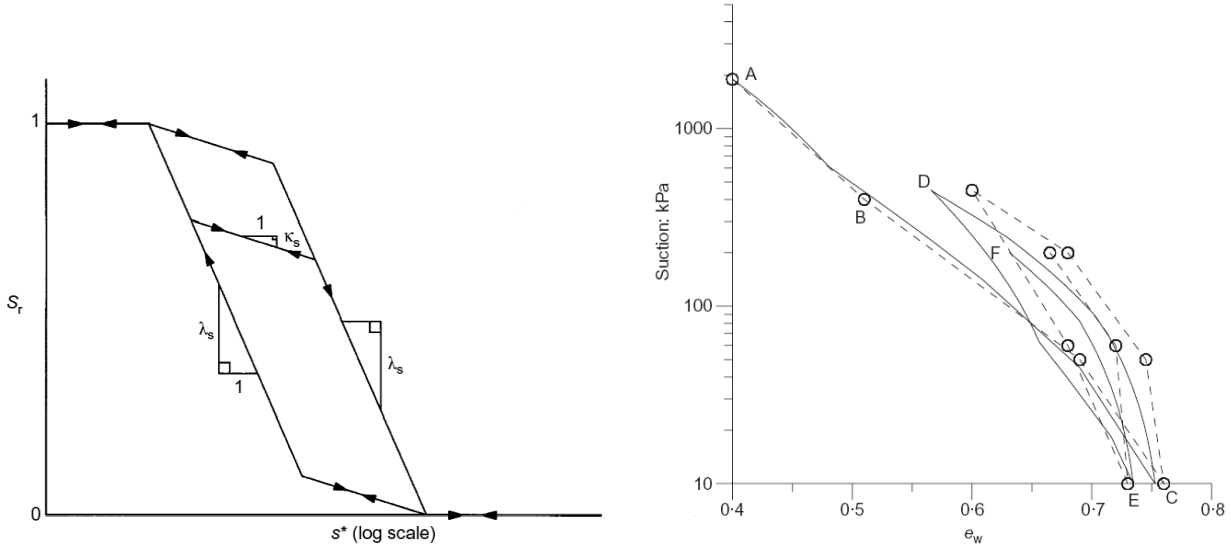

Figure 1.20: Soil property incorporated in a constitutive model and its appropriate agreement (Wheeler et al., 2003; Tamagnini, 2004)

behavior during isotropic loading.

As the result, although many researchers have studied the constitutive equations in regards to both two independent stress variables and stress variables incorporating soil properties, they do not exactly define the variables used for the description of a stress. One of the reasons is that net mean stress and soil suction, which are defined as state of stress in partially saturated soils in terms of two independent variables, can lead to complex constitutive equations with intractable stress-strain relationships because the net mean stress ($\sigma - p_a$) is described at the macroscopic scale and the suction stress ($p_a - p_w$) is described at the pore scale[49]. Hence, more and more researchers carry out their laboratory tests to approach accurate agreement between numerical simulation and experimental results for stress-strain-strength behavior of partially saturated soils.

For elasto-plastic constitutive model for partially saturated soils, a more appropriate yield locus in $p - s$ space could be developed based on the Barcelona Basic Model (BBM)[6]. The shortcomings of BBM that Wheeler et al.[93] discussed some aspects of normal compression lines for different values of suction should be make up for a limitation on the applicability of the BBM. In addition, generally measurement of the soil-water characteristic curve (SWCC) in the laboratory is commonly conducted under zero confining pressure, but the soil is under a confining stress in the field. Hence it should be considered some study the effects of the confining stresses on SWCC[88].

Lastly, in the experiments, the soil samples were subjected to isotropic consolidation under constant suctions. The results show that different compaction pressures produce different fabrics (density) and therefore affect the behavior of the soil. The results also show that the value of yield stress and the location of the loading-collapse (LC) yield curve are functions of soil fabric. It is shown that the slopes of normal consolidation lines for densely and loosely compacted samples differ in partially saturated conditions but are the same in saturated soils. Soil fabric should be considered in order to have proper elasto-plastic constitutive model for partially saturated soils[30].

For fitting material parameters for partially saturated Cam-clay plasticity model, comprehensive laboratory test for partially saturated soil is required. Material parameters for partially saturated soils can be obtained from soil-water characteristic curve and triaxial test for partially

saturated soils. Using van Genuchten[90] model for soil water characteristic curve and partially saturated hydraulic conductivity, the functions of those may be verified and the permeability measurement of partially saturated soil can be calculated from the results of soil-water characteristic curve test. Then the remaining elasto-plasticity parameters are determined from triaxial test data on partially saturated soil. Parameters will be taken from the literature.

1.4 Novel Contributions of Thesis

The novelty of this study rests on the following combined features of the research: (1) monolithic coupling (for semi-implicit and fully-implicit nonlinear), (2) comparison of with and without pore air pressure ($p_a \neq 0$ and $p_a \approx 0$), (3) porosity dependent permeability, (4) comparison of various effective stress definitions, (5) adding partially saturated hyperelasto-plastic Cam-clay model to this framework, and (6) using this numerical framework, simulate plane strain finite element analysis of infiltration into a partially saturated slope under gravity loading.

This contribution allows me to compare within *one mathematical and finite element implementation framework* these various features, and their influence on a plane strain finite element analysis of infiltration into partially saturated slope under gravity loading. The research is currently limited to small strain and rotations. These comparisons are difficult, if not nearly impossible, to make in commercial coupled finite element software like SEEP/W–SIGMA/W, PlaxFlow–Plaxis, or Abaqus, because we do not have access to the source code to make such modifications ourselves. This is particularly important for partially saturated soils, whereas for the saturated case, the different commercial software produce almost the same results for the same soil solid skeleton constitutive model.

1.5 Features of Research

- Numerical finite element implementation and time integration schemes of semi-implicit linear and fully-implicit nonlinear method (for linear isotropic elastic solid skeleton) demonstrate the efficiency of the algorithm as well as a comparison to an analytical solution for

water flow through partially saturated soils.

- Difference between biphasic and triphasic deformation during water infiltration is verified in the vadose zone. The role of the air phase in deformable partially saturated soils can be analyzed depending on the interaction among phases through the balance equations and constitutive behavior of soil solid skeleton

- Monolithic coupled hydromechanical model is preferred to analyze the soil deformation and seepage problem of a partially saturated soil subjected to external loads and rainfall simultaneously. But, most commercial problems used in geotechnical engineering conduct staggered coupled finite element analysis because of ease of implementation.

- The partially saturated hydraulic conductivity is porosity-dependent. It considers the soil solid skeleton's behavior by external loading influences on the partially saturated permeability each time step. The effect of porosity produces a difference of pore water pressure or matric suction according to the passage of time.

- The application of various definitions of effective stress, such as Bishop[8], Lewis and Schrefler[58], Borja[17], Khalili et al.[49], and Lu et al.[63] in this coupled FE model shows the merit and shortcoming of each implementation, and is reviewed.

- In order to enhance soil behavior beyond elastic regime, hyperelasto-plastic Cam-clay model is derived and implemented for partially saturated condition. The constitutive model is nonlinear and has energy-conserving elasticity coupled with Cam-clay plasticity model.

Chapter 2

Triphasic Poro-Elasticity

2.1 Balance of Mass

For three-phase soil mixture composed of solid(s), water(w) and air(a), the volume and mass of mixture should be defined in the mathematical description. I follow the formulations by Coussy[23], Borja[12] and de Boer[27], but consider only small strains. The volume of the mixture is $v = v_s + v_w + v_a$ and the corresponding total mass is $m = m_s + m_w + m_a$. Similarly, for α phase, $m_\alpha = \rho^{\alpha R} v_\alpha$ (nearly homogeneous), where $\alpha = s, w, a$; and $\rho^{\alpha R}$ is the true mass density of the α phase. The volume fraction occupied by the α phase is given by $n^\alpha = v_\alpha / v$, and thus, for water, air and solid,

$$n^s + n = n^s + n^w + n^a = 1$$

where the porosity $n = \dfrac{v_w + v_a}{v} = n^w + n^a$. If material is homogeneous, $n^\alpha = \dfrac{v_\alpha}{v}$, whereas if heterogeneous the volume fraction at a material point $n^\alpha = \dfrac{\mathrm{d}v_\alpha}{\mathrm{d}v}$ for a differential volume of the mixture. The partial mass density of the α phase is given by $\rho^\alpha = n^\alpha \rho^{\alpha R}$, and thus

$$\rho^s + \rho^w + \rho^a = \rho$$

where, $\rho = m/v$ is the total mass density of the mixture. As a general notation, phase designations in the superscript form (for example, ρ^α) pertain to average or partial quantities, and in the superscript form with R (for example, $\rho^{\alpha R}$) to intrinsic or real quantities. Based on the current configuration of the mixture (for small strains, theoretically no different than the reference or

current configurations), the mass balance equations describe the motions of the water and air phases relative to the motion of the solid phase.

We denote the instantaneous intrinsic velocities of the solid, water, and air phases by $\boldsymbol{v}$, $\boldsymbol{v}_w$ and $\boldsymbol{v}_a$, respectively, and the material time derivative with respect to the solid phase and the α phase motion,

$$\frac{\mathrm{D}(\cdot)}{\mathrm{D}t} = \frac{\partial(\cdot)}{\partial t} + \mathrm{grad}(\cdot)\cdot\boldsymbol{v} \quad \text{or} \quad \frac{\mathrm{D}^\alpha(\cdot)}{\mathrm{D}t} = \frac{\mathrm{D}(\cdot)}{\mathrm{D}t} + \mathrm{grad}(\cdot)\cdot\tilde{\boldsymbol{v}}_\alpha, \qquad (\alpha = w, a) \tag{2.1}$$

where $\tilde{\boldsymbol{v}}_\alpha = \boldsymbol{v}_\alpha - \boldsymbol{v}$ is the water or air velocity relative to the solid velocity $\boldsymbol{v}$. The balance of mass of the mixture is obtained by summing the balance of mass equations for each constituent $\alpha\,(= s, w, a)$, but I will end up with separate mass balance equations for water and air using the mass balance of solid. Ignoring mass exchanges among the three phases (no chemical reactivity), balance of mass for the solid, water and air phases then can be written as

$$\frac{\partial \rho^s}{\partial t} + \mathrm{div}(\rho^s \boldsymbol{v}) = 0 \tag{2.2}$$

$$\frac{\partial \rho^\alpha}{\partial t} + \mathrm{div}(\rho^\alpha \boldsymbol{v}) = -\mathrm{div}(\rho^\alpha \tilde{\boldsymbol{v}}_\alpha) \qquad (\alpha = w, a) \tag{2.3}$$

Thus, assuming incompressible solid particles and water (ρ^{sR} and ρ^{wR} are constants), we can write for three-phase motion, respectively,

$$\cancel{\rho^{sR}}\frac{\partial n^s}{\partial t} + \cancel{\rho^{sR}}\mathrm{div}(n^s\boldsymbol{v}) = \frac{\mathrm{D}n^s}{\mathrm{D}t} + n^s\,\mathrm{div}\boldsymbol{v} = 0 \tag{2.4}$$

$$\cancel{\rho^{wR}}\frac{\partial n^w}{\partial t} + \cancel{\rho^{wR}}\mathrm{div}(n^w\boldsymbol{v}) = -\cancel{\rho^{wR}}\,\mathrm{div}(n^w\tilde{\boldsymbol{v}}_w) \tag{2.5}$$

$$\frac{\partial \rho^a}{\partial t} + \mathrm{div}(\rho^a\boldsymbol{v}) = \frac{\mathrm{D}\rho^a}{\mathrm{D}t} + \rho^a\,\mathrm{div}\boldsymbol{v} = -\mathrm{div}(\rho^a\tilde{\boldsymbol{v}}_a) \tag{2.6}$$

The incompressibility assumption for solid and water is reasonable for geomaterials like saturated sand, but ρ^{aR} could be changed due to compressibility of air. The balance of mass for the saturated biphasic mixture becomes

$$\begin{gathered}\frac{\mathrm{D}\rho}{\mathrm{D}t} + \rho\,\mathrm{div}\boldsymbol{v} = -\mathrm{div}\boldsymbol{w} \qquad \left(\text{in index form, } \frac{\mathrm{D}\rho}{\mathrm{D}t} + \rho\, v_{i,i} = -w_{i,i}\right) \\ \boldsymbol{w} = \sum_{\alpha=w} \boldsymbol{w}^\alpha, \quad \boldsymbol{w}^\alpha = \rho^\alpha\tilde{\boldsymbol{v}}_\alpha, \quad \tilde{\boldsymbol{v}}_\alpha = \boldsymbol{v}_\alpha - \boldsymbol{v}\end{gathered} \tag{2.7}$$

where, $\boldsymbol{w}^{\alpha}$ (for α is water) is the relative flow vector of the α phase with respect to the solid matrix, given explicitly by the relations.

The flow vector $\boldsymbol{w}^{\alpha}$ has the "physical significance that its scalar product with the unit normal vector $\mathbf{n}$ to a unit surface area attached to the solid matrix is the mass flux of the α phase relative to the solid matrix flowing across the same unit area," i.e.[12],

$$m^{\alpha} = \int_{a} \boldsymbol{w}^{\alpha} \cdot \mathbf{n} \, \mathrm{d}a = \int_{v} \mathrm{div}(\boldsymbol{w}^{\alpha}) \, \mathrm{d}v \tag{2.8}$$

where m^{α} is the net mass flux and v is total volume. Equation (2.8) shows the net mass flux for the balance of mass for the solid, water and air phases of equation (2.3). If there is no relative motion between the α phase and the solid phase such that the mass m_{α} contained in the volume v moves exactly with the solid matrix, then $\tilde{\boldsymbol{v}}_{\alpha} = \mathbf{0}$ and $\boldsymbol{w}^{\alpha} = \mathbf{0}$. But it is possible that $m^{\alpha} = 0$ even if $\boldsymbol{w}^{\alpha} \neq \mathbf{0}$ provided that $\boldsymbol{w}^{\alpha}$ is divergence free. And then, the net mass flux is zero due to the α material displaced by another same α phase material[12].

The barotropic flows[67] are defined to be flows satisfying a functional relation independent of temperature:

$$f(p_{\alpha}, \rho^{\alpha R}) = 0$$

where p_{α} is the mean stress (or pore pressure) for constituent α. The barotropic flows exist for each phase as follow,

$$\frac{\mathrm{D}\rho^{\alpha R}}{\mathrm{D}t} = \frac{\mathrm{D}\rho^{\alpha R}}{\mathrm{D}p_{\alpha}} \frac{\mathrm{D}p_{\alpha}}{\mathrm{D}t}$$

And so,

$$\frac{\mathrm{D}\rho^{\alpha}}{\mathrm{D}t} = \frac{\mathrm{D}(n^{\alpha}\rho^{\alpha R})}{\mathrm{D}t} = n^{\alpha} \frac{\mathrm{D}\rho^{\alpha R}}{\mathrm{D}t} + \rho^{\alpha R} \frac{\mathrm{D}n^{\alpha}}{\mathrm{D}t} = n^{\alpha} \frac{\mathrm{D}\rho^{\alpha R}}{\mathrm{D}p_{\alpha}} \frac{\mathrm{D}p_{\alpha}}{\mathrm{D}t} + \rho^{\alpha R} \frac{\mathrm{D}n^{\alpha}}{\mathrm{D}t} \tag{2.9}$$

where p_{α} denotes the intrinsic pressure of α phase.

The bulk modulus of the α phase is

$$K_{\alpha} = \rho^{\alpha R} \frac{\mathrm{D}p_{\alpha}}{\mathrm{D}\rho^{\alpha R}} \quad \Longrightarrow \quad \frac{\mathrm{D}\rho^{aR}}{\mathrm{D}p_{a}} = \frac{\rho^{aR}}{K_{a}} \qquad \text{(for compressible air phase)} \tag{2.10}$$

If the bulk modulus of air phase is constant,

$$p_{a} = K_{a} \ln \rho^{aR} \quad \Longrightarrow \quad \frac{p_{a}}{K_{a}} = \ln \rho^{aR}$$

$$\rho^{aR} = \exp\left[\frac{p_a}{K_a}\right] \tag{2.11}$$

Likewise, for solid and water phases,

$$\rho^{sR} = \exp\left[\frac{p_s}{K_s}\right] \ , \quad \rho^{wR} = \exp\left[\frac{p_w}{K_w}\right] \tag{2.12}$$

but I assume $K_s \to \infty$ and $K_w \to \infty$ (incompressible solid and water).

Recall barotropic flow assumption for air phase which is a compressible phase,

$$\begin{aligned}\frac{\mathrm{D}\rho^a}{\mathrm{D}t} = \frac{\mathrm{D}(n^a\rho^{aR})}{\mathrm{D}t} &= \frac{\mathrm{D}n^a}{\mathrm{D}t}\rho^{aR} + n^a\frac{\mathrm{D}\rho^{aR}}{\mathrm{D}t} \\ &= \rho^{aR}\frac{\mathrm{D}n^a}{\mathrm{D}t} + \frac{n^a\rho^{aR}}{K_a}\frac{\mathrm{D}p_a}{\mathrm{D}t}\end{aligned}$$

where,

$$\frac{\mathrm{D}\rho^{aR}}{\mathrm{D}t} = \frac{\mathrm{D}\rho^{aR}}{\mathrm{D}p_a}\frac{\mathrm{D}p_a}{\mathrm{D}t} = \frac{\rho^{aR}}{K_a}\frac{\mathrm{D}p_a}{\mathrm{D}t}$$

Then, balance of mass for air is

$$\rho^{aR}\frac{\mathrm{D}n^a}{\mathrm{D}t} + \frac{n^a\rho^{aR}}{K_a}\frac{\mathrm{D}p_a}{\mathrm{D}t} + n^a\rho^{aR}\mathrm{div}\boldsymbol{v} = -\mathrm{div}(\rho^a\tilde{\boldsymbol{v}}_a) \tag{2.13}$$

$$\frac{\mathrm{D}n^a}{\mathrm{D}t} + \frac{n^a}{K_a}\frac{\mathrm{D}p_a}{\mathrm{D}t} + n^a\mathrm{div}\boldsymbol{v} = -\frac{1}{\rho^{aR}}\mathrm{div}(\rho^a\tilde{\boldsymbol{v}}_a) \tag{2.14}$$

For void fractions $\psi^w = v_w/v_v$, $\psi^a = v_a/v_v$ and $v_v = v_a + v_w$, void fractions regarding volume fractions are written as

$$\begin{aligned}n^s + n^w + n^a &= n^s + \psi^w(1-n^s) + \psi^a(1-n^s) \\ &= n^s(1-\psi^w-\psi^a) + \psi^w + \psi^a = 1 \quad (\text{where, } 1-\psi^w-\psi^a = 0)\end{aligned}$$

Defined as the ratio between the volume of the α phase for the total void volume,

$$\psi^w = \frac{v_w}{v_w+v_a} = \frac{n^w}{1-n^s}, \quad \psi^a = \frac{v_a}{v_w+v_a} = \frac{n^a}{1-n^s}, \quad \psi^w + \psi^a = 1 \tag{2.15}$$

Generally, ψ^w is commonly denoted as the degree of saturation S ($\psi^w = S$) in geotechnical engineering, so $\psi^a = (1-S)$. The material time derivative with respect to the solid phase motion is here used for description of void fractions for three phase motion. Thus volume of voids $v_v = v_a + v_w$ and then, $\psi^\alpha = \dfrac{v_\alpha}{v_v} = \dfrac{n^\alpha}{1-n^s}$, $\alpha = a$ and w. For air phase, $\psi^a = \dfrac{n^a}{1-n^s}$, and

$$\frac{\mathrm{D}n^a}{\mathrm{D}t} = (1-n^s)\frac{\mathrm{D}\psi^a}{\mathrm{D}t} - \psi^a\frac{\mathrm{D}n^s}{\mathrm{D}t} \tag{2.16}$$

If we assume the saturation rate S is a function of the suction $s(= p_a - p_w)$, then

$$\frac{\mathrm{D}\psi^a}{\mathrm{D}t} = -\frac{\mathrm{D}S(s)}{\mathrm{D}t} = -\frac{\partial S}{\partial s}\left(\frac{\mathrm{D}p_a}{\mathrm{D}t} - \frac{\mathrm{D}p_w}{\mathrm{D}t}\right) \tag{2.17}$$

where $\psi^a = 1 - S$. Then, the balance of mass for air with $\dfrac{\mathrm{D}n^s}{\mathrm{D}t} = -n^s \mathrm{div}\,\boldsymbol{v}$ from the balance of mass for solid is

$$\begin{aligned} -(1-n^s)\frac{\partial S}{\partial s}\left(\frac{\mathrm{D}p_a}{\mathrm{D}t} - \frac{\mathrm{D}p_w}{\mathrm{D}t}\right) + (1-S)n^s \mathrm{div}\,\boldsymbol{v} + \frac{n^a}{K_a}\frac{\mathrm{D}p_a}{\mathrm{D}t} + n^a \mathrm{div}\,\boldsymbol{v} \\ = -\frac{1}{\rho^{aR}}\mathrm{div}(\rho^a \tilde{\boldsymbol{v}}_a) \end{aligned} \tag{2.18}$$

where,

$$\begin{aligned} n^w &= n\psi^w = nS \\ n^a &= n\psi^a = n(1-S) \\ n &= n^w + n^a \\ n^s &= 1 - n \\ \frac{\mathrm{D}S}{\mathrm{D}t} &= \frac{\partial S}{\partial s}\left(\frac{\mathrm{D}p_a}{\mathrm{D}t} - \frac{\mathrm{D}p_w}{\mathrm{D}t}\right) \\ \frac{\mathrm{D}p_a}{\mathrm{D}t} - \frac{\mathrm{D}p_w}{\mathrm{D}t} &= \frac{\mathrm{D}s}{\mathrm{D}t} = \frac{\partial s}{\partial t} + \frac{\partial s}{\partial \mathbf{x}} \cdot \boldsymbol{v} \end{aligned}$$

Void volume fraction n (porosity) can be related to soil skeleton volumetric strain through $\dot{n} = (1-n)\dot{\epsilon}_v$, where $\dot{\square}$ denotes material time derivative relative to the solid phase motion.

For the balance of mass for water phase in mixture of equation (2.5),

$$\frac{\mathrm{D}n^w}{\mathrm{D}t} + n^w \mathrm{div}\boldsymbol{v} = -\mathrm{div}(n^w \tilde{\boldsymbol{v}}_w) \tag{2.19}$$

where, $\tilde{\boldsymbol{v}}^w (= n^w \tilde{\boldsymbol{v}}_w)$ is called the superficial Darcy velocity, and $\tilde{\boldsymbol{v}}_w$ is the real seepage velocity. It is written in terms of suction,

$$\begin{aligned} &\frac{\mathrm{D}n^w}{\mathrm{D}t} = (1-n^s)\frac{\mathrm{D}\psi^w}{\mathrm{D}t} - \psi^w \frac{\mathrm{D}n^s}{\mathrm{D}t} \qquad \left(\frac{\mathrm{D}n^s}{\mathrm{D}t} = -n^s \mathrm{div}\boldsymbol{v}\right) \\ &\frac{\mathrm{D}\psi^w}{\mathrm{D}t} = \frac{\partial S}{\partial s}\frac{\mathrm{D}s}{\mathrm{D}t} = \frac{\partial S}{\partial s}\left(\frac{\mathrm{D}p_a}{\mathrm{D}t} - \frac{\mathrm{D}p_w}{\mathrm{D}t}\right), \qquad \psi^w = S(s) \end{aligned}$$

And, so the balance of mass for void phase in mixture can be written as water (w) and air (a) phase, respectively,

$$
\begin{aligned}
(w): \quad & (1-n^s)\frac{\mathrm{D}S}{\mathrm{D}t} + Sn^s \mathrm{div}\,\boldsymbol{v} + n^w \mathrm{div}\,\boldsymbol{v} = -\mathrm{div}(n^w \tilde{\boldsymbol{v}}_w) \\
(a): \quad & -(1-n^s)\frac{\mathrm{D}S}{\mathrm{D}t} + (1-S)n^s \mathrm{div}\,\boldsymbol{v} + \frac{n^a}{K_a}\frac{\mathrm{D}p_a}{\mathrm{D}t} + n^a \mathrm{div}\,\boldsymbol{v} = -\frac{1}{\rho^{aR}}\mathrm{div}(\rho^a \tilde{\boldsymbol{v}}_a) \\
& \frac{\mathrm{D}S}{\mathrm{D}t} = \frac{\partial S}{\partial s}\left(\frac{\mathrm{D}p_a}{\mathrm{D}t} - \frac{\mathrm{D}p_w}{\mathrm{D}t}\right)
\end{aligned}
\tag{2.20}
$$

These two coupled equations will be used to solve for p_a and p_w, along with displacement $\boldsymbol{u}$ from balance of linear momentum. Thus, the above formulation includes the compressible air phase and incompressible solid and water phases for all the constituent phases.

2.2 Balance of Linear Momentum

The total Cauchy stress tensor $\boldsymbol{\sigma}$ is obtained from the sum of the Cauchy partial stress tensors, where $\boldsymbol{\sigma}^\alpha$ denotes the Cauchy partial stress tensor for the α phase (α = solid, water and air).

$$\boldsymbol{\sigma} = \boldsymbol{\sigma}^s + \boldsymbol{\sigma}^w + \boldsymbol{\sigma}^a \tag{2.21}$$

Fredlund and Morgenstern[31] suggested that the fourth-phase stress is contractile skin stress arising from the presence of meniscus between two solids, but we ignore this stress initially for simplicity.

The balance of linear momentum for α phase ignoring inertial terms is

$$\mathrm{div}(\boldsymbol{\sigma}^\alpha) + \rho^\alpha \boldsymbol{g} + \mathbf{h}^\alpha = \mathbf{0} \tag{2.22}$$

where, $\boldsymbol{g}$ is the vector of gravity acceleration, $\mathbf{h}^\alpha$ is the resultant body force per unit current volume exerted on the α phase by the other two phases. The forces $\mathbf{h}^\alpha$ are interaction volume forces between the constituents of the mixture and thus satisfy the relations $\mathbf{h}^s + \mathbf{h}^w + \mathbf{h}^a = \mathbf{0}$.

From equation (2.22), the balance of linear momentum for the entire mixture is simply obtained as follows,

$$\mathrm{div}(\boldsymbol{\sigma}) + \rho\,\boldsymbol{g} = \mathbf{0} \tag{2.23}$$

In order to find $\boldsymbol{u}$, p_w and p_a, the total stress can be represented as[8]

$$\boldsymbol{\sigma} = \boldsymbol{\sigma}' - p_a\mathbf{1} + \chi(p_a - p_w)\mathbf{1} \tag{2.24}$$

If $\chi = 1$ (saturated), then $\boldsymbol{\sigma} = \boldsymbol{\sigma}' - p_w\mathbf{1}$ (the classical effective stress equation by Terzaghi[87]). The pore pressures p_a and p_w are positive in compression, while mean stress of soil solid skeleton $p' = \frac{1}{3}\text{tr}(\boldsymbol{\sigma}')$ is positive in tension. Lewis & Schrefler[58] and Borja[12] derived through thermodynamics that the effective stress parameter $\chi = S$. In which S is the saturation rate. Other choices for χ include that by Khalili[49]

$$\chi = \begin{cases} \left(\dfrac{s}{s_e}\right)^{-0.55} & \text{if } \; s \geq s_e \\ 1 & \text{if } \; s \leq s_e \end{cases} \tag{2.25}$$

where s_e is suction value marking the transition between saturated and partially saturated states. For wetting process of SWCC, s_e is equal to the air expulsion value, whereas for drying processes of SWCC, s_e is equal to the air entry value.

As the alternative of effective stress parameter χ, the suction stress σ^s that Lu et al.[66, 63] presented can be considered. They proposed a form of suction stress as the extension of Terzaghi's effective stress σ' (positive in tension) in saturated condition,

$$\begin{gathered} \sigma' = (\sigma + p_a) + \sigma^s, \quad \sigma^s = -S_e\,(p_a - p_w) \\ S_e = \frac{S - S_r}{1 - S_r} = \left[1 + (\alpha s)^{\mathrm{n}}\right]^{-\mathrm{m}} \end{gathered} \tag{2.26}$$

where S_e is effective degree of saturation, s is matric suction $(p_a - p_w)$, and α, n, m are curve fitting parameters of van Genuchten[90]'s SWCC equation. The effective stress (equation (2.26)) is defined as a closed-form expression for suction stress for the full range of matric suction,

$$\begin{cases} \sigma^s = -(p_a - p_w) & ;\, p_a - p_w \leq 0 \\ \sigma^s = -\dfrac{p_a - p_w}{\left[1 + (\alpha s)^{\mathrm{n}}\right]^{\mathrm{m}}} & ;\, p_a - p_w \geq 0 \end{cases} \tag{2.27}$$

In general, most researchers assume χ is a function of suction, such that we write $\chi(s)$. We will investigate this choice in more detail during the numerical examples.

2.3 Summary of Balance Equations and Constitutive Equations

2.3.1 Triphasic balance and constitutive equations

In order to solve for 3 unknowns $(\boldsymbol{u}, p_w, p_a)$ using given 3 equations, the balance equations can be summarized as follows,

1) The balance of linear momentum of a mixture:

$$\begin{aligned} \mathrm{div}\boldsymbol{\sigma} + \rho\,\boldsymbol{g} &= \mathbf{0} \\ \rho &= \rho^s + \rho^w + \rho^a \\ \boldsymbol{\sigma} &= \boldsymbol{\sigma}' - p_a\mathbf{1} + \chi(s)\Big(p_a - p_w\Big)\mathbf{1} = \boldsymbol{\sigma}' - \bar{p}\mathbf{1} \\ \bar{p} &= p_a - \chi(s)\Big(p_a - p_w\Big) \end{aligned} \tag{2.28}$$

2) The balance of mass of water (porosity $n = n^w + n^a = 1 - n^s$):

$$\begin{aligned} n\frac{\partial S}{\partial s}(\dot{p}_a - \dot{p}_w) + S\mathrm{div}\,\boldsymbol{v} &= -\mathrm{div}\,\tilde{\boldsymbol{v}}^w \\ \dot{n} &= (1-n)\dot{\epsilon}_v \\ \dot{\epsilon}_v &= \mathrm{tr}(\dot{\boldsymbol{\epsilon}}) \end{aligned} \tag{2.29}$$

3) The balance of mass of air:

$$\left[-n\frac{\partial S}{\partial s} + \frac{n(1-S)}{K_a}\right]\dot{p}_a + n\frac{\partial S}{\partial s}\dot{p}_w + (1-S)\,\mathrm{div}\,\boldsymbol{v} = -\frac{1}{\rho^{aR}}\,\mathrm{div}(\rho^{aR}\tilde{\boldsymbol{v}}^a) \tag{2.30}$$

This study considers material properties to define constitutive equations as follows,

1) Relationship between degree of saturation and suction stress by van Genuchten[90]:

$$S = f(s) \quad \text{and} \quad s = p_a - p_w \tag{2.31}$$

$$f(s) = \left[1 + \left(\frac{s}{\mathrm{a}}\right)^{\mathrm{n}}\right]^{-\mathrm{m}}$$

2) Effective stress:

$\boldsymbol{\sigma}'$ (considering Cam-clay plasticity and partially saturated soil model

from the balance of linear momentum for a mixture)

$$\boldsymbol{\sigma}' = \boldsymbol{\sigma} + \bar{p}\,\mathbf{1} \qquad \left(\bar{p} = p_a - \chi(s)(p_a - p_w)\right) \tag{2.32}$$

$$f(\boldsymbol{\sigma}', s, p_c) = 0 \qquad \text{(Yield Function)} \tag{2.33}$$

where, $\boldsymbol{\sigma}'$ is governed by soil solid skeleton constitutive response and p_c is saturated preconsolidation pressure.

Table 2.1: Parameter values for triphasic mixture

$\varkappa$ (fine sands and silts)	$\eta_w(20\ ^{\circ}\mathrm{C})$	$\eta_a(20\ ^{\circ}\mathrm{C})$	$K_a(20\ ^{\circ}\mathrm{C})$
$10^{-12} \sim 10^{-16}(\mathrm{m}^2)$	$\approx 10^{-3}(\mathrm{Pa}\cdot\mathrm{s})$	$\approx 1.8\times 10^{-5}(\mathrm{Pa}\cdot\mathrm{s})$	$10^5(\mathrm{Pa})$

3) Water flow in a partially saturated porous medium[90]:

$$\tilde{\boldsymbol{v}}^w = k_w(n,S)\left[-\frac{\partial p_w}{\partial \mathbf{x}} + \rho^{wR}\boldsymbol{g}\right] \tag{2.34}$$

$$k_w(n,S) = \frac{\varkappa(n)}{\eta_w} k_{rw}(S) \tag{2.35}$$

$$k_{rw}(S) = \sqrt{S}\left(1 - \left(1 - S^{\frac{1}{\mathrm{m}}}\right)^{\mathrm{m}}\right)^2$$

4) Air flow in a porous medium (Section 6.5.2 of Coussy[23]),

$$\tilde{\boldsymbol{v}}^a = k_a(n,S)\left[-\frac{\partial p_a}{\partial \mathbf{x}} + \rho^{aR}\boldsymbol{g}\right] \tag{2.36}$$

$$k_a(n,S) = \frac{\varkappa(n)}{\eta_a} k_{ra}(S) \tag{2.37}$$

$$k_{ra}(S) = \sqrt{1-S}\left(1 - S^{\frac{1}{\mathrm{m}}}\right)^{2\mathrm{m}}$$

5) Real air mass density:

$$\rho^{aR} = \exp\left[\frac{p_a}{K_a}\right] \tag{2.38}$$

where, the material property $\varkappa$ is called the intrinsic permeability of the soil skeleton and the function of porosity n, $k_{r\alpha}$ is the relative permeabilities related to, respectively, water and air, and η_α is the dynamic water and air viscosity[23]. The density of air ρ^{aR} is approximately 1.2 kg/m^3 at sea level and at 20 $^{\circ}$C and air bulk modulus K_a is 10^5 Pa at constant temperature. The approximate

parameter values are given in Table 2.1. The relative permeabilities k_{rw} and k_{ra} as function of S are given in Figure 2.1.

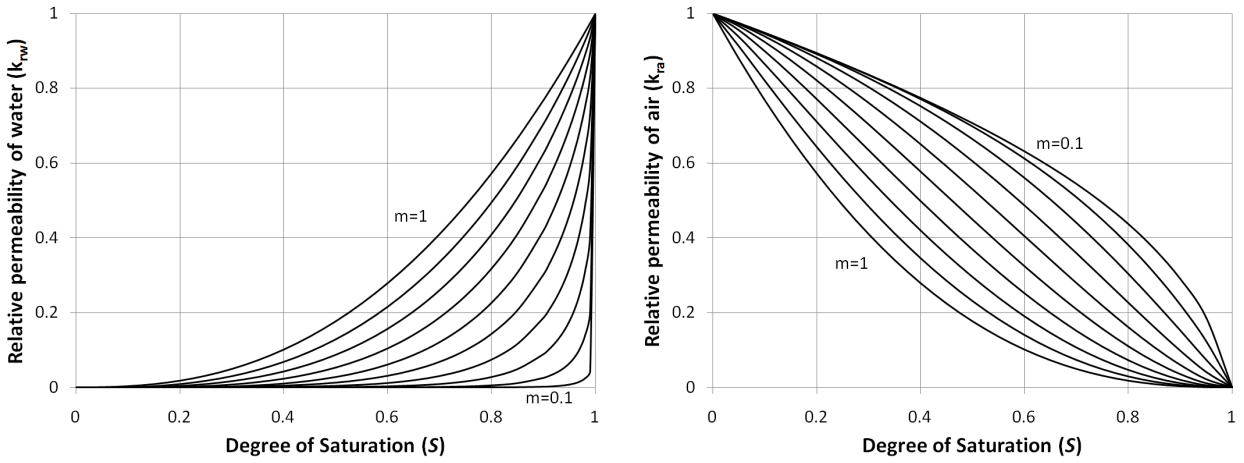

Figure 2.1: Relative permeabilities k_{rw}(left) and k_{ra}(right) plotted against S when varying m from 0.1 to 1

It can be shown (page.46 in Coussy[23]) that $\varkappa(n) = l^2\delta(n)$, where l^2 is a parameter of dimension area (m^2) and $\delta(n)$ by the Kozeny-Carman's relation (pore space formed by regular packing of spheres),

$$\delta(n) = \frac{n^3}{1-n^2}$$

2.3.2 Biphasic balance and constitutive equations

For many quasi-static geotechnical engineering problems, we can assume that pore air pressure, p_a, is approximately equal to zero ($p_a \approx 0$, atmospheric), but the soil suction still corresponds to negative pore water pressure ($s \approx -p_w$). In order to solve for 2 unknown ($\boldsymbol{u}$, p_w and $p_a \approx 0$) using given 2 equations, the balance equations are summarized as follows,

1) The balance of linear momentum of a mixture:

$$\begin{aligned} \mathrm{div}\boldsymbol{\sigma} + \rho\,\boldsymbol{g} &= \mathbf{0} \\ \rho &= \rho^s + \rho^w \end{aligned} \tag{2.39}$$

$$\boldsymbol{\sigma} \;=\; \boldsymbol{\sigma}' - \bar{p}\,\mathbf{1}, \quad \bar{p} = \chi(s) p_w$$

2) The balance of mass of water (porosity $n = n^w + n^a$):

$$\begin{aligned} -n\frac{\partial S}{\partial s}\,\dot{p}_w + S\mathrm{div}\,\boldsymbol{v} &= -\mathrm{div}\,\tilde{\boldsymbol{v}}^w \\ \dot{n} &= (1-n)\dot{\epsilon}_v \end{aligned} \tag{2.40}$$

Likewise, the material properties to define constitutive equations are

1) Relationship between degree of saturation and suction stress:

$$S = f(s) \quad \text{and} \quad s = -p_w \tag{2.41}$$

$$f(s) = \left[1 + \left(\frac{s}{\mathrm{a}}\right)^{\mathrm{n}}\right]^{-\mathrm{m}}$$

2) Effective stress:

$\boldsymbol{\sigma}'$ (considering Cam-clay plasticity and partially saturated soil model from the balance of linear momentum for a mixture)

$$\boldsymbol{\sigma}' = \boldsymbol{\sigma} + \bar{p}\,\mathbf{1} \qquad \left(\bar{p} = \chi(s) p_w\right) \tag{2.42}$$

$$f(\boldsymbol{\sigma}', s, p_c) = 0 \qquad \text{(Yield Function)} \tag{2.43}$$

where, $\boldsymbol{\sigma}'$ is soil skeleton constitutive response and p_c is saturated preconsolidation pressure.

3) Water flow in a biphasic partially saturated porous medium (Section 6.5.2 of Coussy[23]):

$$\tilde{\boldsymbol{v}}^w = k_w(n,S)\left[-\frac{\partial p_w}{\partial \mathbf{x}} + \rho^{wR}\boldsymbol{g}\right] \tag{2.44}$$

$$k_w(n,S) = \frac{\varkappa(n)}{\eta_w} k_{rw}(S) \tag{2.45}$$

$$\begin{aligned} \varkappa(n) &= l^2\delta(n), \qquad \delta(n) = \frac{n^3}{1-n^2} \\ k_{rw}(S) &= \sqrt{S}\left(1 - \left(1 - S^{\frac{1}{\mathrm{m}}}\right)^{\mathrm{m}}\right)^2 \end{aligned}$$

where, the material property $\varkappa$ is called the intrinsic permeability of the skeleton that is a function of porosity n, k_{rw} is the relative permeabilities related to water, and η_w is the dynamic water viscosity. The function $\delta(n)$ is referred to as the Kozeny-Carman formula[23].

2.4 Coupled Finite Element Formulation of Triphasic Deformable Continuum

To demonstrate how a coupled nonlinear finite element formulation will be carried out for a triphasic deformable mixture (solid, water and air) as part of the research, and I first present linear and nonlinear poro-elasticity of a triphasic finite element formulation and then develop nonlinear poro-elastoplasticity formulation.

2.4.1 Weak form

To describe the implementation of coupled finite element model, the weak form illustrates integral expression of the coupled governing equations.

Consider the weighting functions which can be thought of as variation of displacement, pore water pressure and pore air pressure fields.

$$\begin{aligned} \boldsymbol{w}(\boldsymbol{x},t) &= \delta\boldsymbol{u}(\boldsymbol{x},t) \\ \eta(\boldsymbol{x},t) &= \delta p_w(\boldsymbol{x},t) \\ \varphi(\boldsymbol{x},t) &= \delta p_a(\boldsymbol{x},t) \end{aligned} \tag{2.46}$$

Derive the balance of linear momentum in weighted residual form by using the divergence theorem as $\int_B (w_i\,\sigma_{ij})_{,j}\mathrm{d}v = \int_\Gamma w_i\,\sigma_{ij}\,n_j\,\mathrm{d}a$

$$\int_B w_i(\sigma_{ij,j} + \rho\, g_i)\,\mathrm{d}v = 0 \tag{2.47}$$

By integrating by parts, using the chain rule $(w_i\sigma_{ij})_{,j} = w_{i,j}\sigma_{ij} + w_i\sigma_{ij,j}$

$$\begin{aligned} \int_B w_i\,\sigma_{ij,j}\,\mathrm{d}v &= \int_\Gamma w_i\,\sigma_{ij}\,n_j\,\mathrm{d}a - \int_B w_{i,j}\,\sigma_{ij}\,\mathrm{d}v \\ &= \left(\underbrace{\int_{\Gamma_g} \cancel{w_i}\,\sigma_{ij}\,n_j\,\mathrm{d}a}_{u_i = g_i^u} + \int_{\Gamma_t} w_i\,\underbrace{\sigma_{ij}\,n_j}_{t_i}\,\mathrm{d}a\right) - \int_B w_{i,j}\,\sigma_{ij}\,\mathrm{d}v \end{aligned} \tag{2.48}$$

where, $\sigma_{ij,j} = \dfrac{\partial\sigma_{ij}}{\partial x_j}$ and $w_i = \delta u_i = \delta g_i^u = 0$ on Γ_g.

Thus,

$$\boxed{\int_B w_{i,j}\left[\sigma'_{ij} - \chi p_w\delta_{ij} - (1-\chi)p_a\delta_{ij}\right]\mathrm{d}v = \int_B \rho\, w_i g_i\,\mathrm{d}v + \int_{\Gamma_t} w_i t_i\,\mathrm{d}a}$$

Applying the method of weighted residuals to the balance of mass of mixture in the water phase,

$$\int_{B_w} \eta \left[n\frac{\partial S}{\partial s}(\dot{p}_a - \dot{p}_w) + S\,\mathrm{div}\,\boldsymbol{v} + \mathrm{div}\,\tilde{\boldsymbol{v}}^w \right] \mathrm{d}v = 0 \tag{2.49}$$

$$\int_{B_w} \eta\, n\frac{\partial S}{\partial s}(\dot{p}_a - \dot{p}_w)\,\mathrm{d}v + \int_{B_w} \eta\, S v_{i,i}\,\mathrm{d}v = -\int_{B_w} \eta\, \tilde{v}^w_{i,i}\,\mathrm{d}v$$

Applying chain rule, we can obtained as

$$\int_{B_w} \eta\, \tilde{v}^w_{i,i}\mathrm{d}v = \int_{B_w} \Big(\underbrace{[\eta\, \tilde{v}^w_i]_{,i}}_{\int_{\Gamma_w} \eta\, \tilde{v}^w_i\, n_i\,\mathrm{d}a = \int_{\Gamma^w_r} \eta\, \tilde{v}^w_i\, n_i\,\mathrm{d}a + \int_{\Gamma^w_s} \eta\, \tilde{v}^w_i\, n_i\,\mathrm{d}a} - \eta_{,i}\, \tilde{v}^w_i \Big) \mathrm{d}v \tag{2.50}$$

where, $\Gamma_w = \Gamma^w_s \cup \Gamma^w_r$, $\eta = \delta p_w = \delta r_w = 0$ on Γ^w_r, $v_{i,i} = \dot{u}_{i,i}$, $\tilde{v}^w_i\, n_i = -S^w$ on Γ^w_s, and S^w is boundary seepage positive for in-flow of water into Γ^w_s. Thus,

$$\boxed{\int_{B_w} \eta\, n\frac{\partial S}{\partial s}(\dot{p}_a - \dot{p}_w)\,\mathrm{d}v + \int_{B_w} \eta\, S\, v_{i,i}\,\mathrm{d}v - \int_{B_w} \eta_{,i}\, \tilde{v}^w_i \mathrm{d}v = \int_{\Gamma^w_s} \eta\, S^w\,\mathrm{d}s}$$

In the air phase, applying the method of weighted residuals to the balance of mass of mixture,

$$\int_{B_a} \varphi \left\{ \left[-n\frac{\partial S}{\partial s} + \frac{n(1-S)}{K_a} \right] \dot{p}_a + n\frac{\partial S}{\partial s}\,\dot{p}_w + (1-S)\,\mathrm{div}\,\boldsymbol{v} + \frac{1}{\rho^{aR}}\,\mathrm{div}(\rho^{aR}\tilde{\boldsymbol{v}}^a) \right\} \mathrm{dv} = 0 \tag{2.51}$$

$$-\int_{B_a} \varphi\, n\frac{\partial S}{\partial s}\dot{p}_a\,\mathrm{d}v + \int_{B_a} \varphi\, \frac{n(1-S)}{K_a}\dot{p}_a\,\mathrm{d}v + \int_{B_a} \varphi\, n\frac{\partial S}{\partial s}\,\dot{p}_w\,\mathrm{d}v + \int_{B_a} \varphi\,(1-S)\,v_{i,i}\,\mathrm{d}v + \int_{B_a} \varphi\, \frac{1}{\rho^{aR}}\,(\rho^{aR})_{,i}\,\tilde{v}^a_i\,\mathrm{d}v + \int_{B_a} \varphi\,\tilde{v}^a_{i,i}\,\mathrm{d}v = 0$$

Likewise, by applying chain rule and using $(\rho^{aR})_{,i} = \dfrac{\rho^{aR}}{K_a}(p_a)_{,i}$ we have,

$$\boxed{\begin{aligned} -\int_{B_a} \varphi\, n\frac{\partial S}{\partial s}\dot{p}_a\,\mathrm{d}v + \int_{B_a} \varphi\, \frac{n(1-S)}{K_a}\dot{p}_a\,\mathrm{d}v + \int_{B_a} \varphi\, n\frac{\partial S}{\partial s}\,\dot{p}_w\,\mathrm{d}v + \int_{B_a} \varphi\,(1-S)\,v_{i,i}\,\mathrm{d}v \\ + \int_{B_a} \varphi\, \frac{(p_a)_{,i}}{K_a}\,\tilde{v}^a_i\,\mathrm{d}v - \int_{B_a} \varphi_{,i}\,\tilde{v}^a_i\,\mathrm{d}v = \int_{\Gamma^a_s} \varphi\, S^a\,\mathrm{d}s \end{aligned}}$$

where, $\Gamma_a = \Gamma^a_s \cup \Gamma^a_r$ and $\varphi = \delta p_a = \delta r_a = 0$ on Γ^a_r, $\tilde{v}^a_i\, n_i = -S^a$ on Γ^a_s, and S^a is seepage positive for in-flow of air into Γ^a_s.

Therefore, the coupled Weak form for triphasic mixture is written as,

$$
(\mathcal{W})\begin{cases}
\text{Find } \boldsymbol{u}(\boldsymbol{x},t)\in\mathcal{D}^{u},\ p_{_w}(\boldsymbol{x},t)\in\mathcal{D}^{p_w} \text{ and } p_a(\boldsymbol{x},t)\in\mathcal{D}^{p_a},\ \text{ with }\ t\in[\,0,T\,]\ \text{ such that}\\
\displaystyle\int_B\left[\boldsymbol{\nabla}\,\boldsymbol{w}:(\boldsymbol{\sigma}'-\chi\,p_w\mathbf{1}-(1-\chi)p_a\mathbf{1})\right]\mathrm{d}v=\int_B\rho\,\boldsymbol{w}\cdot\boldsymbol{g}\,\mathrm{d}v+\int_{\Gamma_t}\boldsymbol{w}\cdot\mathbf{t}\,\mathrm{d}a\,,\\
\displaystyle\int_{B_w}\eta\,n\frac{\partial S}{\partial s}(\dot{p}_a-\dot{p}_w)\,\mathrm{d}v+\int_{B_w}\eta\,S\,\mathrm{div}\,\boldsymbol{v}\,\mathrm{d}v-\int_{B_w}\boldsymbol{\nabla}\eta\cdot\tilde{\boldsymbol{v}}^{w}\mathrm{d}v=\int_{\Gamma_s^w}\eta\,S^{w}\,\mathrm{d}s\,,\\
\displaystyle-\int_{B_a}\varphi\,n\frac{\partial S}{\partial s}\dot{p}_a\,\mathrm{d}v+\int_{B_a}\varphi\,\frac{n(1-S)}{K_a}\dot{p}_a\,\mathrm{d}v+\int_{B_a}\varphi\,n\frac{\partial S}{\partial s}\,\dot{p}_w\,\mathrm{d}v\\
\displaystyle\quad+\int_{B_a}\varphi(1-S)\,\mathrm{div}\,\boldsymbol{v}\,\mathrm{d}v+\int_{B_a}\frac{\varphi}{K_a}\,\boldsymbol{\nabla}p_a\cdot\tilde{\boldsymbol{v}}^{a}\,\mathrm{d}v-\int_{B_a}\boldsymbol{\nabla}\varphi\cdot\tilde{\boldsymbol{v}}^{a}\,\mathrm{d}v=\int_{\Gamma_s^a}\varphi\,S^{a}\,\mathrm{d}s\\
\text{for all}\quad \boldsymbol{w}\,(\boldsymbol{x})\in\mathcal{V}^{u},\ \eta\,(\boldsymbol{x})\in\mathcal{V}^{p_w}\ \text{ and }\ \varphi\,(\boldsymbol{x})\in\mathcal{V}^{p_a}
\end{cases}
\tag{2.52}
$$

In the trial solution spaces,

$$
\begin{aligned}
\mathcal{D}^{u} &= \left\{\boldsymbol{u}\,(\boldsymbol{x},t):B\times\,]0,T[\ \mapsto\ \mathcal{R}^3,\quad \boldsymbol{u}(t)|_{\Gamma_g}=\boldsymbol{g}^{u}(t),\ \boldsymbol{u}(\boldsymbol{x},0)=\boldsymbol{u}_0(\boldsymbol{x})\right\}\\
\mathcal{D}^{p_w} &= \left\{p_{_w}\,(\boldsymbol{x},t):B_w\times\,]0,T[\ \mapsto\ \mathcal{R},\quad p_{_w}(t)|_{\Gamma_r^w}=r_w(t)\right\}\\
\mathcal{D}^{p_a} &= \left\{p_{_a}\,(\boldsymbol{x},t):B_a\times\,]0,T[\ \mapsto\ \mathcal{R},\quad p_{_a}(t)|_{\Gamma_r^a}=r_a(t)\right\}
\end{aligned}
\tag{2.53}
$$

where $t\in[0,T]$. In the variation spaces,

$$
\begin{aligned}
\mathcal{V}^{u} &= \left\{w_i\,(\boldsymbol{x}):B\ \mapsto\ \mathcal{R}^3,\quad w_i|_{\Gamma_g}=0\right\}\\
\mathcal{V}^{p_w} &= \left\{\eta\,(\boldsymbol{x}):B_w\ \mapsto\ \mathcal{R},\quad \eta|_{\Gamma_r^w}=0\right\}\\
\mathcal{V}^{p_a} &= \left\{\varphi\,(\boldsymbol{x}):B_a\ \mapsto\ \mathcal{R},\quad \varphi|_{\Gamma_r^a}=0\right\}
\end{aligned}
\tag{2.54}
$$

In the discretization of domain and spaces, Galerkin Form can be written as,

$$
B^h\subset B
$$

where, "h" discretization parameter is satisfied by $B_w^h\subset B_w$ and $B_a^h\subset B_a$, therefore, we can restate the Weak form with superscript h's

$$
\begin{aligned}
&(\mathcal{D}^{u})^h\ \subset\ \mathcal{D}^{u}\ ,\quad (\mathcal{V}^{u})^h\ \subset\ \mathcal{V}^{u}\\
&(\mathcal{D}^{p_w})^h\subset\ \mathcal{D}^{p_w}\ ,\quad (\mathcal{V}^{p_w})^h\subset\ \mathcal{V}^{p_w}\\
&(\mathcal{D}^{p_a})^h\ \subset\ \mathcal{D}^{p_a}\ ,\quad (\mathcal{V}^{p_a})^h\ \subset\ \mathcal{V}^{p_a}
\end{aligned}
\qquad
\begin{cases}
u_i^h(\boldsymbol{x},t)\subset\ (\mathcal{D}^{u})^h\ ,\quad w_i^h(\boldsymbol{x})\subset\ (\mathcal{V}^{u})^h\\
p_w^h(\boldsymbol{x},t)\subset\ (\mathcal{D}^{p_w})^h\ ,\quad \eta(\boldsymbol{x})\ \subset\ (\mathcal{V}^{p_w})^h\\
p_a^h(\boldsymbol{x},t)\subset\ (\mathcal{D}^{p_a})^h\ ,\quad \varphi(\boldsymbol{x})\ \subset\ (\mathcal{V}^{p_a})^h
\end{cases}
\tag{2.55}
$$

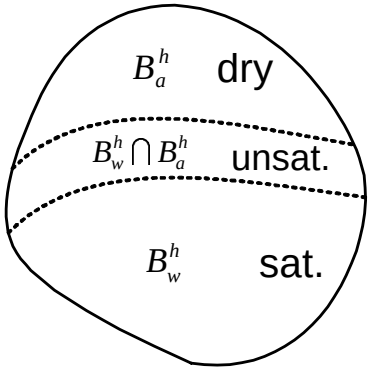

Figure 2.2: Discretization of triphasic domain and spaces in Galerkin Form

2.4.2 Coupled FE form for 2D semi-implicit linear poro-elasticity

For the coupled finite element (FE) form of 2D nonlinear poromechanics, it is used here linear isotropic elasticity for the solid skeleton effective stress $\boldsymbol{\sigma}'$, and assumed the density and permeability are described in equation (2.35) and (2.37) for water and air phases respectively, and porosity n is a function of the solid skeleton volumetric strain ϵ_v, such as in matrix form

$$\begin{aligned}
\boldsymbol{\sigma}' &= \mathbf{D} \cdot \boldsymbol{\epsilon} = \mathbf{D} \cdot \boldsymbol{B}^{e,u} \cdot \boldsymbol{d}^e \\
\boldsymbol{k}^w &= k_w(n,S)\,\mathbf{1} \quad \text{and} \quad \boldsymbol{k}^a = k_a(n,S)\,\mathbf{1} \\
n_{n+1} &= \frac{n_n + \Delta\epsilon_v}{1+\Delta\epsilon_v} \quad \text{and} \quad \Delta\epsilon_v = \mathrm{tr}(\Delta\boldsymbol{\epsilon}) \\
\rho &= \rho^{sR} - n(\rho^{sR} - \rho^{aR}) + n^w(\rho^{wR} - \rho^{aR})
\end{aligned}$$

where $\mathbf{D}$ is the elastic modulus matrix, $\boldsymbol{\epsilon}$ the solid strain, $\boldsymbol{B}^{e,u}$ the strain-displacement matrix for element e, $\boldsymbol{d}^e$ the nodal displacement vector for element e, and we can discretize into mixed quadrilateral finite elements as shown in Figure 2.3.

In Figure 2.3, element characteristic length is h^e, element domain is B^e, discrete domain is $B^h = \mathop{\mathbf{A}}_{e=1}^{n_{\mathrm{el}}} B^e$, $\mathop{\mathbf{A}}_{e=1}^{n_{\mathrm{el}}}$ is the element assembly operator, and the convergent, mixed and quadrilateral finite element is biquadratic in displacement and bilinear in pore water pressure and pore air pressure[59].

For a biquadratic element in displacement and a bilinear isoparametric element in pore water

pressure and pore air pressure, it is necessary to define the interpolating functions for three phases for coupled finite element form as follows,

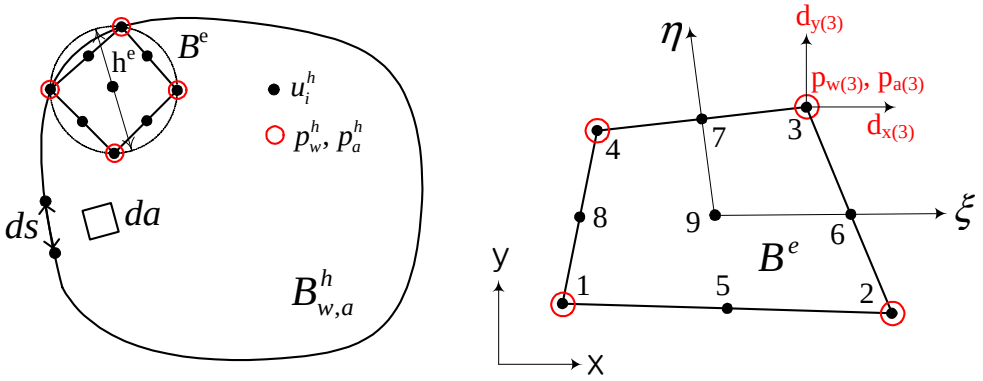

Figure 2.3: Discretization into triphasic mixed quadrilateral finite elements

1) *Solid* : (displacement, $\boldsymbol{u}$)

$$\begin{aligned} \boldsymbol{u}^h(\boldsymbol{\xi},t) &= \sum_{a=1}^{9} N_a^u(\boldsymbol{\xi})\,\boldsymbol{d}_a^e(t) = \boldsymbol{N}^{e,u}\cdot\boldsymbol{d}^e \\ &= \begin{bmatrix} \boldsymbol{N}_1^u & \cdots & \boldsymbol{N}_9^u \end{bmatrix}\cdot\begin{bmatrix} \boldsymbol{d}_1^e \\ \vdots \\ \boldsymbol{d}_9^e \end{bmatrix} \end{aligned} \tag{2.56}$$

$$\boldsymbol{N}_a^u = \begin{bmatrix} N_a^u & 0 \\ 0 & N_a^u \end{bmatrix} \quad , \quad \boldsymbol{d}_a^e = \begin{bmatrix} d_{x(a)}^e \\ d_{y(a)}^e \end{bmatrix} \tag{2.57}$$

where $\boldsymbol{d}^e$ are element nodal displacements, and weighting function,

$$\boldsymbol{w}^h(\boldsymbol{\xi}) = \boldsymbol{N}^{e,u}\cdot\boldsymbol{c}^e \tag{2.58}$$

2) *Water* :

$$p_w^h(\boldsymbol{\xi},t) = \sum_{b=1}^{4} N_b^p(\boldsymbol{\xi})\,\theta_b^e(t) = \boldsymbol{N}^{e,p}\cdot\boldsymbol{\theta}^e$$

$$= \begin{bmatrix} N_1^p & N_2^p & N_3^p & N_4^p \end{bmatrix} \cdot \begin{bmatrix} \theta_1^e \\ \theta_2^e \\ \theta_3^e \\ \theta_4^e \end{bmatrix} \tag{2.59}$$

The pore water pressure time derivative is

$$\dot{p}_w^h(\boldsymbol{\xi}, t) = \boldsymbol{N}^{e,p} \cdot \dot{\boldsymbol{\theta}}^e$$

And weighting function for water portion η^h,

$$\eta^h = \boldsymbol{N}^{e,p} \cdot \boldsymbol{\alpha}^e \tag{2.60}$$

3) *Air* :

$$\begin{aligned} p_a^h(\boldsymbol{\xi}, t) &= \sum_{c=1}^{4} N_c^p(\boldsymbol{\xi})\, \zeta_c^e(t) = \boldsymbol{N}^{e,p} \cdot \boldsymbol{\zeta}^e \\ &= \begin{bmatrix} N_1^p & N_2^p & N_3^p & N_4^p \end{bmatrix} \cdot \begin{bmatrix} \zeta_1^e \\ \zeta_2^e \\ \zeta_3^e \\ \zeta_4^e \end{bmatrix} \end{aligned} \tag{2.61}$$

The pore air pressure time derivative is

$$\dot{p}_a^h(\boldsymbol{\xi}, t) = \boldsymbol{N}^{e,p} \cdot \dot{\boldsymbol{\zeta}}^e$$

And weighting function for air portion φ^h,

$$\varphi^h = \boldsymbol{N}^{e,p} \cdot \boldsymbol{\beta}^e \tag{2.62}$$

In the practical application of elements it is necessary to find the value of the partial derivatives of the interpolating functions with respect to global coordinates x and y. For the interpolating function $\boldsymbol{N}$ of three terms, we will have

1) *Solid* :

$$\begin{aligned}
\dot{u}^h_{i,i}(\boldsymbol{\xi},t) &= \sum_{a=1}^{9}\left[\frac{\partial N^u_a}{\partial x} \quad \frac{\partial N^u_a}{\partial y}\right]\cdot\begin{bmatrix}\dot{d}^e_{x(a)}\\ \dot{d}^e_{y(a)}\end{bmatrix}\\
&= \left[\tilde{\boldsymbol{B}}^u_1 \quad \cdots \quad \tilde{\boldsymbol{B}}^u_9\right]\cdot\begin{bmatrix}\dot{\boldsymbol{d}}^e_1\\ \vdots\\ \dot{\boldsymbol{d}}^e_9\end{bmatrix} = \tilde{\boldsymbol{B}}^{e,u}\cdot\dot{\boldsymbol{d}}^e \qquad (2.63)\\
\tilde{\boldsymbol{B}}^u_a &= \begin{bmatrix}\frac{dN^u_a}{dx} & \frac{dN^u_a}{dy}\end{bmatrix}
\end{aligned}$$

$$\begin{aligned}
w^h_{i,j}(\boldsymbol{\xi}) &= \sum_{a=1}^{9}\frac{\partial N^u_a(\boldsymbol{\xi})}{\partial x_j}c^e_{i(a)}\\
\begin{bmatrix}w^h_{1,1}\\ w^h_{2,2}\\ w^h_{1,2}+w^h_{2,1}\end{bmatrix} &= \left[\boldsymbol{B}^u_1 \quad \cdots \quad \boldsymbol{B}^u_9\right]\cdot\begin{bmatrix}\boldsymbol{c}^e_1\\ \vdots\\ \boldsymbol{c}^e_9\end{bmatrix} \qquad (2.64)\\
\boldsymbol{B}^u_a &= \begin{bmatrix}\frac{dN^u_a}{dx} & 0\\ 0 & \frac{dN^u_a}{dy}\\ \frac{dN^u_a}{dy} & \frac{dN^u_a}{dx}\end{bmatrix}
\end{aligned}$$

$$\boldsymbol{\nabla}\boldsymbol{w}^h(\boldsymbol{\xi}) = \boldsymbol{B}^{e,u}\cdot\boldsymbol{c}^e$$

2) *Water* :

$$\begin{aligned}
\eta^h_{,i}(\boldsymbol{\xi}) &= \sum_{b=1}^{4}\frac{\partial N^p_b(\boldsymbol{\xi})}{\partial x_i}\alpha^e_b = \sum_{b=1}^{4}\begin{bmatrix}\frac{\partial N^p_b(\boldsymbol{\xi})}{\partial x}\\ \frac{\partial N^p_b(\boldsymbol{\xi})}{\partial y}\end{bmatrix}\alpha^e_b\\
&= \sum_{b=1}^{4}\boldsymbol{B}^p_b\,\alpha^e_b = \begin{bmatrix}\boldsymbol{B}^p_1 & \boldsymbol{B}^p_2 & \boldsymbol{B}^p_3 & \boldsymbol{B}^p_4\end{bmatrix}\cdot\begin{bmatrix}\alpha^e_1\\ \alpha^e_2\\ \alpha^e_3\\ \alpha^e_4\end{bmatrix} \qquad (2.65)
\end{aligned}$$

$$\boldsymbol{\nabla}\eta^h = \boldsymbol{B}^{e,p}\cdot\boldsymbol{\alpha}^e$$

$$\boldsymbol{\nabla}p_w^h = \boldsymbol{B}^{e,p}\cdot\boldsymbol{\theta}^e$$

3) *Air* :

$$\begin{aligned}\varphi_{,i}^h(\boldsymbol{\xi}) &= \sum_{c=1}^{4}\frac{\partial N_c^p(\boldsymbol{\xi})}{\partial x_i}\beta_c^e = \sum_{c=1}^{4}\begin{bmatrix}\dfrac{\partial N_c^p(\boldsymbol{\xi})}{\partial x}\\ \dfrac{\partial N_c^p(\boldsymbol{\xi})}{\partial y}\end{bmatrix}\beta_c^e\\ &= \sum_{c=1}^{4}\boldsymbol{B}_c^p\,\beta_c^e = \begin{bmatrix}\boldsymbol{B}_1^p & \boldsymbol{B}_2^p & \boldsymbol{B}_3^p & \boldsymbol{B}_4^p\end{bmatrix}\cdot\begin{bmatrix}\beta_1^e\\ \beta_2^e\\ \beta_3^e\\ \beta_4^e\end{bmatrix}\end{aligned} \tag{2.66}$$

$$\boldsymbol{\nabla}\varphi^h = \boldsymbol{B}^{e,p}\cdot\boldsymbol{\beta}^e$$

$$\boldsymbol{\nabla}p_a^h = \boldsymbol{B}^{e,p}\cdot\boldsymbol{\zeta}^e$$

The finite element equations are nonlinear because (i) the porosity $n(\boldsymbol{u})$ is a nonlinear function of displacement, (ii) the degree of saturation $S(s)$ is a nonlinear function of suction s, and (iii) the relative permeabilities $k_w(n,S)$ and $k_a(n,S)$ are nonlinear functions of $\boldsymbol{u}$ and S. To compare the formulation for demonstration purposes, both linear and nonlinear behavior are considered. Thus,

$$\begin{aligned}\rho(\boldsymbol{d},\boldsymbol{\theta},\boldsymbol{\zeta}) &= \rho^s+\rho^w+\rho^a = n^s\rho^{sR}+n^w\rho^{wR}+n^a\rho^{aR}\\ &= \Big(1-n(\boldsymbol{d})\Big)\rho^{sR}+n(\boldsymbol{d})\,S(\boldsymbol{\theta},\boldsymbol{\zeta})\,\rho^{wR}+n(\boldsymbol{d})\Big(1-S(\boldsymbol{\theta},\boldsymbol{\zeta})\Big)\rho^{aR}(\boldsymbol{\zeta})\end{aligned} \tag{2.67}$$

Since the porosity $n(\boldsymbol{d})$ is a nonlinear function of displacement and $S(\boldsymbol{\theta},\boldsymbol{\zeta})$ is a nonlinear function of pore air and pore water pressures, then so is the mixture mass density $\rho(\boldsymbol{d},\boldsymbol{\theta},\boldsymbol{\zeta})$. This holds for $n(\boldsymbol{d})$, $S(\boldsymbol{\theta},\boldsymbol{\zeta})$ and $\rho^{aR}(\boldsymbol{\zeta})$ as well. It is assumed $\chi(\boldsymbol{\theta}^e,\boldsymbol{\zeta}^e) = S(\boldsymbol{\theta}^e,\boldsymbol{\zeta}^e)$ for the solid phase related to the effective stress (revisit later). The coupled nonlinear FE equations are written then as,

1) *Solid* :

$$\begin{aligned}\mathop{\mathbf{A}}_{e=1}^{n_{\mathrm{el}}}(\boldsymbol{c}^e)^T\cdot\Bigg[&\left(\int_{B^e}(\boldsymbol{B}^{e,u})^T\cdot\boldsymbol{D}\cdot\boldsymbol{B}^{e,u}\,\mathrm{d}a\right)\cdot\boldsymbol{d}^e-\left(\int_{B^e}\chi(\boldsymbol{\theta}^e,\boldsymbol{\zeta}^e)(\tilde{\boldsymbol{B}}^{e,u})^T\cdot\boldsymbol{N}^{e,p}\,\mathrm{d}a\right)\cdot\boldsymbol{\theta}^e\\&-\left(\int_{B^e}\Big(1-\chi(\boldsymbol{\theta}^e,\boldsymbol{\zeta}^e)\Big)(\tilde{\boldsymbol{B}}^{e,u})^T\cdot\boldsymbol{N}^{e,p}\,\mathrm{d}a\right)\cdot\boldsymbol{\zeta}^e\\&=\int_{B^e}\rho(\boldsymbol{d}^e,\boldsymbol{\theta}^e,\boldsymbol{\zeta}^e)(\boldsymbol{N}^{e,u})^T\cdot\boldsymbol{g}\,\mathrm{d}a+\int_{\Gamma_t^e}(\boldsymbol{N}^{e,u})^T\cdot\boldsymbol{t}\,\mathrm{d}a\Bigg]\end{aligned}\tag{2.68}$$

$$\begin{aligned}\text{thus,}\quad\mathop{\mathbf{A}}_{e=1}^{n_{\mathrm{el}}}(\boldsymbol{c}^e)^T\cdot\Big[&\boldsymbol{k}^{e,dd}\cdot\boldsymbol{d}^e-\boldsymbol{k}^{e,d\theta}(\boldsymbol{\theta}^e,\boldsymbol{\zeta}^e)\cdot\boldsymbol{\theta}^e-\boldsymbol{k}^{e,d\zeta}(\boldsymbol{\theta}^e,\boldsymbol{\zeta}^e)\cdot\boldsymbol{\zeta}^e\\&=\boldsymbol{f}_f^{e,d}(\boldsymbol{d}^e,\boldsymbol{\theta}^e,\boldsymbol{\zeta}^e)+\boldsymbol{f}_t^{e,d}\Big]\end{aligned}\tag{2.69}$$

2) *Water* :

$$\begin{aligned}\mathop{\mathbf{A}}_{e=1}^{n_{\mathrm{el}}}(\boldsymbol{\alpha}^e)^T\cdot\Bigg[&\left(\int_{B_w^e}n(\boldsymbol{d}^e)\frac{\partial S(\boldsymbol{\theta}^e,\boldsymbol{\zeta}^e)}{\partial s}(\boldsymbol{N}^{e,p})^T\cdot\boldsymbol{N}^{e,p}\,\mathrm{d}a\right)\cdot\dot{\boldsymbol{\zeta}}^e\\&-\left(\int_{B_w^e}n(\boldsymbol{d}^e)\frac{\partial S(\boldsymbol{\theta}^e,\boldsymbol{\zeta}^e)}{\partial s}(\boldsymbol{N}^{e,p})^T\cdot\boldsymbol{N}^{e,p}\,\mathrm{d}a\right)\cdot\dot{\boldsymbol{\theta}}^e\\&+\left(\int_{B_w^e}S(\boldsymbol{\theta}^e,\boldsymbol{\zeta}^e)\,(\boldsymbol{N}^{e,p})^T\cdot\tilde{\boldsymbol{B}}^{e,u}\,\mathrm{d}a\right)\cdot\dot{\boldsymbol{d}}^e\\&+\left(\int_{B_w^e}(\boldsymbol{B}^{e,p})^T\cdot\boldsymbol{k}^w(\boldsymbol{d}^e,\boldsymbol{\theta}^e,\boldsymbol{\zeta}^e)\cdot\boldsymbol{B}^{e,p}\,\mathrm{d}a\right)\cdot\boldsymbol{\theta}^e\\&=\int_{B_w^e}\rho^{wR}(\boldsymbol{B}^{e,p})^T\cdot\boldsymbol{k}^w(\boldsymbol{d}^e,\boldsymbol{\theta}^e,\boldsymbol{\zeta}^e)\cdot\boldsymbol{g}\,\mathrm{d}a+\int_{\Gamma_{s(w)}^e}(\boldsymbol{N}^{e,p})^TS^w\,\mathrm{d}s\Bigg]\end{aligned}\tag{2.70}$$

$$\begin{aligned}\text{thus,}\quad\mathop{\mathbf{A}}_{e=1}^{n_{\mathrm{el}}}(\boldsymbol{\alpha}^e)^T\cdot\Big[&\boldsymbol{k}^{e,\theta\zeta}(\boldsymbol{d}^e,\boldsymbol{\theta}^e,\boldsymbol{\zeta}^e)\cdot\dot{\boldsymbol{\zeta}}^e-\boldsymbol{k}^{e,\theta\zeta}(\boldsymbol{d}^e,\boldsymbol{\theta}^e,\boldsymbol{\zeta}^e)\cdot\dot{\boldsymbol{\theta}}^e\\&+\boldsymbol{k}^{e,\theta d}(\boldsymbol{\theta}^e,\boldsymbol{\zeta}^e)\cdot\dot{\boldsymbol{d}}^e+\boldsymbol{k}^{e,\theta\theta}(\boldsymbol{d}^e,\boldsymbol{\theta}^e,\boldsymbol{\zeta}^e)\cdot\boldsymbol{\theta}^e=\boldsymbol{f}^{e,\theta}(\boldsymbol{d}^e,\boldsymbol{\theta}^e,\boldsymbol{\zeta}^e)+\boldsymbol{f}_s^{e,\theta}\Big]\end{aligned}\tag{2.71}$$

3) *Air* :

$$
\begin{aligned}
\mathop{\mathbf{A}}_{e=1}^{n_{\mathrm{el}}} (\boldsymbol{\beta}^e)^T \cdot \Bigg[& - \left(\int_{B_a^e} n(\boldsymbol{d}^e) \frac{\partial S(\boldsymbol{\theta}^e, \boldsymbol{\zeta}^e)}{\partial s} (\boldsymbol{N}^{e,p})^T \cdot \boldsymbol{N}^{e,p} \, \mathrm{d}a \right) \cdot \dot{\boldsymbol{\zeta}}^e \\
& + \left(\int_{B_a^e} \frac{n(\boldsymbol{d}^e)}{K_a} \Big(1 - S(\boldsymbol{\theta}^e, \boldsymbol{\zeta}^e) \Big) (\boldsymbol{N}^{e,p})^T \cdot \boldsymbol{N}^{e,p} \, \mathrm{d}a \right) \cdot \dot{\boldsymbol{\zeta}}^e \\
& + \left(\int_{B_a^e} n(\boldsymbol{d}^e) \frac{\partial S(\boldsymbol{\theta}^e, \boldsymbol{\zeta}^e)}{\partial s} (\boldsymbol{N}^{e,p})^T \cdot \boldsymbol{N}^{e,p} \, \mathrm{d}a \right) \cdot \dot{\boldsymbol{\theta}}^e \\
& + \left(\int_{B_a^e} \Big(1 - S(\boldsymbol{\theta}^e, \boldsymbol{\zeta}^e) \Big) (\boldsymbol{N}^{e,p})^T \cdot \tilde{\boldsymbol{B}}^{e,u} \, \mathrm{d}a \right) \cdot \dot{\boldsymbol{d}}^e \\
& - \left(\int_{B_a^e} \frac{1}{K_a} (\boldsymbol{N}^{e,p})^T \otimes (\boldsymbol{\nabla} p_a)_n \cdot \boldsymbol{B}^{e,p} \cdot \boldsymbol{k}^a(\boldsymbol{d}^e, \boldsymbol{\theta}^e, \boldsymbol{\zeta}^e) \, \mathrm{d}a \right) \cdot \boldsymbol{\zeta}^e \\
& + \left(\int_{B_a^e} (\boldsymbol{B}^{e,p})^T \cdot \boldsymbol{k}^a(\boldsymbol{d}^e, \boldsymbol{\theta}^e, \boldsymbol{\zeta}^e) \cdot \boldsymbol{B}^{e,p} \, \mathrm{d}a \right) \cdot \boldsymbol{\zeta}^e \\
= & \int_{B_a^e} \rho^{aR}(\boldsymbol{\zeta}^e) (\boldsymbol{B}^{e,p})^T \cdot \boldsymbol{k}^a(\boldsymbol{d}^e, \boldsymbol{\theta}^e, \boldsymbol{\zeta}^e) \cdot \boldsymbol{g} \, \mathrm{d}a + \int_{\Gamma^e_{s(a)}} (\boldsymbol{N}^{e,p})^T S^a \, \mathrm{d}s \\
& - \int_{B_a^e} \frac{1}{K_a} (\boldsymbol{N}^{e,p})^T \otimes (\boldsymbol{\nabla} p_a)_n \cdot \boldsymbol{k}^a(\boldsymbol{d}^e, \boldsymbol{\theta}^e, \boldsymbol{\zeta}^e) \cdot \boldsymbol{g} \, \rho^{aR}(\boldsymbol{\zeta}^e) \, \mathrm{d}a \Bigg]
\end{aligned}
\tag{2.72}
$$

$$
\begin{aligned}
\text{thus,} \quad & \mathop{\mathbf{A}}_{e=1}^{n_{\mathrm{el}}} (\boldsymbol{\beta}^e)^T \cdot \Big[\boldsymbol{k}^{e,\zeta\theta}(\boldsymbol{d}^e, \boldsymbol{\theta}^e, \boldsymbol{\zeta}^e) \cdot \dot{\boldsymbol{\zeta}}^e + \boldsymbol{k}^{e,\theta\zeta}(\boldsymbol{d}^e, \boldsymbol{\theta}^e, \boldsymbol{\zeta}^e) \cdot \dot{\boldsymbol{\theta}}^e \\
& + \boldsymbol{k}^{e,\zeta d}(\boldsymbol{\theta}^e, \boldsymbol{\zeta}^e) \cdot \dot{\boldsymbol{d}}^e + \boldsymbol{k}^{e,\zeta\zeta}(\boldsymbol{d}^e, \boldsymbol{\theta}^e, \boldsymbol{\zeta}^e) \cdot \boldsymbol{\zeta}^e = \boldsymbol{f}^{e,\zeta}(\boldsymbol{d}^e, \boldsymbol{\theta}^e, \boldsymbol{\zeta}^e) + \boldsymbol{f}_s^{e,\zeta} \Big]
\end{aligned}
\tag{2.73}
$$

Hence the element stiffness matrix for displacement, pore water pressure and pore air pressure of d.o.f (degree of freedom), and the coupling element stiffness and permeability matrices are written as,

$$
\begin{aligned}
\boldsymbol{k}^{e,dd} &= \int_{B^e} (\boldsymbol{B}^{e,u})^T \cdot \mathbf{D} \cdot \boldsymbol{B}^{e,u} \,\mathrm{d}a \;=\; \int_{-1}^{1}\int_{-1}^{1} (\boldsymbol{B}^{e,u})^T \cdot \mathbf{D} \cdot \boldsymbol{B}^{e,u} \, j \mathrm{d}\xi \mathrm{d}\eta \\
\boldsymbol{k}^{e,\theta\theta}(\boldsymbol{d}^e, \boldsymbol{\theta}^e, \boldsymbol{\zeta}^e) &= \int_{B^e} (\boldsymbol{B}^{e,p})^T \cdot \boldsymbol{k}^w(\boldsymbol{d}^e, \boldsymbol{\theta}^e, \boldsymbol{\zeta}^e) \cdot \boldsymbol{B}^{e,p} \,\mathrm{d}a \\
&= \int_{-1}^{1}\int_{-1}^{1} (\boldsymbol{B}^{e,p})^T \cdot \boldsymbol{k}^w(\boldsymbol{d}^e, \boldsymbol{\theta}^e, \boldsymbol{\zeta}^e) \cdot \boldsymbol{B}^{e,p} \, j \mathrm{d}\xi \mathrm{d}\eta \\
\boldsymbol{k}^{e,\zeta\zeta}(\boldsymbol{d}^e, \boldsymbol{\theta}^e, \boldsymbol{\zeta}^e) &= \int_{B^e} (\boldsymbol{B}^{e,p})^T \cdot \boldsymbol{k}^a(\boldsymbol{d}^e, \boldsymbol{\theta}^e, \boldsymbol{\zeta}^e) \cdot \boldsymbol{B}^{e,p} \,\mathrm{d}a \\
&= \int_{-1}^{1}\int_{-1}^{1} (\boldsymbol{B}^{e,p})^T \cdot \boldsymbol{k}^a(\boldsymbol{d}^e, \boldsymbol{\theta}^e, \boldsymbol{\zeta}^e) \cdot \boldsymbol{B}^{e,p} \, j \mathrm{d}\xi \mathrm{d}\eta \\
\boldsymbol{k}^{e,d\theta}(\boldsymbol{\theta}^e, \boldsymbol{\zeta}^e) &= \int_{B^e} \chi(\boldsymbol{\theta}^e, \boldsymbol{\zeta}^e)(\tilde{\boldsymbol{B}}^{e,u})^T \cdot \boldsymbol{N}^{e,p} \,\mathrm{d}a \\
&= \int_{-1}^{1}\int_{-1}^{1} \chi(\boldsymbol{\theta}^e, \boldsymbol{\zeta}^e)(\tilde{\boldsymbol{B}}^{e,u})^T \cdot \boldsymbol{N}^{e,p} \, j \mathrm{d}\xi \mathrm{d}\eta \\
\boldsymbol{k}^{e,d\zeta}(\boldsymbol{\theta}^e, \boldsymbol{\zeta}^e) &= \int_{B^e} \Big(1 - \chi(\boldsymbol{\theta}^e, \boldsymbol{\zeta}^e)\Big)(\tilde{\boldsymbol{B}}^{e,u})^T \cdot \boldsymbol{N}^{e,p} \,\mathrm{d}a \\
&= \int_{-1}^{1}\int_{-1}^{1} \Big(1 - \chi(\boldsymbol{\theta}^e, \boldsymbol{\zeta}^e)\Big)(\tilde{\boldsymbol{B}}^{e,u})^T \cdot \boldsymbol{N}^{e,p} \, j \mathrm{d}\xi \mathrm{d}\eta \qquad (2.74) \\
\boldsymbol{k}^{e,\theta\zeta}(\boldsymbol{d}^e, \boldsymbol{\theta}^e, \boldsymbol{\zeta}^e) &= \int_{B^e} n(\boldsymbol{d}^e) \frac{\partial S(\boldsymbol{\theta}^e, \boldsymbol{\zeta}^e)}{\partial s} (\boldsymbol{N}^{e,p})^T \cdot \boldsymbol{N}^{e,p} \,\mathrm{d}a \\
&= \int_{-1}^{1}\int_{-1}^{1} n(\boldsymbol{d}^e) \frac{\partial S(\boldsymbol{\theta}^e, \boldsymbol{\zeta}^e)}{\partial s} (\boldsymbol{N}^{e,p})^T \cdot \boldsymbol{N}^{e,p} \, j \mathrm{d}\xi \mathrm{d}\eta \\
\boldsymbol{k}^{e,\theta d}(\boldsymbol{\theta}^e, \boldsymbol{\zeta}^e) &= \int_{B^e} S(\boldsymbol{\theta}^e, \boldsymbol{\zeta}^e)(\boldsymbol{N}^{e,p})^T \cdot \tilde{\boldsymbol{B}}^{e,u} \,\mathrm{d}a \\
&= \int_{-1}^{1}\int_{-1}^{1} S(\boldsymbol{\theta}^e, \boldsymbol{\zeta}^e)(\boldsymbol{N}^{e,p})^T \cdot \tilde{\boldsymbol{B}}^{e,u} \, j \mathrm{d}\xi \mathrm{d}\eta \\
\boldsymbol{k}^{e,\zeta d}(\boldsymbol{\theta}^e, \boldsymbol{\zeta}^e) &= \int_{B^e} \Big(1 - S(\boldsymbol{\theta}^e, \boldsymbol{\zeta}^e)\Big)(\boldsymbol{N}^{e,p})^T \cdot \tilde{\boldsymbol{B}}^{e,u} \,\mathrm{d}a \\
&= \int_{-1}^{1}\int_{-1}^{1} \Big(1 - S(\boldsymbol{\theta}^e, \boldsymbol{\zeta}^e)\Big)(\boldsymbol{N}^{e,p})^T \cdot \tilde{\boldsymbol{B}}^{e,u} \, j \mathrm{d}\xi \mathrm{d}\eta \\
\boldsymbol{k}^{e,\zeta\theta}(\boldsymbol{d}^e, \boldsymbol{\theta}^e, \boldsymbol{\zeta}^e) &= \int_{B^e} \left(\frac{n(\boldsymbol{d}^e)}{K_a}\Big(1 - S(\boldsymbol{\theta}^e, \boldsymbol{\zeta}^e)\Big) - n(\boldsymbol{d}^e) \frac{\partial S(\boldsymbol{\theta}^e, \boldsymbol{\zeta}^e)}{\partial s} \right) (\boldsymbol{N}^{e,p})^T \cdot \boldsymbol{N}^{e,p} \,\mathrm{d}a \\
&= \int_{-1}^{1}\int_{-1}^{1} \left(\frac{n(\boldsymbol{d}^e)}{K_a}\Big(1 - S(\boldsymbol{\theta}^e, \boldsymbol{\zeta}^e)\Big) - n(\boldsymbol{d}^e) \frac{\partial S(\boldsymbol{\theta}^e, \boldsymbol{\zeta}^e)}{\partial s} \right) (\boldsymbol{N}^{e,p})^T \cdot \boldsymbol{N}^{e,p} \, j \mathrm{d}\xi \mathrm{d}\eta
\end{aligned}
$$

Recall,

$$\boldsymbol{B}^{e,u} = \left[\begin{array}{cccc} \boldsymbol{B}_1^u & \boldsymbol{B}_2^u & \cdots & \boldsymbol{B}_9^u \end{array} \right] \qquad \tilde{\boldsymbol{B}}^{e,u} = \left[\begin{array}{cccc} \tilde{\boldsymbol{B}}_1^u & \tilde{\boldsymbol{B}}_2^u & \cdots & \tilde{\boldsymbol{B}}_9^u \end{array} \right]$$

$$\boldsymbol{B}_a^u = \left[\begin{array}{cc} \dfrac{dN_a^u}{dx} & 0 \\ 0 & \dfrac{dN_a^u}{dy} \\ \dfrac{dN_a^u}{dy} & \dfrac{dN_a^u}{dx} \end{array} \right] \qquad \tilde{\boldsymbol{B}}_a^u = \left[\begin{array}{cc} \dfrac{dN_a^u}{dx} & \dfrac{dN_a^u}{dy} \end{array} \right]$$

$$\boldsymbol{N}^{e,p} = \left[\begin{array}{cccc} N_1^p & N_2^p & N_3^p & N_4^p \end{array} \right] \qquad \mathbf{D} = \left[\begin{array}{ccc} \lambda + 2\mu & \lambda & 0 \\ \lambda & \lambda + 2\mu & 0 \\ 0 & 0 & \mu \end{array} \right]$$

For plane strain, the tangent modulus, $\mathbf{D}$, is given for linear isotropic elasticity. The hydraulic equations exist relating the suction stress s to the degree of saturation S (e.g., the Brooks-Corey[18], van Genuchten[90] and Fredlund-Xing[33] equations). The main drying and wetting curves of the soil-water characteristic curve (SWCC) are both described by van Genuchten's equation in this study.

$$\begin{aligned} S_e &= \left[\frac{1}{1 + \left(\frac{s}{\mathrm{a}}\right)^{\mathrm{n}}} \right]^{\mathrm{m}}, \qquad s = p_a - p_w = \boldsymbol{N}^{e,p} \cdot (\boldsymbol{\zeta}^e - \boldsymbol{\theta}^e) \\ S &= S_r + S_e(1 - S_r) = S_r + \frac{1 - S_r}{\left[1 + (\alpha s)^{\mathrm{n}}\right]^{\mathrm{m}}} \qquad (\text{where, } \alpha = 1/\mathrm{a}) \end{aligned} \tag{2.75}$$

where, an "effective" degree of saturation S_e may be normalized by the fully saturated condition ($S = 1$) with the residual saturated condition S_r as, $S_e = \dfrac{S - S_r}{1 - S_r}$, and $\alpha(= 1/\mathrm{a})$, n and m are curve fitting parameters of the soil-water characteristic curve (or, water retention curve). For a natural soil, if the residual saturation S_r is equal to zero, then the effective degree of saturation S_e is equal to the degree of saturation S. The classical relations proposed by van Genuchten[90], namely, the degree of saturation S of equation (2.75) is considered in this study. It is written as the function

of suction stress s, and for suction stress derivative we have,

$$\frac{dS}{ds} = -(1 - S_r)\left[1 + \left(\frac{s}{\mathrm{a}}\right)^{\mathrm{n}}\right]^{(-\mathrm{m}-1)} s^{\mathrm{n}-1}\frac{\mathrm{m}\cdot\mathrm{n}}{\mathrm{a}^{\mathrm{n}}} \tag{2.76}$$

In this study, the element force vectors (body, traction, water and air) are then written as,

$$\begin{aligned}
\boldsymbol{f}_f^{e,d}(\boldsymbol{d}^e, \boldsymbol{\theta}^e, \boldsymbol{\zeta}^e) &= \int_{B^e} \rho(\boldsymbol{d}^e, \boldsymbol{\theta}^e, \boldsymbol{\zeta}^e)(\boldsymbol{N}^{e,u})^T \cdot \boldsymbol{g}\mathrm{d}a \\
&= \int_{-1}^{1}\int_{-1}^{1} \rho(\boldsymbol{d}^e, \boldsymbol{\theta}^e, \boldsymbol{\zeta}^e)(\boldsymbol{N}^{e,u})^T \cdot \boldsymbol{g}\, j\mathrm{d}\xi\mathrm{d}\eta \\
\boldsymbol{f}^{e,\theta}(\boldsymbol{d}^e, \boldsymbol{\theta}^e, \boldsymbol{\zeta}^e) &= \int_{B_w^e} \rho^{wR}(\boldsymbol{B}^{e,p})^T \cdot \boldsymbol{k}^w(\boldsymbol{d}^e, \boldsymbol{\theta}^e, \boldsymbol{\zeta}^e) \cdot \boldsymbol{g}\,\mathrm{d}a \\
&= \int_{-1}^{1}\int_{-1}^{1} \rho^{wR}(\boldsymbol{B}^{e,p})^T \cdot \boldsymbol{k}^w \cdot \boldsymbol{g}\, j\mathrm{d}\xi\mathrm{d}\eta \\
\boldsymbol{f}^{e,\zeta}(\boldsymbol{d}^e, \boldsymbol{\theta}^e, \boldsymbol{\zeta}^e) &= \int_{B_a^e} \rho^{aR}(\boldsymbol{\zeta}^e)(\boldsymbol{B}^{e,p})^T \cdot \boldsymbol{k}^a(\boldsymbol{d}^e, \boldsymbol{\theta}^e, \boldsymbol{\zeta}^e) \cdot \boldsymbol{g}\,\mathrm{d}a \\
&= \int_{-1}^{1}\int_{-1}^{1} \rho^{aR}(\boldsymbol{\zeta}^e)(\boldsymbol{B}^{e,p})^T \cdot \boldsymbol{k}^a \cdot \boldsymbol{g}\, j\mathrm{d}\xi\mathrm{d}\eta
\end{aligned} \tag{2.77}$$

$$\begin{aligned}
\boldsymbol{f}_t^{e,d} &= \int_{\Gamma_t^e} (\boldsymbol{N}^{e,u})^T \cdot \boldsymbol{t}^\sigma \mathrm{d}a \\
\boldsymbol{f}_s^{e,\theta} &= \int_{\Gamma_{s(w)}^e} (\boldsymbol{N}^{e,p})^T S^w \mathrm{d}s \\
\boldsymbol{f}_s^{e,\zeta} &= \int_{\Gamma_{s(a)}^e} (\boldsymbol{N}^{e,p})^T S^a \mathrm{d}s
\end{aligned} \tag{2.78}$$

Recall,

$$\boldsymbol{N}^{e,u} = \begin{bmatrix} \boldsymbol{N}_1^u & \boldsymbol{N}_2^u & \cdots & \boldsymbol{N}_9^u \end{bmatrix} \qquad \boldsymbol{B}^{e,p} = \begin{bmatrix} \boldsymbol{B}_1^p & \boldsymbol{B}_2^p & \boldsymbol{B}_2^p & \boldsymbol{B}_4^p \end{bmatrix}$$

$$\boldsymbol{N}_a^u = \begin{bmatrix} N_a^u & 0 \\ 0 & N_a^u \end{bmatrix} \qquad \boldsymbol{B}_b^p = \begin{bmatrix} \dfrac{dN_b^p}{dx} \\ \dfrac{dN_b^p}{dy} \end{bmatrix}$$

After element assembly, we have the coupled nonlinear parabolic PDEs to solve using generalized trapezoidal integration in time.

$$\boldsymbol{C}(\boldsymbol{D}) \cdot \dot{\boldsymbol{D}} + \boldsymbol{K}(\boldsymbol{D}) \cdot \boldsymbol{D} = \boldsymbol{F}(\boldsymbol{D}) \tag{2.79}$$

$$\dot{\boldsymbol{D}} = \begin{bmatrix} \dot{\boldsymbol{d}} \\ \dot{\boldsymbol{\theta}} \\ \dot{\boldsymbol{\zeta}} \end{bmatrix}, \ \boldsymbol{D} = \begin{bmatrix} \boldsymbol{d} \\ \boldsymbol{\theta} \\ \boldsymbol{\zeta} \end{bmatrix}, \ \boldsymbol{C}(\boldsymbol{D}) = \begin{bmatrix} \boldsymbol{0} & \boldsymbol{0} & \boldsymbol{0} \\ \boldsymbol{K}^{\theta d}(\boldsymbol{D}) & -\boldsymbol{K}^{\theta\zeta}(\boldsymbol{D}) & \boldsymbol{K}^{\theta\zeta}(\boldsymbol{D}) \\ \boldsymbol{K}^{\zeta d}(\boldsymbol{D}) & \boldsymbol{K}^{\theta\zeta}(\boldsymbol{D}) & \boldsymbol{K}^{\zeta\theta}(\boldsymbol{D}) \end{bmatrix}$$

$$\boldsymbol{K}(\boldsymbol{D}) = \begin{bmatrix} \boldsymbol{K}^{dd} & -\boldsymbol{K}^{d\theta}(\boldsymbol{D}) & -\boldsymbol{K}^{d\zeta}(\boldsymbol{D}) \\ \boldsymbol{0} & \boldsymbol{K}^{\theta\theta}(\boldsymbol{D}) & \boldsymbol{0} \\ \boldsymbol{0} & \boldsymbol{0} & \boldsymbol{K}^{\zeta\zeta}(\boldsymbol{D}) \end{bmatrix} \tag{2.80}$$

$$\boldsymbol{F}(\boldsymbol{D}) = \begin{bmatrix} \boldsymbol{f}_f^{e,d}(\boldsymbol{D}) + \boldsymbol{f}_t^{e,d} \\ \boldsymbol{f}^{e,\theta}(\boldsymbol{D}) + \boldsymbol{f}_s^{e,\theta} \\ \boldsymbol{f}^{e,\zeta}(\boldsymbol{D}) + \boldsymbol{f}_s^{e,\zeta} \end{bmatrix} = \begin{bmatrix} \boldsymbol{F}^d(\boldsymbol{D}) \\ \boldsymbol{F}^\theta(\boldsymbol{D}) \\ \boldsymbol{F}^\zeta(\boldsymbol{D}) \end{bmatrix}$$

where $\boldsymbol{C}$ is the combination of damping matrix and stiffness matrix of d.o.f vector time derivative, and $\boldsymbol{K}$ is stiffness matrix. Then, the Location Matrix (LM)[45] can be used to assemble the individual 26×26 and 26×3 contributions to the global "damping" matrix $\boldsymbol{C}$, stiffness matrix $\boldsymbol{K}$, and forcing vector $\boldsymbol{F}$, and use generalized trapezoidal integration to solve transient equations[45].

For consolidation analysis, generalized trapezoidal rule[45] is used to integrate transient through FE coupled balance of mass and linear momentum equations at time t_{n+1}, and introduced difference formulas for $\boldsymbol{D}_{n+1}$ and $\boldsymbol{V}_{n+1}$, where velocity $\boldsymbol{V}_{n+1}$ is $\dot{\boldsymbol{D}}(t_{n+1})$ and α is the time integration parameter, written as

$$\begin{aligned} \boldsymbol{C}(\boldsymbol{D}_{n+1}) \cdot \boldsymbol{V}_{n+1} + \boldsymbol{K}(\boldsymbol{D}_{n+1}) \cdot \boldsymbol{D}_{n+1} &= \boldsymbol{F}_{n+1}(\boldsymbol{D}_{n+1}) \\ \boldsymbol{D}_{n+1} &= \boldsymbol{D}_n + \Delta t \, \boldsymbol{V}_{n+\alpha} \\ \boldsymbol{V}_{n+\alpha} &= (1-\alpha)\boldsymbol{V}_n + \alpha \, \boldsymbol{V}_{n+1} \end{aligned} \tag{2.81}$$

The form of equation (2.81) allows us to consider a semi-implicit integration scheme, leading to a linear form, which is written as

$$\boldsymbol{C}(\boldsymbol{D}_n) \cdot \boldsymbol{V}_{n+1} + \boldsymbol{K}(\boldsymbol{D}_n) \cdot \boldsymbol{D}_{n+1} = \boldsymbol{F}(\boldsymbol{D}_n) \tag{2.82}$$

Table 2.2: Generalized trapezoidal family

α	METHOD	TYPE
0	forward Euler	explicit (if $\boldsymbol{C}$ diagonal, which it is not)
1/2	trapezoidal rule	implicit
1	backward Euler	implicit

Table 2.3: Procedure of semi-implicit linear scheme for triphasic mixture

1) Initialize :	given initial displacement and pore pressure $\boldsymbol{D}_0$, solve for $\boldsymbol{V}_0$ $\boldsymbol{C}(\boldsymbol{D}_0) \cdot \boldsymbol{V}_0 = \boldsymbol{F}_0(\boldsymbol{D}_0) - \boldsymbol{K}(\boldsymbol{D}_0) \cdot \boldsymbol{D}_0$
2) Predictor :	$\tilde{\boldsymbol{D}}_{n+1} = \boldsymbol{D}_n + (1-\alpha)\Delta t\, \boldsymbol{V}_n$
3) Solution :	$\Big(\boldsymbol{C}(\boldsymbol{D}_n) + \alpha\Delta t\, \boldsymbol{K}(\boldsymbol{D}_n)\Big)\boldsymbol{V}_{n+1} = \boldsymbol{F}_{n+1}(\boldsymbol{D}_n) - \boldsymbol{K}(\boldsymbol{D}_n)\tilde{\boldsymbol{D}}_{n+1}$
4) Corrector :	$\boldsymbol{D}_{n+1} = \tilde{\boldsymbol{D}}_{n+1} + \alpha\Delta t\, \boldsymbol{V}_{n+1}$
5) Stability :	It will be chosen an unconditionally-stable method ($\alpha = 1$; Backward Euler)

Some well-known members of the generalized trapezoidal family are identified in Table 2.2, and then generalized trapezoidal rule for consolidation analysis is implemented for linear form (semi-implicit) by the procedure given in Table 2.3. The full nonlinear Newton-Raphson procedure is presented for the biphasic case ($p_a \approx 0$, atmospheric) in Section 2.5.3.

2.4.3 FE form for 2D fully-implicit nonlinear triphasic poro-elasticity

The coupled finite element (FE) form for fully-implicit nonlinear triphasic poro-elasticity with solution by Newton-Raphson method, and all derivatives are need to apply to the hyperelastic Cam-clay plasticity model. The nonlinear triphasic poro-elasticity also assumes the solid skeleton effective stress $\boldsymbol{\sigma}'$(eventually will be a function of suction in plasticity) can be governed by a nonlinear constitutive model, and that the density and permeability are functions of displacement and porosity, and porosity is a function of the solid skeleton volumetric strain ϵ_v. The coupled FE equations for triphasic mixture written then as

1) *Solid* (nonlinear triphasic) :

$$\begin{aligned}\mathop{\mathbf{A}}_{e=1}^{n_{\mathrm{el}}}(\boldsymbol{c}^e)^T\cdot\Bigg[&\underbrace{\left(\int_{B^e}(\boldsymbol{B}^{e,u})^T\cdot\boldsymbol{\sigma}'(\boldsymbol{d}^e,\boldsymbol{\theta}^e)\,\mathrm{d}a\right)}_{\boldsymbol{f}_e^{d,INT}(\boldsymbol{d}^e,\boldsymbol{\theta}^e)}-\underbrace{\left(\int_{B^e}\chi(\boldsymbol{\theta}^e,\boldsymbol{\zeta}^e)(\tilde{\boldsymbol{B}}^{e,u})^T\cdot\boldsymbol{N}^{e,p}\cdot\boldsymbol{\theta}^e\,\mathrm{d}a\right)}_{\boldsymbol{f}_e^{d\theta,INT}(\boldsymbol{\theta}^e,\boldsymbol{\zeta}^e)}\\&-\underbrace{\left(\int_{B^e}\Big(1-\chi(\boldsymbol{\theta}^e,\boldsymbol{\zeta}^e)\Big)(\tilde{\boldsymbol{B}}^{e,u})^T\cdot\boldsymbol{N}^{e,p}\cdot\boldsymbol{\zeta}^e\,\mathrm{d}a\right)}_{\boldsymbol{f}_e^{d\zeta,INT}(\boldsymbol{\theta}^e,\boldsymbol{\zeta}^e)}\\&=\underbrace{\int_{B^e}\rho(\boldsymbol{d}^e,\boldsymbol{\theta}^e,\boldsymbol{\zeta}^e)(\boldsymbol{N}^{e,u})^T\cdot\boldsymbol{g}\,\mathrm{d}a+\int_{\Gamma_t^e}(\boldsymbol{N}^{e,u})^T\cdot\boldsymbol{t}\,\mathrm{d}s}_{\boldsymbol{f}_e^{d,EXT}(\boldsymbol{d}^e,\boldsymbol{\theta}^e,\boldsymbol{\zeta}^e)}\Bigg]\end{aligned}\tag{2.83}$$

2) *Water* (nonlinear triphasic) :

$$\begin{aligned}
\mathop{\mathbf{A}}_{e=1}^{n_{\mathrm{el}}} (\boldsymbol{\alpha}^e)^T \cdot \Bigg[& \underbrace{\left(\int_{B_w^e} S(\boldsymbol{\theta}^e, \boldsymbol{\zeta}^e) \, (\boldsymbol{N}^{e,p})^T \cdot \tilde{\boldsymbol{B}}^{e,u} \, \mathrm{d}a \right)}_{\boldsymbol{k}_e^{\theta d, INT}(\boldsymbol{\theta}^e, \boldsymbol{\zeta}^e)} \cdot \dot{\boldsymbol{d}}^e \\
& - \underbrace{\left(\int_{B_w^e} n(\boldsymbol{d}^e) \frac{\partial S(\boldsymbol{\theta}^e, \boldsymbol{\zeta}^e)}{\partial s} (\boldsymbol{N}^{e,p})^T \cdot \boldsymbol{N}^{e,p} \, \mathrm{d}a \right)}_{\boldsymbol{k}_e^{\theta\theta, INT}(\boldsymbol{d}^e, \boldsymbol{\theta}^e, \boldsymbol{\zeta}^e)} \cdot \dot{\boldsymbol{\theta}}^e \\
& + \underbrace{\left(\int_{B_w^e} n(\boldsymbol{d}^e) \frac{\partial S(\boldsymbol{\theta}^e, \boldsymbol{\zeta}^e)}{\partial s} (\boldsymbol{N}^{e,p})^T \cdot \boldsymbol{N}^{e,p} \, \mathrm{d}a \right)}_{\boldsymbol{k}_e^{\theta\zeta, INT}(\boldsymbol{d}^e, \boldsymbol{\theta}^e, \boldsymbol{\zeta}^e)} \cdot \dot{\boldsymbol{\zeta}}^e \\
& \underbrace{- \left(\int_{B_w^e} (\boldsymbol{B}^{e,p})^T \cdot \tilde{\boldsymbol{v}}_w^s(\boldsymbol{d}^e, \boldsymbol{\theta}^e, \boldsymbol{\zeta}^e) \, \mathrm{d}a \right)}_{\boldsymbol{f}_e^{\theta 1, INT}(\boldsymbol{d}^e, \boldsymbol{\theta}^e, \boldsymbol{\zeta}^e)} = \underbrace{\int_{\Gamma_{s(w)}^e} (\boldsymbol{N}^{e,p})^T S^w \, \mathrm{d}s}_{\boldsymbol{f}_e^{\theta, EXT}} \Bigg]
\end{aligned} \tag{2.84}$$

3) *Air* (nonlinear triphasic) :

$$\begin{aligned}
\mathop{\mathbf{A}}_{e=1}^{n_{\mathrm{el}}} (\boldsymbol{\beta}^e)^T \cdot \Bigg[& \underbrace{\left(\int_{B_a^e} \Big(1 - S(\boldsymbol{\theta}^e, \boldsymbol{\zeta}^e)\Big) \, (\boldsymbol{N}^{e,p})^T \cdot \tilde{\boldsymbol{B}}^{e,u} \, \mathrm{d}a \right)}_{\boldsymbol{k}_e^{\zeta d, INT}(\boldsymbol{\theta}^e, \boldsymbol{\zeta}^e)} \cdot \dot{\boldsymbol{d}}^e \\
& + \underbrace{\left(\int_{B_a^e} n(\boldsymbol{d}^e) \frac{\partial S(\boldsymbol{\theta}^e, \boldsymbol{\zeta}^e)}{\partial s} (\boldsymbol{N}^{e,p})^T \cdot \boldsymbol{N}^{e,p} \, \mathrm{d}a \right)}_{\boldsymbol{k}_e^{\zeta\theta, INT}(\boldsymbol{d}^e, \boldsymbol{\theta}^e, \boldsymbol{\zeta}^e)} \cdot \dot{\boldsymbol{\theta}}^e \\
& + \underbrace{\left(\int_{B_a^e} \left[\frac{n(\boldsymbol{d}^e)}{K_a} \Big(1 - S(\boldsymbol{\theta}^e, \boldsymbol{\zeta}^e)\Big) - n(\boldsymbol{d}^e) \frac{\partial S(\boldsymbol{\theta}^e, \boldsymbol{\zeta}^e)}{\partial s} \right] (\boldsymbol{N}^{e,p})^T \cdot \boldsymbol{N}^{e,p} \, \mathrm{d}a \right)}_{\boldsymbol{k}_e^{\zeta\zeta, INT}(\boldsymbol{d}^e, \boldsymbol{\theta}^e, \boldsymbol{\zeta}^e)} \cdot \dot{\boldsymbol{\zeta}}^e \\
& \underbrace{- \left(\int_{B_a^e} (\boldsymbol{B}^{e,p})^T \cdot \tilde{\boldsymbol{v}}_a^s(\boldsymbol{d}^e, \boldsymbol{\theta}^e, \boldsymbol{\zeta}^e) \, \mathrm{d}a \right)}_{\boldsymbol{f}_e^{\zeta 1, INT}(\boldsymbol{d}^e, \boldsymbol{\theta}^e, \boldsymbol{\zeta}^e)} = \underbrace{\int_{\Gamma_{s(a)}^e} (\boldsymbol{N}^{e,p})^T S^a \, \mathrm{d}s}_{\boldsymbol{f}_e^{\zeta, EXT}} \Bigg]
\end{aligned} \tag{2.85}$$

where Darcy's water and air velocity, $\tilde{\boldsymbol{v}}_w^s = -\boldsymbol{k}^w(\boldsymbol{d}^e, \boldsymbol{\theta}^e) \cdot [\boldsymbol{\nabla} p_w - \rho^{wR} \boldsymbol{g}]$ and $\tilde{\boldsymbol{v}}_a^s = -\boldsymbol{k}^a(\boldsymbol{d}^e, \boldsymbol{\theta}^e) \cdot$

$[\boldsymbol{\nabla} p_a - \rho^{aR}\boldsymbol{g}]$, is defined by Darcy's law with porosity and saturation rate dependent permeability, $\boldsymbol{k}^w = k_w(n,S)\,\mathbf{1}$ and $\boldsymbol{k}^a = k_a(n,S)\,\mathbf{1}$. And then these nonlinear FE equations are written as

$$\begin{aligned}
&\mathop{\mathbf{A}}_{e=1}^{n_{\mathrm{el}}} (\boldsymbol{c}^e)^T \cdot \left[\boldsymbol{f}_e^{d,INT}(\boldsymbol{d}^e,\boldsymbol{\theta}^e) - \boldsymbol{f}_e^{d\theta,INT}(\boldsymbol{\theta}^e,\boldsymbol{\zeta}^e) - \boldsymbol{f}_e^{d\zeta,INT}(\boldsymbol{\theta}^e,\boldsymbol{\zeta}^e) = \boldsymbol{f}_e^{d,EXT}(\boldsymbol{d}^e,\boldsymbol{\theta}^e,\boldsymbol{\zeta}^e) \right] \\
&\mathop{\mathbf{A}}_{e=1}^{n_{\mathrm{el}}} (\boldsymbol{\alpha}^e)^T \cdot \Big[\boldsymbol{k}_e^{\theta d,INT}(\boldsymbol{\theta}^e,\boldsymbol{\zeta}^e)\cdot\dot{\boldsymbol{d}}^e - \boldsymbol{k}_e^{\theta\theta,INT}(\boldsymbol{d}^e,\boldsymbol{\theta}^e,\boldsymbol{\zeta}^e)\cdot\dot{\boldsymbol{\theta}}^e + \boldsymbol{k}_e^{\theta\zeta,INT}(\boldsymbol{d}^e,\boldsymbol{\theta}^e,\boldsymbol{\zeta}^e)\cdot\dot{\boldsymbol{\zeta}}^e \\
&\qquad\qquad - \boldsymbol{f}_e^{\theta 1,INT}(\boldsymbol{d}^e,\boldsymbol{\theta}^e,\boldsymbol{\zeta}^e) = \boldsymbol{f}_e^{\theta,EXT} \Big] \\
&\mathop{\mathbf{A}}_{e=1}^{n_{\mathrm{el}}} (\boldsymbol{\beta}^e)^T \cdot \Big[\boldsymbol{k}_e^{\zeta d,INT}(\boldsymbol{\theta}^e,\boldsymbol{\zeta}^e)\cdot\dot{\boldsymbol{d}}^e + \boldsymbol{k}_e^{\zeta\theta,INT}(\boldsymbol{d}^e,\boldsymbol{\theta}^e,\boldsymbol{\zeta}^e)\cdot\dot{\boldsymbol{\theta}}^e + \boldsymbol{k}_e^{\zeta\zeta,INT}(\boldsymbol{d}^e,\boldsymbol{\theta}^e,\boldsymbol{\zeta}^e)\cdot\dot{\boldsymbol{\zeta}}^e \\
&\qquad\qquad - \boldsymbol{f}_e^{\zeta 1,INT}(\boldsymbol{d}^e,\boldsymbol{\theta}^e,\boldsymbol{\zeta}^e) = \boldsymbol{f}_e^{\zeta,EXT} \Big]
\end{aligned} \tag{2.86}$$

After element assembly, we have the coupled nonlinear parabolic PDEs to solve using generalized trapezoidal integration in time, and Newton-Raphson iteration

$$\boldsymbol{F}^{d,INT}(\boldsymbol{d},\boldsymbol{\theta}) - \boldsymbol{F}^{d\theta,INT}(\boldsymbol{\theta},\boldsymbol{\zeta}) - \boldsymbol{F}^{d\zeta,INT}(\boldsymbol{\theta},\boldsymbol{\zeta}) = \boldsymbol{F}^{d,EXT}(\boldsymbol{d},\boldsymbol{\theta},\boldsymbol{\zeta}) \tag{2.87}$$

$$\begin{aligned}
&\boldsymbol{K}^{\theta d,INT}(\boldsymbol{\theta},\boldsymbol{\zeta})\cdot\dot{\boldsymbol{d}} - \boldsymbol{K}^{\theta\theta,INT}(\boldsymbol{d},\boldsymbol{\theta},\boldsymbol{\zeta})\cdot\dot{\boldsymbol{\theta}} + \boldsymbol{K}^{\theta\zeta,INT}(\boldsymbol{d},\boldsymbol{\theta},\boldsymbol{\zeta})\cdot\dot{\boldsymbol{\zeta}} - \boldsymbol{F}^{\theta 1,INT}(\boldsymbol{d},\boldsymbol{\theta},\boldsymbol{\zeta}) \\
&\qquad\qquad = \boldsymbol{F}^{\theta,EXT}
\end{aligned} \tag{2.88}$$

$$\begin{aligned}
&\boldsymbol{K}^{\zeta d,INT}(\boldsymbol{\theta},\boldsymbol{\zeta})\cdot\dot{\boldsymbol{d}} + \boldsymbol{K}^{\zeta\theta,INT}(\boldsymbol{d},\boldsymbol{\theta},\boldsymbol{\zeta})\cdot\dot{\boldsymbol{\theta}} + \boldsymbol{K}^{\zeta\zeta,INT}(\boldsymbol{d},\boldsymbol{\theta},\boldsymbol{\zeta})\cdot\dot{\boldsymbol{\zeta}} - \boldsymbol{F}^{\zeta 1,INT}(\boldsymbol{d},\boldsymbol{\theta},\boldsymbol{\zeta}) \\
&\qquad\qquad = \boldsymbol{F}^{\zeta,EXT}
\end{aligned} \tag{2.89}$$

which we may rewrite as

$$\boldsymbol{C}(\boldsymbol{D})\cdot\dot{\boldsymbol{D}} + \boldsymbol{F}^{INT}(\boldsymbol{D}) = \boldsymbol{F}^{EXT}(\boldsymbol{D}) \tag{2.90}$$

where,

$$\boldsymbol{C}(\boldsymbol{D}) = \begin{bmatrix} \mathbf{0} & \mathbf{0} & \mathbf{0} \\ \boldsymbol{K}^{\theta d,INT}(\boldsymbol{\theta},\boldsymbol{\zeta}) & -\boldsymbol{K}^{\theta\theta,INT}(\boldsymbol{d},\boldsymbol{\theta},\boldsymbol{\zeta}) & \boldsymbol{K}^{\theta\zeta,INT}(\boldsymbol{d},\boldsymbol{\theta},\boldsymbol{\zeta}) \\ \boldsymbol{K}^{\zeta d,INT}(\boldsymbol{\theta},\boldsymbol{\zeta}) & \boldsymbol{K}^{\zeta\theta,INT}(\boldsymbol{d},\boldsymbol{\theta},\boldsymbol{\zeta}) & \boldsymbol{K}^{\zeta\zeta,INT}(\boldsymbol{d},\boldsymbol{\theta},\boldsymbol{\zeta}) \end{bmatrix}$$

$$\boldsymbol{F}^{INT}(\boldsymbol{D}) = \begin{bmatrix} \boldsymbol{F}^{d,INT}(\boldsymbol{d},\boldsymbol{\theta}) - \boldsymbol{F}^{d\theta,INT}(\boldsymbol{\theta},\boldsymbol{\zeta}) - \boldsymbol{F}^{d\zeta,INT}(\boldsymbol{\theta},\boldsymbol{\zeta}) \\ -\boldsymbol{F}^{\theta 1,INT}(\boldsymbol{d},\boldsymbol{\theta},\boldsymbol{\zeta}) \\ -\boldsymbol{F}^{\zeta 1,INT}(\boldsymbol{d},\boldsymbol{\theta},\boldsymbol{\zeta}) \end{bmatrix}$$

$$\boldsymbol{D} = \begin{bmatrix} \boldsymbol{d} \\ \boldsymbol{\theta} \\ \boldsymbol{\zeta} \end{bmatrix}, \quad \dot{\boldsymbol{D}} = \begin{bmatrix} \dot{\boldsymbol{d}} \\ \dot{\boldsymbol{\theta}} \\ \dot{\boldsymbol{\zeta}} \end{bmatrix}, \quad \boldsymbol{F}^{EXT}(\boldsymbol{D}) = \begin{bmatrix} \boldsymbol{F}^{d,EXT}(\boldsymbol{d},\boldsymbol{\theta},\boldsymbol{\zeta}) \\ \boldsymbol{F}^{\theta,EXT} \\ \boldsymbol{F}^{\zeta,EXT} \end{bmatrix}$$

Recall the generalized trapezoidal integration:

$$\begin{gathered} \boldsymbol{C}(\boldsymbol{D}_{n+1}) \cdot \boldsymbol{V}_{n+1} + \boldsymbol{F}^{INT}(\boldsymbol{D}_{n+1}) = \boldsymbol{F}^{EXT}(\boldsymbol{D}_{n+1}) \\ \boldsymbol{D}_{n+1} = \tilde{\boldsymbol{D}}_{n+1} + \alpha\Delta t\, \boldsymbol{V}_{n+1}\,, \qquad \tilde{\boldsymbol{D}}_{n+1} = \boldsymbol{D}_n + (1-\alpha)\Delta t\, \boldsymbol{V}_n \end{gathered} \tag{2.91}$$

$$\begin{gathered} \boldsymbol{C}(\boldsymbol{D}_0) \cdot \boldsymbol{V}_0 + \boldsymbol{F}^{INT}(\boldsymbol{D}_0) - \boldsymbol{F}^{EXT}(\boldsymbol{D}_0) = \mathbf{0} \\ \boldsymbol{V}_0 = \boldsymbol{C}_0^{-1} \cdot \left(\boldsymbol{F}_0^{EXT} - \boldsymbol{F}_0^{INT}\right) \end{gathered} \tag{2.92}$$

It can be expressed in residual form, solving for $\boldsymbol{V}_{n+1}^{k+1}$ in a Newton-Raphson iteration algorithm with current iteration $(k+1)$:

$$\begin{aligned} \boldsymbol{R}(\boldsymbol{V}_{n+1}^{k+1}) &= \boldsymbol{C}(\boldsymbol{D}_{n+1}^{k+1}) \cdot \boldsymbol{V}_{n+1}^{k+1} + \boldsymbol{F}^{INT}(\boldsymbol{D}_{n+1}^{k+1}) - \boldsymbol{F}^{EXT}(\boldsymbol{D}_{n+1}^{k+1}) = \mathbf{0} \\ &= \boldsymbol{R}^k + \frac{\partial \boldsymbol{R}^k}{\partial \boldsymbol{V}} \cdot \delta\boldsymbol{V} \approx \mathbf{0} \end{aligned} \tag{2.93}$$

Therefore,

$$\begin{aligned} \delta\boldsymbol{V} &= -\left(\frac{\partial \boldsymbol{R}^k}{\partial \boldsymbol{V}}\right)^{-1} \cdot \boldsymbol{R}^k \\ \boldsymbol{V}_{n+1}^{k+1} &= \boldsymbol{V}_{n+1}^{k} + \delta\boldsymbol{V} \\ \boldsymbol{D}_{n+1}^{k+1} &= \tilde{\boldsymbol{D}}_{n+1} + \alpha\Delta t\, \boldsymbol{V}_{n+1}^{k+1} \end{aligned} \tag{2.94}$$

For consistent tangent,

$$\frac{\partial \boldsymbol{R}}{\partial \boldsymbol{V}} = \left(\frac{\partial \boldsymbol{C}}{\partial \boldsymbol{D}} \cdot \frac{\partial \boldsymbol{D}}{\partial \boldsymbol{V}}\right) \cdot \boldsymbol{V} + \boldsymbol{C}(\boldsymbol{D}) + \frac{\partial \boldsymbol{F}^{INT}}{\partial \boldsymbol{D}} \cdot \frac{\partial \boldsymbol{D}}{\partial \boldsymbol{V}} - \frac{\partial \boldsymbol{F}^{EXT}}{\partial \boldsymbol{D}} \cdot \frac{\partial \boldsymbol{D}}{\partial \boldsymbol{V}} \tag{2.95}$$

where $\dfrac{\partial \boldsymbol{D}}{\partial \boldsymbol{V}} = \alpha \Delta t$. Equivalently, in component form, we have

$$\begin{aligned}
R_{A} &= C_{AB} \cdot V_{B} + F^{INT}_{A} - F^{EXT}_{A} \qquad \Big(A, B, C \ \text{ and } \ E = 1, \cdots, n_{dof}\Big) \\
\frac{\partial R_{A}}{\partial V_{C}} &= \left(\frac{\partial C_{AB}}{\partial D_{E}} \frac{\partial D_{E}}{\partial V_{C}}\right) \cdot V_{B} + C_{AB} \frac{\partial V_{B}}{\partial V_{C}} + \frac{\partial F^{INT}_{A}}{\partial D_{B}} \frac{\partial D_{B}}{\partial V_{C}} - \frac{\partial F^{EXT}_{A}}{\partial D_{B}} \frac{\partial D_{B}}{\partial V_{C}} \\
&= \left(\frac{\partial C_{AB}}{\partial D_{E}} \delta_{EC}\, \alpha \Delta t\right) \cdot V_{B} + C_{AB}\, \delta_{BC} + \frac{\partial F^{INT}_{A}}{\partial D_{B}} \delta_{BC}\, \alpha \Delta t - \frac{\partial F^{EXT}_{A}}{\partial D_{B}} \delta_{BC}\, \alpha \Delta t \\
&= \alpha \Delta t \frac{\partial C_{AB}}{\partial D_{C}} V_{B} + C_{AC} + \frac{\partial F^{INT}_{A}}{\partial D_{C}} \alpha \Delta t - \frac{\partial F^{EXT}_{A}}{\partial D_{C}} \alpha \Delta t
\end{aligned} \tag{2.96}$$

where $\boldsymbol{C} \cdot \boldsymbol{V} = \begin{bmatrix} \mathbf{0} \\ \boldsymbol{K}^{\theta d, INT} \cdot \dot{\boldsymbol{d}} - \boldsymbol{K}^{\theta\theta, INT} \cdot \dot{\boldsymbol{\theta}} + \boldsymbol{K}^{\theta\zeta, INT} \cdot \dot{\boldsymbol{\zeta}} \\ \boldsymbol{K}^{\zeta d, INT} \cdot \dot{\boldsymbol{d}} + \boldsymbol{K}^{\zeta\theta, INT} \cdot \dot{\boldsymbol{\theta}} + \boldsymbol{K}^{\zeta\zeta, INT} \cdot \dot{\boldsymbol{\zeta}} \end{bmatrix}$, and then implied

$$\frac{\partial \boldsymbol{C}}{\partial \boldsymbol{D}} \cdot \boldsymbol{V} \left(= \frac{\partial C_{AB}}{\partial D_C} V_B \right) = \begin{bmatrix} \mathbf{0} \\ -\dfrac{\partial \boldsymbol{K}^{\theta\theta,INT}}{\partial \boldsymbol{d}} \cdot \dot{\boldsymbol{\theta}} + \dfrac{\partial \boldsymbol{K}^{\theta\zeta,INT}}{\partial \boldsymbol{d}} \cdot \dot{\boldsymbol{\zeta}} \\ \dfrac{\partial \boldsymbol{K}^{\zeta\theta,INT}}{\partial \boldsymbol{d}} \cdot \dot{\boldsymbol{\theta}} + \dfrac{\partial \boldsymbol{K}^{\zeta\zeta,INT}}{\partial \boldsymbol{d}} \cdot \dot{\boldsymbol{\zeta}} \end{bmatrix}$$

$$\begin{bmatrix} \mathbf{0} \\ \dfrac{\partial \boldsymbol{K}^{\theta d,INT}}{\partial \boldsymbol{\theta}} \cdot \dot{\boldsymbol{d}} - \dfrac{\partial \boldsymbol{K}^{\theta\theta,INT}}{\partial \boldsymbol{\theta}} \cdot \dot{\boldsymbol{\theta}} + \dfrac{\partial \boldsymbol{K}^{\theta\zeta,INT}}{\partial \boldsymbol{\theta}} \cdot \dot{\boldsymbol{\zeta}} \\ \dfrac{\partial \boldsymbol{K}^{\zeta d,INT}}{\partial \boldsymbol{\theta}} \cdot \dot{\boldsymbol{d}} + \dfrac{\partial \boldsymbol{K}^{\zeta\theta,INT}}{\partial \boldsymbol{\theta}} \cdot \dot{\boldsymbol{\theta}} + \dfrac{\partial \boldsymbol{K}^{\zeta\zeta,INT}}{\partial \boldsymbol{\theta}} \cdot \dot{\boldsymbol{\zeta}} \end{bmatrix} \tag{2.97}$$

$$\begin{bmatrix} \mathbf{0} \\ \dfrac{\partial \boldsymbol{K}^{\theta d,INT}}{\partial \boldsymbol{\zeta}} \cdot \dot{\boldsymbol{d}} - \dfrac{\partial \boldsymbol{K}^{\theta\theta,INT}}{\partial \boldsymbol{\zeta}} \cdot \dot{\boldsymbol{\theta}} + \dfrac{\partial \boldsymbol{K}^{\theta\zeta,INT}}{\partial \boldsymbol{\zeta}} \cdot \dot{\boldsymbol{\zeta}} \\ \dfrac{\partial \boldsymbol{K}^{\zeta d,INT}}{\partial \boldsymbol{\zeta}} \cdot \dot{\boldsymbol{d}} + \dfrac{\partial \boldsymbol{K}^{\zeta\theta,INT}}{\partial \boldsymbol{\zeta}} \cdot \dot{\boldsymbol{\theta}} + \dfrac{\partial \boldsymbol{K}^{\zeta\zeta,INT}}{\partial \boldsymbol{\zeta}} \cdot \dot{\boldsymbol{\zeta}} \end{bmatrix}$$

$$\frac{\partial \boldsymbol{F}^{INT}}{\partial \boldsymbol{D}} = \begin{bmatrix} \dfrac{\partial \boldsymbol{F}^{INT}}{\partial \boldsymbol{d}} & \dfrac{\partial \boldsymbol{F}^{INT}}{\partial \boldsymbol{\theta}} & \dfrac{\partial \boldsymbol{F}^{INT}}{\partial \boldsymbol{\zeta}} \end{bmatrix} \tag{2.98}$$

$$\frac{\partial \boldsymbol{F}^{INT}}{\partial \boldsymbol{d}} = \begin{bmatrix} \dfrac{\partial \boldsymbol{F}^{d,INT}}{\partial \boldsymbol{d}} \\ -\dfrac{\partial \boldsymbol{F}^{\theta 1,INT}}{\partial \boldsymbol{d}} \\ -\dfrac{\partial \boldsymbol{F}^{\zeta 1,INT}}{\partial \boldsymbol{d}} \end{bmatrix}, \quad \frac{\partial \boldsymbol{F}^{INT}}{\partial \boldsymbol{\theta}} = \begin{bmatrix} \dfrac{\partial \boldsymbol{F}^{d,INT}}{\partial \boldsymbol{\theta}} - \dfrac{\partial \boldsymbol{F}^{d\theta,INT}}{\partial \boldsymbol{\theta}} - \dfrac{\partial \boldsymbol{F}^{d\zeta,INT}}{\partial \boldsymbol{\theta}} \\ -\dfrac{\partial \boldsymbol{F}^{\theta 1,INT}}{\partial \boldsymbol{\theta}} \\ -\dfrac{\partial \boldsymbol{F}^{\zeta 1,INT}}{\partial \boldsymbol{\theta}} \end{bmatrix}$$

$$\frac{\partial \boldsymbol{F}^{INT}}{\partial \boldsymbol{\zeta}} = \begin{bmatrix} -\dfrac{\partial \boldsymbol{F}^{d\theta,INT}}{\partial \boldsymbol{\zeta}} - \dfrac{\partial \boldsymbol{F}^{d\zeta,INT}}{\partial \boldsymbol{\zeta}} \\ -\dfrac{\partial \boldsymbol{F}^{\theta 1,INT}}{\partial \boldsymbol{\zeta}} \\ -\dfrac{\partial \boldsymbol{F}^{\zeta 1,INT}}{\partial \boldsymbol{\zeta}} \end{bmatrix}$$

$$\frac{\partial \boldsymbol{F}^{EXT}}{\partial \boldsymbol{D}} = \begin{bmatrix} \dfrac{\partial \boldsymbol{F}^{EXT}}{\partial \boldsymbol{d}} & \dfrac{\partial \boldsymbol{F}^{EXT}}{\partial \boldsymbol{\theta}} & \dfrac{\partial \boldsymbol{F}^{EXT}}{\partial \boldsymbol{\zeta}} \end{bmatrix} \tag{2.99}$$

$$\frac{\partial \boldsymbol{F}^{EXT}}{\partial \boldsymbol{d}} = \begin{bmatrix} \dfrac{\partial \boldsymbol{F}^{d,EXT}}{\partial \boldsymbol{d}} \\ \mathbf{0} \\ \mathbf{0} \end{bmatrix}, \quad \frac{\partial \boldsymbol{F}^{EXT}}{\partial \boldsymbol{\theta}} = \begin{bmatrix} \dfrac{\partial \boldsymbol{F}^{d,EXT}}{\partial \boldsymbol{\theta}} \\ \mathbf{0} \\ \mathbf{0} \end{bmatrix}, \quad \frac{\partial \boldsymbol{F}^{EXT}}{\partial \boldsymbol{\zeta}} = \begin{bmatrix} \dfrac{\partial \boldsymbol{F}^{d,EXT}}{\partial \boldsymbol{\zeta}} \\ \mathbf{0} \\ \mathbf{0} \end{bmatrix}$$

In which its components are

$$\begin{aligned} \frac{\partial \boldsymbol{K}^{\theta\theta,INT}}{\partial \boldsymbol{d}} \cdot \dot{\boldsymbol{\theta}} &= \mathop{\mathbf{A}}_{e=1}^{n_{\text{el}}} \frac{\partial \boldsymbol{k}_e^{\theta\theta,INT}}{\partial \boldsymbol{d}^e} \cdot \dot{\boldsymbol{\theta}}^e \\ &= \mathop{\mathbf{A}}_{e=1}^{n_{\text{el}}} \int_{B_w^e} \left[\dot{p}_w \frac{\partial S(\boldsymbol{\theta}^e, \boldsymbol{\zeta}^e)}{\partial s} (\boldsymbol{N}^{e,p})^T \right] \otimes \frac{\partial n(\boldsymbol{d}^e)}{\partial \boldsymbol{d}^e} \, \mathrm{d}a \end{aligned} \tag{2.100}$$

$$\begin{aligned} \frac{\partial \boldsymbol{K}^{\theta\zeta,INT}}{\partial \boldsymbol{d}} \cdot \dot{\boldsymbol{\zeta}} &= \mathop{\mathbf{A}}_{e=1}^{n_{\text{el}}} \frac{\partial \boldsymbol{k}_e^{\theta\zeta,INT}}{\partial \boldsymbol{d}^e} \cdot \dot{\boldsymbol{\zeta}}^e \\ &= \mathop{\mathbf{A}}_{e=1}^{n_{\text{el}}} \int_{B_w^e} \left[\dot{p}_a \frac{\partial S(\boldsymbol{\theta}^e, \boldsymbol{\zeta}^e)}{\partial s} (\boldsymbol{N}^{e,p})^T \right] \otimes \frac{\partial n(\boldsymbol{d}^e)}{\partial \boldsymbol{d}^e} \, \mathrm{d}a \end{aligned} \tag{2.101}$$

$$\begin{aligned} \frac{\partial \boldsymbol{K}^{\zeta\theta,INT}}{\partial \boldsymbol{d}} \cdot \dot{\boldsymbol{\theta}} &= \mathop{\mathbf{A}}_{e=1}^{n_{\text{el}}} \frac{\partial \boldsymbol{k}_e^{\zeta\theta,INT}}{\partial \boldsymbol{d}^e} \cdot \dot{\boldsymbol{\theta}}^e \\ &= \mathop{\mathbf{A}}_{e=1}^{n_{\text{el}}} \int_{B_a^e} \left[\dot{p}_w \frac{\partial S(\boldsymbol{\theta}^e, \boldsymbol{\zeta}^e)}{\partial s} (\boldsymbol{N}^{e,p})^T \right] \otimes \frac{\partial n(\boldsymbol{d}^e)}{\partial \boldsymbol{d}^e} \, \mathrm{d}a \end{aligned} \tag{2.102}$$

$$\begin{aligned} \frac{\partial \boldsymbol{K}^{\zeta\zeta,INT}}{\partial \boldsymbol{d}} \cdot \dot{\boldsymbol{\zeta}} &= \mathop{\mathbf{A}}_{e=1}^{n_{\text{el}}} \frac{\partial \boldsymbol{k}_e^{\zeta\zeta,INT}}{\partial \boldsymbol{d}^e} \cdot \dot{\boldsymbol{\zeta}}^e \\ &= \mathop{\mathbf{A}}_{e=1}^{n_{\text{el}}} \int_{B_a^e} \left[\dot{p}_a \left(\frac{1}{K_a} - \frac{S(\boldsymbol{\theta}^e, \boldsymbol{\zeta}^e)}{K_a} - \frac{\partial S(\boldsymbol{\theta}^e, \boldsymbol{\zeta}^e)}{\partial s} \right) (\boldsymbol{N}^{e,p})^T \right] \\ &\qquad \otimes \frac{\partial n(\boldsymbol{d}^e)}{\partial \boldsymbol{d}^e} \, \mathrm{d}a \end{aligned} \tag{2.103}$$

where $\dot{p}_w = \boldsymbol{N}^{e,p} \cdot \dot{\boldsymbol{\theta}}^e$, $\dot{p}_a = \boldsymbol{N}^{e,p} \cdot \dot{\boldsymbol{\zeta}}^e$ and $\dfrac{\partial n}{\partial \boldsymbol{d}^e} = \left(\dfrac{1-n}{1+\Delta\epsilon_v} \right) \tilde{\boldsymbol{B}}^{e,u}$.

$$\begin{aligned} \frac{\partial \boldsymbol{K}^{\theta d,INT}}{\partial \boldsymbol{\theta}} \cdot \dot{\boldsymbol{d}} &= \mathop{\mathbf{A}}_{e=1}^{n_{\text{el}}} \frac{\partial \boldsymbol{k}_e^{\theta d,INT}}{\partial \boldsymbol{\theta}^e} \cdot \dot{\boldsymbol{d}}^e = \mathop{\mathbf{A}}_{e=1}^{n_{\text{el}}} \int_{B_w^e} \left[\dot{\epsilon}_v (\boldsymbol{N}^{e,p})^T \right] \otimes \frac{\partial S(\boldsymbol{\theta}^e, \boldsymbol{\zeta}^e)}{\partial \boldsymbol{\theta}^e} \, \mathrm{d}a \\ &= \mathop{\mathbf{A}}_{e=1}^{n_{\text{el}}} \int_{B_w^e} \dot{\epsilon}_v \left[(\boldsymbol{N}^{e,p})^T \right] \otimes \left(-\frac{\partial S(\boldsymbol{\theta}^e, \boldsymbol{\zeta}^e)}{\partial s} \boldsymbol{N}^{e,p} \right) \, \mathrm{d}a \end{aligned} \tag{2.104}$$

$$\begin{aligned}\frac{\partial \boldsymbol{K}^{\theta\theta,INT}}{\partial \boldsymbol{\theta}} \cdot \dot{\boldsymbol{\theta}} &= \mathop{\mathsf{A}}_{e=1}^{n_{\text{el}}} \frac{\partial \boldsymbol{k}_e^{\theta\theta,INT}}{\partial \boldsymbol{\theta}^e} \cdot \dot{\boldsymbol{\theta}}^e \\ &= \mathop{\mathsf{A}}_{e=1}^{n_{\text{el}}} \int_{B_w^e} \dot{p}_w \, n(\boldsymbol{d}^e) \Big[(\boldsymbol{N}^{e,p})^T \Big] \otimes \left(-\frac{\partial^2 S(\boldsymbol{\theta}^e, \boldsymbol{\zeta}^e)}{\partial s^2} \boldsymbol{N}^{e,p} \right) \mathrm{d}a \end{aligned} \tag{2.105}$$

$$\begin{aligned}\frac{\partial \boldsymbol{K}^{\theta\zeta,INT}}{\partial \boldsymbol{\theta}} \cdot \dot{\boldsymbol{\zeta}} &= \mathop{\mathsf{A}}_{e=1}^{n_{\text{el}}} \frac{\partial \boldsymbol{k}_e^{\theta\zeta,INT}}{\partial \boldsymbol{\theta}^e} \cdot \dot{\boldsymbol{\zeta}}^e \\ &= \mathop{\mathsf{A}}_{e=1}^{n_{\text{el}}} \int_{B_w^e} \dot{p}_a \, n(\boldsymbol{d}^e) \Big[(\boldsymbol{N}^{e,p})^T \Big] \otimes \left(-\frac{\partial^2 S(\boldsymbol{\theta}^e, \boldsymbol{\zeta}^e)}{\partial s^2} \boldsymbol{N}^{e,p} \right) \mathrm{d}a \end{aligned} \tag{2.106}$$

$$\begin{aligned}\frac{\partial \boldsymbol{K}^{\zeta d,INT}}{\partial \boldsymbol{\theta}} \cdot \dot{\boldsymbol{d}} &= \mathop{\mathsf{A}}_{e=1}^{n_{\text{el}}} \frac{\partial \boldsymbol{k}_e^{\zeta d,INT}}{\partial \boldsymbol{\theta}^e} \cdot \dot{\boldsymbol{d}}^e \\ &= \mathop{\mathsf{A}}_{e=1}^{n_{\text{el}}} \int_{B_a^e} -\dot{\epsilon}_v \Big[(\boldsymbol{N}^{e,p})^T \Big] \otimes \left(-\frac{\partial S(\boldsymbol{\theta}^e, \boldsymbol{\zeta}^e)}{\partial s} \boldsymbol{N}^{e,p} \right) \mathrm{d}a \end{aligned} \tag{2.107}$$

$$\begin{aligned}\frac{\partial \boldsymbol{K}^{\zeta\theta,INT}}{\partial \boldsymbol{\theta}} \cdot \dot{\boldsymbol{\theta}} &= \mathop{\mathsf{A}}_{e=1}^{n_{\text{el}}} \frac{\partial \boldsymbol{k}_e^{\zeta\theta,INT}}{\partial \boldsymbol{\theta}^e} \cdot \dot{\boldsymbol{\theta}}^e \\ &= \mathop{\mathsf{A}}_{e=1}^{n_{\text{el}}} \int_{B_a^e} \dot{p}_w \, n(\boldsymbol{d}^e) \Big[(\boldsymbol{N}^{e,p})^T \Big] \otimes \left(-\frac{\partial^2 S(\boldsymbol{\theta}^e, \boldsymbol{\zeta}^e)}{\partial s^2} \boldsymbol{N}^{e,p} \right) \mathrm{d}a \end{aligned} \tag{2.108}$$

$$\begin{aligned}\frac{\partial \boldsymbol{K}^{\zeta\zeta,INT}}{\partial \boldsymbol{\theta}} \cdot \dot{\boldsymbol{\zeta}} &= \mathop{\mathsf{A}}_{e=1}^{n_{\text{el}}} \frac{\partial \boldsymbol{k}_e^{\zeta\zeta,INT}}{\partial \boldsymbol{\theta}^e} \cdot \dot{\boldsymbol{\zeta}}^e \\ &= \mathop{\mathsf{A}}_{e=1}^{n_{\text{el}}} \int_{B_a^e} \left[\frac{\dot{p}_a n(\boldsymbol{d}^e)}{K_a} \Big[(\boldsymbol{N}^{e,p})^T \Big] \otimes \left(-\frac{\partial S(\boldsymbol{\theta}^e, \boldsymbol{\zeta}^e)}{\partial s} \boldsymbol{N}^{e,p} \right) \right. \\ &\qquad \left. - \dot{p}_a \, n(\boldsymbol{d}^e) \Big[(\boldsymbol{N}^{e,p})^T \Big] \otimes \left(-\frac{\partial^2 S(\boldsymbol{\theta}^e, \boldsymbol{\zeta}^e)}{\partial s^2} \boldsymbol{N}^{e,p} \right) \right] \mathrm{d}a \end{aligned} \tag{2.109}$$

where $\dot{\epsilon}_v = \tilde{\boldsymbol{B}}^{e,u} \cdot \dot{\boldsymbol{d}}^e$ and $\dfrac{\partial s}{\partial \boldsymbol{\theta}^e} = -\boldsymbol{N}^{e,p}$.

$$\begin{aligned}\frac{\partial \boldsymbol{K}^{\theta d,INT}}{\partial \boldsymbol{\zeta}} \cdot \dot{\boldsymbol{d}} &= \mathop{\mathsf{A}}_{e=1}^{n_{\text{el}}} \frac{\partial \boldsymbol{k}_e^{\theta d,INT}}{\partial \boldsymbol{\zeta}^e} \cdot \dot{\boldsymbol{d}}^e = \mathop{\mathsf{A}}_{e=1}^{n_{\text{el}}} \int_{B_w^e} \dot{\epsilon}_v \Big[(\boldsymbol{N}^{e,p})^T \Big] \otimes \frac{\partial S(\boldsymbol{\theta}^e, \boldsymbol{\zeta}^e)}{\partial \boldsymbol{\zeta}^e} \, \mathrm{d}a \\ &= \mathop{\mathsf{A}}_{e=1}^{n_{\text{el}}} \int_{B_w^e} \dot{\epsilon}_v \Big[(\boldsymbol{N}^{e,p})^T \Big] \otimes \left(\frac{\partial S(\boldsymbol{\theta}^e, \boldsymbol{\zeta}^e)}{\partial s} \boldsymbol{N}^{e,p} \right) \mathrm{d}a \end{aligned} \tag{2.110}$$

$$\begin{aligned}\frac{\partial \boldsymbol{K}^{\theta\theta,INT}}{\partial \boldsymbol{\zeta}} \cdot \dot{\boldsymbol{\theta}} &= \mathop{\mathsf{A}}_{e=1}^{n_{\mathrm{el}}} \frac{\partial \boldsymbol{k}_e^{\theta\theta,INT}}{\partial \boldsymbol{\zeta}^e} \cdot \dot{\boldsymbol{\theta}}^e \\ &= \mathop{\mathsf{A}}_{e=1}^{n_{\mathrm{el}}} \int_{B_w^e} \dot{p}_w \, n(\boldsymbol{d}^e) \Big[(\boldsymbol{N}^{e,p})^T \Big] \otimes \left(\frac{\partial^2 S(\boldsymbol{\theta}^e, \boldsymbol{\zeta}^e)}{\partial s^2} \boldsymbol{N}^{e,p} \right) \mathrm{d}a \end{aligned} \tag{2.111}$$

$$\begin{aligned}\frac{\partial \boldsymbol{K}^{\theta\zeta,INT}}{\partial \boldsymbol{\zeta}} \cdot \dot{\boldsymbol{\zeta}} &= \mathop{\mathsf{A}}_{e=1}^{n_{\mathrm{el}}} \frac{\partial \boldsymbol{k}_e^{\theta\zeta,INT}}{\partial \boldsymbol{\zeta}^e} \cdot \dot{\boldsymbol{\zeta}}^e \\ &= \mathop{\mathsf{A}}_{e=1}^{n_{\mathrm{el}}} \int_{B_w^e} \dot{p}_a \, n(\boldsymbol{d}^e) \Big[(\boldsymbol{N}^{e,p})^T \Big] \otimes \left(\frac{\partial^2 S(\boldsymbol{\theta}^e, \boldsymbol{\zeta}^e)}{\partial s^2} \boldsymbol{N}^{e,p} \right) \mathrm{d}a \end{aligned} \tag{2.112}$$

$$\begin{aligned}\frac{\partial \boldsymbol{K}^{\zeta d,INT}}{\partial \boldsymbol{\zeta}} \cdot \dot{\boldsymbol{d}} &= \mathop{\mathsf{A}}_{e=1}^{n_{\mathrm{el}}} \frac{\partial \boldsymbol{k}_e^{\zeta d,INT}}{\partial \boldsymbol{\zeta}^e} \cdot \dot{\boldsymbol{d}}^e \\ &= \mathop{\mathsf{A}}_{e=1}^{n_{\mathrm{el}}} \int_{B_a^e} -\dot{\epsilon}_v \Big[(\boldsymbol{N}^{e,p})^T \Big] \otimes \left(\frac{\partial S(\boldsymbol{\theta}^e, \boldsymbol{\zeta}^e)}{\partial s} \boldsymbol{N}^{e,p} \right) \mathrm{d}a \end{aligned} \tag{2.113}$$

$$\begin{aligned}\frac{\partial \boldsymbol{K}^{\zeta\theta,INT}}{\partial \boldsymbol{\zeta}} \cdot \dot{\boldsymbol{\theta}} &= \mathop{\mathsf{A}}_{e=1}^{n_{\mathrm{el}}} \frac{\partial \boldsymbol{k}_e^{\zeta\theta,INT}}{\partial \boldsymbol{\zeta}^e} \cdot \dot{\boldsymbol{\theta}}^e \\ &= \mathop{\mathsf{A}}_{e=1}^{n_{\mathrm{el}}} \int_{B_a^e} \dot{p}_w \, n(\boldsymbol{d}^e) \Big[(\boldsymbol{N}^{e,p})^T \Big] \otimes \left(\frac{\partial^2 S(\boldsymbol{\theta}^e, \boldsymbol{\zeta}^e)}{\partial s^2} \boldsymbol{N}^{e,p} \right) \mathrm{d}a \end{aligned} \tag{2.114}$$

$$\begin{aligned}\frac{\partial \boldsymbol{K}^{\zeta\zeta,INT}}{\partial \boldsymbol{\zeta}} \cdot \dot{\boldsymbol{\zeta}} &= \mathop{\mathsf{A}}_{e=1}^{n_{\mathrm{el}}} \frac{\partial \boldsymbol{k}_e^{\zeta\zeta,INT}}{\partial \boldsymbol{\zeta}^e} \cdot \dot{\boldsymbol{\zeta}}^e \\ &= \mathop{\mathsf{A}}_{e=1}^{n_{\mathrm{el}}} \int_{B_a^e} \left[\frac{\dot{p}_a n(\boldsymbol{d}^e)}{K_a} \Big[(\boldsymbol{N}^{e,p})^T \Big] \otimes \frac{\partial S(\boldsymbol{\theta}^e, \boldsymbol{\zeta}^e)}{\partial s} \boldsymbol{N}^{e,p} \right. \\ &\qquad \left. - \dot{p}_a \, n(\boldsymbol{d}^e) \Big[(\boldsymbol{N}^{e,p})^T \Big] \otimes \left(\frac{\partial^2 S(\boldsymbol{\theta}^e, \boldsymbol{\zeta}^e)}{\partial s^2} \boldsymbol{N}^{e,p} \right) \right] \mathrm{d}a \end{aligned} \tag{2.115}$$

where $\dfrac{\partial s}{\partial \boldsymbol{\zeta}^e} = \boldsymbol{N}^{e,p}$,

$$\frac{\partial S}{\partial s} = (1 - S_r) \frac{\partial S_e}{\partial s} = -(1 - S_r) \left[1 + \left(\frac{s}{\mathrm{a}} \right)^{\mathrm{n}} \right]^{(-\mathrm{m}-1)} s^{(\mathrm{n}-1)} \frac{\mathrm{mn}}{\mathrm{a}^{\mathrm{n}}}$$

$$\begin{aligned}\frac{\partial^2 S}{\partial s^2} = (1 - S_r) \frac{\partial^2 S_e}{\partial s^2} = -(1 - S_r) \frac{\mathrm{mn}}{\mathrm{a}^{\mathrm{n}}} \Bigg(& (\mathrm{n}-1) s^{(\mathrm{n}-2)} \left[1 + \left(\frac{s}{\mathrm{a}} \right)^{\mathrm{n}} \right]^{(-\mathrm{m}-1)} \\ & - s^{(2\mathrm{n}-2)} (\mathrm{m}+1) \left[1 + \left(\frac{s}{\mathrm{a}} \right)^{\mathrm{n}} \right]^{(-\mathrm{m}-2)} \mathrm{n} \left(\frac{1}{\mathrm{a}} \right)^{\mathrm{n}} \Bigg) \end{aligned}$$

$$\frac{\partial \boldsymbol{F}^{d,INT}}{\partial \boldsymbol{d}} = \mathop{\mathsf{A}}_{e=1}^{n_{\rm el}} \frac{\partial \boldsymbol{f}_e^{d,INT}}{\partial \boldsymbol{d}^e} = \mathop{\mathsf{A}}_{e=1}^{n_{\rm el}} \int_{B^e} (\boldsymbol{B}^{e,u})^T \cdot \frac{\partial \boldsymbol{\sigma}'(\boldsymbol{d}^e, \boldsymbol{\theta}^e)}{\partial \boldsymbol{\epsilon}} \cdot \boldsymbol{B}^{e,u} \, \mathrm{d}a \tag{2.116}$$

$$\frac{\partial \boldsymbol{F}^{\theta 1,INT}}{\partial \boldsymbol{d}} = \mathop{\mathsf{A}}_{e=1}^{n_{\rm el}} \frac{\partial \boldsymbol{f}_e^{\theta 1,INT}}{\partial \boldsymbol{d}^e} = \mathop{\mathsf{A}}_{e=1}^{n_{\rm el}} \int_{B_w^e} (\boldsymbol{B}^{e,p})^T \cdot \frac{\partial \tilde{\boldsymbol{v}}_w^s(\boldsymbol{d}^e, \boldsymbol{\theta}^e, \boldsymbol{\zeta}^e)}{\partial \boldsymbol{d}^e} \, \mathrm{d}a \tag{2.117}$$

$$\frac{\partial \boldsymbol{F}^{\zeta 1,INT}}{\partial \boldsymbol{d}} = \mathop{\mathsf{A}}_{e=1}^{n_{\rm el}} \frac{\partial \boldsymbol{f}_e^{\zeta 1,INT}}{\partial \boldsymbol{d}^e} = \mathop{\mathsf{A}}_{e=1}^{n_{\rm el}} \int_{B_a^e} (\boldsymbol{B}^{e,p})^T \cdot \frac{\partial \tilde{\boldsymbol{v}}_a^s(\boldsymbol{d}^e, \boldsymbol{\theta}^e, \boldsymbol{\zeta}^e)}{\partial \boldsymbol{d}^e} \, \mathrm{d}a \tag{2.118}$$

where $\dfrac{\partial \boldsymbol{\epsilon}'}{\partial \boldsymbol{d}^e} = \boldsymbol{B}^{e,u}$ and Darcy's law extends to the partially saturated case for water and air phases.

$$\begin{aligned}
\frac{\partial \tilde{\boldsymbol{v}}_w^s}{\partial \boldsymbol{d}^e} &= -[\boldsymbol{\nabla} p_w - \rho^{wR} \boldsymbol{g}] \otimes \frac{\partial k_w}{\partial n} \frac{\partial n}{\partial \boldsymbol{d}^e} \,, \quad \delta(n) = \frac{n^3}{1-n^2} \,, \quad \boldsymbol{\nabla} p_w = \boldsymbol{B}^{e,p} \cdot \boldsymbol{\theta}^e \\
k_w(n,S) &= \frac{\varkappa(n)}{\eta_w} k_{rw}(S) = \frac{l^2}{\eta_w} \delta(n) \, k_{rw}(S) \,, \quad k_{rw}(S) = \sqrt{S} \left(1 - \left(1 - S^{\frac{1}{\mathrm{m}}}\right)^{\mathrm{m}}\right)^2 \\
\frac{\partial k_w}{\partial n} &= \frac{l^2}{\eta_w} \left[\frac{3n^2 - n^4}{(1-n^2)^2}\right] k_{rw}(S) \,, \quad \frac{\partial n}{\partial \boldsymbol{d}^e} = \left(\frac{1-n}{1+\Delta\epsilon_v}\right) \tilde{\boldsymbol{B}}^{e,u}
\end{aligned}$$

$$\begin{aligned}
\frac{\partial \tilde{\boldsymbol{v}}_a^s}{\partial \boldsymbol{d}^e} &= -[\boldsymbol{\nabla} p_a - \rho^{aR} \boldsymbol{g}] \otimes \frac{\partial k_a}{\partial n} \frac{\partial n}{\partial \boldsymbol{d}^e} \,, \quad \boldsymbol{\nabla} p_a = \boldsymbol{B}^{e,p} \cdot \boldsymbol{\zeta}^e \\
k_a(n,S) &= \frac{\varkappa(n)}{\eta_a} k_{ra}(1-S) = \frac{l^2}{\eta_a} \delta(n) \, k_{ra}(1-S) \,, \quad k_{ra}(1-S) = \sqrt{1-S} \left(1 - S^{\frac{1}{\mathrm{m}}}\right)^{2\mathrm{m}} \\
\frac{\partial k_a}{\partial n} &= \frac{l^2}{\eta_a} \left[\frac{3n^2 - n^4}{(1-n^2)^2}\right] k_{ra}(1-S)
\end{aligned}$$

In Figure 2.1 the relative permeability of water and air are plotted against S for various values of m.

$$\frac{\partial \boldsymbol{F}^{d,INT}}{\partial \boldsymbol{\theta}} = \mathop{\mathsf{A}}_{e=1}^{n_{\rm el}} \frac{\partial \boldsymbol{f}_e^{d,INT}}{\partial \boldsymbol{\theta}^e} = \mathop{\mathsf{A}}_{e=1}^{n_{\rm el}} \int_{B^e} (\boldsymbol{B}^{e,u})^T \cdot \frac{\partial \boldsymbol{\sigma}'}{\partial s} \cdot \frac{\partial s}{\partial \boldsymbol{\theta}^e} \, \mathrm{d}a \tag{2.119}$$

where $\dfrac{\partial \boldsymbol{\sigma}'}{\partial s} = \mathbf{0}$ for linear elasticity, $\dfrac{\partial \boldsymbol{\sigma}'}{\partial s} \neq \mathbf{0}$ for partially saturated hyperelasto-plasticity and $\dfrac{\partial s}{\partial \boldsymbol{\theta}^e} = -\boldsymbol{N}^{e,p}$.

$$\frac{\partial \boldsymbol{F}^{d\theta,INT}}{\partial \boldsymbol{\theta}} = \mathop{\mathbf{A}}_{e=1}^{n_{\text{el}}} \frac{\partial \boldsymbol{f}_e^{d\theta,INT}}{\partial \boldsymbol{\theta}^e} = \mathop{\mathbf{A}}_{e=1}^{n_{\text{el}}} \int_{B^e} \left(-p_w \frac{\partial \chi}{\partial s} + \chi\right) (\tilde{\boldsymbol{B}}^{e,u})^T \cdot \boldsymbol{N}^{e,p} \, \mathrm{d}a \tag{2.120}$$

$$\frac{\partial \boldsymbol{F}^{d\zeta,INT}}{\partial \boldsymbol{\theta}} = \mathop{\mathbf{A}}_{e=1}^{n_{\text{el}}} \frac{\partial \boldsymbol{f}_e^{d\zeta,INT}}{\partial \boldsymbol{\theta}^e} = \mathop{\mathbf{A}}_{e=1}^{n_{\text{el}}} \int_{B^e} p_a \frac{\partial \chi}{\partial s} (\tilde{\boldsymbol{B}}^{e,u})^T \cdot \boldsymbol{N}^{e,p} \, \mathrm{d}a \tag{2.121}$$

$$\frac{\partial \boldsymbol{F}^{\theta 1,INT}}{\partial \boldsymbol{\theta}} = \mathop{\mathbf{A}}_{e=1}^{n_{\text{el}}} \frac{\partial \boldsymbol{f}_e^{\theta 1,INT}}{\partial \boldsymbol{\theta}^e} = \mathop{\mathbf{A}}_{e=1}^{n_{\text{el}}} \int_{B_w^e} (\boldsymbol{B}^{e,p})^T \cdot \frac{\partial \tilde{\boldsymbol{v}}_w^e}{\partial \boldsymbol{\theta}^e} \, \mathrm{d}a \tag{2.122}$$

$$\frac{\partial \boldsymbol{F}^{\zeta 1,INT}}{\partial \boldsymbol{\theta}} = \mathop{\mathbf{A}}_{e=1}^{n_{\text{el}}} \frac{\partial \boldsymbol{f}_e^{\zeta 1,INT}}{\partial \boldsymbol{\theta}^e} = \mathop{\mathbf{A}}_{e=1}^{n_{\text{el}}} \int_{B_a^e} (\boldsymbol{B}^{e,p})^T \cdot \frac{\partial \tilde{\boldsymbol{v}}_a^e}{\partial \boldsymbol{\theta}^e} \, \mathrm{d}a \tag{2.123}$$

$$\frac{\partial \boldsymbol{F}^{d\zeta,INT}}{\partial \boldsymbol{\theta}} = \mathop{\mathbf{A}}_{e=1}^{n_{\text{el}}} \frac{\partial \boldsymbol{f}_e^{d\zeta,INT}}{\partial \boldsymbol{\theta}^e} = \mathop{\mathbf{A}}_{e=1}^{n_{\text{el}}} \int_{B^e} p_w \frac{\partial \chi}{\partial s} (\tilde{\boldsymbol{B}}^{e,u})^T \cdot \boldsymbol{N}^{e,p} \, \mathrm{d}a \tag{2.124}$$

$$\frac{\partial \boldsymbol{F}^{d\zeta,INT}}{\partial \boldsymbol{\zeta}} = \mathop{\mathbf{A}}_{e=1}^{n_{\text{el}}} \frac{\partial \boldsymbol{f}_e^{d\zeta,INT}}{\partial \boldsymbol{\zeta}^e} = \mathop{\mathbf{A}}_{e=1}^{n_{\text{el}}} \int_{B^e} \left(-p_a \frac{\partial \chi}{\partial s} + \chi + 1\right) (\tilde{\boldsymbol{B}}^{e,u})^T \cdot \boldsymbol{N}^{e,p} \, \mathrm{d}a \tag{2.125}$$

$$\frac{\partial \boldsymbol{F}^{\theta 1,INT}}{\partial \boldsymbol{\zeta}} = \mathop{\mathbf{A}}_{e=1}^{n_{\text{el}}} \frac{\partial \boldsymbol{f}_e^{\theta 1,INT}}{\partial \boldsymbol{\zeta}^e} = \mathop{\mathbf{A}}_{e=1}^{n_{\text{el}}} \int_{B_w^e} (\boldsymbol{B}^{e,p})^T \cdot \frac{\partial \tilde{\boldsymbol{v}}_w^e}{\partial \boldsymbol{\zeta}^e} \, \mathrm{d}a \tag{2.126}$$

$$\frac{\partial \boldsymbol{F}^{\zeta 1,INT}}{\partial \boldsymbol{\zeta}} = \mathop{\mathbf{A}}_{e=1}^{n_{\text{el}}} \frac{\partial \boldsymbol{f}_e^{\zeta 1,INT}}{\partial \boldsymbol{\zeta}^e} = \mathop{\mathbf{A}}_{e=1}^{n_{\text{el}}} \int_{B_a^e} (\boldsymbol{B}^{e,p})^T \cdot \frac{\partial \tilde{\boldsymbol{v}}_a^e}{\partial \boldsymbol{\zeta}^e} \, \mathrm{d}a \tag{2.127}$$

where by using chain rule,

$$\frac{\partial \tilde{\boldsymbol{v}}_w^e}{\partial \boldsymbol{\theta}^e} = -k_w \, \boldsymbol{B}^{e,p} - [\boldsymbol{\nabla} p_w - \rho^{wR} \boldsymbol{g}] \otimes \frac{\partial k_w}{\partial \boldsymbol{\theta}^e} = -k_w \, \boldsymbol{B}^{e,p} + \left(\boldsymbol{B}^{e,p} \cdot \boldsymbol{\theta}^e - \rho^{wR} \boldsymbol{g}\right) \frac{\partial k_w}{\partial S} \frac{\partial S}{\partial s} \boldsymbol{N}^{e,p}$$

$$\frac{\partial k_w}{\partial S} = \frac{\varkappa(n)}{\eta_w} \left[\frac{1}{2\sqrt{S}} \left(1 - \left(1 - S^{\frac{1}{\mathrm{m}}}\right)^{\mathrm{m}}\right)^2 + \frac{2}{\sqrt{S}} \left(1 - \left(1 - S^{\frac{1}{\mathrm{m}}}\right)^{\mathrm{m}}\right) \left(1 - S^{\frac{1}{\mathrm{m}}}\right)^{\mathrm{m}-1} S^{\frac{1}{\mathrm{m}}}\right]$$

$$\frac{\partial \tilde{\boldsymbol{v}}_a^e}{\partial \boldsymbol{\theta}^e} = \frac{\partial \tilde{\boldsymbol{v}}_w^e}{\partial \boldsymbol{\zeta}^e} = \mathbf{0}$$

$$\frac{\partial \tilde{\boldsymbol{v}}_a^e}{\partial \boldsymbol{\zeta}^e} = -k_a\, \boldsymbol{B}^{e,p} - [\boldsymbol{\nabla} p_a - \rho^{aR}\boldsymbol{g}] \otimes \frac{\partial k_a}{\partial \boldsymbol{\zeta}^e} = -k_a\, \boldsymbol{B}^{e,p} - \left(\boldsymbol{B}^{e,p}\cdot\boldsymbol{\zeta}^e - \rho^{aR}\boldsymbol{g}\right)\frac{\partial k_a}{\partial S}\frac{\partial S}{\partial s}\boldsymbol{N}^{e,p}$$

$$\frac{\partial k_a}{\partial S} = \frac{\varkappa(n)}{\eta_a}\left(1 - S^{\frac{1}{\mathrm{m}}}\right)^{2\mathrm{m}}\left[-\frac{1}{2\sqrt{1-S}} - 2\sqrt{1-S}\,\frac{S^{\frac{1}{\mathrm{m}}}}{S\left(1-S^{\frac{1}{\mathrm{m}}}\right)}\right]$$

For the external force derivatives,

$$\frac{\partial \boldsymbol{F}^{d,EXT}}{\partial \boldsymbol{d}} = \mathop{\mathsf{A}}_{e=1}^{n_{\mathrm{el}}} \frac{\partial \boldsymbol{f}_e^{d,EXT}}{\partial \boldsymbol{d}^e} = \mathop{\mathsf{A}}_{e=1}^{n_{\mathrm{el}}} \int_{B^e} (\boldsymbol{N}^{e,u})^T \cdot \boldsymbol{g} \otimes \frac{\partial \rho(\boldsymbol{d}^e, \boldsymbol{\theta}^e, \boldsymbol{\zeta}^e)}{\partial \boldsymbol{d}^e}\, \mathrm{d}a \tag{2.128}$$

$$\frac{\partial \boldsymbol{F}^{d,EXT}}{\partial \boldsymbol{\theta}} = \mathop{\mathsf{A}}_{e=1}^{n_{\mathrm{el}}} \frac{\partial \boldsymbol{f}_e^{d,EXT}}{\partial \boldsymbol{\theta}^e} = \mathop{\mathsf{A}}_{e=1}^{n_{\mathrm{el}}} \int_{B^e} (\boldsymbol{N}^{e,u})^T \cdot \boldsymbol{g} \otimes \frac{\partial \rho(\boldsymbol{d}^e, \boldsymbol{\theta}^e, \boldsymbol{\zeta}^e)}{\partial \boldsymbol{\theta}^e}\, \mathrm{d}a \tag{2.129}$$

$$\frac{\partial \boldsymbol{F}^{d,EXT}}{\partial \boldsymbol{\zeta}} = \mathop{\mathsf{A}}_{e=1}^{n_{\mathrm{el}}} \frac{\partial \boldsymbol{f}_e^{d,EXT}}{\partial \boldsymbol{\zeta}^e} = \mathop{\mathsf{A}}_{e=1}^{n_{\mathrm{el}}} \int_{B^e} (\boldsymbol{N}^{e,u})^T \cdot \boldsymbol{g} \otimes \frac{\partial \rho(\boldsymbol{d}^e, \boldsymbol{\theta}^e, \boldsymbol{\zeta}^e)}{\partial \boldsymbol{\zeta}^e}\, \mathrm{d}a \tag{2.130}$$

where,

$$\begin{aligned}
\frac{\partial \rho}{\partial \boldsymbol{d}^e} &= -\frac{\partial n}{\partial \boldsymbol{d}^e}\rho^{sR} + \frac{\partial n}{\partial \boldsymbol{d}^e} S\,\rho^{wR} + \frac{\partial n}{\partial \boldsymbol{d}^e}(1-S)\,\rho^{aR} \\
&= \Big(-\rho^{sR} + S\,\rho^{wR} + (1-S)\rho^{aR}\Big)\left(\frac{1-n}{1+\Delta\epsilon_v}\right)\tilde{\boldsymbol{B}}^{e,u} \\
\frac{\partial \rho}{\partial \boldsymbol{\theta}^e} &= n\rho^{wR}\frac{\partial S}{\partial \boldsymbol{\theta}^e} + n\rho^{aR}\left(-\frac{\partial S}{\partial \boldsymbol{\theta}^e}\right) = n\left(\rho^{wR} - \rho^{aR}\right)\frac{\partial S}{\partial \boldsymbol{\theta}^e} = -n\left(\rho^{wR} - \rho^{aR}\right)\frac{\partial S}{\partial s}\boldsymbol{N}^{e,p} \\
\frac{\partial \rho}{\partial \boldsymbol{\zeta}^e} &= n\rho^{wR}\frac{\partial S}{\partial \boldsymbol{\zeta}^e} + n\rho^{aR}\left(-\frac{\partial S}{\partial \boldsymbol{\zeta}^e}\right) = n\left(\rho^{wR} - \rho^{aR}\right)\frac{\partial S}{\partial \boldsymbol{\zeta}^e} = n\left(\rho^{wR} - \rho^{aR}\right)\frac{\partial S}{\partial s}\boldsymbol{N}^{e,p}
\end{aligned}$$

For linear elasticity in the saturated case, $\dfrac{\partial \boldsymbol{\sigma}'}{\partial s} = \boldsymbol{0}$, but for nonlinear hyperelasto-plasticity with suction in the partially saturated case, $\dfrac{\partial \boldsymbol{\sigma}'}{\partial s} \neq \boldsymbol{0}$.

2.5 Coupled Finite Element Formulation of Biphasic Deformable Continuum

Likewise, a biphasic deformable mixture for partially saturated soil can be simplified from the triphasic deformable mixture derivation. In this derivation, the pore air pressure is assumed

as atmospheric pressure, that is, p_a is approximately equal to zero ($p_a \approx 0$) in the triphasic finite element formulation. This simplifies the nonlinear finite element implementation involving the complicated relationship among solid, water and air, and allows comparison for various loadings between $p_a \neq 0$ (triphasic) and $p_a \approx 0$ (biphasic) FE implementations.

2.5.1 Weak form

To describe the implementation of biphasic coupled finite element model, the weak form illustrates integral expression of the coupled governing equations. By setting $p_a = 0$ in equation (2.52), we arrive at the weak form for partially saturated biphasic mixture as,

$$(\mathcal{W}) \begin{cases} \text{Find } \boldsymbol{u}(\boldsymbol{x},t) \in \mathcal{D}^u \text{ and } p_{_w}(\boldsymbol{x},t) \in \mathcal{D}^{p_w}, \;\; \text{with} \;\; t \in [\,0,T\,] \;\; \text{such that} \\ \quad \displaystyle\int_B \left[\boldsymbol{\nabla}\, \boldsymbol{w} : (\boldsymbol{\sigma}' - \chi\, p_w \mathbf{1})\right] \mathrm{d}v = \int_B \rho\, \boldsymbol{w} \cdot \boldsymbol{g}\, \mathrm{d}v + \int_{\Gamma_t} \boldsymbol{w} \cdot \mathbf{t}\, \mathrm{d}a \\ \quad \displaystyle\int_{B_w} \eta\, n \frac{\partial S}{\partial s}(-\dot{p}_w)\, \mathrm{d}v + \int_{B_w} \eta\, S \operatorname{div} \boldsymbol{v}\, \mathrm{d}v - \int_{B_w} \boldsymbol{\nabla}\eta \cdot \tilde{\boldsymbol{v}}^w \mathrm{d}v = \int_{\Gamma_s^w} \eta\, S^w\, \mathrm{d}s \\ \text{for all} \quad \boldsymbol{w}\,(\boldsymbol{x},t) \in \mathcal{V}^u \;\; \text{and} \;\; \eta\,(\boldsymbol{x},t) \in \mathcal{V}^{p_w} \end{cases} \tag{2.131}$$

In the trial solution spaces,

$$\begin{aligned} \mathcal{D}^u &= \left\{\boldsymbol{u}\,(\boldsymbol{x},t) : B \times\,]0,T[\;\mapsto\; \mathcal{R}^3, \quad \boldsymbol{u}(t)|_{\Gamma_g} = \boldsymbol{g}^u(t),\; \boldsymbol{u}(\boldsymbol{x},0) = \boldsymbol{u}_0(\boldsymbol{x})\right\} \\ \mathcal{D}^{p_w} &= \left\{p_{_w}\,(\boldsymbol{x},t) : B_w \times\,]0,T[\;\mapsto\; \mathcal{R}, \quad p_{_w}(t)|_{\Gamma_r^w} = r_w(t)\right\} \end{aligned} \tag{2.132}$$

In the variation spaces,

$$\begin{aligned} \mathcal{V}^u &= \left\{w_i\,(\boldsymbol{x}) : B \;\mapsto\; \mathcal{R}^3, \quad w_i|_{\Gamma_g} = 0\right\} \\ \mathcal{V}^{p_w} &= \left\{\eta\,(\boldsymbol{x}) : B_w \;\mapsto\; \mathcal{R}, \quad \eta|_{\Gamma_r^w} = 0\right\} \end{aligned} \tag{2.133}$$

In the discretization of domain and spaces, Galerkin Form can be written as,

$$B^h \subset B$$

where, "h" discretization parameter is satisfied by $B_w^h \subset B_w$, therefore, we can restate the Weak

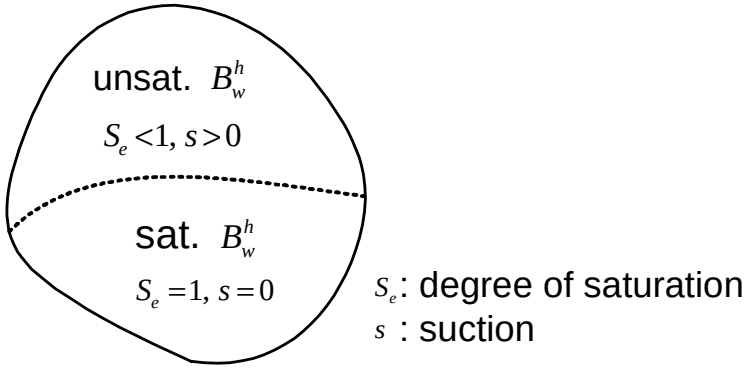

Figure 2.4: Discretization of biphasic domain and spaces in Galerkin Form

form with superscript h's

$$\begin{array}{ll} (\mathcal{D}^u)^h \subset \mathcal{D}^u\ , & (\mathcal{V}^u)^h \subset \mathcal{V}^u \\ (\mathcal{D}^{p_w})^h \subset \mathcal{D}^{p_w}, & (\mathcal{V}^{p_w})^h \subset \mathcal{V}^{p_w} \end{array} \quad \left\{ \begin{array}{ll} u_i^h(\boldsymbol{x},t) \subset (\mathcal{D}^u)^h\ , & w_i^h(\boldsymbol{x}) \subset (\mathcal{V}^u)^h \\ p_w^h(\boldsymbol{x},t) \subset (\mathcal{D}^{p_w})^h, & \eta(\boldsymbol{x}) \subset (\mathcal{V}^{p_w})^h \end{array} \right. \tag{2.134}$$

2.5.2 Coupled FE form for 2D semi-implicit linear poro-elasticity

For the coupled finite element (FE) form of 2D nonlinear poromechanics, it is used linear isotropic elasticity for the solid skeleton stress $\boldsymbol{\sigma}'$, and assumed the density and permeability are described in equation (2.45) for water phases, and porosity n is a function of the solid skeleton volumetric strain ϵ_v, such as in matrix form

$$\begin{aligned} \boldsymbol{\sigma}' &= \mathbf{D}\cdot\boldsymbol{\epsilon} = \mathbf{D}\cdot\boldsymbol{B}^{e,u}\cdot\boldsymbol{d}^e \\ \boldsymbol{k}^w(n,S) &= k_w(n,S)\,\mathbf{1} \\ n_{n+1} &= \frac{n_n+\Delta\epsilon_v}{1+\Delta\epsilon_v} \quad \text{and} \quad \Delta\epsilon_v = \mathrm{tr}(\Delta\boldsymbol{\epsilon}) \\ \rho &= \Big[1-n(\boldsymbol{d})\Big]\rho^{sR} + n(\boldsymbol{d})\,S(\boldsymbol{\theta})\,\rho^{wR} \end{aligned}$$

where $\mathbf{D}$ is the elastic modulus matrix. $n^w < n$ indicates $S<1$ and $n^w = n$ indicates $S=1$ for the density, and we can discretize into mixed quadrilateral finite elements as shown in Figure 2.5.

In Figure 2.5, element characteristic length is h^e, element domain is B^e, discrete domain is

$B_w^h = \mathop{\mathbf{A}}_{e=1}^{n_{\text{el}}} B^e$, $\mathop{\mathbf{A}}_{e=1}^{n_{\text{el}}}$ is the element assembly operator, and the convergent, mixed and quadrilateral finite element is biquadratic in displacement and bilinear in pore water pressure[59].

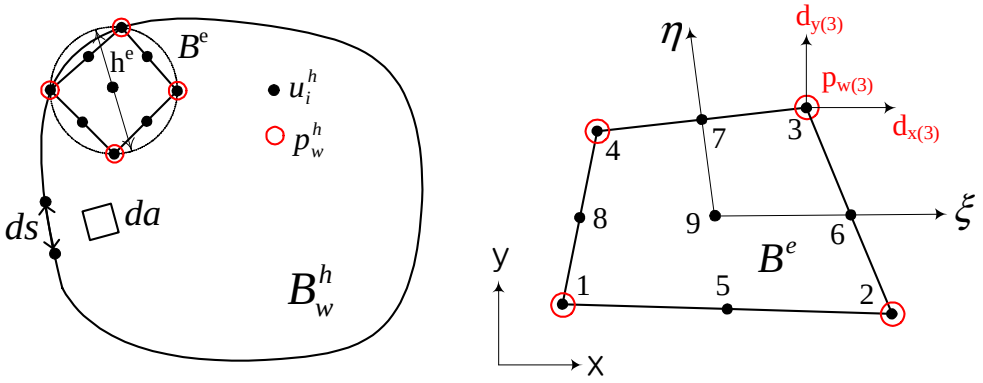

Figure 2.5: Discretization into biphasic mixed quadrilateral finite elements

For a biquadratic element in displacement and a bilinear isoparametric element in pore water pressure, it is necessary to define the interpolating functions for the two phases for coupled finite element form, or take triphasic formulation and set $\boldsymbol{\zeta}^e = \mathbf{0}$ with similar finite element interpolations and spatial derivatives as in Section 2.4.2, we arrive at the nonlinear coupled FE equations:

1) *Solid* :

$$\mathop{\mathbf{A}}_{e=1}^{n_{\text{el}}} (\boldsymbol{c}^e)^T \cdot \left[\left(\int_{B^e} (\boldsymbol{B}^{e,u})^T \cdot \boldsymbol{D} \cdot \boldsymbol{B}^{e,u} \, \mathrm{d}a \right) \cdot \boldsymbol{d}^e - \left(\int_{B^e} \chi(\boldsymbol{\theta}^e) (\tilde{\boldsymbol{B}}^{e,u})^T \cdot \boldsymbol{N}^{e,p} \, \mathrm{d}a \right) \cdot \boldsymbol{\theta}^e \right.$$
$$\left. = \int_{B^e} \rho(\boldsymbol{d}^e, \boldsymbol{\theta}^e) (\boldsymbol{N}^{e,u})^T \cdot \boldsymbol{g} \, \mathrm{d}a + \int_{\Gamma_t^e} (\boldsymbol{N}^{e,u})^T \cdot \boldsymbol{t} \, \mathrm{d}a \right] \tag{2.135}$$

$$\text{thus,} \quad \mathop{\mathbf{A}}_{e=1}^{n_{\text{el}}} (\boldsymbol{c}^e)^T \cdot \left[\boldsymbol{k}^{e,dd} \cdot \boldsymbol{d}^e - \boldsymbol{k}^{e,d\theta}(\boldsymbol{\theta}^e) \cdot \boldsymbol{\theta}^e = \boldsymbol{f}_f^{e,d}(\boldsymbol{d}^e, \boldsymbol{\theta}^e) + \boldsymbol{f}_t^{e,d} \right] \tag{2.136}$$

2) $Water$:

$$\begin{aligned}
\mathop{\mathbf{A}}_{e=1}^{n_{\mathrm{el}}} (\boldsymbol{\alpha}^e)^T \cdot \Bigg[& \left(\int_{B_w^e} S(\boldsymbol{\theta}^e) \, (\boldsymbol{N}^{e,p})^T \cdot \tilde{\boldsymbol{B}}^{e,u} \, \mathrm{d}a \right) \cdot \dot{\boldsymbol{d}}^e \\
& - \left(\int_{B_w^e} n \frac{\partial S}{\partial s} (\boldsymbol{N}^{e,p})^T \cdot \boldsymbol{N}^{e,p} \, \mathrm{d}a \right) \cdot \dot{\boldsymbol{\theta}}^e \\
& + \left(\int_{B_w^e} (\boldsymbol{B}^{e,p})^T \cdot \boldsymbol{k}^w(\boldsymbol{d}^e, \boldsymbol{\theta}^e) \cdot \boldsymbol{B}^{e,p} \, \mathrm{d}a \right) \cdot \boldsymbol{\theta}^e \\
= & \int_{B_w^e} \rho^{wR} (\boldsymbol{B}^{e,p})^T \cdot \boldsymbol{k}^w(\boldsymbol{d}^e, \boldsymbol{\theta}^e) \cdot \boldsymbol{g} \, \mathrm{d}a + \int_{\Gamma_{s(w)}^e} (\boldsymbol{N}^{e,p})^T S^w \, \mathrm{d}s \Bigg]
\end{aligned} \tag{2.137}$$

$$\begin{aligned}
\text{thus,} \quad \mathop{\mathbf{A}}_{e=1}^{n_{\mathrm{el}}} (\boldsymbol{\alpha}^e)^T \cdot \Big[& \boldsymbol{k}^{e,\theta d}(\boldsymbol{\theta}^e) \cdot \dot{\boldsymbol{d}}^e - \boldsymbol{k}^{e,\theta\zeta}(\boldsymbol{d}^e, \boldsymbol{\theta}^e) \cdot \dot{\boldsymbol{\theta}}^e + \boldsymbol{k}^{e,\theta\theta}(\boldsymbol{d}^e, \boldsymbol{\theta}^e) \cdot \boldsymbol{\theta}^e \\
& = \boldsymbol{f}^{e,\theta}(\boldsymbol{d}^e, \boldsymbol{\theta}^e) + \boldsymbol{f}_s^{e,\theta} \Big]
\end{aligned} \tag{2.138}$$

Thus, the element stiffness matrix for displacement and pore water pressure of d.o.f (degree of freedom), the coupling element stiffness and permeability matrices are written as,

$$\begin{aligned}
\boldsymbol{k}^{e,dd} &= \int_{B^e} (\boldsymbol{B}^{e,u})^T \cdot \mathbf{D} \cdot \boldsymbol{B}^{e,u} \, \mathrm{d}a = \int_{-1}^{1} \int_{-1}^{1} (\boldsymbol{B}^{e,u})^T \cdot \mathbf{D} \cdot \boldsymbol{B}^{e,u} \, j \mathrm{d}\xi \mathrm{d}\eta \\
\boldsymbol{k}^{e,\theta\theta}(\boldsymbol{d}^e, \boldsymbol{\theta}^e) &= \int_{B^e} (\boldsymbol{B}^{e,p})^T \cdot \boldsymbol{k}^w(\boldsymbol{d}^e, \boldsymbol{\theta}^e) \cdot \boldsymbol{B}^{e,p} \, \mathrm{d}a \\
&= \int_{-1}^{1} \int_{-1}^{1} (\boldsymbol{B}^{e,p})^T \cdot \boldsymbol{k}^w(\boldsymbol{d}^e, \boldsymbol{\theta}^e) \cdot \boldsymbol{B}^{e,p} \, j \mathrm{d}\xi \mathrm{d}\eta \\
\boldsymbol{k}^{e,d\theta}(\boldsymbol{\theta}^e) &= \int_{B^e} \chi(\boldsymbol{\theta}^e) (\tilde{\boldsymbol{B}}^{e,u})^T \cdot \boldsymbol{N}^{e,p} \, \mathrm{d}a \\
&= \int_{-1}^{1} \int_{-1}^{1} \chi(\boldsymbol{\theta}^e) (\tilde{\boldsymbol{B}}^{e,u})^T \cdot \boldsymbol{N}^{e,p} \, j \mathrm{d}\xi \mathrm{d}\eta \\
\boldsymbol{k}^{e,\theta\zeta}(\boldsymbol{d}^e, \boldsymbol{\theta}^e) &= \int_{B^e} n(\boldsymbol{d}^e) \frac{\partial S(\boldsymbol{\theta}^e)}{\partial s} (\boldsymbol{N}^{e,p})^T \cdot \boldsymbol{N}^{e,p} \, \mathrm{d}a \\
&= \int_{-1}^{1} \int_{-1}^{1} n(\boldsymbol{d}^e) \frac{\partial S(\boldsymbol{\theta}^e)}{\partial s} (\boldsymbol{N}^{e,p})^T \cdot \boldsymbol{N}^{e,p} \, j \mathrm{d}\xi \mathrm{d}\eta \\
\boldsymbol{k}^{e,\theta d}(\boldsymbol{\theta}^e) &= \int_{B^e} S(\boldsymbol{\theta}^e) (\boldsymbol{N}^{e,p})^T \cdot \tilde{\boldsymbol{B}}^{e,u} \, \mathrm{d}a \\
&= \int_{-1}^{1} \int_{-1}^{1} S(\boldsymbol{\theta}^e) (\boldsymbol{N}^{e,p})^T \cdot \tilde{\boldsymbol{B}}^{e,u} \, j \mathrm{d}\xi \mathrm{d}\eta
\end{aligned} \tag{2.139}$$

Like the case of triphasic mixture, the tangent modulus, $\mathbf{D}$, is given for linear isotropic elasticity for plane strain. The hydraulic equations exist relating the suction stress s to the degree of saturation S (e.g., the Brooks-Corey[18], van Genuchten[90] and Fredlund-Xing[33] equations). The main drying and wetting curves of the soil-water characteristic curve (SWCC) are both described by van Genuchten's equation in this study.

$$\begin{aligned} S_e &= \left[\frac{1}{1+\left(\frac{s}{\mathrm{a}}\right)^{\mathrm{n}}}\right]^{\mathrm{m}}, \qquad s = -p_w = -\boldsymbol{N}^{e,p}\cdot\boldsymbol{\theta}^e \\ S &= S_r + S_e(1-S_r) = S_r + \frac{1-S_r}{\left[1+(\alpha s)^{\mathrm{n}}\right]^{\mathrm{m}}} \qquad (\text{where, } \alpha = 1/\mathrm{a}) \end{aligned} \tag{2.140}$$

In the literature, the curve fitting parameter α (1/cm or 1/Pa) is proposed by van Genuchten[90] and a (cm or Pa) is proposed by Fredlund and Xing[33] corresponding to the unit of suction stress s (cm or Pa). The classical relations proposed by van Genuchten[90], namely, the degree of saturation S of equation (2.140) is considered in this study. It is written as the function of suction stress s, and for suction stress derivative we have,

$$\begin{aligned} (1-S_r)\frac{dS_e}{ds} &= -(1-S_r)\left[\frac{1}{1+(\alpha s)^{\mathrm{n}}}\right]^{\mathrm{m}} \frac{\mathrm{m}}{1+(\alpha s)^{\mathrm{n}}}(\alpha s)^{\mathrm{n}}\frac{\mathrm{n}}{s} \\ &= -(1-S_r)\mathrm{mn}\alpha^{\mathrm{n}}\left[1+(\alpha s)^{\mathrm{n}}\right]^{-\mathrm{m}-1} s^{(\mathrm{n}-1)} \end{aligned} \tag{2.141}$$

The element force vectors (body, traction and water) are then written as,

$$\begin{aligned} \boldsymbol{f}_f^{e,d}(\boldsymbol{d}^e,\boldsymbol{\theta}^e) &= \int_{B^e}\rho(\boldsymbol{d}^e,\boldsymbol{\theta}^e)(\boldsymbol{N}^{e,u})^T\cdot\boldsymbol{g}\,\mathrm{d}a \;=\; \int_{-1}^{1}\int_{-1}^{1}\rho(\boldsymbol{d}^e,\boldsymbol{\theta}^e)(\boldsymbol{N}^{e,u})^T\cdot\boldsymbol{g}\,j\mathrm{d}\xi\mathrm{d}\eta \\ \boldsymbol{f}^{e,\theta}(\boldsymbol{d}^e,\boldsymbol{\theta}^e) &= \int_{B_w^e}\rho^{wR}(\boldsymbol{B}^{e,p})^T\cdot\boldsymbol{k}^w(\boldsymbol{d}^e,\boldsymbol{\theta}^e)\cdot\boldsymbol{g}\,\mathrm{d}a \\ &= \int_{-1}^{1}\int_{-1}^{1}\rho^{wR}(\boldsymbol{B}^{e,p})^T\cdot\boldsymbol{k}^w(\boldsymbol{d}^e,\boldsymbol{\theta}^e)\cdot\boldsymbol{g}\,j\mathrm{d}\xi\mathrm{d}\eta \\ \boldsymbol{f}_t^{e,d} &= \int_{\Gamma_t^e}(\boldsymbol{N}^{e,u})^T\cdot\boldsymbol{t}^\sigma\mathrm{d}a \\ \boldsymbol{f}_s^{e,\theta} &= \int_{\Gamma_{s(w)}^e}(\boldsymbol{N}^{e,p})^T S^w\mathrm{d}s \end{aligned} \tag{2.142}$$

After element assembly, we have the coupled parabolic PDEs to solve using generalized trapezoidal integration in time.

$$\boldsymbol{C}(\boldsymbol{D}) \cdot \dot{\boldsymbol{D}} + \boldsymbol{K}(\boldsymbol{D}) \cdot \boldsymbol{D} = \boldsymbol{F}(\boldsymbol{D}) \tag{2.143}$$

$$\begin{aligned}
\dot{\boldsymbol{D}} &= \begin{bmatrix} \dot{\boldsymbol{d}} \\ \dot{\boldsymbol{\theta}} \end{bmatrix}, \quad \boldsymbol{D} = \begin{bmatrix} \boldsymbol{d} \\ \boldsymbol{\theta} \end{bmatrix}, \quad \boldsymbol{C}(\boldsymbol{D}) = \begin{bmatrix} \mathbf{0} & \mathbf{0} \\ \boldsymbol{K}^{\theta d}(\boldsymbol{D}) & -\boldsymbol{K}^{\theta\zeta}(\boldsymbol{D}) \end{bmatrix} \\
\boldsymbol{K}(\boldsymbol{D}) &= \begin{bmatrix} \boldsymbol{K}^{dd} & -\boldsymbol{K}^{d\theta}(\boldsymbol{D}) \\ \mathbf{0} & \boldsymbol{K}^{\theta\theta}(\boldsymbol{D}) \end{bmatrix}, \; \boldsymbol{F}(\boldsymbol{D}) = \begin{bmatrix} \boldsymbol{f}_f^{e,d}(\boldsymbol{D}) + \boldsymbol{f}_t^{e,d} \\ \boldsymbol{f}^{e,\theta}(\boldsymbol{D}) + \boldsymbol{f}_s^{e,\theta} \end{bmatrix} = \begin{bmatrix} \boldsymbol{F}^d(\boldsymbol{D}) \\ \boldsymbol{F}^\theta(\boldsymbol{D}) \end{bmatrix}
\end{aligned} \tag{2.144}$$

$$\begin{aligned}
-\boldsymbol{K}_0^{\theta\zeta} \cdot \dot{\boldsymbol{\theta}}_0 + \boldsymbol{K}_0^{\theta\theta} \cdot \boldsymbol{\theta}_0 &= \boldsymbol{F}_0^\theta \\
\dot{\boldsymbol{\theta}}_0 &= \boldsymbol{K}_0^{\theta\zeta^{-1}} \cdot \left(\boldsymbol{K}_0^{\theta\theta} \cdot \boldsymbol{\theta}_0 - \boldsymbol{F}_0^\theta \right)
\end{aligned} \tag{2.145}$$

where $\boldsymbol{C}$ is the combination of damping matrix and stiffness matrix of d.o.f vector time derivative, and $\boldsymbol{K}$ is stiffness matrix. For two phases of a soil we must assemble the element stiffness and damping matrices. Then, the Location Matrix (LM) can be used to assemble the individual 22×22 and 22×3 contributions to the global "damping" matrix, stiffness matrix, and forcing vector, and use generalized trapezoidal integration to solve transient equations[45].

For consolidation analysis, generalized trapezoidal rule[45] is used to integrate the transient FE coupled balance of mass and linear momentum equations at time t_{n+1}, with introduced difference formulas for $\boldsymbol{D}_{n+1}$ and $\boldsymbol{V}_{n+1}$, where velocity $\boldsymbol{V}_{n+1}$ is $\dot{\boldsymbol{D}}(t_{n+1})$ and α is the time integration parameter, written as

$$\begin{aligned}
\boldsymbol{C}(\boldsymbol{D}_{n+1}) \cdot \boldsymbol{V}_{n+1} + \boldsymbol{K}(\boldsymbol{D}_{n+1}) \cdot \boldsymbol{D}_{n+1} &= \boldsymbol{F}(\boldsymbol{D}_{n+1}) \\
\boldsymbol{D}_{n+1} &= \boldsymbol{D}_n + \Delta t \, \boldsymbol{V}_{n+\alpha} \\
\boldsymbol{V}_{n+\alpha} &= (1-\alpha)\boldsymbol{V}_n + \alpha \, \boldsymbol{V}_{n+1}
\end{aligned} \tag{2.146}$$

A semi-implicit integration scheme leads to a linear form, and is written as

$$\boldsymbol{C}(\boldsymbol{D}_n) \cdot \boldsymbol{V}_{n+1} + \boldsymbol{K}(\boldsymbol{D}_n) \cdot \boldsymbol{D}_{n+1} = \boldsymbol{F}(\boldsymbol{D}_n) \tag{2.147}$$

which solved by the following generalized trapezoidal rule procedure as shown in Table 2.5.

Table 2.4: Generalized trapezoidal family

α	METHOD	TYPE
0	forward Euler	explicit (if $\boldsymbol{C}$ diagonal, which it is not)
1/2	trapezoidal rule	implicit
1	backward Euler	implicit

Table 2.5: Procedure of semi-implicit linear scheme for biphasic mixture

1) Initialize :	given initial displacement and pore pressure $\boldsymbol{D}_0$, solve for $\boldsymbol{V}_0$ $\boldsymbol{C}(\boldsymbol{D}_0) \cdot \boldsymbol{V}_0 = \boldsymbol{F}_0(\boldsymbol{D}_0) - \boldsymbol{K}(\boldsymbol{D}_0) \cdot \boldsymbol{D}_0$
2) Predictor :	$\tilde{\boldsymbol{D}}_{n+1} = \boldsymbol{D}_n + (1-\alpha)\Delta t\, \boldsymbol{V}_n$
3) Solution :	$\Big(\boldsymbol{C}(\boldsymbol{D}_n) + \alpha\Delta t\, \boldsymbol{K}(\boldsymbol{D}_n)\Big)\boldsymbol{V}_{n+1} = \boldsymbol{F}_{n+1}(\boldsymbol{D}_n) - \boldsymbol{K}(\boldsymbol{D}_n) \cdot \tilde{\boldsymbol{D}}_{n+1}$
4) Corrector :	$\boldsymbol{D}_{n+1} = \tilde{\boldsymbol{D}}_{n+1} + \alpha\Delta t\, \boldsymbol{V}_{n+1}$
5) Stability :	It will be chosen an unconditionally-stable method ($\alpha = 1$; Backward Euler)

2.5.3 FE form for 2D fully-implicit nonlinear biphasic poro-elasticity

Linear theory (linear elastic solid skeleton, and semi-implicit time integration) has been assumed in Section 2.5.2 allowing for easier numerical solution as will be shown in the Numerical Examples. However, because the partially saturated soil balance equations have been shown to be nonlinear, the solution procedure should be extended for Newton-Raphson method.

Assume the solid skeleton effective stress $\boldsymbol{\sigma}'$(eventually will be a function of suction in plasticity) can be governed by a nonlinear constitutive model, and that the density and permeability are functions of displacement and porosity, and porosity is a function of the solid skeleton volumetric strain ϵ_v. The coupled FE equations for biphasic mixture written then as

1) *Solid* (nonlinear biphasic) :

$$\begin{aligned}\mathop{\mathbf{A}}_{e=1}^{n_{\mathrm{el}}}(\boldsymbol{c}^e)^T\cdot\Bigg[&\underbrace{\left(\int_{B^e}(\boldsymbol{B}^{e,u})^T\cdot\boldsymbol{\sigma}'(\boldsymbol{d}^e,\boldsymbol{\theta}^e)\,\mathrm{d}a\right)}_{\boldsymbol{f}_e^{d,INT}(\boldsymbol{d}^e,\boldsymbol{\theta}^e)}-\underbrace{\left(\int_{B^e}\chi(\boldsymbol{\theta}^e)(\tilde{\boldsymbol{B}}^{e,u})^T\cdot\boldsymbol{N}^{e,p}\cdot\boldsymbol{\theta}^e\,\mathrm{d}a\right)}_{\boldsymbol{f}_e^{d\theta,INT}(\boldsymbol{\theta}^e)}\\&=\underbrace{\int_{B^e}\rho(\boldsymbol{d}^e,\boldsymbol{\theta}^e)(\boldsymbol{N}^{e,u})^T\cdot\boldsymbol{g}\,\mathrm{d}a+\int_{\Gamma_t^e}(\boldsymbol{N}^{e,u})^T\cdot\boldsymbol{t}\,\mathrm{d}a}_{\boldsymbol{f}_e^{d,EXT}(\boldsymbol{d}^e,\boldsymbol{\theta}^e)}\Bigg]\end{aligned}\tag{2.148}$$

2) *Water* (nonlinear biphasic) :

$$\begin{aligned}\mathop{\mathbf{A}}_{e=1}^{n_{\mathrm{el}}}(\boldsymbol{\alpha}^e)^T\cdot\Bigg[&\underbrace{\left(\int_{B_w^e}S(\boldsymbol{\theta}^e)\,(\boldsymbol{N}^{e,p})^T\cdot\tilde{\boldsymbol{B}}^{e,u}\,\mathrm{d}a\right)}_{\boldsymbol{k}_e^{\theta d,INT}(\boldsymbol{\theta}^e)}\cdot\dot{\boldsymbol{d}}^e\\&-\underbrace{\left(\int_{B_w^e}n(\boldsymbol{d}^e)\frac{\partial S}{\partial s}(\boldsymbol{\theta}^e)(\boldsymbol{N}^{e,p})^T\cdot\boldsymbol{N}^{e,p}\,\mathrm{d}a\right)}_{\boldsymbol{k}_e^{\theta 1,INT}(\boldsymbol{d}^e,\boldsymbol{\theta}^e)}\cdot\dot{\boldsymbol{\theta}}^e\\&-\underbrace{\left(\int_{B_w^e}(\boldsymbol{B}^{e,p})^T\cdot\tilde{\boldsymbol{v}}_w^s(\boldsymbol{d}^e,\boldsymbol{\theta}^e)\,\mathrm{d}a\right)}_{\boldsymbol{f}_e^{\theta 2,INT}(\boldsymbol{d}^e,\boldsymbol{\theta}^e)}=\underbrace{\int_{\Gamma_{s(w)}^e}(\boldsymbol{N}^{e,p})^T S^w\,\mathrm{d}s}_{\boldsymbol{f}_e^{\theta,EXT}}\Bigg]\end{aligned}\tag{2.149}$$

where Darcy's velocity, $\tilde{\boldsymbol{v}}_w^s = -\boldsymbol{k}^w(\boldsymbol{d}^e, \boldsymbol{\theta}^e)\cdot[\boldsymbol{\nabla} p_w - \rho^{wR}\boldsymbol{g}]$, is defined by Darcy's law with porosity and saturation rate dependent permeability, $\boldsymbol{k}^w = k_w(n, S)\ \mathbf{1}$. And then these nonlinear FE equations are written as

$$\begin{aligned}
&\mathop{\mathsf{A}}_{e=1}^{n_{\text{el}}} (\boldsymbol{c}^e)^T \cdot \left[\boldsymbol{f}_e^{d,INT}(\boldsymbol{d}^e, \boldsymbol{\theta}^e) - \boldsymbol{f}_e^{d\theta,INT}(\boldsymbol{\theta}^e) = \boldsymbol{f}_e^{d,EXT}(\boldsymbol{d}^e, \boldsymbol{\theta}^e) \right] \\
&\mathop{\mathsf{A}}_{e=1}^{n_{\text{el}}} (\boldsymbol{\alpha}^e)^T \cdot \left[\boldsymbol{k}_e^{\theta d,INT}(\boldsymbol{\theta}^e)\cdot\dot{\boldsymbol{d}}^e - \boldsymbol{k}_e^{\theta 1,INT}(\boldsymbol{d}^e, \boldsymbol{\theta}^e)\cdot\dot{\boldsymbol{\theta}}^e - \boldsymbol{f}_e^{\theta 2,INT}(\boldsymbol{d}^e, \boldsymbol{\theta}^e) = \boldsymbol{f}_e^{\theta,EXT} \right]
\end{aligned} \tag{2.150}$$

After element assembly, we have the coupled nonlinear parabolic PDEs to solve using generalized trapezoidal integration in time, and Newton-Raphson iteration

$$\boldsymbol{F}^{d,INT}(\boldsymbol{d}, \boldsymbol{\theta}) - \boldsymbol{F}^{d\theta,INT}(\boldsymbol{\theta}) = \boldsymbol{F}^{d,EXT}(\boldsymbol{d}, \boldsymbol{\theta}) \tag{2.151}$$

$$\boldsymbol{K}^{\theta d,INT}(\boldsymbol{\theta})\cdot\dot{\boldsymbol{d}} - \boldsymbol{K}^{\theta 1,INT}(\boldsymbol{d}, \boldsymbol{\theta})\cdot\dot{\boldsymbol{\theta}} - \boldsymbol{F}^{\theta 2,INT}(\boldsymbol{d}, \boldsymbol{\theta}) = \boldsymbol{F}^{\theta,EXT} \tag{2.152}$$

which we may rewrite as

$$\boldsymbol{C}(\boldsymbol{D})\cdot\dot{\boldsymbol{D}} + \boldsymbol{F}^{INT}(\boldsymbol{D}) = \boldsymbol{F}^{EXT}(\boldsymbol{D}) \tag{2.153}$$

where,

$$\begin{aligned}
\boldsymbol{C}(\boldsymbol{D}) &= \begin{bmatrix} \mathbf{0} & \mathbf{0} \\ \boldsymbol{K}^{\theta d,INT}(\boldsymbol{\theta}) & -\boldsymbol{K}^{\theta 1,INT}(\boldsymbol{d}, \boldsymbol{\theta}) \end{bmatrix}, \quad \boldsymbol{D} = \begin{bmatrix} \boldsymbol{d} \\ \boldsymbol{\theta} \end{bmatrix}, \quad \dot{\boldsymbol{D}} = \begin{bmatrix} \dot{\boldsymbol{d}} \\ \dot{\boldsymbol{\theta}} \end{bmatrix} \\
\boldsymbol{F}^{INT}(\boldsymbol{D}) &= \begin{bmatrix} \boldsymbol{F}^{d,INT}(\boldsymbol{d}, \boldsymbol{\theta}) - \boldsymbol{F}^{d\theta,INT}(\boldsymbol{\theta}) \\ -\boldsymbol{F}^{\theta 2,INT}(\boldsymbol{d}, \boldsymbol{\theta}) \end{bmatrix}, \quad \boldsymbol{F}^{EXT}(\boldsymbol{D}) = \begin{bmatrix} \boldsymbol{F}^{d,EXT}(\boldsymbol{d}, \boldsymbol{\theta}) \\ \boldsymbol{F}^{\theta,EXT} \end{bmatrix}
\end{aligned}$$

Recall the generalized trapezoidal integration:

$$\begin{aligned}
&\boldsymbol{C}(\boldsymbol{D}_{n+1})\cdot\boldsymbol{V}_{n+1} + \boldsymbol{F}^{INT}(\boldsymbol{D}_{n+1}) = \boldsymbol{F}^{EXT}(\boldsymbol{D}_{n+1}) \\
&\boldsymbol{D}_{n+1} = \tilde{\boldsymbol{D}}_{n+1} + \alpha\Delta t\,\boldsymbol{V}_{n+1}\,, \qquad \tilde{\boldsymbol{D}}_{n+1} = \boldsymbol{D}_n + (1-\alpha)\Delta t\,\boldsymbol{V}_n
\end{aligned} \tag{2.154}$$

$$\begin{aligned}
&\boldsymbol{C}(\boldsymbol{D}_0)\cdot\boldsymbol{V}_0 + \boldsymbol{F}^{INT}(\boldsymbol{D}_0) - \boldsymbol{F}^{EXT}(\boldsymbol{D}_0) = \mathbf{0} \\
&\boldsymbol{V}_0 = \boldsymbol{C}_0^{-1}\cdot\left(\boldsymbol{F}_0^{EXT} - \boldsymbol{F}_0^{INT}\right)
\end{aligned} \tag{2.155}$$

It can be expressed in residual form, solving for $\boldsymbol{V}_{n+1}^{k+1}$ in a Newton-Raphson iteration algorithm with current iteration $(k+1)$:

$$\begin{aligned} \boldsymbol{R}(\boldsymbol{V}_{n+1}^{k+1}) &= \boldsymbol{C}(\boldsymbol{D}_{n+1}^{k+1}) \cdot \boldsymbol{V}_{n+1}^{k+1} + \boldsymbol{F}^{INT}(\boldsymbol{D}_{n+1}^{k+1}) - \boldsymbol{F}^{EXT}(\boldsymbol{D}_{n+1}^{k+1}) = \boldsymbol{0} \\ &= \boldsymbol{R}^k + \frac{\partial \boldsymbol{R}^k}{\partial \boldsymbol{V}} \cdot \delta \boldsymbol{V} \approx \boldsymbol{0} \end{aligned} \tag{2.156}$$

Therefore,

$$\begin{aligned} \delta \boldsymbol{V} &= -\left(\frac{\partial \boldsymbol{R}^k}{\partial \boldsymbol{V}}\right)^{-1} \cdot \boldsymbol{R}^k \\ \boldsymbol{V}_{n+1}^{k+1} &= \boldsymbol{V}_{n+1}^{k} + \delta \boldsymbol{V} \\ \boldsymbol{D}_{n+1}^{k+1} &= \tilde{\boldsymbol{D}}_{n+1} + \alpha \Delta t \, \boldsymbol{V}_{n+1}^{k+1} \end{aligned} \tag{2.157}$$

For consistent tangent,

$$\frac{\partial \boldsymbol{R}}{\partial \boldsymbol{V}} = \left(\frac{\partial \boldsymbol{C}}{\partial \boldsymbol{D}} \cdot \frac{\partial \boldsymbol{D}}{\partial \boldsymbol{V}}\right) \cdot \boldsymbol{V} + \boldsymbol{C}(\boldsymbol{D}) + \frac{\partial \boldsymbol{F}^{INT}}{\partial \boldsymbol{D}} \cdot \frac{\partial \boldsymbol{D}}{\partial \boldsymbol{V}} - \frac{\partial \boldsymbol{F}^{EXT}}{\partial \boldsymbol{D}} \cdot \frac{\partial \boldsymbol{D}}{\partial \boldsymbol{V}} \tag{2.158}$$

where $\dfrac{\partial \boldsymbol{D}}{\partial \boldsymbol{V}} = \alpha \Delta t$. Equivalently, in component form, we have

$$\begin{aligned} R_{A} &= C_{AB} \cdot V_{B} + F_{A}^{INT} - F_{A}^{EXT} \qquad \left(A, B, C \text{ and } E = 1, \cdots, n_{dof}\right) \\ \frac{\partial R_{A}}{\partial V_{C}} &= \left(\frac{\partial C_{AB}}{\partial D_{E}} \frac{\partial D_{E}}{\partial V_{C}}\right) \cdot V_{B} + C_{AB} \frac{\partial V_{B}}{\partial V_{C}} + \frac{\partial F_{A}^{INT}}{\partial D_{B}} \frac{\partial D_{B}}{\partial V_{C}} - \frac{\partial F_{A}^{EXT}}{\partial D_{B}} \frac{\partial D_{B}}{\partial V_{C}} \\ &= \left(\frac{\partial C_{AB}}{\partial D_{E}} \delta_{EC} \, \alpha \Delta t\right) \cdot V_{B} + C_{AB} \, \delta_{BC} + \frac{\partial F_{A}^{INT}}{\partial D_{B}} \delta_{BC} \, \alpha \Delta t - \frac{\partial F_{A}^{EXT}}{\partial D_{B}} \delta_{BC} \, \alpha \Delta t \\ &= \alpha \Delta t \frac{\partial C_{AB}}{\partial D_{C}} V_{B} + C_{AC} + \frac{\partial F_{A}^{INT}}{\partial D_{C}} \alpha \Delta t - \frac{\partial F_{A}^{EXT}}{\partial D_{C}} \alpha \Delta t \end{aligned} \tag{2.159}$$

where $\boldsymbol{C} \cdot \boldsymbol{V} = \begin{bmatrix} \boldsymbol{0} \\ \boldsymbol{K}^{\theta d, INT} \cdot \dot{\boldsymbol{d}} - \boldsymbol{K}^{\theta 1, INT} \cdot \dot{\boldsymbol{\theta}} \end{bmatrix}$, and then implied

$$\frac{\partial \boldsymbol{C}}{\partial \boldsymbol{D}} \cdot \boldsymbol{V} \left(= \frac{\partial C_{AB}}{\partial D_{C}} V_{B}\right) = \begin{bmatrix} \boldsymbol{0} & \boldsymbol{0} \\ -\dfrac{\partial \boldsymbol{K}^{\theta 1, INT}}{\partial \boldsymbol{d}} \cdot \dot{\boldsymbol{\theta}} & \dfrac{\partial \boldsymbol{K}^{\theta d, INT}}{\partial \boldsymbol{\theta}} \cdot \dot{\boldsymbol{d}} - \dfrac{\partial \boldsymbol{K}^{\theta 1, INT}}{\partial \boldsymbol{\theta}} \cdot \dot{\boldsymbol{\theta}} \end{bmatrix} \tag{2.160}$$

where

$$\frac{\partial \boldsymbol{F}^{INT}}{\partial \boldsymbol{D}} = \left[\frac{\partial \boldsymbol{F}^{INT}}{\partial \boldsymbol{d}} \quad \frac{\partial \boldsymbol{F}^{INT}}{\partial \boldsymbol{\theta}}\right]$$

$$\frac{\partial \boldsymbol{F}^{INT}}{\partial \boldsymbol{d}} = \begin{bmatrix} \dfrac{\partial \boldsymbol{F}^{d,INT}}{\partial \boldsymbol{d}} \\ -\dfrac{\partial \boldsymbol{F}^{\theta 2,INT}}{\partial \boldsymbol{d}} \end{bmatrix}, \quad \frac{\partial \boldsymbol{F}^{INT}}{\partial \boldsymbol{\theta}} = \begin{bmatrix} \dfrac{\partial \boldsymbol{F}^{d,INT}}{\partial \boldsymbol{\theta}} - \dfrac{\partial \boldsymbol{F}^{d\theta,INT}}{\partial \boldsymbol{\theta}} \\ -\dfrac{\partial \boldsymbol{F}^{\theta 2,INT}}{\partial \boldsymbol{\theta}} \end{bmatrix}$$

$$\frac{\partial \boldsymbol{F}^{EXT}}{\partial \boldsymbol{D}} = \left[\frac{\partial \boldsymbol{F}^{EXT}}{\partial \boldsymbol{d}} \quad \frac{\partial \boldsymbol{F}^{EXT}}{\partial \boldsymbol{\theta}}\right], \quad \frac{\partial \boldsymbol{F}^{EXT}}{\partial \boldsymbol{d}} = \begin{bmatrix} \dfrac{\partial \boldsymbol{F}^{d,EXT}}{\partial \boldsymbol{d}} \\ \mathbf{0} \end{bmatrix}, \quad \frac{\partial \boldsymbol{F}^{EXT}}{\partial \boldsymbol{\theta}} = \begin{bmatrix} \dfrac{\partial \boldsymbol{F}^{d,EXT}}{\partial \boldsymbol{\theta}} \\ \mathbf{0} \end{bmatrix}$$

In which its components are

$$\begin{aligned} \frac{\partial \boldsymbol{K}^{\theta 1,INT}}{\partial \boldsymbol{d}} \cdot \dot{\boldsymbol{\theta}} &= \mathop{\mathbf{A}}_{e=1}^{n_{\text{el}}} \frac{\partial \boldsymbol{k}_e^{\theta 1,INT}}{\partial \boldsymbol{d}^e} \cdot \dot{\boldsymbol{\theta}}^e \\ &= \mathop{\mathbf{A}}_{e=1}^{n_{\text{el}}} \int_{B_w^e} \left[\dot{p}_w \frac{\partial S(\boldsymbol{\theta}^e)}{\partial s} (\boldsymbol{N}^{e,p})^T\right] \otimes \frac{\partial n(\boldsymbol{d}^e)}{\partial \boldsymbol{d}^e} \, \mathrm{d}a \end{aligned} \tag{2.161}$$

where $\dot{p}_w = \boldsymbol{N}^{e,p} \cdot \dot{\boldsymbol{\theta}}^e$

$$\begin{aligned} \frac{\partial \boldsymbol{K}^{\theta d,INT}}{\partial \boldsymbol{\theta}} \cdot \dot{\boldsymbol{d}} &= \mathop{\mathbf{A}}_{e=1}^{n_{\text{el}}} \frac{\partial \boldsymbol{k}_e^{\theta d,INT}}{\partial \boldsymbol{\theta}^e} \cdot \dot{\boldsymbol{d}}^e = \mathop{\mathbf{A}}_{e=1}^{n_{\text{el}}} \int_{B_w^e} \left[\dot{\epsilon}_v (\boldsymbol{N}^{e,p})^T\right] \otimes \frac{\partial S(\boldsymbol{\theta}^e)}{\partial \boldsymbol{\theta}^e} \, \mathrm{d}a \\ &= \mathop{\mathbf{A}}_{e=1}^{n_{\text{el}}} \int_{B_w^e} \dot{\epsilon}_v \left[(\boldsymbol{N}^{e,p})^T\right] \otimes \left(-\frac{\partial S(\boldsymbol{\theta}^e)}{\partial s} \boldsymbol{N}^{e,p}\right) \mathrm{d}a \end{aligned} \tag{2.162}$$

where $\dot{\epsilon}_v = \tilde{\boldsymbol{B}}^{e,u} \cdot \dot{\boldsymbol{d}}^e$

$$\begin{aligned} \frac{\partial \boldsymbol{K}^{\theta 1,INT}}{\partial \boldsymbol{\theta}} \cdot \dot{\boldsymbol{\theta}} &= \mathop{\mathbf{A}}_{e=1}^{n_{\text{el}}} \frac{\partial \boldsymbol{k}_e^{\theta 1,INT}}{\partial \boldsymbol{\theta}^e} \cdot \dot{\boldsymbol{\theta}}^e \\ &= \mathop{\mathbf{A}}_{e=1}^{n_{\text{el}}} \int_{B_w^e} \left[\dot{p}_w n(\boldsymbol{d}^e) (\boldsymbol{N}^{e,p})^T\right] \otimes \frac{\partial}{\partial \boldsymbol{\theta}^e} \left(\frac{\partial S}{\partial s}\right) \mathrm{d}a \\ &= \mathop{\mathbf{A}}_{e=1}^{n_{\text{el}}} \int_{B_w^e} \left[\dot{p}_w \, n(\boldsymbol{d}^e) (\boldsymbol{N}^{e,p})^T\right] \otimes \left(-\frac{\partial^2 S}{\partial s^2} \boldsymbol{N}^{e,p}\right) \mathrm{d}a \end{aligned} \tag{2.163}$$

where,

$$\frac{\partial S}{\partial s} = (1 - S_r) \frac{\partial S_e}{\partial s} = -(1 - S_r) \left[1 + \left(\frac{s}{\mathrm{a}}\right)^{\mathrm{n}}\right]^{(-\mathrm{m}-1)} s^{(\mathrm{n}-1)} \frac{\mathrm{mn}}{\mathrm{a}^{\mathrm{n}}}$$

$$\frac{\partial^2 S}{\partial s^2} = (1-S_r)\frac{\partial^2 S_e}{\partial s^2} = -(1-S_r)\frac{\mathrm{mn}}{\mathrm{a^n}}\Bigg((\mathrm{n}-1)s^{(\mathrm{n}-2)}\left[1+\left(\frac{s}{\mathrm{a}}\right)^{\mathrm{n}}\right]^{(-\mathrm{m}-1)} - s^{(2\mathrm{n}-2)}(\mathrm{m}+1)\left[1+\left(\frac{s}{\mathrm{a}}\right)^{\mathrm{n}}\right]^{(-\mathrm{m}-2)}\mathrm{n}\left(\frac{1}{\mathrm{a}}\right)^{\mathrm{n}}\Bigg)$$

where,

$$\begin{aligned}
\frac{\partial}{\partial \boldsymbol{\theta}^e}\left(\frac{\partial S}{\partial s}\right) &= \frac{\partial^2 S}{\partial s^2}\frac{\partial s}{\partial \boldsymbol{\theta}^e} = -\frac{\partial^2 S}{\partial s^2}\boldsymbol{N}^{e,p} \\
\frac{\partial S}{\partial \boldsymbol{\theta}^e} &= \frac{\partial S}{\partial s}\frac{\partial s}{\partial \boldsymbol{\theta}^e} = -\frac{\partial S}{\partial s}\boldsymbol{N}^{e,p} \\
\frac{\partial n}{\partial \boldsymbol{d}^e} &= \left(\frac{1-n}{1+\Delta\epsilon_v}\right)\tilde{\boldsymbol{B}}^{e,u}
\end{aligned}$$

$$\frac{\partial \boldsymbol{F}^{d,INT}}{\partial \boldsymbol{d}} = \mathop{\mathbf{A}}_{e=1}^{n_{\mathrm{el}}}\frac{\partial \boldsymbol{f}_e^{d,INT}}{\partial \boldsymbol{d}^e} = \mathop{\mathbf{A}}_{e=1}^{n_{\mathrm{el}}}\int_{B^e}(\boldsymbol{B}^{e,u})^T\cdot\frac{\partial \boldsymbol{\sigma}'}{\partial \boldsymbol{\epsilon}}\cdot\boldsymbol{B}^{e,u}\,\mathrm{d}a \tag{2.164}$$

$$\frac{\partial \boldsymbol{F}^{\theta 2,INT}}{\partial \boldsymbol{d}} = \mathop{\mathbf{A}}_{e=1}^{n_{\mathrm{el}}}\frac{\partial \boldsymbol{f}_e^{\theta 2,INT}}{\partial \boldsymbol{d}^e} = \mathop{\mathbf{A}}_{e=1}^{n_{\mathrm{el}}}\int_{B_w^e}(\boldsymbol{B}^{e,p})^T\cdot\frac{\partial \tilde{\boldsymbol{v}}_w^s}{\partial \boldsymbol{d}^e}\,\mathrm{d}a \tag{2.165}$$

where,

$$\begin{aligned}
\frac{\partial \tilde{\boldsymbol{v}}_w^s}{\partial \boldsymbol{d}^e} &= -[\boldsymbol{\nabla}p_w - \rho^{wR}\boldsymbol{g}]\otimes\frac{\partial k_w}{\partial n}\frac{\partial n}{\partial \boldsymbol{d}^e}\,, \quad \delta(n) = \frac{n^3}{1-n^2}\,, \quad \boldsymbol{\nabla}p_w = \boldsymbol{B}^{e,p}\cdot\boldsymbol{\theta}^e \\
k_w(n,S) &= \frac{\varkappa(n)}{\eta_w}k_{rw}(S) = \frac{l^2}{\eta_w}\delta(n)\,k_{rw}(S)\,, \quad k_{rw}(S) = \sqrt{S}\left(1-\left(1-S^{\frac{1}{\mathrm{m}}}\right)^{\mathrm{m}}\right)^2 \\
\frac{\partial k_w}{\partial n} &= \frac{l^2}{\eta_w}\left[\frac{3n^2-n^4}{(1-n^2)^2}\right]k_{rw}(S) \\
\frac{\partial n}{\partial \boldsymbol{d}^e} &= \left(\frac{1-n}{1+\Delta\epsilon_v}\right)\tilde{\boldsymbol{B}}^{e,u}
\end{aligned}$$

And by taking derivatives with relation to the nodal pore water pressure vector, $\boldsymbol{\theta}$,

$$\frac{\partial \boldsymbol{F}^{d,INT}}{\partial \boldsymbol{\theta}} = \mathop{\mathbf{A}}_{e=1}^{n_{\mathrm{el}}}\frac{\partial \boldsymbol{f}_e^{d,INT}}{\partial \boldsymbol{\theta}^e} = \mathop{\mathbf{A}}_{e=1}^{n_{\mathrm{el}}}\int_{B^e}(\boldsymbol{B}^{e,u})^T\cdot\frac{\partial \boldsymbol{\sigma}'}{\partial s}\cdot\frac{\partial s}{\partial \boldsymbol{\theta}^e}\,\mathrm{d}a \tag{2.166}$$

where $\dfrac{\partial \boldsymbol{\sigma}'}{\partial s} = \mathbf{0}$ for linear elasticity.

$$\frac{\partial \boldsymbol{F}^{d\theta,INT}}{\partial \boldsymbol{\theta}} = \mathop{\mathsf{A}}_{e=1}^{n_{\rm el}} \frac{\partial \boldsymbol{f}_e^{d\theta,INT}}{\partial \boldsymbol{\theta}^e} = \mathop{\mathsf{A}}_{e=1}^{n_{\rm el}} \int_{B^e} \left(-p_w \frac{\partial \chi}{\partial s} + \chi \right) (\tilde{\boldsymbol{B}}^{e,u})^T \cdot \boldsymbol{N}^{e,p} \, \mathrm{d}a \tag{2.167}$$

$$\frac{\partial \boldsymbol{F}^{\theta 2,INT}}{\partial \boldsymbol{\theta}} = \mathop{\mathsf{A}}_{e=1}^{n_{\rm el}} \frac{\partial \boldsymbol{f}_e^{\theta 2,INT}}{\partial \boldsymbol{\theta}^e} = \mathop{\mathsf{A}}_{e=1}^{n_{\rm el}} \int_{B_w^e} (\boldsymbol{B}^{e,p})^T \cdot \frac{\partial \tilde{\boldsymbol{v}}_w^e}{\partial \boldsymbol{\theta}^e} \, \mathrm{d}a \tag{2.168}$$

where,

$$\frac{\partial \tilde{\boldsymbol{v}}_w^e}{\partial \boldsymbol{\theta}^e} = -k_w \, \boldsymbol{B}^{e,p} - [\boldsymbol{\nabla} p_w - \rho^{wR} \boldsymbol{g}] \otimes \frac{\partial k_w}{\partial \boldsymbol{\theta}^e} = -k_w \, \boldsymbol{B}^{e,p} + \left(\boldsymbol{B}^{e,p} \cdot \boldsymbol{\theta}^e - \rho^{wR} \boldsymbol{g} \right) \frac{\partial k_w}{\partial S} \frac{\partial S}{\partial s} \boldsymbol{N}^{e,p}$$

$$\frac{\partial k_w}{\partial \boldsymbol{\theta}^e} = \frac{\partial k_w}{\partial S} \frac{\partial S}{\partial \boldsymbol{\theta}^e}$$

$$\frac{\partial k_w}{\partial S} = \frac{\varkappa(n)}{\eta_w} \left[\frac{1}{2\sqrt{S}} \left(1 - \left(1 - S^{\frac{1}{\mathrm{m}}} \right)^{\mathrm{m}} \right)^2 + \frac{2}{\sqrt{S}} \left(1 - \left(1 - S^{\frac{1}{\mathrm{m}}} \right)^{\mathrm{m}} \right) \left(1 - S^{\frac{1}{\mathrm{m}}} \right)^{\mathrm{m}-1} S^{\frac{1}{\mathrm{m}}} \right]$$

By taking derivatives with relation to $\boldsymbol{d}$ and $\boldsymbol{\theta}$ for the external force vectors,

$$\frac{\partial \boldsymbol{F}^{d,EXT}}{\partial \boldsymbol{d}} = \mathop{\mathsf{A}}_{e=1}^{n_{\rm el}} \frac{\partial \boldsymbol{f}_e^{d,EXT}}{\partial \boldsymbol{d}^e} = \mathop{\mathsf{A}}_{e=1}^{n_{\rm el}} \int_{B^e} (\boldsymbol{N}^{e,u})^T \cdot \boldsymbol{g} \otimes \frac{\partial \rho(\boldsymbol{d}^e, \boldsymbol{\theta}^e)}{\partial \boldsymbol{d}^e} \, \mathrm{d}a \tag{2.169}$$

$$\frac{\partial \boldsymbol{F}^{d,EXT}}{\partial \boldsymbol{\theta}} = \mathop{\mathsf{A}}_{e=1}^{n_{\rm el}} \frac{\partial \boldsymbol{f}_e^{d,EXT}}{\partial \boldsymbol{\theta}^e} = \mathop{\mathsf{A}}_{e=1}^{n_{\rm el}} \int_{B^e} (\boldsymbol{N}^{e,u})^T \cdot \boldsymbol{g} \otimes \frac{\partial \rho(\boldsymbol{d}^e, \boldsymbol{\theta}^e)}{\partial \boldsymbol{\theta}^e} \, \mathrm{d}a \tag{2.170}$$

where,

$$\begin{aligned} \frac{\partial \rho}{\partial \boldsymbol{d}^e} &= -\frac{\partial n^w}{\partial \boldsymbol{d}^e} \rho^{sR} + \frac{\partial n^w}{\partial \boldsymbol{d}^e} S \, \rho^{wR} \\ &= \left(-\rho^{sR} + S \, \rho^{wR} \right) \left(\frac{1 - n^w}{1 + \Delta \epsilon_v} \right) \tilde{\boldsymbol{B}}^{e,u} \\ \frac{\partial \rho}{\partial \boldsymbol{\theta}^e} &= n \rho^{wR} \frac{\partial S}{\partial \boldsymbol{\theta}^e} = -n \rho^{wR} \frac{\partial S}{\partial s} \boldsymbol{N}^{e,p} \end{aligned}$$

For linear elasticity, $\dfrac{\partial \boldsymbol{\sigma}'}{\partial s} = \boldsymbol{0}$, but for Cam-Clay hyperelasto-plasticity with suction, $\dfrac{\partial \boldsymbol{\sigma}'}{\partial s} \neq \boldsymbol{0}$. I will show comparison of convergence profiles for semi-implicit linear and fully-implicit nonlinear in Numerical Examples chapter.

Chapter 3

Cam-clay Elasto-Plasticity for Partially Saturated Soil

The framework of Cam-clay plasticity model for partially saturated soils has been focused on more appropriate yield locus in the space of net mean stress $(p - p_a)$ and suction s to approach to the experimental behavior of a soil based on the Barcelona Basic Model (BBM)[6] by numerous researchers. However, the shortcomings of BBM have reviewed from several researchers, such as compression curve at constant soil suction, effects of the confining stress on SWCC and yield surface depended on soil fabric[95, 88, 30]. In this study, a new version contains the suction stress s as an additional variable compared to saturated Cam-clay plasticity models. This model is also developed with the stored energy functions and pressure-dependent elastic moduli to represent the mechanical behavior of partially saturated soils with energy-conserving elasticity[12, 16].

3.1 Coupling Plasticity and Energy-Conserving Elasticity

In order to develop the coupling plasticity and energy-conserving elasticity for partially saturated soils, first of all, the derivation of stored energy functions appropriate for classical Cam-clay plasticity model is needed for saturated condition. In this Section 3.1, the void ratio e and the specific volume $v\,(= 1 + e)$ denote respectively e_{sat} and v_{sat} due to the description of saturated condition.

3.1.1 Nonlinear hyper-elasticity model

The elasticity model is an important portion in an elasto-plasticity constitutive model for soil because it is shown to be a function of stress[16]. Cam-clay model has a linearly increased elastic bulk modulus due to mean effective stress, but the elastic shear modulus of it is constant. The elastic shear modulus should be determined from stored energy function because of the nonlinearities of soil in even elastic region. Energy conservative models can be derived from the assumption of a stored energy function of the form[16, 12]

$$\begin{aligned} \psi(\epsilon^e_{ij}) = \psi(\epsilon^e_v, \epsilon^e_s) = \tilde{\psi}(\epsilon^e_v) + \frac{3}{2}\mu^e(\epsilon^e_s)^2 \\ \tilde{\psi}(\epsilon^e_v) = -p'_0\tilde{\kappa}\exp\omega\,, \qquad \omega = -\frac{\epsilon^e_v - \epsilon^e_{v0}}{\tilde{\kappa}} \end{aligned} \tag{3.1}$$

where, ϵ^e_{v0} is elastic volumetric strain corresponding to a reference mean effective stress of p'_0 and $\tilde{\kappa}$ is elastic compressibility index. It is the stored energy function $\psi(\epsilon^e_{ij})$ for isotropic loading, and $\mu^e = \mu^e(\epsilon^e_v)$ is the elastic shear modulus defined by the expression,

$$\mu^e(\epsilon^e_v) = \mu_0 + \frac{\bar{\alpha}}{\tilde{\kappa}}\tilde{\psi}(\epsilon^e_v) \tag{3.2}$$

where μ_0 is a constant term, and μ^e varies with the elastic volumetric strain through the constant coefficient $\bar{\alpha}$. If $\bar{\alpha} > 0$ and $\mu_0 = 0$, the nonlinear elastic model is proceeded; if $\bar{\alpha} = 0$ and $\mu_0 > 0$, the elastic model is defined by linear elastic model using a variable elastic bulk modulus and a constant elastic shear modulus.

First, the effective Cauchy stress tensor σ'_{ij} can be expressed in terms of ψ, and the elastic moduli tensor c^e_{ijkl} can be written as,

$$\sigma'_{ij} = \frac{\partial\psi}{\partial\epsilon^e_{ij}}\,, \qquad c^e_{ijkl} = \frac{\partial\sigma'_{ij}}{\partial\epsilon^e_{kl}} = \frac{\partial^2\psi}{\partial\epsilon^e_{ij}\partial\epsilon^e_{kl}} \tag{3.3}$$

We can consider a class of stored energy functions of the volumetric and deviatoric invariants of the small elastic strain tensor, denoted by ϵ^e_v and ϵ^e_s, respectively.

$$\epsilon_v^e = \epsilon_{kk}^e\,, \qquad \epsilon_s^e = \sqrt{\frac{2}{3} e_{ij}^e e_{ij}^e}\,, \qquad e_{ij}^e = \epsilon_{ij}^e - \frac{1}{3}\epsilon_v^e \delta_{ij} \tag{3.4}$$

where δ_{ij} is Kronecker delta. Assuming a stored energy function of the form $\psi = \psi(\epsilon_v^e, \epsilon_s^e)$, then we can use the chain rule to expand the stress tensor of equation (3.3) in the form

$$\sigma'_{ij} = \frac{\partial \psi}{\partial \epsilon_v^e}\frac{\partial \epsilon_v^e}{\partial \epsilon_{ij}^e} + \frac{\partial \psi}{\partial \epsilon_s^e}\frac{\partial \epsilon_s^e}{\partial \epsilon_{ij}^e}\,, \qquad \frac{\partial \epsilon_v^e}{\partial \epsilon_{ij}^e} = \delta_{ij}\,; \quad \frac{\partial \epsilon_s^e}{\partial \epsilon_{ij}^e} = \sqrt{\frac{2}{3}}\,\hat{n}_{ij} \tag{3.5}$$

where $\hat{n}_{ij} = e_{ij}^e / ||\boldsymbol{e}^e||$, then equation (3.5) can be rewritten in

$$\boldsymbol{\sigma}' = p'\mathbf{1} + \sqrt{\frac{2}{3}}\, q\, \hat{\boldsymbol{n}} = p'\mathbf{1} + \mathbf{s}, \qquad p' = \frac{\partial \psi(\epsilon_v^e, \epsilon_s^e)}{\partial \epsilon_v^e}\,; \quad q = \frac{\partial \psi(\epsilon_v^e, \epsilon_s^e)}{\partial \epsilon_s^e} \tag{3.6}$$

where $\mathbf{s}$ is the deviatoric part of $\boldsymbol{\sigma}'$, thus we have

$$p' = p'_0 \exp\omega \left[1 + \frac{3\bar{\alpha}}{2\tilde{\kappa}}(\epsilon_s^e)^2\right], \quad q = 3(\mu_0 - \bar{\alpha} p_0 \exp\omega)\epsilon_s^e \tag{3.7}$$

The form of the stored energy function results in coupled elastic volumetric and deviatoric responses, thus the first time derivative of the stress invariants is

$$\begin{Bmatrix} \dot{p}' \\ \dot{q} \end{Bmatrix} = \begin{bmatrix} D_{11}^e & D_{12}^e \\ D_{21}^e & D_{22}^e \end{bmatrix} \begin{Bmatrix} \dot{\epsilon}_v^e \\ \dot{\epsilon}_s^e \end{Bmatrix} = \begin{bmatrix} \dfrac{\partial^2 \psi}{\partial \epsilon_v^e \epsilon_v^e} & \dfrac{\partial^2 \psi}{\partial \epsilon_v^e \epsilon_s^e} \\ \dfrac{\partial^2 \psi}{\partial \epsilon_s^e \epsilon_v^e} & \dfrac{\partial^2 \psi}{\partial \epsilon_s^e \epsilon_s^e} \end{bmatrix} \begin{Bmatrix} \dot{\epsilon}_v^e \\ \dot{\epsilon}_s^e \end{Bmatrix} \tag{3.8}$$

where, $\boldsymbol{D}^e$ is a 2×2 Hessian matrix of ψ given explicitly, we have individually

$$\begin{aligned} D_{11}^e &= -\frac{p'_0}{\tilde{\kappa}} \exp\,\omega \left[1 + \frac{3\bar{\alpha}}{2\tilde{\kappa}}(\epsilon_s^e)^2\right], \qquad D_{22}^e = 3\mu_0 - 3\bar{\alpha}\, p'_0 \exp\,\omega \\ D_{12}^e &= \frac{3p'_0\,\bar{\alpha}\epsilon_s^e}{\tilde{\kappa}} \exp\,\omega \qquad\qquad\qquad , \qquad D_{21}^e = D_{12}^e \end{aligned} \tag{3.9}$$

where K is the elastic bulk modulus ($= D_{11}^e$) depended on a linear function of p' in equation (3.7). The condition of $\mu_0 = 0$ and $\bar{\alpha} \neq 0$ mean nonlinear elasticity model in which the volumetric and

deviatoric elastic responses are fully coupled. Thus, we can obtain the desired elasticity model in which the elastic shear modulus increases linearly with the effective mean normal stress.

The tangential elasticity tensor generated by the coupled nonlinear elasticity model described above is

$$\dot{\boldsymbol{\sigma}}' = \boldsymbol{c}^e : \dot{\boldsymbol{\epsilon}}^e = \dot{p}'\mathbf{1} + \sqrt{\frac{2}{3}}\,\dot{q}\hat{\boldsymbol{n}} + \sqrt{\frac{2}{3}}\,q\dot{\hat{\boldsymbol{n}}} \tag{3.10}$$

$$\dot{\hat{\boldsymbol{n}}} = \frac{\mathrm{d}}{\mathrm{d}t}\left(\frac{\boldsymbol{e}^e}{||\boldsymbol{e}^e||}\right) = \frac{1}{||\boldsymbol{e}^e||}(\mathbf{I} - \hat{\boldsymbol{n}} \otimes \hat{\boldsymbol{n}}) : \dot{\boldsymbol{e}}^e \tag{3.11}$$

where, $\dot{\hat{\boldsymbol{n}}}$ is the time variation of second-order tensor $\hat{\boldsymbol{n}}$, $\mathbf{I}$ is the rank-four identity tensor defined such that $\mathrm{I}_{ijkl} = (\delta_{ik}\delta_{jl} + \delta_{il}\delta_{jk})/2$. Substituting equation (3.11) and the constitutive equation (3.8) in equation (3.10) then tangential elasticity tensor is as follow

$$\boldsymbol{c}^e = \left(D^e_{11} - \frac{2q}{9\epsilon^e_s}\right)\mathbf{1} \otimes \mathbf{1} + \sqrt{\frac{2}{3}}\,D^e_{12}(\mathbf{1} \otimes \hat{\boldsymbol{n}} + \hat{\boldsymbol{n}} \otimes \mathbf{1}) + \frac{2q}{3\epsilon^e_s}(\boldsymbol{I} - \hat{\boldsymbol{n}} \otimes \hat{\boldsymbol{n}}) + \frac{2}{3}D^e_{22}\hat{\boldsymbol{n}} \otimes \hat{\boldsymbol{n}} \tag{3.12}$$

3.1.2 Saturated Cam-clay plasticity model

Generally, plasticity model consists of a yield function, a flow rule, and a hardening law. Cam-clay model is demonstrated as a two-invariant yield function of the form

$$F = F(p', q, p'_c) = \frac{q^2}{M^2} + p'(p' - p'_c) = 0 \tag{3.13}$$

where p' and q are the mean and deviatoric effective stresses, respectively.

$$p' = \frac{1}{3}\mathrm{tr}(\boldsymbol{\sigma}'), \quad q = \sqrt{\frac{3}{2}}||\mathbf{s}||, \quad \mathbf{s} = \boldsymbol{\sigma}' - p'\mathbf{1} \tag{3.14}$$

where $\boldsymbol{\sigma}'$ is the effective Cauchy stress tensor with its deviatoric component $\mathbf{s}$.

We assume that the small strain rate tensor $\dot{\boldsymbol{\epsilon}}$ can be decomposed into an elastic and a plastic portion,

$$\dot{\boldsymbol{\epsilon}} = \dot{\boldsymbol{\epsilon}}^e + \dot{\boldsymbol{\epsilon}}^p = \dot{\boldsymbol{\epsilon}}^e + \dot{\gamma}\,\frac{\partial F}{\partial \boldsymbol{\sigma}'} \tag{3.15}$$

For the case of a two-invariant yield function of the equation (3.13), the stress derivative yield function is

$$\frac{\partial F}{\partial \boldsymbol{\sigma}'} = \frac{1}{3}\left(\frac{\partial F}{\partial p'}\right)\mathbf{1} + \sqrt{\frac{3}{2}}\left(\frac{\partial F}{\partial q}\right)\hat{\boldsymbol{n}}\,, \qquad \frac{\partial F}{\partial p'} = 2p' - p'_c\,, \quad \frac{\partial F}{\partial q} = \frac{2q}{M^2} \tag{3.16}$$

The consistency parameter $\dot{\gamma}$ and the yield function F satisfy the Kuhn-Tucker consistency conditions $\dot{\gamma} \geq 0$, $F(p', q, p'_c) \leq 0$, and $\dot{\gamma}F = 0$.

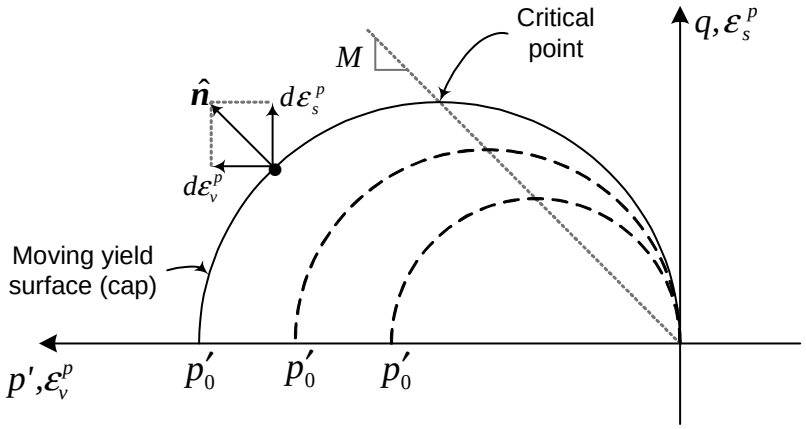

Figure 3.1: Yield locus in $p' - q$ space of saturated Cam-clay model

Bilogarithmic compressibility law

The yield function defines the ellipsoid of the modified Cam-clay model. The aspect ratio of this ellipsoid is controlled by the material parameter M (the slope of the critical state line), while its size is described by the state variable p'_c, called the preconsolidation effective pressure. The growth of the preconsolidation pressure is conventionally defined by a linear variation of the void ratio e, the ratio between the volume of voids to the volume of the solid phase in a soil mass, with respect to the logarithm of the preconsolidation pressure p'_c. In terms of specific volume $v\,(= 1 + e)$, an equivalent hardening law for infinitesimal strain analysis takes the form[16]

$$\frac{\dot{v}}{v} = -\tilde{\lambda}\frac{\dot{p}'_c}{p'_c} \tag{3.17}$$

where $\tilde{\lambda}$ is the virgin compression index of a soil. Upon integration, the hardening law of equation (3.17) defines the following linear relationship between the specific volume v and the logarithm of p'_c

$$\ln\left(\frac{v}{v_o}\right) = 1 - \tilde{\lambda}\ln\left(\frac{p'_c}{p'_{c0}}\right) \tag{3.18}$$

Equation (3.18) now indicates a linear variation of $\ln v$ with $\ln p'_c$. Rewriting this relationship in the form

$$\frac{v}{v_0} = \left(\frac{p'_{c0}}{p'_c}\right)^{\tilde{\lambda}} \tag{3.19}$$

It shows that v can not be zero no matter how large is the value of p'_c.

Although the equation (3.18) of the bilogarithmic hardening law is useful for behaviors in the limit of small volumetric strains as well as finite deformation, hyperelastic Cam-clay model uses the natural volumetric strain, $\ln\dfrac{v}{v_0} = \ln\left(1 - \dfrac{\Delta v}{v_0}\right)$, corresponding to the nominal volumetric strain $\dfrac{\Delta v}{v_0}$ of the infinitesimal theory, where $\Delta v = v_0 - v$. This bilogarithmic hardening law is verified that it is more accurate than the unilogarithmic compressibility equation by experimental data from more compressible soils undergoing virgin consolidation[19].

3.1.3 Nonlinear numerical integration of Cam-clay model

For nonlinear numerical integration of saturated hyperelasto-plasticity Cam-clay model, the integrated flow rule in the strain invariant space takes the form (leaving off $n+1$ subscript)[16],

$$\begin{aligned} \Delta\gamma &= \Delta t\,\dot{\gamma} \\ \epsilon_v^e &= \epsilon_v^{e,tr} - \Delta\gamma\frac{\partial F}{\partial p'} \\ \epsilon_s^e &= \epsilon_s^{e,tr} - \Delta\gamma\frac{\partial F}{\partial q} \end{aligned} \tag{3.20}$$

where time t_{n+1} is implied, and the elastic strains are

$$\begin{aligned} \epsilon_v^e &= \epsilon_{ii}^e = \epsilon_{ii}^{e,tr} - \Delta\gamma\left(\frac{\partial F}{\partial \sigma_{ii}}\right) = \epsilon_v^{e,tr} - \Delta\gamma(2p' - p'_c) \\ &= \epsilon_v^{e,tr} - \Delta\gamma\frac{\partial F}{\partial p'} \end{aligned} \tag{3.21}$$

$$\epsilon_s^e = \sqrt{\frac{2}{3}}\sqrt{e_{ab}^e e_{ab}^e} = \sqrt{\frac{2}{3}}\,||\boldsymbol{e}^{e,tr}|| - \Delta\gamma\frac{\partial F}{\partial q} = \epsilon_s^{e,tr} - \Delta\gamma\frac{\partial F}{\partial q} \tag{3.22}$$

$$\begin{aligned} e_{ab}^e &= \epsilon_{ab}^e - \frac{1}{3}\epsilon_{ii}^e\delta_{ab} = \epsilon_{ab}^{e,tr} - \Delta\gamma\frac{\partial F}{\partial \sigma_{ab}} - \frac{1}{3}\left(\epsilon_{ii}^{e,tr} - \Delta\gamma\frac{\partial F}{\partial \sigma_{ii}}\right)\delta_{ab} \\ &= \epsilon_{ab}^{e,tr} - \frac{1}{3}\epsilon_{ii}^{e,tr}\delta_{ab} - \Delta\gamma\left(\frac{\partial F}{\partial \sigma_{ab}} - \frac{1}{3}\frac{\partial F}{\partial \sigma_{ii}}\delta_{ab}\right) \\ &= e_{ab}^{e,tr} - \Delta\gamma\frac{\partial F}{\partial s_{ab}} \end{aligned}$$

$$\begin{aligned} e_{ab}^{e,tr}e_{ab}^{e,tr} &= \left(e_{ab}^{e,tr} - \Delta\gamma\,\frac{\partial F}{\partial s_{ab}}\right)\left(e_{ab}^{e,tr} - \Delta\gamma\,\frac{\partial F}{\partial s_{ab}}\right) \\ &= e_{ab}^{e,tr}e_{ab}^{e,tr} - 2e_{ab}^{e,tr}\Delta\gamma\,\frac{\partial F}{\partial s_{ab}} + (\Delta\gamma)^2\frac{\partial F}{\partial s_{ab}}\frac{\partial F}{\partial s_{ab}} \\ &= ||\boldsymbol{e}^{e,tr}||^2 - 2e_{ab}^{e,tr}\Delta\gamma\frac{\partial F}{\partial q}\sqrt{\frac{3}{2}}\,\hat{n}_{ab} + (\Delta\gamma)^2\frac{3}{2}\left(\frac{\partial F}{\partial q}\right)^2\hat{n}_{ab}\,\hat{n}_{ab} \\ &= ||\boldsymbol{e}^{e,tr}||^2 - 2e_{ab}^{e,tr}\Delta\gamma\frac{\partial F}{\partial q}\sqrt{\frac{3}{2}}\,\frac{e_{ab}^e}{||\boldsymbol{e}^e||} + (\Delta\gamma)^2\frac{3}{2}\left(\frac{\partial F}{\partial q}\right)^2\frac{e_{ab}^e\,e_{ab}^e}{||\boldsymbol{e}^e||^2} \\ &= ||\boldsymbol{e}^{e,tr}||^2 - 2\Delta\gamma\frac{\partial F}{\partial q}\sqrt{\frac{3}{2}}\,||\boldsymbol{e}^{e,tr}|| + (\Delta\gamma)^2\frac{3}{2}\left(\frac{\partial F}{\partial q}\right)^2 \\ &= \left(||\boldsymbol{e}^{e,tr}|| - \Delta\gamma\frac{\partial F}{\partial q}\sqrt{\frac{3}{2}}\right)^2 \end{aligned}$$

The consistency condition is imposed by the yield function in terms of the elastic strain invariants as,

$$\begin{aligned} &F\Big[p'(\epsilon_v^e,\epsilon_s^e), q(\epsilon_v^e,\epsilon_s^e), p_c'\Big] = \frac{q^2}{M^2} + p'(p'-p_c') = 0 \\ &p_c' = p_{c,n}'\exp\left(\frac{\epsilon_v^p - \epsilon_{v,n}^p}{\lambda-\kappa}\right) = p_{c,n}'\exp\left(\frac{\epsilon_v^{e,tr} - \epsilon_v^e}{\lambda-\kappa}\right) \end{aligned} \tag{3.23}$$

Three equations relative to elastic volumetric strain ϵ_v^e, deviatoric strain ϵ_s^e, and yield function F can be viewed as a system of three nonlinear equations with three unknowns (ϵ_v^e, ϵ_s^e, $\Delta\gamma$). The evolution of p_c' can be developed from the bilogarithmic compressibility in equation 3.17, and $p_{c,n}'$ is the converged value of p_c' at time step t_n. Then, the matrix $\dfrac{\partial \mathbf{R}}{\partial \mathbf{x}}$ (3×3) can be calculated by using the static condensation technique with the linearized system, which solve the problem of the matrix size.

The Backward Euler integrated evolution equations for the volumetric and deviatoric strain, and plastic multiplier are written in residual form

$$\mathbf{R}(\mathbf{x}) = \mathbf{0}\ , \quad \mathbf{x} = \begin{bmatrix} \epsilon_v^e \\ \epsilon_s^e \\ \Delta\gamma \end{bmatrix}\ , \quad \mathbf{R}\Big(\mathbf{x}^{k+1}\Big) \approx \mathbf{0}$$

$$\mathbf{R}\Big(\mathbf{x}^k\Big) + \left(\frac{\partial \mathbf{R}}{\partial \mathbf{x}}\right)^k \delta\mathbf{x} \approx \mathbf{0} \quad \Longrightarrow \quad \therefore \delta\mathbf{x} = -\left[\left(\frac{\partial \mathbf{R}}{\partial \mathbf{x}}\right)^k\right]^{-1} \cdot \mathbf{R}(\mathbf{x}^k) \tag{3.24}$$

$$\mathbf{x}^{k+1} = \mathbf{x}^k + \delta\mathbf{x}$$

$$\frac{||\mathbf{R}(\mathbf{x}^{k+1})||}{||\mathbf{R}(\mathbf{x}^0)||} \ < \ \text{tol.}(10^{-8})$$

These equations are linearized for solution by the Newton-Raphson method. The integrated flow rule in strain invariant space can be viewed as a system of three nonlinear equations in three unknowns, namely ϵ_v^e, ϵ_s^e, and $\Delta\gamma$ $\Big[$leave off $(\cdot)_{n+1}\Big]$.

$$\mathbf{R}(\mathbf{x}) = \begin{bmatrix} R_v \\ R_s \\ R_F \end{bmatrix} = \begin{bmatrix} \epsilon_v^e - \epsilon_v^{e,tr} + \Delta\gamma \dfrac{\partial F}{\partial p'} \\ \epsilon_s^e - \epsilon_s^{e,tr} + \Delta\gamma \dfrac{\partial F}{\partial q} \\ \dfrac{q^2}{M^2} + p'(p' - p_c') \end{bmatrix} = \mathbf{0} \tag{3.25}$$

The elastic volumetric strain ϵ_v^e and deviatoric strain ϵ_s^e derivatives for mean stress p' and deviatoric stress q,

$$
\begin{aligned}
\frac{\partial p'}{\partial \epsilon_v^e} &= p'_0 \beta \exp\omega \left(-\frac{1}{\tilde{\kappa}}\right)(1) = -\frac{p}{\tilde{\kappa}} \\
\frac{\partial p'}{\partial \epsilon_s^e} &= p'_0 \exp\omega \, \frac{\partial \beta}{\partial \epsilon_s^e} = \frac{3\alpha\, \epsilon_s^e}{\tilde{\kappa}} p'_0 \exp\omega \\
\frac{\partial q}{\partial \epsilon_v^e} &= 3\epsilon_s^e \frac{\partial \mu}{\partial \epsilon_v^e} = \frac{3\epsilon_s^e \alpha}{\tilde{\kappa}} p'_0 \exp\omega = \frac{\partial p'}{\partial \epsilon_s^e} \\
\frac{\partial q}{\partial \epsilon_s^e} &= 3\mu \\
\frac{\partial p'_c}{\partial \epsilon_v^e} &= (p'_c)_n \exp\left[\frac{-(\epsilon_v^{e,tr} - \epsilon_v^e)}{\tilde{\lambda} - \tilde{\kappa}}\right]\left(\frac{1}{\tilde{\lambda} - \tilde{\kappa}}\right)
\end{aligned}
\tag{3.26}
$$

The matrix $\dfrac{\partial \mathbf{R}}{\partial \mathbf{x}}$ (3×3) for the static condensation is

$$
\begin{aligned}
\frac{\partial \mathbf{R}}{\partial \mathbf{x}} &= \begin{bmatrix}
\dfrac{\partial R_v}{\partial \epsilon_v^e} & \dfrac{\partial R_v}{\partial \epsilon_s^e} & \dfrac{\partial R_v}{\partial \Delta\gamma} \\
\dfrac{\partial R_s}{\partial \epsilon_v^e} & \dfrac{\partial R_s}{\partial \epsilon_s^e} & \dfrac{\partial R_s}{\partial \Delta\gamma} \\
\dfrac{\partial R_F}{\partial \epsilon_v^e} & \dfrac{\partial R_F}{\partial \epsilon_s^e} & \dfrac{\partial R_F}{\partial \Delta\gamma}
\end{bmatrix} \\
&= \begin{bmatrix}
1 + \Delta\gamma\left(2\dfrac{\partial p'}{\partial \epsilon_v^e} - \dfrac{\partial p'_c}{\partial \epsilon_v^e}\right) & \Delta\gamma\, 2\dfrac{\partial p'}{\partial \epsilon_s^e} & \dfrac{\partial F}{\partial p'} \\
\Delta\gamma\, \dfrac{2}{M^2}\dfrac{\partial q}{\partial \epsilon_v^e} & 1 + \Delta\gamma\, \dfrac{2}{M^2}\dfrac{\partial q}{\partial \epsilon_s^e} & \dfrac{\partial F}{\partial q} \\
\dfrac{\partial F}{\partial p'}\dfrac{\partial p'}{\partial \epsilon_v^e} + \dfrac{\partial F}{\partial q}\dfrac{\partial q}{\partial \epsilon_v^e} + \dfrac{\partial F}{\partial p'_c}\dfrac{\partial p'_c}{\partial \epsilon_v^e} & \dfrac{\partial F}{\partial p'}\dfrac{\partial p'}{\partial \epsilon_s^e} + \dfrac{\partial F}{\partial q}\dfrac{\partial q}{\partial \epsilon_s^e} & 0
\end{bmatrix}
\end{aligned}
\tag{3.27}
$$

Therefore,

$$
\delta \mathbf{x} =
$$

$$
-\begin{bmatrix}
1 + \Delta\gamma\left(2\dfrac{\partial p'}{\partial \epsilon_v^e} - \dfrac{\partial p'_c}{\partial \epsilon_v^e}\right) & \Delta\gamma\, 2\dfrac{\partial p'}{\partial \epsilon_s^e} & \dfrac{\partial F}{\partial p'} \\
\Delta\gamma\, \dfrac{2}{M^2}\dfrac{\partial q}{\partial \epsilon_v^e} & 1 + \Delta\gamma\, \dfrac{2}{M^2}\dfrac{\partial q}{\partial \epsilon_s^e} & \dfrac{\partial F}{\partial q} \\
\dfrac{\partial F}{\partial p'}\dfrac{\partial p'}{\partial \epsilon_v^e} + \dfrac{\partial F}{\partial q}\dfrac{\partial q}{\partial \epsilon_v^e} + \dfrac{\partial F}{\partial p'_c}\dfrac{\partial p'_c}{\partial \epsilon_v^e} & \dfrac{\partial F}{\partial p'}\dfrac{\partial p'}{\partial \epsilon_s^e} + \dfrac{\partial F}{\partial q}\dfrac{\partial q}{\partial \epsilon_s^e} & 0
\end{bmatrix}^{-1}
\begin{bmatrix}
\epsilon_v^e - \epsilon_v^{e,tr} + \Delta\gamma \dfrac{\partial F}{\partial p'} \\
\epsilon_s^e - \epsilon_s^{e,tr} + \Delta\gamma \dfrac{\partial F}{\partial q} \\
\dfrac{q^2}{M^2} + p'(p' - p'_c)
\end{bmatrix}
\tag{3.28}
$$

To take advantage of $\dfrac{\partial R_F}{\partial \Delta\gamma} = 0$, we can conduct a static condensation by writing,

$$\begin{aligned}
&\begin{bmatrix} R_v \\ R_s \\ R_F \end{bmatrix} + \begin{bmatrix} \begin{bmatrix} \dfrac{\partial R_v}{\partial \epsilon_v^e} & \dfrac{\partial R_v}{\partial \epsilon_s^e} \\ \dfrac{\partial R_s}{\partial \epsilon_v^e} & \dfrac{\partial R_s}{\partial \epsilon_s^e} \end{bmatrix} & \begin{bmatrix} \dfrac{\partial R_v}{\partial \Delta\gamma} \\ \dfrac{\partial R_s}{\partial \Delta\gamma} \end{bmatrix} \\ \begin{bmatrix} \dfrac{\partial R_F}{\partial \epsilon_v^e} & \dfrac{\partial R_F}{\partial \epsilon_s^e} \end{bmatrix} & 0 \end{bmatrix} \begin{bmatrix} \delta\epsilon_v^e \\ \delta\epsilon_s^e \\ \delta(\Delta\gamma) \end{bmatrix} \\
&= \begin{bmatrix} R_v \\ R_s \\ R_F \end{bmatrix} + \begin{bmatrix} \overset{2\times 2}{\begin{bmatrix} \mathbf{A} \end{bmatrix}} & \overset{2\times 1}{\begin{bmatrix} \mathbf{B} \end{bmatrix}} \\ \overset{1\times 2}{\begin{bmatrix} \mathbf{C} \end{bmatrix}} & 0 \end{bmatrix} \begin{bmatrix} \delta\epsilon_v^e \\ \delta\epsilon_s^e \\ \delta(\Delta\gamma) \end{bmatrix} = \begin{bmatrix} 0 \\ 0 \\ 0 \end{bmatrix}
\end{aligned} \tag{3.29}$$

For iteration k, rewrite the first two equations as,

$$\begin{aligned}
\begin{bmatrix} R_v \\ R_s \end{bmatrix} + \begin{bmatrix} \mathbf{A} \end{bmatrix} \begin{bmatrix} \delta\epsilon_v^e \\ \delta\epsilon_s^e \end{bmatrix} + \begin{bmatrix} \mathbf{B} \end{bmatrix} \delta(\Delta\gamma) = \mathbf{0} \\
R_F + \begin{bmatrix} \mathbf{C} \end{bmatrix} \begin{bmatrix} \delta\epsilon_v^e \\ \delta\epsilon_s^e \end{bmatrix} = 0
\end{aligned} \tag{3.30}$$

Let's multiply equation (3.30) by $\left[\mathbf{A}\right]^{-1}$

$$\begin{aligned}
\begin{bmatrix} \mathbf{A} \end{bmatrix}^{-1} \begin{bmatrix} R_v \\ R_s \end{bmatrix} + \begin{bmatrix} \delta\epsilon_v^e \\ \delta\epsilon_s^e \end{bmatrix} + \delta(\Delta\gamma) \begin{bmatrix} \mathbf{A} \end{bmatrix}^{-1} \begin{bmatrix} \mathbf{B} \end{bmatrix} = \mathbf{0} \\
\delta(\Delta\gamma) \begin{bmatrix} \mathbf{A} \end{bmatrix}^{-1} \begin{bmatrix} \mathbf{B} \end{bmatrix} = - \begin{bmatrix} \mathbf{A} \end{bmatrix}^{-1} \begin{bmatrix} R_v \\ R_s \end{bmatrix} - \begin{bmatrix} \delta\epsilon_v^e \\ \delta\epsilon_s^e \end{bmatrix}
\end{aligned} \tag{3.31}$$

By multipling by $\left[\mathbf{C}\right]$ on both sides,

$$\delta(\Delta\gamma) \begin{bmatrix} \overset{1\times 2}{\mathbf{C}} \end{bmatrix} \begin{bmatrix} \overset{2\times 2}{\mathbf{A}} \end{bmatrix}^{-1} \begin{bmatrix} \overset{2\times 1}{\mathbf{B}} \end{bmatrix} = - \begin{bmatrix} \overset{1\times 2}{\mathbf{C}} \end{bmatrix} \begin{bmatrix} \overset{2\times 2}{\mathbf{A}} \end{bmatrix}^{-1} \begin{bmatrix} R_v \\ R_s \end{bmatrix} \underbrace{- \begin{bmatrix} \mathbf{C} \end{bmatrix} \begin{bmatrix} \delta\epsilon_v^e \\ \delta\epsilon_s^e \end{bmatrix}}_{+R_F} \tag{3.32}$$

Therefore, we have the scalar equation of plastic multiplier $\delta(\Delta\gamma)$,

$$\delta(\Delta\gamma) = \frac{-\left[\ \mathbf{C}\ \right]\left[\ \mathbf{A}\ \right]^{-1}\begin{bmatrix} R_v \\ \\ R_s \end{bmatrix} + R_F}{\left[\ \mathbf{C}\ \right]\left[\ \mathbf{A}\ \right]^{-1}\left[\ \mathbf{B}\ \right]} \tag{3.33}$$

Then, solving for volumetric and deviatoric strain from equation (3.31),

$$\begin{bmatrix} \delta\epsilon_v^e \\ \\ \delta\epsilon_s^e \end{bmatrix} = -\left[\ \mathbf{A}\ \right]^{-1}\left(\begin{bmatrix} R_v \\ \\ R_s \end{bmatrix} + \delta(\Delta\gamma)\left[\ \mathbf{B}\ \right]\right) \tag{3.34}$$

Update;

$$(\epsilon_v^e)^{k+1} = (\epsilon_v^e)^k + \delta\epsilon_v^e \tag{3.35}$$

$$(\epsilon_s^e)^{k+1} = (\epsilon_s^e)^k + \delta\epsilon_s^e \tag{3.36}$$

$$(\Delta\gamma)^{k+1} = (\Delta\gamma)^k + \delta(\Delta\gamma) \tag{3.37}$$

Update $\mathbf{R}(\mathbf{x}^{k+1})$ and check $\dfrac{\mathbf{R}(\mathbf{x}^{k+1})}{\mathbf{R}(\mathbf{x}^0)} <$ tolerance.

Once the elastic invariant strains ϵ_v^e and ϵ_s^e have been determined, the effective stress tensor σ'_{ij} can be evaluated from the hyperelastic constitutive equation in equation (3.6).

Continuum elastoplastic tangent

Ideally, the consistent tangent $\left(\dfrac{\partial\boldsymbol{\sigma}'}{\partial\boldsymbol{\epsilon}}\right)_{n+1}$ is derived, and this will be done for future work to obtain global quadratic convergence. For now, for simplicity, we use the continuum elastoplastic tangent instead. To determine the continuum elastoplastic tangent for hyperelasto-plasticity Cam-clay model, we start by recalling the stress-strain relationship,

$$\begin{aligned}
&\dot{\boldsymbol{\sigma}}' = \boldsymbol{c}^e : \dot{\boldsymbol{\epsilon}}^e, \qquad \boldsymbol{c}^e = \frac{\partial \boldsymbol{\sigma}'}{\partial \boldsymbol{\epsilon}^e} \qquad \text{for hyperelasticity} \\
&\dot{\boldsymbol{\epsilon}}^e = \dot{\boldsymbol{\epsilon}} - \dot{\boldsymbol{\epsilon}}^p, \quad \dot{\boldsymbol{\epsilon}}^p = \dot{\gamma}\frac{\partial F}{\partial \boldsymbol{\sigma}'}, \quad \frac{\partial F}{\partial \boldsymbol{\sigma}'} = \frac{2q}{M^2}\sqrt{\frac{3}{2}}\,\hat{\boldsymbol{n}} + (2p' - p'_c)\frac{1}{3}\,\mathbf{1}
\end{aligned} \tag{3.38}$$

Thus,

$$\dot{\boldsymbol{\sigma}}' = \boldsymbol{c}^{ep} : \dot{\boldsymbol{\epsilon}}, \qquad \boldsymbol{c}^{ep} \quad \text{is elastoplastic tangent} \tag{3.39}$$

For time derivative yield function,

$$\begin{aligned}
F &= \left(\frac{q}{M^2}\right)^2 + p'(p' - p'_c) \\
\dot{F} &= 0 \\
&= \frac{\partial F}{\partial \boldsymbol{\sigma}'} : \dot{\boldsymbol{\sigma}}' + \frac{\partial F}{\partial p'_c}\,\dot{p}'_c
\end{aligned} \tag{3.40}$$

Substitute flow rule by plastic multiplier $\dot{\gamma}$,

$$\dot{\boldsymbol{\sigma}}' = \boldsymbol{c}^e : \left(\dot{\boldsymbol{\epsilon}} - \dot{\gamma}\,\frac{\partial F}{\partial \boldsymbol{\sigma}'}\right)$$

Time derivative of preconsolidation pressure p'_c is

$$\begin{aligned}
p'_c &= (p'_c)_n \exp\left[\frac{-(\epsilon_v^p - (\epsilon_v^p)_n)}{\tilde{\lambda} - \tilde{\kappa}}\right] \\
\dot{p}'_c &= (p'_c)_n \exp\left[\frac{-(\epsilon_v^p - (\epsilon_v^p)_n)}{\tilde{\lambda} - \tilde{\kappa}}\right]\left(\frac{-1}{\tilde{\lambda} - \tilde{\kappa}}\right)\dot{\epsilon}_v^p \\
&= \dot{\gamma}\, h^{p_c}
\end{aligned} \tag{3.41}$$

where

$$\dot{\epsilon}_v^p = \operatorname{tr}(\dot{\boldsymbol{\epsilon}}^p) = \dot{\gamma}\operatorname{tr}\left(\frac{\partial F}{\partial \boldsymbol{\sigma}'}\right) = \dot{\gamma}\,(2p' - p'_c)$$

$$h^{p_c} = (p'_c)_n \exp\left[\frac{-(\epsilon_v^p - (\epsilon_v^p)_n)}{\tilde{\lambda} - \tilde{\kappa}}\right]\left(\frac{-1}{\tilde{\lambda} - \tilde{\kappa}}\right)(2p' - p'_c)$$

Time derivative of yield function is

$$\begin{aligned}
\dot{F} &= \frac{\partial F}{\partial \boldsymbol{\sigma}'} : \boldsymbol{c}^e : \left(\dot{\boldsymbol{\epsilon}} - \dot{\gamma} \frac{\partial F}{\partial \boldsymbol{\sigma}'} \right) + \frac{\partial F}{\partial p'_c} h^{p_c} \dot{\gamma} = 0 \\
\frac{\partial F}{\partial \boldsymbol{\sigma}'} : \boldsymbol{c}^e : \dot{\boldsymbol{\epsilon}} &- \dot{\gamma} \frac{\partial F}{\partial \boldsymbol{\sigma}'} : \boldsymbol{c}^e : \frac{\partial F}{\partial \boldsymbol{\sigma}'} + \frac{\partial F}{\partial p'_c} h^{p_c} \dot{\gamma} = 0 \\
\dot{\gamma} &= \frac{\dfrac{\partial F}{\partial \boldsymbol{\sigma}'} : \boldsymbol{c}^e : \dot{\boldsymbol{\epsilon}}}{\dfrac{\partial F}{\partial \boldsymbol{\sigma}'} : \boldsymbol{c}^e : \dfrac{\partial F}{\partial \boldsymbol{\sigma}'} - \dfrac{\partial F}{\partial p'_c} h^{p_c}}
\end{aligned} \tag{3.42}$$

Therefore, the stress-strain relationship including continuum elastoplastic tangent is,

$$\begin{aligned}
\dot{\boldsymbol{\sigma}}' &= \boldsymbol{c}^e : \dot{\boldsymbol{\epsilon}} - \left(\frac{\dfrac{\partial F}{\partial \boldsymbol{\sigma}'} : \boldsymbol{c}^e : \dot{\boldsymbol{\epsilon}}}{\dfrac{\partial F}{\partial \boldsymbol{\sigma}'} : \boldsymbol{c}^e : \dfrac{\partial F}{\partial \boldsymbol{\sigma}'} - \dfrac{\partial F}{\partial p'_c} h^{p_c}} \right) \boldsymbol{c}^e : \frac{\partial F}{\partial \boldsymbol{\sigma}'} \\
&= \underbrace{\left(\boldsymbol{c}^e - \frac{1}{\chi^{ep}} \boldsymbol{c}^e : \frac{\partial F}{\partial \boldsymbol{\sigma}'} \otimes \frac{\partial F}{\partial \boldsymbol{\sigma}'} : \boldsymbol{c}^e \right)}_{\boldsymbol{c}^{ep}} : \dot{\boldsymbol{\epsilon}}
\end{aligned} \tag{3.43}$$

where

$$\chi^{ep} = \frac{\dfrac{\partial F}{\partial \boldsymbol{\sigma}'} : \boldsymbol{c}^e : \dot{\boldsymbol{\epsilon}}}{\dfrac{\partial F}{\partial \boldsymbol{\sigma}'} : \boldsymbol{c}^e : \dfrac{\partial F}{\partial \boldsymbol{\sigma}'} - \dfrac{\partial F}{\partial p'_c} h^{p_c}}$$

3.2 Cam-clay Plasticity for Partially Saturated Soil

Based on Borja[12] model, the constitutive framework of partially saturated soil should be considered the constitutive effective stress $\boldsymbol{\sigma}'$ with the evolution of solid matrix deformation $\boldsymbol{\epsilon}$, the degree of saturation S with suction stress s, the intrinsic mass densities of all three phases, and the relative flow vector $\tilde{\boldsymbol{v}}_\alpha$ with intrinsic pressure p_α for water and air phases. This model is a combination of features from other partially saturated soil constitutive models[6, 95, 84, 12, 54, 47, 35, 94, 83, 50].

3.2.1 Constitutive framework for partially saturated soils

For constitutive model for the solid matrix, a yield function of an elasto-plastic behavior is assumed as $F = F(\boldsymbol{\sigma}', s, p'_c) = 0$, where the scalar variable p'_c is the effective preconsolidation

pressure at saturated condition ($s = 0$). The rate expression for the effective constitutive stress $\boldsymbol{\sigma}'$ is

$$\dot{\boldsymbol{\sigma}}' = \mathbf{c}^e : (\dot{\boldsymbol{\epsilon}} - \dot{\gamma}\,\boldsymbol{g}), \quad \boldsymbol{g} = \frac{\partial G}{\partial \boldsymbol{\sigma}'} \tag{3.44}$$

where $\mathbf{c}^e = \partial^2\Psi/\partial\boldsymbol{\epsilon}^e\partial\boldsymbol{\epsilon}^e$ regarding the free energy function Ψ, $\dot{\boldsymbol{\epsilon}}$ is the total strain rate tensor, G is the plastic potential function, and $\dot{\gamma}$ is a plastic multiplier satisfying the Kuhn–Tucker conditions

$$\dot{\gamma} \geq 0, \quad F(\boldsymbol{\sigma}', s, p_c') \leq 0, \quad \dot{\gamma}F(\boldsymbol{\sigma}', s, p_c') = 0 \tag{3.45}$$

For preconsolidation pressure, a hardening law of the form can be written as,

$$\dot{p_c'} = \dot{\gamma}\,h(\boldsymbol{\sigma}', p_c') \tag{3.46}$$

where h is a scalar-valued function. For Modified Cam-clay model $\dot{p_c'}$ usually varies with $\dot{\gamma}$ through the volumetric component of the plastic strain, $\dot{\boldsymbol{\epsilon}}_v^p = \mathrm{tr}(\dot{\boldsymbol{\epsilon}}^p) = \dot{\gamma}\,\mathrm{tr}(\boldsymbol{g})$. The quantity h is generally a function of $\boldsymbol{\sigma}'$ and p_c'. The consistency condition can be written as

$$\dot{F} = \boldsymbol{f} : \dot{\boldsymbol{\sigma}}' + \varphi\dot{s} - H\dot{\gamma} = 0 \tag{3.47}$$

where

$$\boldsymbol{f} = \frac{\partial F}{\partial \boldsymbol{\sigma}'}, \qquad \varphi = \frac{\partial F}{\partial s}, \qquad H = -\frac{\partial F}{\partial p_c'}h(\boldsymbol{\sigma}', p_c') \tag{3.48}$$

For a constant suction stress s, the sign of plastic modulus H determines the behavior of materials, that is, H of hardening behavior is larger than 0, softening behavior is less than 0, and perfectly plastic behavior is $H = 0$.

Solving for the plastic multiplier gives

$$\dot{\gamma} = \frac{1}{\chi}(\boldsymbol{f} : \mathbf{c}^e : \dot{\boldsymbol{\epsilon}} + \varphi\,\dot{s}), \qquad \chi = \boldsymbol{f} : \mathbf{c}^e : \boldsymbol{g} + H \tag{3.49}$$

When a plastic behavior occurs, $\dot{\gamma} > 0$ and $\chi > 0$, it must be satisfied as follows,

$$\boldsymbol{f} : \mathbf{c}^e : \dot{\boldsymbol{\epsilon}} + \varphi\,\dot{s} > 0 \tag{3.50}$$

When considering both values of $\boldsymbol{f} : \mathbf{c}^e : \dot{\boldsymbol{\epsilon}}$ and $\varphi\,\dot{s}$, either of elastic or plastic process can be predicted. By solving the form for $\dot{\gamma}$, the rate constitutive equation is obtained,

$$\dot{\boldsymbol{\sigma}}' = \mathbf{c}^{ep} : \dot{\boldsymbol{\epsilon}} - \frac{1}{\chi}(\mathbf{c}^e : \boldsymbol{g})\varphi\,\dot{s} \tag{3.51}$$

where,

$$\mathbf{c}^{ep} = \mathbf{c}^e - \frac{1}{\chi}\mathbf{c}^e : \boldsymbol{g} \otimes \boldsymbol{f} : \mathbf{c}^e \tag{3.52}$$

$\mathbf{c}^{ep}$ is the elasto-plastic tangent, and if the rate of suction stress $\dot{s} = 0$ and $s = 0$ becomes, the classical elastoplastic constitutive relations for fully saturated condition return.

For the relationship relating the matric suction s to the effective degree of saturation S_e, van Genuchten[90] relation is used as,

$$S_e = \left[\frac{1}{1 + (\alpha s)^{\mathrm{n}}}\right]^{\mathrm{m}}, \qquad S = S_r + S_e(1 - S_r) \tag{3.53}$$

The relation between S and s may be affected by the air entry value (or bubbling pressure), which is the characteristic pressure required before the air enters the pores.

$$\frac{dS}{ds} = -(1 - S_r)\mathrm{m}\,\mathrm{n}\,\alpha^{\mathrm{n}}\left[1 + (\alpha s)^{\mathrm{n}}\right]^{(-\mathrm{m}-1)} s^{\mathrm{n}-1} \tag{3.54}$$

where an effective degree of saturation S_e is normalized by the fully saturated condition with the residual saturated condition S_r, thus $S_e = \dfrac{S - S_r}{1 - S_r}$, and α, n, and m are curve fitting parameters.

For the bulk modulus of three phases, the bulk moduli K_s and K_w of solid and water are assumed infinity values due to incompressible phases even though both values are available from the reference[67] of material properties. The bulk modulus K_a of the air typically depends on the temperature, but it is used by about 10^5 Pa at 20 $^{\mathrm{o}}$C as a constant for isothermal deformations of Boyle-Mariotte's law[7], i.e., $p_a V_a = p_a M_a/\rho_a$. The net change in the total air mass contained in the total volume V of the moving solid matrix is equal to zero. Hence, the bulk modulus K_a of the air phase is equal to the absolute intrinsic air pressure p_a, i.e., $K_a = p_a$.

3.2.2 Hyperelasto-plastic constitutive model

Many researchers have developed over the years to enhance the classic Cam-clay model for mechanical behavior of partially saturated soils[6, 39, 95, 91, 35, 12, 50]. Their models contain the suction stress as a partially saturated factor which influences both of the effective size of the elastic region and the amount of plastic deformation based on the classic Cam-clay plasticity model of saturated condition.

For coupling plasticity with energy conserving elasticity model, the analytical model of a free energy function follows Section 3.1, but the yield function and other forms related to suction stress s should be derived as follows[12],

$$
\begin{aligned}
F(\boldsymbol{\sigma}', s, p_c') &= \frac{q^2}{M^2} + (p' - p_s')(p' - \bar{p}_c') = 0 && (3.55)\\
p_s' &= k \cdot s && (3.56)\\
\bar{p}_c'(\boldsymbol{\epsilon}_v^p, s) &= -\exp\Big[p_a(\pi)\Big](-p_c')^{p_b(\pi)} && (3.57)
\end{aligned}
$$

where,

$$
\begin{aligned}
p_a(\pi) = \frac{\mathrm{N}[c(\pi) - 1]}{\tilde{\lambda}\, c(\pi) - \tilde{\kappa}}\,, \qquad p_b(\pi) = \frac{\tilde{\lambda} - \tilde{\kappa}}{\tilde{\lambda}\, c(\pi) - \tilde{\kappa}}\\
\pi = \left(1 + \frac{s/p_{\mathrm{atm}}}{10.7 + 2.4(s/p_{\mathrm{atm}})}\right)(1 - S)
\end{aligned}
\qquad (3.58)
$$

The yield surface has the shape of an ellipsoid in principal stress space, and critical state line M defines the geometric axis ratio of the yield surface. p_s' is the suction stress resulting from the application of the matric suction. It leads the suction-dependent critical state line to shift to the tension side[6]. k is a dimensionless material parameter that can be zero at saturated condition, and greater than zero at partially saturated condition[6]. $\bar{p}_c$ is the effective preconsolidation stress depending on the plastic volumetric strain ϵ_v^p and the matric suction s, and it has influence on the size of active yield surface depending on the applied matric suction s regardless of any plastic deformation. π is the bonding variable and varies with the air void fraction $(1 - S)$ and a suction s. p_{atm} is the atmospheric pressure, 101.3 kPa.

The function $c(\pi)$ represents the ratio between the specific volume v of the virgin compression curve in the partially saturated state and the specific volume v_{sat} in the fully saturated state. Gallipoli et al.[35] presented the ratio between the void ratio e in the partially saturated state and the void ratio e_{sat} in the fully saturated state as follow

$$\begin{aligned} \frac{e}{e_{\text{sat}}} &= 1 - \tilde{c}_1\Big[1 - \exp(c_2\pi)\Big] \\ c(\pi) = \frac{v}{v_{\text{sat}}} = \frac{1+e}{1+e_{\text{sat}}} &= \frac{1/e_{\text{sat}} + e/e_{\text{sat}}}{1/e_{\text{sat}} + 1} = 1 - c_1\Big[1 - \exp(c_2\pi)\Big] \end{aligned} \tag{3.59}$$

where, $\tilde{c}_1$ and c_2 are fitting parameters and $c_1 = \dfrac{\tilde{c}_1}{1/e_{\text{sat}} + 1}$.

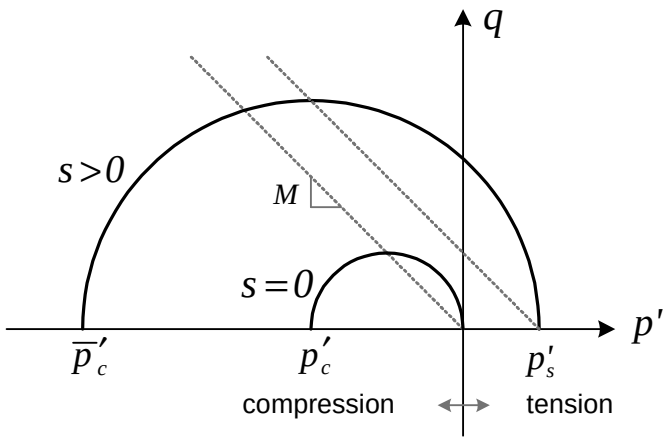

Figure 3.2: Yield surface on the $p' - q$ plane with suction s

Alonso et at.[6] proposed a non-associative flow rule based on a plastic potential function G, and then the plastic strain rate form in the partially saturated condition is written as

$$\begin{aligned} \dot{\boldsymbol{\epsilon}}^p &= \dot{\gamma}\,\frac{\partial G}{\partial \boldsymbol{\sigma}'} = \dot{\gamma}\left[\frac{1}{3}(2p' - p'_s - \bar{p}'_c)\,\mathbf{1} + \frac{2q\beta'}{M^2}\sqrt{\frac{3}{2}}\frac{\mathbf{s}}{||\mathbf{s}||}\right] \\ \beta' &= \frac{M(M-9)(M-3)}{9(6-M)}\left[\frac{1}{1-\kappa/\lambda}\right] \end{aligned} \tag{3.60}$$

where β' is a constant which can be derived by requiring that the direction of plastic strain rate for zero lateral deformation.

For the saturated condition, these functions are defined as $p_a(\pi) = 0$, $p_b(\pi) = 1$ and $c(\pi) = 1$,

and the effective preconsolidation stress $\bar{p}_c'$ is also equal to the preconsolidation stress p_c' which varies with the plastic deformation, not matric suction s.

3.3 Implementation of Effective Stress and Pore Air Pressure

The governing equations are derived based on the equations of equilibrium for triphasic mixture in Section 2.4. The coupling effect from the relationship among the water, the solid particles, and the air is identified comparing the behavior of biphasic mixture, numerical analysis and experimental results in the literature. And different expressions of the effective stress principle have been presented in the literature, for example Bishop et al.[8], Lewis and Schrefler[58], Khalili et al.[49], and Borja[12], Lu and Likos[66] and Lu et al.[63]. Various link with matric suction and degree of saturation of the soil particle for the effective stress principle is established regarding shear strength and volume change in partially saturated soils.

3.3.1 Effect of pore air pressure in triphasic mixture

The air (or gas) pore pressure in three phase porous media is generally necessary to consider for an air storage problem in an aquifer[70] and CO_2 geo-sequestration problems[56] related to CO_2 injection or gas energy exstraction via offshore structures.

In order to validate the formulation of air pore pressure in triphasic mixture, although various researchers[57, 76, 75] have simulated the experimental tests on drainage of soil column and performed numerical analysis, they premised that the it is not the exact solution for the effect of air pore pressure in partially saturated soils. The comparison between the numerical solutions and experimental data in the literature needs to acknowledge the influence of the initial conditions and the air flow assumptions on the numerical simulations.

3.3.2 Various effective stress equations of partially saturated soils

The role of effective stress in the solid skeleton is to control stress-strain relation, volume change and strength behavior in a porous medium. In the partially saturated soil, the application

of the effective stress principle is to determine the most fundamental contribution in the mechanical constitutive relationship because it participates in elastic as well as elastoplastic constitutive equations of the solid phase. Based on the concept of effective stress of Terzaghi[86] and Skempton[80] for the saturated soils, the effective stress principle of the partially saturated soil has been evaluated by Bishop[8], Lewis and Schrefler[58], Khalili et al.[49], Borja[17], and Lu et al.[63], among others.

The form used for effective stress principle in the partially saturated soils was first developed by Bishop[8] using effective stress parameter χ,

$$\begin{aligned} \boldsymbol{\sigma}' &= \boldsymbol{\sigma} + p_a\mathbf{1} - \chi(p_a - p_w)\mathbf{1} \\ &= \boldsymbol{\sigma} + \chi p_w\mathbf{1} + (1-\chi)p_a\mathbf{1} \end{aligned} \tag{3.61}$$

where consistent with our sign convention, $\boldsymbol{\sigma}'$ and $\boldsymbol{\sigma}$ are positive is tension ($p' = \frac{1}{3}\,\mathrm{tr}(\boldsymbol{\sigma}')$ and $p = \frac{1}{3}\,\mathrm{tr}(\boldsymbol{\sigma}) > 0$ tension) and p_w and p_a are positive in compression (p_w and $p_a > 0$ compression) such that suction $s = p_w - p_a$ is positive or 0, i.e., $s \geq 0$.

Bishop takes into account the surface tension $(p_a - p_w)$ to extend Terzaghi's effective stress of saturation condition. For the experimental evidence of equation (3.61), Bishop and Blight[9] provided experimental results to support the validity of Bishop's effective stress with χ, to be determined experimentally. It is substituted for the degree of saturation ($\chi = S$) of the soil by some researchers based on thermodynamic arguments[58, 12]. But, in Bishop's effective stress concept, the shear strength and volumetric characteristics do not change when the individual components of the effective stress vary because both of the net stress $(\boldsymbol{\sigma} + p_a\mathbf{1})$ and matric suction $(p_a - p_w)$ keep at a constant value.

Lewis and Schrefler[58] assumed that external and internal water pressure p_w causes only a uniform, volumetric strain by compressing the solid skeletons. They also assumed that the main deformation of the solid skeleton is governed by the effective stress $\boldsymbol{\sigma}'$. They replaced Bishop's parameter χ by the degree of saturation S, i.e. the ratio between pore space occupied by water and total pore space available, thus assumes the following form

$$\boldsymbol{\sigma}' = \boldsymbol{\sigma} + \Big[Sp_w + S_{(a)}p_a\Big]\mathbf{1} \tag{3.62}$$

where non-wetting phase saturation $S_{(a)} = 1 - S$ using volume average for the bulk materials. Its form has been often used to estimate the effective stress in partially saturated soil at small strain by many researchers.

Recently, to address shortcoming of Bishop's effective stress principle, Khalili et al.[49] proposed the effective stress principle adequate for shear strength as well as volumetric change of partially saturated soils. They also provided experimental evidence to support the validity of the effective stress equation and derived the incremental form of it. From Bishop's effective stress in equation (3.61), the effective stress parameter χ was obtained using the best-fit relationship as shown in Figure 3.3.

$$\chi = \begin{cases} \left(\dfrac{s}{s_e}\right)^{-0.55} & \text{if} \quad s \geq s_e \\ 1 & \text{if} \quad s \leq s_e \end{cases} \tag{3.63}$$

where, s_e is the air expulsion value s_{ex} for wetting processes or the air entry value s_{ae} for drying processes of SWCC.

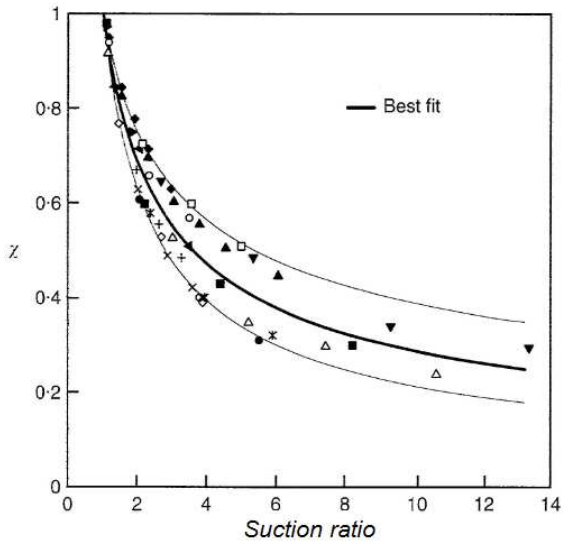

Figure 3.3: Effective stress parameter χ versus suction ratio s/s_{ae}

In Figure 3.3, the suction ratio is the ratio of matric suction s over the air entry value s_{ae} and it may be obtained for most soils as a unique relationship. When the effective stress is applied in partially saturated soils, the difference between the total and incremental forms of the effective stress equation occurs. Its total form is proceeded by calculating stress-path-independent quantities, for example shear strength or volume change in linearly elastic materials, whereas its incremental form is performed in path-dependent processes by using tangent material properties.

$$\begin{aligned} \boldsymbol{\sigma}' &= \boldsymbol{\sigma} + p_a\mathbf{1} - \chi\, s\mathbf{1} = \boldsymbol{\sigma}_{net} - \chi\, s\mathbf{1} \\ \mathrm{d}\boldsymbol{\sigma}' &= \mathrm{d}\boldsymbol{\sigma}_{net} - (s\,\mathrm{d}\chi + \chi\,\mathrm{d}s)\mathbf{1} = \mathrm{d}\boldsymbol{\sigma}_{net} - 0.45\chi\,\mathrm{d}s \end{aligned} \tag{3.64}$$

where, $\boldsymbol{\sigma}_{net} = \boldsymbol{\sigma} + p_a\mathbf{1}$ and 0.45χ is the result obtained by substituting for χ of equation (3.63).

Borja and White[17] suggested the effective stress equation for partially saturated porous material. It is demonstrated this expression for the constitutive stress tensor to be energy-conjugate to the solid rate of deformation[13, 14] but this form is similar to Bishop's effective stress equation when assumed as incompressible solid grains ($K_s \to \infty$).

$$\boldsymbol{\sigma}' = \boldsymbol{\sigma} + \left(1 - \frac{K}{K_s}\right)\bar{p}\,\mathbf{1}, \quad \bar{p} = Sp_w + (1-S)p_a \tag{3.65}$$

where K and K_s are the elastic bulk moduli for the solid skeleton matrix and solid constituent, respectively. The ratio K/K_s is typically in the range 0.1-0.5 for saturated rocks and concrete[80] and so, Biot's coefficient B represents $(1 - K/K_s)$. Actually, the ratio is very small for soils, and so it is customary to take B=1, i.e., $K_s \gg K$. They used this ratio in the critical state soil mechanic problem which can predict an initial stress condition within the slope that lies on the dilatant side of the critical state line[17].

Lu et al.[66, 63] presented the concept of a suction stress characteristic curve (SSCC) for a partially saturated soil. The SSCC can represent the effective stress behavior to describe the state of stress in partially saturated soil. In a microscopic stress, the physical origin of suction stress can be conceptualized in the forms of van der Waals attraction, electrical double-layer repulsion, surface tension, and physical and chemical force of the soil-water system[66]. On the other hand, the suction stress can be represented as the tensile stress concept in a macroscopic stress. The

Table 3.1: van Genuchten[90]'s curve fitting parameters of three soils

Soil	α(1/kPa)	n
Loam	0.2	2.76
Silt	0.0432	2.06
Clay	0.0152	1.17

Note: m=1-1/n

isotropic tensile strength projected from a linear extension of the Mohr-Coulomb failure criterion can be used for formulating suction stress. Thus the isotropic tensile strength can unify shear strength behaviors obtained from various suction conditions onto the Mohr-Coulomb criterion[64].

Lu et al.[66, 63] proposed a form of suction stress as the extension of Terzaghi's effective stress σ' (positive in tension) in saturated condition,

$$\begin{aligned} \sigma' &= (\sigma + p_a) + \sigma^s \\ \sigma^s &= -S_e\,(p_a - p_w), \quad S_e = \frac{S - S_r}{1 - S_r} = \Big[1 + (\alpha s)^{\mathrm{n}}\Big]^{-\mathrm{m}} \end{aligned} \tag{3.66}$$

where S_e is effective degree of saturation, s is matric suction $(p_a - p_w)$, and α, n, m are curve fitting parameters of van Genuchten[90]'s SWCC equation. The effective stress (equation (3.66)) is defined as a closed-form expression for suction stress for the full range of matric suction,

$$\begin{cases} \sigma^s = -(p_a - p_w) & ;\, p_a - p_w \le 0 \\ \sigma^s = -\dfrac{p_a - p_w}{\Big[1 + (\alpha s)^{\mathrm{n}}\Big]^{\mathrm{m}}} & ;\, p_a - p_w \ge 0 \end{cases} \tag{3.67}$$

Lewis and Schrefler[58] used the degree of saturation S instead of the effective stress parameter χ of Bishop's equation, however Lu and Likos[66]'s equation is treated as a function of both matric suction and the effective degree of saturation. Its merit is to describe effectively suction stress of various soils regardless the wide range of matric suction like clay or the narrow range of matric suction like sand. Figure 3.4-3.6 show the general patterns of the SSCC interrelated with SWCC for three different types of soil as shown in Table 3.1.

Figure 3.4 shows the soil-water characteristic curves (SWCCs) for loam, silt, and clay, and Figure 3.5 shows the suction stress characteristic curves (SSCCs) predicted by equation (3.67). For

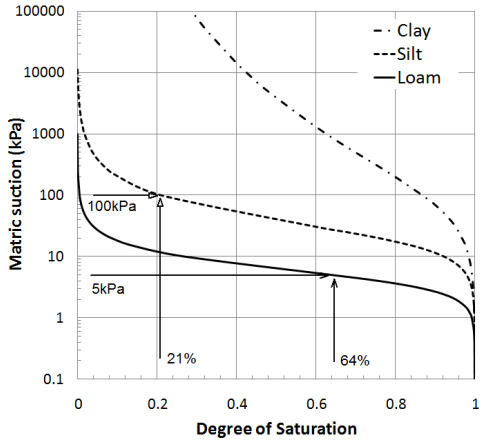

Figure 3.4: SWCC[90] for three soils in Table 3.1

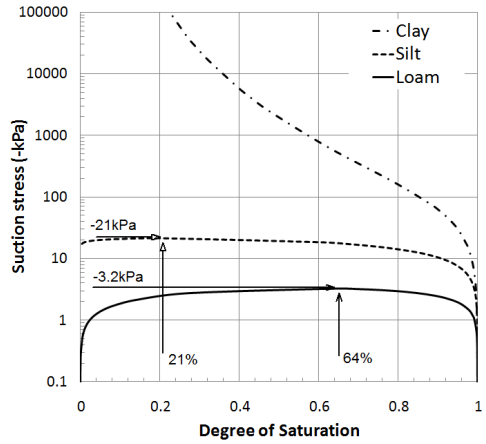

Figure 3.5: SSCC[63] for three soils in Table 3.1 in terms of effective degree of saturation

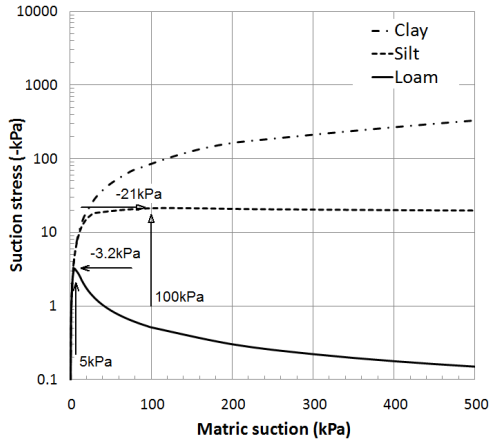

Figure 3.6: SSCC[63] for three soils in Table 3.1 in terms of matric suction

loam soil, suction stress is zero when matric suction is zero (saturated condition) and suction stress approaches zero at a large value of matric suction as shown in Figure 3.6. Suction stress reaches a minimum value -3.2 kPa at 5 kPa matric suction or 64% degree of saturation as shown in Figure 3.5-3.6.

For silty soil, the minimum value of suction stress is -21 kPa at 100 kPa matric suction or 21% degree of saturation. But a similar suction stress remains through several hundreds kPa values beyond the minimum value because a soil still keep some suction stresses even under dry condition. In order to verify this phenomenon in practice field, the behavior of loess cut slopes demonstrates that loess cut slope which has several tens kPa is capable of maintaining near-vertical cuts of some meters in height under dry condition without cohesive clay films or any support[63].

For clay soil, Figure 3.5-3.6 show that the distribution of suction stress is distinguished from that of other soils. Suction stress is zero at zero matric suction (saturated condition), but suction stress increases quickly by about 40 kPa matric suction, then after this increases gradually through several thousands kPa. It is difficult to define the minimum suction stress because suction stress of clay soil usually is very high value under dry condition or high matric suction condition. The distribution of matric suction of clay in SWCC (Figure 3.4) is similar to that of suction stress of clay in SSCC (Figure 3.5), namely, there is little difference between matric suction and suction stress of clay under dry condition for the effective stress of clay.

Chapter 4

Numerical Examples

For finite element implementation of partially saturated soils, three commercial codes, such as SEEP/W–SIGMA/W[40], Plaxis–PlaxFlow[74, 73], Abaqus[1], are analyzed at the same condition and compared with water flow and deformation for an example of a column consolidation test. The main point for the comparison of the program's results is to check the difference between the staggered coupling program (SEEP/W–SIGMA/W) and my monolithically coupled program (Matlab code). In order to prove the validity of numerical simulations, experimental data from laboratory test in the literature will be compared with numerical results, using parameters for a plasticity model in the literature. Also, it will be compared to Schrefler[75, 38]'s result for the effect of air pore pressure in triphasic mixture through a drainage test, and to Cho and Lee[21]'s result for water infiltration and instability of rainfall-induced soil slope through flow-deformation coupled finite element analysis.

Numerical simulations by commercial softwares are performed in this Section are showed in Appendix **B**. The Appendix **B** includes how to run UNSAT-H 1D flow program and SEEP/W–SIGMA/W coupled program for partially saturated case, as well as ABAQUS for the saturated case.

4.1 Numerical Simulation for Partially Saturated Flow

4.1.1 Boundary conditions

The profiles of water flow and its pressure in vadose zone may be evaluated with consideration of the matric suction, negative pore water pressure, profile in the partially saturated soils. It is influenced by soil type, the thickness of the partially saturated zone, and the fluid fluxes occurring at the subsurface-atmosphere interface. Hence the profile of matric suction can be assumed as hydrostatic condition initially although the state of stress for partially saturated soil in the field is rarely a constant[65]. As the first step, unsaturated flow analysis is performed by UNSAT-H[89] and SEEP/W prior to the application of coupled pore fluid diffusion and stress analysis with SEEP/W–SIGMA/W (staggered coupling program), my Matlab code and Abaqus (only use for saturated case) which is monolithically coupled program for partially saturated soil problems.

In order to describe the negative pore water pressure distribution under one-dimensional infiltration, Figure 4.1 shows the geometry of the soil column for comparing numerical results of UNSAT-H, SEEP/W, and my Matlab code (the mesh on the right is used in the Matlab code). In order to see more accurate result of partially saturated flow, the mesh might be discretized by 8 elements for smooth suction profile. Above water table the pore water pressure is negative, representing capillary tension causing the water to rise against the gravitational force and creating a capillary zone. The saturation associated with particular values of capillary pressure for absorption and exsorption of water from the partially saturated soil is a physical property called soil-water characteristic curve. It is defined from laboratory test (see Figure 1.13 in earlier chapter).

The bottom and vertical boundary on the both sides of soil column are fixed in displacement, and it is impermeable on the right and left sides of soil column. The initial condition of capillary zone above the water table has hydrostatic profile as shown in the left of Figure 4.1. For positive pore pressure below the water table, the flow velocity is proportional to the pore pressure value. The infiltration rate on the top of the soil column is applied to see transient partially saturated flow. The right of Figure 4.1 shows a numerical mesh(8 elements) which the smaller node spacing

near the surface is necessary for a correct solution because of rapid changes in initial suction value due to infiltration. The hydraulic conductivity of a partially saturated soil is calculated by van Genuchten's equation[90] using the degree of saturation $S(s)$ and fitting parameters of the soil-water characteristic curve as shown in equation (4.2).

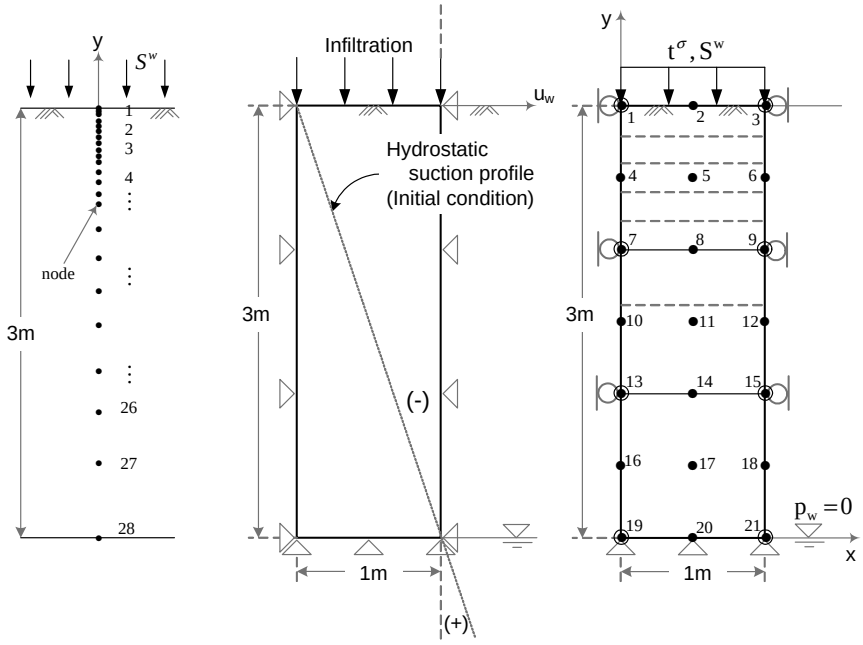

Figure 4.1: Boundary and initial condition and numerical mesh on vadose zone; UNSAT-H(left) and FE codes(right)

4.1.2 Hydraulic conductivity function estimation methods

It is difficult and complex work for the partially saturated hydraulic conductivity function to be measured directly, thus many researchers have predicted the partially saturated hydraulic conductivity functions from a measured and predicted volumetric water content function, such as air-entry value, residual volumetric water content and coefficient of volume compressibility[40, 73, 89]. This is the preferred approach to simulate experimental and practical water flow. Most commercial software have famous models, for example Fredlund et al.[33] and van Genuchten[90] methods, used to predict partially saturated hydraulic conductivity function. These functions have

yet used the function of suction or water content as partially saturated hydraulic conductivity functions. Equations (4.1) and (4.2) are respectively Fredlund et al. and van Genuchten functions.

$$k_w = k_s \frac{\sum_{i=j}^{N} \frac{n^w(e^y) - n^w(s)}{e^{y_i}} S'_e(e^{y_i})}{\sum_{i=1}^{N} \frac{n^w(e^y) - n^w_s}{e^{y_i}} S'_e(e^{y_i})} \tag{4.1}$$

$$k_w = k_s \frac{\left[1 - (\alpha s)^{\mathrm{n}-1} \left(1 + (\alpha s)^{\mathrm{n}}\right)^{-\mathrm{m}}\right]^2}{\left[1 + (\alpha s)^{\mathrm{n}}\right]^{\mathrm{m}/2}} \tag{4.2}$$

where, k_w is calculated conductivity for a specified water content or negative pore water pressure(m/s), k_s is measured saturated conductivity(m/s), n^w is volumetric water content, e is natural number(2.71828), y is a dummy variable of integration representing the logarithm of negative pore water pressure, i is the interval between the range of j to N, j is the least negative pore water pressure to be described by the final function, N is the maximum negative pore water pressure to be described by the final function, s is the suction corresponding to the j^{th} interval, S'_e is the first derivative of the equation $C(s)\frac{n^w}{\{\ln[e + (s/\mathrm{a})^{\mathrm{n}}]\}^{\mathrm{m}}}$, $C(s)$ is Fredlund et al.'s correcting function and curve fitting parameters are α, a, n, m. Fredlund et al. suggested that the function consists of developing the partially saturated hydraulic conductivity function by integrating along the entire curve of the volumetric water content function. van Genuchten proposed the closed form equation to describe the hydraulic conductivity of a soil as a function of matric suction. van Genuchten showed that the curve fitting parameters can be calculated graphically based on the volumetric water content function of the soil. According to van Genuchten, the best point to evaluate the curve fitting parameters is the halfway point between the residual and saturated water content of the volumetric water content function[90, 40].

For constitutive behavior for pore fluid flow in Abaqus, the partially saturated flow is governed by Forchheimer's law[7]. Darcy's law is generally applicable to low fluid (saturated) flow velocities, whereas Forchheimer's law is commonly used for situations involving higher (partially saturated) flow velocities. According to Forchheimer's law, high flow velocities have the effect of reducing the effective permeability. As the fluid flow velocity reduces, Forchheimer's law approximates the

well-known Darcy's law. Thus, Forchheimer's law is to add the velocity-dependent term in Darcy's law. Forchheimer's law is written as

$$\mathbf{q}(1+\beta\sqrt{\boldsymbol{v}_w\cdot\boldsymbol{v}_w}) \quad = \quad -\frac{k_{rw}}{\gamma_w}k_s\left(\frac{\partial p_w}{\partial \mathbf{x}}-\rho^{wR}\mathbf{g}\right) \tag{4.3}$$

where $\mathbf{q}$ is the volumetric flow rate of water per unit area of a partially saturated soil. Under uniform condition, Darcy's law states that the volumetric flow rate of water through a unit area of the medium, $Sn\boldsymbol{v}_w$, is proportional to the negative of the gradient of the piezometric head $(z+p_w/\gamma_w)$. $\boldsymbol{v}_w$ is the water velocity, β is a velocity coefficient dependent on the void ratio of the soil, k_{rw} is the relative permeability dependent on the degree of saturation S such that obtained from experiments ($k_{rw}=1$ at $S=1$), k_s is the saturated permeability(m/s), and other terms is the same with equation (2.35). Hence, the partially saturated permeability in Abaqus is defined as

$$k_w = \frac{k_{rw}}{(1+\beta\sqrt{\boldsymbol{v}_w\cdot\boldsymbol{v}_w})}k_s \tag{4.4}$$

This nonlinear permeability can be defined to be dependent on the void ratio of the soil, so the fluid velocity tends to zero, Forchheimer's law approaches Darcy's law. Although the partially saturated permeability in Abaqus refers that it depends on $\beta(\mathbf{x},e)$ which is the function of the position vector $\mathbf{x}$ and void ratio e, Tariq[85] suggested $\beta=\dfrac{2.33\times10^{10}}{k_s^{1.201}}$ for only sandstone and limestone. Hence, Abaqus does not consider the porosity or void ratio dependence for the partially saturated permeability too.

4.1.3 Analytical solution of transient infiltration

PlaxFlow/Plaxis is based on the staggered coupling analysis for seepage and deformation in partially saturated soils. Plaxis is a finite element program intended for 2D and 3D analysis of deformation, stability and groundwater flow in geotechnical engineering. PlaxFlow is also a finite element package intended for the two-dimensional and steady-state analyses of saturated and unsaturated groundwater flow problems in geotechnical engineering and hydrology. PlaxFlow incorporates several models for saturated and unsaturated groundwater flow, including the well-known van Genuchten[90] relations between pore pressure, saturation and permeability. PlaxFlow

allows the model to calculate partially saturated conductivity with the relation between degree of saturation and negative pore water pressure. Using PlaxFlow code the initial condition and boundary condition for the analytical solution of transient seepage problem are shown in Figure 4.2.

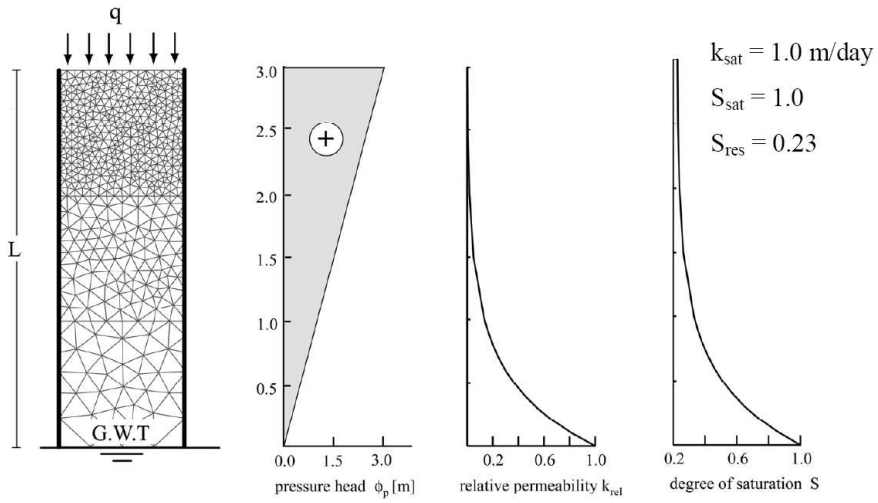

Figure 4.2: Problem geometry and finite element mesh (PlaxFlow Validation Manual chapter.4)

The analytical solution at steady state is presented by Gardner[37] for the particular permeability function. The negative pore water pressure head ϕ_p is the function of vertical position for steady-state as

$$\phi_p = -\frac{1}{\alpha} \ln \left[\left(1 - \frac{q}{k_{sat}} \right) e^{-\alpha y} + \frac{q}{k_{sat}} \right] \tag{4.5}$$

where α is a fitting parameter, y is elevation, q is infiltration rate and k_{sat} is the saturated permeability. And the analytical solution at transient flow is presented by Srivastava and Yeh[81] for the particular water characteristic and permeability functions. The negative pore water pressure head ϕ_p is the function of time and vertical position for transient condition as follows,

$$\phi_p = \frac{1}{\alpha} \ln(R) \tag{4.6}$$

where,

$$R = \frac{q}{k_{sat}} - \left(\frac{q}{k_{sat}} - 1\right) e^{-y} - \frac{4q}{k_{sat}} e^{(L-y)/2} \cdot e^{-t^*/4} \cdot \sum_{i=1}^{\infty} \frac{\sin(\lambda_i \cdot y)\sin(\lambda_i \cdot L) e^{-\lambda_i^2 \cdot t^*}}{1 + (L/2) + 2\lambda_i^2 L}$$
$$t^* = \frac{n \cdot \alpha \cdot k_{sat} \cdot t}{S_{sat} - S_{res}}\,, \qquad \tan(\lambda \cdot L) + 2\lambda = 0 \tag{4.7}$$

where λ_i is the i^{th} root of the characteristic equation and t is the time.

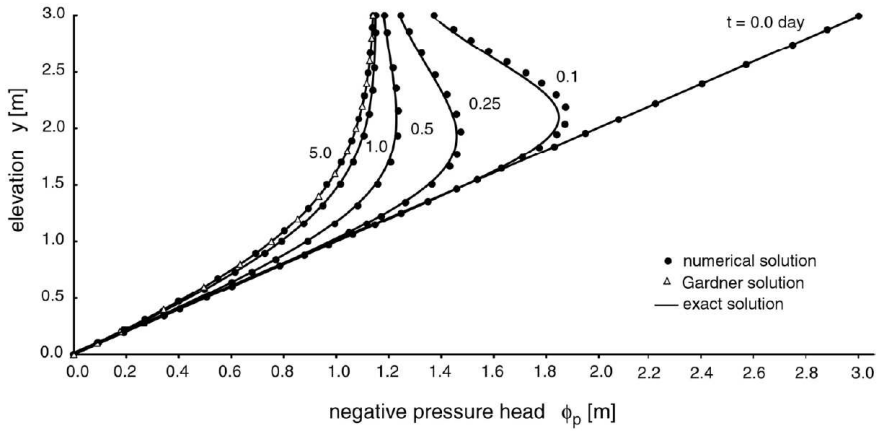

Figure 4.3: Negative pressure head at different time steps (PlaxFlow Validation Manual chapter.4)

Figure 4.3 shows the distribution of negative pore water pressure under one-dimensional infiltration. The results are compared with analytical solutions for both steady state(Gardner, equation (4.5)) and transient groundwater flow (Srivastava and Yeh[81], equations (4.6) and (4.7)).

Figure 4.2 shows the finite element mesh for a one-dimensional infiltration problem to simulate the problem of Srivastava and Yeh[81]. The ground surface is exposed to an infiltration rate of $q = 1.16 \times 10^{-6} m/s$. For transient calculations, the initial negative pore water pressure head distribution is considered to be hydrostatic. The negative pore water pressure head distribution is calculated using the steady state option. The same problem is reanalyzed using the transient calculation option to a final time of 5 days. Figure 4.3 shows the distribution at different time intervals. In the case of transient flow, the analytical solution as a function of time presented by Srivastava and Yeh[81] is presented by solid lines, and Gardner's solution[37] for steady state is obtained after 5 days of continuous infiltration[73].

In this study, PlaxFlow-Plaxis program is not compared with SEEP/W–SIGMA/W, Abaqus and Matlab due to the technical problem of getting the coupled analysis to work.

4.1.4 Comparison of seepage analysis in rigid soil column

For the simulation of partially saturated hydraulic conductivity, suction profile on vadose zone are compared with UNSAT-H, SEEP/W and Matlab code built into the model that can be used to predict partially saturated hydraulic conductivity functions. The UNSAT-H (version 3) model was developed at Pacific Northwest National Laboratory (PNNL) for simulating soil water infiltration, redistribution, evaporation, plant transpiration, deep drainage, and soil heat flow as one-dimensional processes. It is one of numerical methods used to estimate the flux of water moving through the vadose zone for verifing flow processes in unsaturated soils. The model simulates infiltration in a two-step process. First, infiltration is set equal to the precipitation rate during each time step. Second, if the surface soil saturates, the solution of that time step is repeated using a Dirichlet boundary condition (with the surface node saturated). The resulting flux from the surface into the profile is the infiltration rate[89].

For flow rate of infiltration applied in the seepage simulation, since the flow across the edge of an element is uniform, the total flow across the edge is the flow rate times the length of the element edge. In order to calculate a unit rate of flow across the edge of an element, it is necessary to integrate along the edge of the element and convert the unit rate of flow (q) into nodal flows which is Neumann boundary condition, Q ($= S^w$ in equation (2.4.1)).

SEEP/W can model both saturated and partially saturated flow but no deformation. The saturated and unsaturated formulation of SEEP/W makes it possible to analyze seepage as a function of time and to consider such processes as the infiltration of precipitation. The transient feature allows us to analyze such problems as the migration of a wetting front and the dissipation of excess pore-water pressure. For staggered coupled analysis, using SEEP/W computed pore-water pressures in SIGMA/W makes it possible to deal with irregular saturated and partially saturated conditions or transient pore-water pressure conditions in a stress-strain behavior analysis. Thus,

Table 4.1: Soil material parameters (van Genuchten[90])

Soil	$\theta_s(\mathrm{cm}^3/\mathrm{cm}^3)$	$\theta_r(S_r)$	k_s(m/s)	$\alpha(1/\mathrm{cm})^*$	n
Loam	0.434	0.218(0.5)	3.7×10^{-6} $3.8 \times 10^{-13\dagger}$	0.02	2.76
Silt loam	0.396	0.131(0.33)	5.7×10^{-7} $5.8 \times 10^{-14\dagger}$	0.00432	2.06
Clay	0.446	0.01(0.01)	9.5×10^{-9} $9.7 \times 10^{-16\dagger}$	0.00152	1.17

* curve fitting parameter; $\alpha = 1/\mathrm{a}$
† intrinsic permeability $\varkappa(\mathrm{m}^2)$ used in Matlab code

deformation coupling seepage flow may be analyzed using SIGMA/W program. In Table 4.1, θ_s and θ_r are saturated and residual volumetric water content, respectively, S_r is residual degree of saturation, k_s is saturated permeability, α and n are fitting parameters of van Genuchten equation.

For transient seepage analysis of rainfall infiltration, various factors of the subsurface properties affect the process of partially saturated flow into soil, such as the intensity and duration of rainfall, and the initial water content and hydraulic properties of the subsurface. The instantaneous infiltration rate is maximal at the start of a rainfall event. While rainfall duration, the rate decreases or increases gradually to a value approaching the saturated conductivity of the surface soil with increasing the wetted depth of soil. Thus, in the initial stage, infiltration is controlled by the supply of water and then it is controlled by the initial matric suction profile of soil by calculating the partially saturated permeability of soil depended on the soil-water characteristic curve to transmit water downward.

Three soil types are used in UNSAT-H, SEEP/W and Matlab code as shown in Table 4.1. The simulation of UNSAT-H (finite difference) is modeled in one dimension in the vertical direction and requires discretization (i.e., nodal spacing). For a correct solution, the node spacing should be very small beneath the ground and become gradually larger downward through the profile as shown in Figure 4.1(left). Therefore, the number of node is 28 in soil column height of 3m. The first node (node 1) is at the surface and the last node (node 28) is at the bottom of the soil profile to be

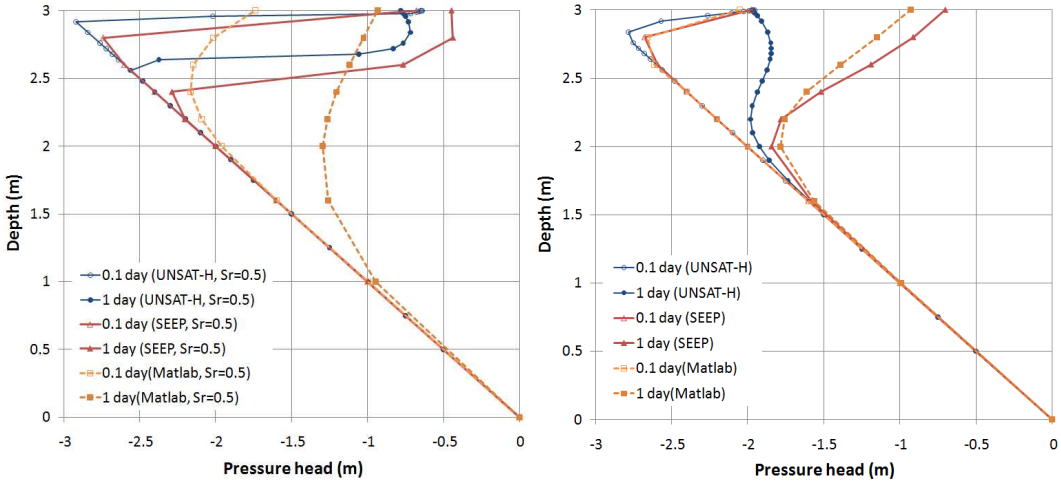

Figure 4.4: Suction profile of loam(left) and silt(right) by use of S_r

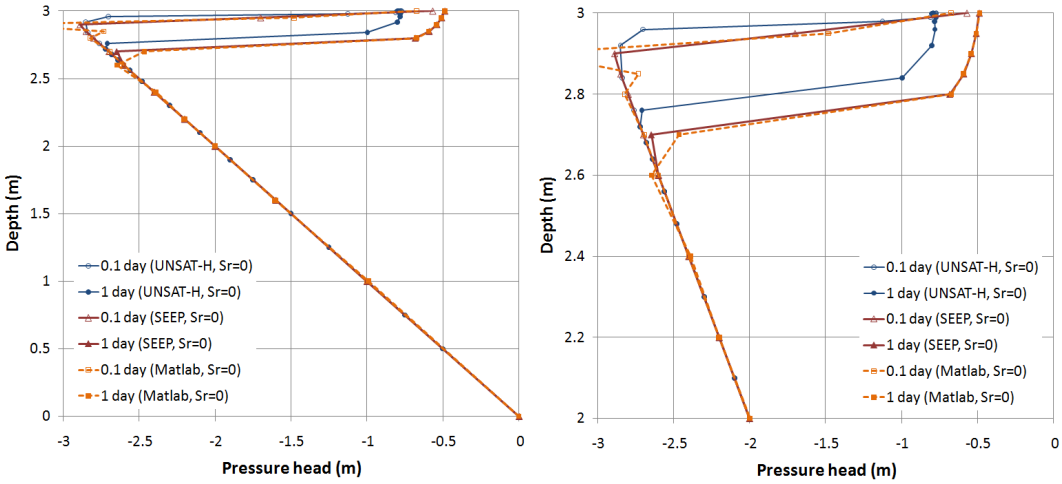

Figure 4.5: Suction profile of loam at $S_r = 0$ and zoom in top area(right)

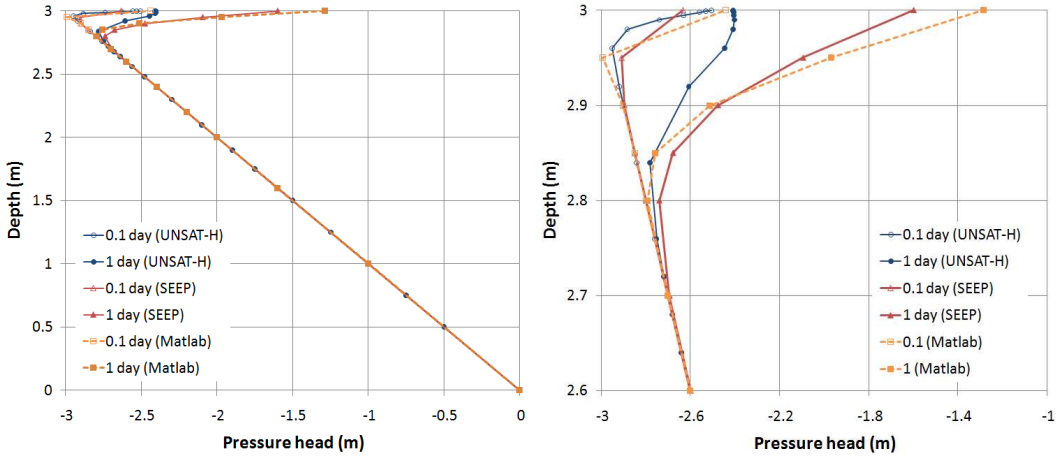

Figure 4.6: Suction profile of clay and and zoom in top area(right)

simulated. Total water applied is infiltration rate 0.21 cm/hr $= 5.83 \times 10^{-7}$ m/s for loam and silt and 0.00324 cm/hr $= 9 \times 10^{-9}$ m/s for clay. Two infiltration rates is applied because SEEP/W and Matlab codes have some troubles to converge when infiltration rate of 5.83×10^{-7} m/s is applied on clay.

As shown in Figures 4.4-4.6, qualitatively these suction profiles are similar to analytical solution[81] as shown in Figure 4.3 and experimental data in the field[32]. The left figures show the profiles of real size(H:3m $\times$ W:1m) and the right figures show the size-enlargement of the profiles. UNSAT-H and SEEP/W use partially saturated hydraulic conductivity as function only of suction, and Matlab code uses hydraulic conductivity as function of both suction and porosity. However this comparison does not consider the effect of porosity due to fixed mesh. The profiles of UNSAT-H for three kinds of soil generally show surface boundary problem. It makes iteration trouble for convergence because the first node on surface boundary node in UNSAT-H affects the second node and other nodes of the geometry due to 1D analysis[89]. Hence, the suction profiles of UNSAT-H show some different pattern comparing with those of SEEP/W and Matlab codes.

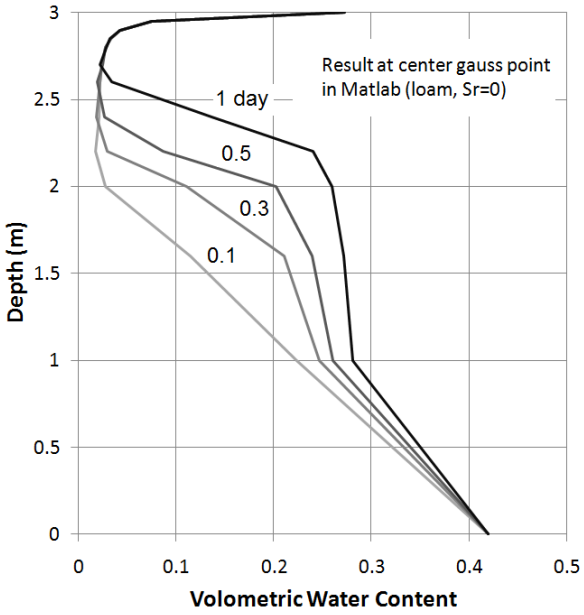

Figure 4.7: Distribution of volumetric water content in loam (Matlab), $S_r = 0$

When the residual degree of saturation S_r is considered in the flow analysis, the profile of loam shows big differences between two codes and Matlab code because there are two important factors applied. One is relative permeability for a partially saturated soil. SEEP/W used the function of suction and Matlab used the function of degree of saturation for relative permeability. Both equations are derived by van Genuchten[90], however the relative permeability of the function of suction is derived from the effective degree of saturation S_e. It has to include the assumption that the residual degree of saturation is equal to zero ($S_r = 0$). If the residual degree of saturation is considered as some values, not zero, in the simulation, two equations ($k_{rw}(S), k_{rw}(s)$) will provide different results. The other is the effect of capillary zone. In SEEP/W, the amount of water above the water table that is stored in a soil depends on capillary force. The capillary force exists below saturated zone of soil surface due to rainfall as well as above the water table.

$$\left.\begin{aligned} k_{rw}(S) &= \sqrt{S}\left(1-\left(1-S^{\frac{1}{\mathrm{m}}}\right)^{\mathrm{m}}\right)^2 \\ S &= S_r + S_e(1-S_r) = S_r + \frac{1-S_r}{\left[1+(\alpha s)^{\mathrm{n}}\right]^{\mathrm{m}}} \end{aligned}\right\} \quad \text{in Coupled code} \tag{4.8}$$

$$\left.\begin{aligned} k_{rw}(s) &= \frac{\left[1-(\alpha s)^{\mathrm{n}-1}\left(1+(\alpha s)^{\mathrm{n}}\right)^{-\mathrm{m}}\right]^2}{\left[1+(\alpha s)^{\mathrm{n}}\right]^{\mathrm{m}/2}} \\ S &= \frac{\Theta_w}{n} = \bar{S}_r + \bar{S}_e(1-\bar{S}_r) \end{aligned}\right\} \quad \text{in SEEP/W} \tag{4.9}$$

where Θ_w is volumetric water content, $\bar{S}_r$ is degree of saturation due to capillary forces and $\bar{S}_e$ is bounded degree of saturation due to adhesion ($\bar{S}_e^*$), $\bar{S}_e =< 1 - \bar{S}_e^* > +1$. The adhesive component[40] is a bounded value since it is possible at low suctions for the value $\bar{S}_e^*$ to be greater than 1. The bounded value ensures that for a $\bar{S}_e^*$ greater or equal to 1, $\bar{S}_r = 1$ and if $\bar{S}_e^*$ is less than 1, then $\bar{S}_e = \bar{S}_e^*$. The capillary saturation $\bar{S}_r$, which depends essentially on the pore diameter and the pore size distribution, is given by[40],

$$\bar{S}_r = 1 - \left[\left(\frac{h_{cap}}{s}\right)^2 + 1\right]^{\mathrm{m}} \exp\left[-\mathrm{m}\left(\frac{h_{cap}}{s}\right)^2\right] \tag{4.10}$$

where h_{cap} is mean capillary rise.

The suction profiles of Figure 4.4 through SEEP/W is plotted by the effect of capillary force on soil surface. The surface of loam can be easily saturated due to seepage force because the permeability of loam is larger than infiltration rate. Thus, results of loam show more different suction profiles.

The consideration of the residual degree of saturation as shown in Figure 4.8 illustrate that two relative permeabilities in equation (4.8) and (4.9) can cause different soil-water characteristic curves. The relative permeability of the function of saturation rate takes the residual degree of saturation into account, but that of the function of suction (UNSAT-H also uses this function for relative permeability) does not because the effective degree of saturation is calculated by hydraulic relation of van Genuchten[90]. SEEP/W controls the residual degree of saturation using their own method as shown in equation (4.9).

Figure 4.9 shows plots of relative permeability (k_{rw}) versus suction (s) and effective degree of saturation rate (S_e) by using hydraulic parameters (α, n) summarized in Table 4.1. At 30 kPa of initial suction state, the effective degree of saturation and degree of saturation on loam surface shows dry condition rather than silt and clay as shown in Table 4.2. The relative permeability of loam surface also shows slower infiltration rate than silt and clay.

In Figure 4.5 and 4.6, the profiles of loam ($S_r = 0$), silt and clay show similar patterns between SEEP/W and Matlab codes. For the suction profile of clay, Matlab code makes bouncing point on the second node at the ground surface because of too small hydraulic conductivity when 8 elements (Figure 4.4) for the soil column mesh are used, so the top portion of soil column which needs to discretize for the calculation of infiltration is split by 12 elements (Figure 4.5 and 4.6).

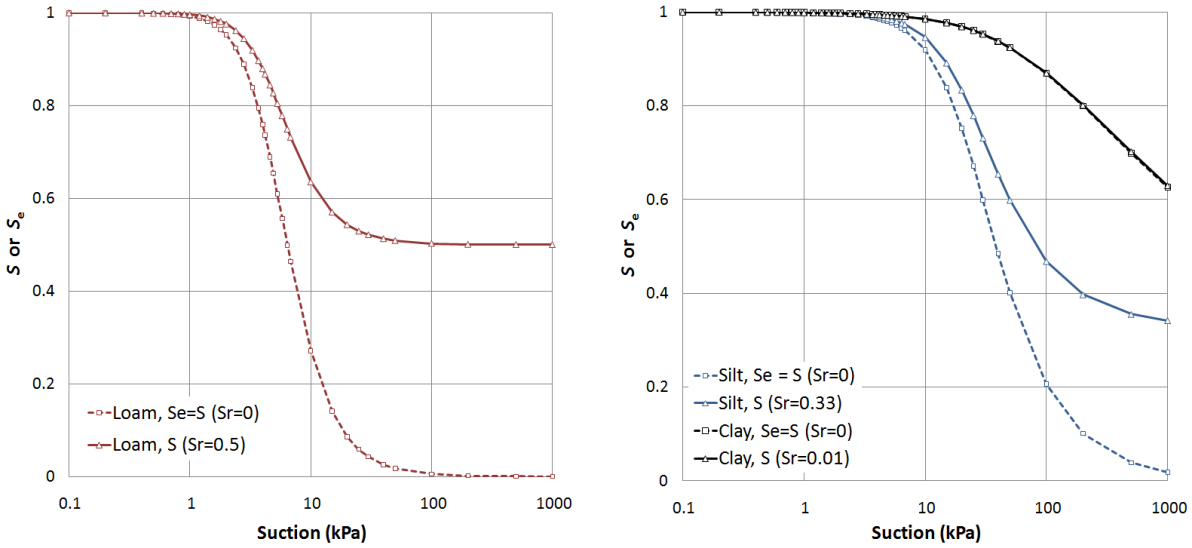

Figure 4.8: Difference of soil-water characteristic curves by use of S_r

Table 4.2: Values at initial suction state (30 kPa) on soil surface

	Loam	Silt	Clay
S_e	0.0425	0.599	0.952
S	0.521	0.731	0.953
k_{rw}	4.2×10^{-6}	3.5×10^{-2}	2.7×10^{-2}

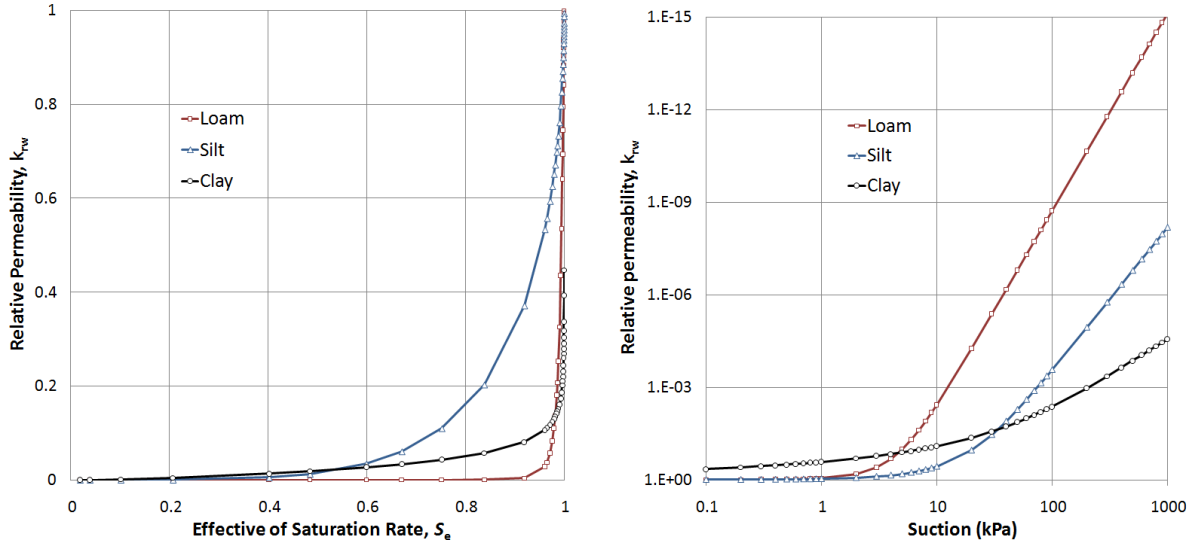

Figure 4.9: Curves of relative permeability (k_{rw}) versus suction (s) and effective of saturation rate (S_e)

4.2 Verification of Coupled Finite Element Analysis

4.2.1 Consolidation analysis in saturated condition

The one-dimensional saturated consolidation example was simulated to verify first the biphasic mixture finite element formulation as compared to theory for 1D consolidation settlement. The stress within a semi-infinite, homogeneous, and isotropic mass has a linear stress-strain relationship due to a load on the surface[24]. The stress due to surface loads distributed over a large area can be obtained by integration from the load. In order to estimate consolidation settlement of the analytical solution, it is assumed that the layer of saturated soil of thickness of H_0, total displacement ΔH and the total vertical stress in an elemental layer of thickness dz at depth z is increased by $\Delta\sigma$ due to the traction t^σ on the surface as shown in Figure 4.10.

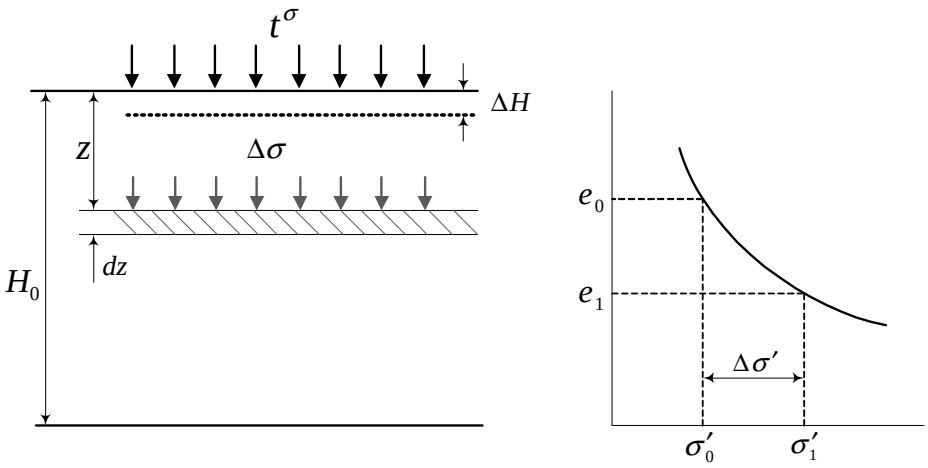

Figure 4.10: 1D Consolidation settlement theory[24]

It is also assumed that the lateral strain in the soil layer is equal to zero (similar to oedometer test). At the completion of total displacement, the effective vertical stress $\Delta\sigma'$ increases corresponding to a change from σ'_0 to σ'_1 and a decrease in void ratio from e_0 to e_1 on the $e - \sigma'$ curve in Figure 4.10. The reduction of volume per unit volume of soil can be written in terms of

void ratio,

$$\begin{aligned} \frac{\Delta V}{V_0} &= \frac{e_0 - e_1}{1 + e_0} \\ \Delta H &= \left(\frac{e_0 - e_1}{\sigma_1' - \sigma_0'}\right)\left(\frac{\sigma_1' - \sigma_0'}{1 + e_0}\right) \mathrm{d}z = m_v \Delta\sigma' \mathrm{d}z \end{aligned} \tag{4.11}$$

The reduction in volume per unit volume is equal to the reduction in thickness per unit thickness, so this summation means the total displacement ΔH per initial thickness H_0.

$$\Delta H = \int_0^H m_v \Delta\sigma' \mathrm{d}z = m_v \Delta\sigma' H_0 \tag{4.12}$$

where, m_v is the coefficient of volume compressibility $(= 1/(\lambda + 2\mu))$, hence the total displacement of the analytical solution is (Figure 4.12)

$$\Delta H = \frac{t^\sigma H_0}{\lambda + 2\mu} \approx 2.8 \text{ mm} \tag{4.13}$$

The stresses due to surface traction act in addition to the in-situ stresses due to the self-weight of the soil. Thus, the result of analytical solution does not consider the gravity. The example used the plane strain 2D finite element in saturated condition considering the deformation and pore water pressure of each node. Soil parameters for simulation is as shown in Table 4.3 and geometry is as shown in Figure 4.11.

In Table 4.3, λ and μ are Lamé constants, t^σ is traction, k_s is saturated permeability, n^{s0} and n^{w0} are initial solid and water volume fraction, ρ^{sR} and ρ^{wR} are real mass densities, and then initial mass density of the mixture finite element $\rho_0 = n^{s0}\rho^{sR} + n^{f0}\rho^{fR}$. Geometry shows normal displacements fixed and impermeable boundary at sides and bottom as shown in the Table 4.3 and Figure 4.11 to generate the 1D case.

In the implementation of numerical analysis in consolidation of 2D plane strain soil column, the element force vectors, such as body force $\boldsymbol{f}_f^{e,d}$, traction force $\boldsymbol{f}_t^{e,d}$, fluid force $\boldsymbol{f}^{e,\theta}$, air force $\boldsymbol{f}^{e,\zeta}$, seepage force $\boldsymbol{f}_s^{e,\theta}$, and air pressure force $\boldsymbol{f}_s^{e,\zeta}$, are then written as equations (4.14) and (4.15),

Table 4.3: Soil parameters for saturated consolidation test

Soil parameters	Value
λ	2.9×10^7 Pa
μ	7×10^6 Pa
t^σ	4×10^4 Pa
k_s	10^{-6} m$^3 \cdot$ s/kg
n^{s0}	0.58
n^{w0}	0.42
ρ^{sR}	2700 kg/m^3
ρ^{wR}	1000 kg/m^3
ρ_0	1986 kg/m^3

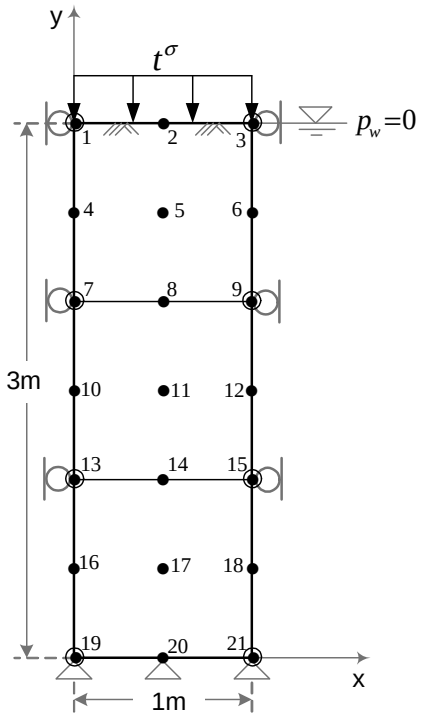

Figure 4.11: 3 element mesh for Matlab code for saturated consolidation

$$
\begin{aligned}
\boldsymbol{f}_f^{e,d}(\boldsymbol{d}^e,\boldsymbol{\theta}^e,\boldsymbol{\zeta}^e) &= \int_{B^e} \rho(\boldsymbol{d}^e,\boldsymbol{\theta}^e,\boldsymbol{\zeta}^e)(\boldsymbol{N}^{e,u})^T\cdot\boldsymbol{g}\mathrm{d}a \\
&= \int_{-1}^{1}\int_{-1}^{1} \rho(\boldsymbol{d}^e,\boldsymbol{\theta}^e,\boldsymbol{\zeta}^e)(\boldsymbol{N}^{e,u})^T\cdot\boldsymbol{g}\, j^e\mathrm{d}\xi\mathrm{d}\eta \\
\boldsymbol{f}^{e,\theta}(\boldsymbol{d}^e,\boldsymbol{\theta}^e,\boldsymbol{\zeta}^e) &= \int_{B_w^e} \rho^{wR}(\boldsymbol{B}^{e,p})^T\cdot\boldsymbol{k}^w(\boldsymbol{d}^e,\boldsymbol{\theta}^e,\boldsymbol{\zeta}^e)\cdot\boldsymbol{g}\,\mathrm{d}a \\
&= \int_{-1}^{1}\int_{-1}^{1} \rho^{wR}(\boldsymbol{B}^{e,p})^T\cdot\boldsymbol{k}^w\cdot\boldsymbol{g}\, j^e\mathrm{d}\xi\mathrm{d}\eta \\
\boldsymbol{f}^{e,\zeta}(\boldsymbol{d}^e,\boldsymbol{\theta}^e,\boldsymbol{\zeta}^e) &= \int_{B_a^e} \rho^{aR}(\boldsymbol{\zeta}^e)(\boldsymbol{B}^{e,p})^T\cdot\boldsymbol{k}^a(\boldsymbol{d}^e,\boldsymbol{\theta}^e,\boldsymbol{\zeta}^e)\cdot\boldsymbol{g}\,\mathrm{d}a \\
&= \int_{-1}^{1}\int_{-1}^{1} \rho^{aR}(\boldsymbol{\zeta}^e)(\boldsymbol{B}^{e,p})^T\cdot\boldsymbol{k}^a\cdot\boldsymbol{g}\, j^e\mathrm{d}\xi\mathrm{d}\eta
\end{aligned}
\tag{4.14}
$$

$$
\begin{aligned}
\boldsymbol{f}_t^{e,d} &= \int_{\Gamma_t^e} (\boldsymbol{N}^{e,u})^T\cdot\boldsymbol{t}^\sigma\mathrm{d}s \;=\; \int_{-1}^{1}\Big[\boldsymbol{N}^{e,u}(\eta=1)\Big]^T\cdot\boldsymbol{t}^\sigma(0.5)\,\mathrm{d}\xi \\
\boldsymbol{f}_s^{e,\theta} &= \int_{\Gamma_{s(w)}^e} (\boldsymbol{N}^{e,p})^T S^w\mathrm{d}s \;=\; \int_{-1}^{1}(\boldsymbol{N}^{e,p})^T S^w(0.5)\,\mathrm{d}\xi \\
\boldsymbol{f}_s^{e,\zeta} &= \int_{\Gamma_{s(a)}^e} (\boldsymbol{N}^{e,p})^T S^a\mathrm{d}s \;=\; \int_{-1}^{1}(\boldsymbol{N}^{e,p})^T S^a(0.5)\,\mathrm{d}\xi
\end{aligned}
\tag{4.15}
$$

Note that air terms ($\boldsymbol{\zeta}^e, \boldsymbol{f}^{e,\zeta}, \boldsymbol{f}_s^{e,\zeta}$) are ignored in the saturated problem, but these terms will be applied to triphasic mixture problem.

The element body force vector may use 3×3 Gauss integration (because of biquadratic displacement interpolation), the element fluid force and air force vector may use 2×2 Gauss integration (because of bilinear pore pressure interpolation), and element traction, seepage, air pressure force vectors as the equation (4.14) use 3 point Gauss integration along ξ in quadrilateral finite element.

$$
\begin{aligned}
&\boldsymbol{N}^{e,u} = \begin{bmatrix} \boldsymbol{N}_1^u & \boldsymbol{N}_2^u & \cdots & \boldsymbol{N}_9^u \end{bmatrix}, \qquad \boldsymbol{B}^{e,p} = \begin{bmatrix} \boldsymbol{B}_1^p & \boldsymbol{B}_2^p & \boldsymbol{B}_2^p & \boldsymbol{B}_4^p \end{bmatrix} \\
&\boldsymbol{N}_a^u = \begin{bmatrix} N_a^u & 0 \\ 0 & N_a^u \end{bmatrix}, \quad \boldsymbol{B}_b^p = \begin{bmatrix} \dfrac{dN_b^p}{dx} \\ \dfrac{dN_b^p}{dy} \end{bmatrix}, \quad \boldsymbol{t}^\sigma = \begin{bmatrix} t_x^\sigma(=0) \\ t_y^\sigma(=-t^\sigma) \end{bmatrix}, \quad \boldsymbol{g} = \begin{bmatrix} 0 \\ -g \end{bmatrix}
\end{aligned}
\tag{4.16}
$$

$$\boldsymbol{N}^{e,u}(\eta=1) = \begin{bmatrix} \mathbf{0} & \mathbf{0} & \boldsymbol{N}_3^u & \boldsymbol{N}_4^u & \mathbf{0} & \mathbf{0} & \boldsymbol{N}_7^u & \mathbf{0} & \mathbf{0} \end{bmatrix}$$

$$= \begin{bmatrix} 0 & 0 & 0 & 0 & \frac{1}{2}\xi(\xi+1) & 0 & \frac{1}{2}\xi(\xi-1) & 0 & 0 & 0 & 0 & 0 \\ 0 & 0 & 0 & 0 & 0 & \frac{1}{2}\xi(\xi+1) & 0 & \frac{1}{2}\xi(\xi-1) & 0 & 0 & 0 & 0 \\ 0 & 0 & 0 & 0 & 1-\xi^2 & 0 & 0 & 0 & 0 & 0 & 0 & 0 \\ 0 & 0 & 0 & 0 & 0 & 1-\xi^2 & 0 & 0 & 0 & 0 & 0 & 0 \end{bmatrix} \tag{4.17}$$

If soil surface is horizontal (no slope), $\boldsymbol{t}^{\sigma}$, S^w and S^a are respectively traction, seepage and air pressure force acting on the top surface of a soil ($\eta = 1,$ in top element), $\boldsymbol{g}$ is the vector of gravity acceleration, 9.8 m/s^2.

SEEP/W–SIGMA/W, Abaqus and Matlab codes are compared to perform a fully coupled consolidation analysis in saturated condition. A fully coupled analysis is required to correctly model the pore water pressure response to an applied load on the top surface. The maximum pore water pressure under an applied load can be greater than the applied load. The excess pore water pressure increase at the initial stage with reaching the peak, and then dissipate gradually. It is different from what assumed by Terzaghi[87]'s consolidation theory. This phenomenon is then called the Mandel-Cryer effect[68, 26]. The Mandel-Cryer effect can be seen in the results of consolidation analyses carried out with three codes.

Figure 4.12 shows the comparison of analytical solution for steady-state displacement[87], SEEP/W–SIGMA/W, Abaqus and Matlab code for 2D plane strain consolidation simulation, and it is a saturated case without gravity (SEEP/W–SIGMA/W should use gravity to simulate for p_w, so its result does not match with other results in the profile of p_w without gravity in Figure 4.12).

Figure 4.13 shows the comparison of consolidation simulations from Abaqus, SEEP/W–SIGAM/W, and Matlab code, and it is a saturated case with gravity. The difference of monolithic analysis, Abaqus and Matlab code, and staggered analysis, SEEP/W–SIGMA/W is negligible. The results of Matlab code was obtained from triphasic mixture finite element implementation with suction value is equal to zero($s = 0$) that is assumed in saturated condition. The first case is the consolidation result without the gravity and compared also to analytical solution, and the second case is with the gravity.

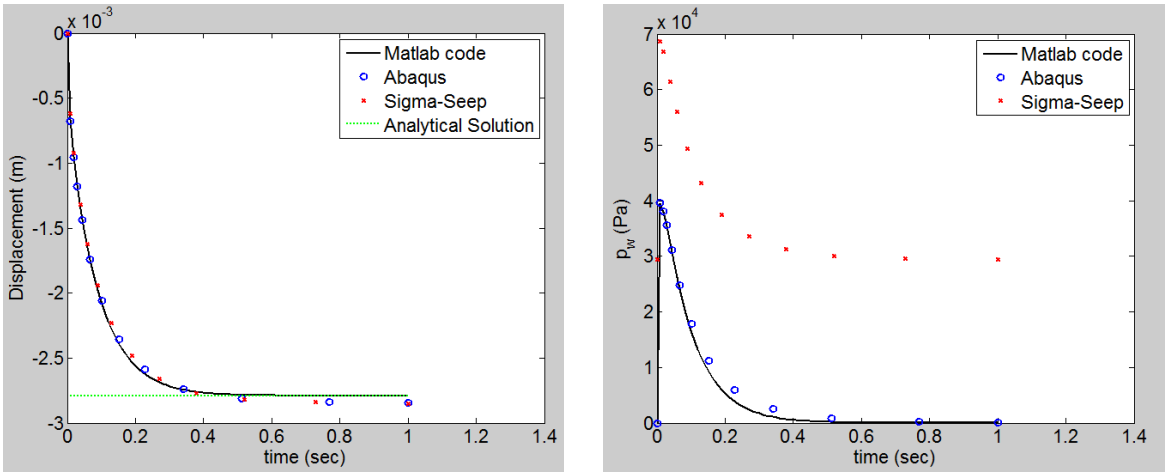

Figure 4.12: Verification of two-field($p_a \approx 0$) mixture for saturated case ($s = 0$, without gravity)

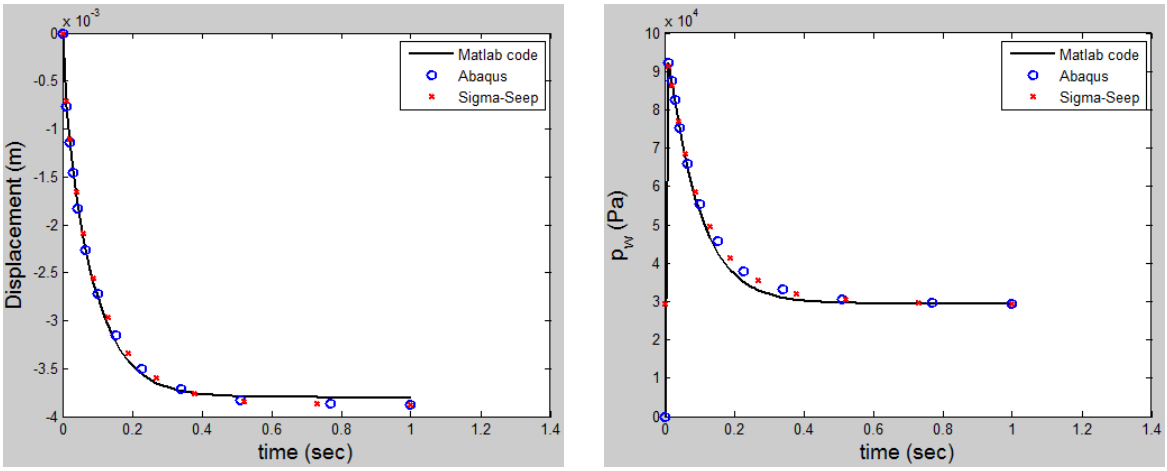

Figure 4.13: Verification of two-field($p_a \approx 0$) mixture for saturated case ($s = 0$, with gravity)

The comparisons are close, giving me confidence that the three coupled deformation-pore fluid flow codes (SEEP/W–SIGMA/W, Abaqus, and Matlab) are being used correctly for saturated analysis.

4.2.2 Semi-implicit linear and fully-implicit nonlinear solution for partially saturated flow and deformation, and analytical solution

This example is a verification of the numerical finite element implementation and time integration schemes between semi-implicit and fully-implicit for two-field ($p_a \approx 0$, Section 2.3.2) and three-field ($p_a \neq 0$, Section 2.3.1) formulations and implementations. To verify, we take the analytical solution of Srivastava and Yeh[81], for water flow through partially saturated rigid porous media with water table $p_w = 0$ at $z = 0$m, and infiltration seepage S^w at $z = 1$m as shown in Figure 4.14. The normal displacements are fixed at sides and bottom and it is impermeable at sides. The right figure of Figure 4.14 shows the profile of negative pore water head in vadose zone as the analytical solution for transient partially saturated flow[81].

All simulations are conducted in plane strain condition, but the analytical solution of Srivastava and Yeh[81] is essentially 1-Dimensional for the flow problem as is our solution for the flow. The BCs in Figure 4.14 lead to a 1D solution for partially saturated flow. After verification and comparison between semi-implicit linear and fully-implicit nonlinear solution methods, a top traction is applied to simulate coupled change in p_w and downward displacement.

For verification, the constitutive equations for the water phase are modified slightly as follows[81]

$$\begin{aligned} k_w(s) &= \frac{K_s}{\gamma_w} \exp(-\alpha s/\gamma_w) \\ S(s) &= \frac{1}{\Theta}\Big[\Theta_r + (\Theta_s - \Theta_r) \exp(\alpha s/\gamma_w)\Big] \end{aligned} \tag{4.18}$$

where K_s is the saturated permeability, γ_w the unit weight of water, α a parameter, Θ_r the residual volumetric water content (same concept with volume fraction of water, $\Theta_r = n_r^w$), and Θ_s the saturated volumetric water content ($\Theta_s = n_s^w$). Table 4.4 shows these parameters applied to the

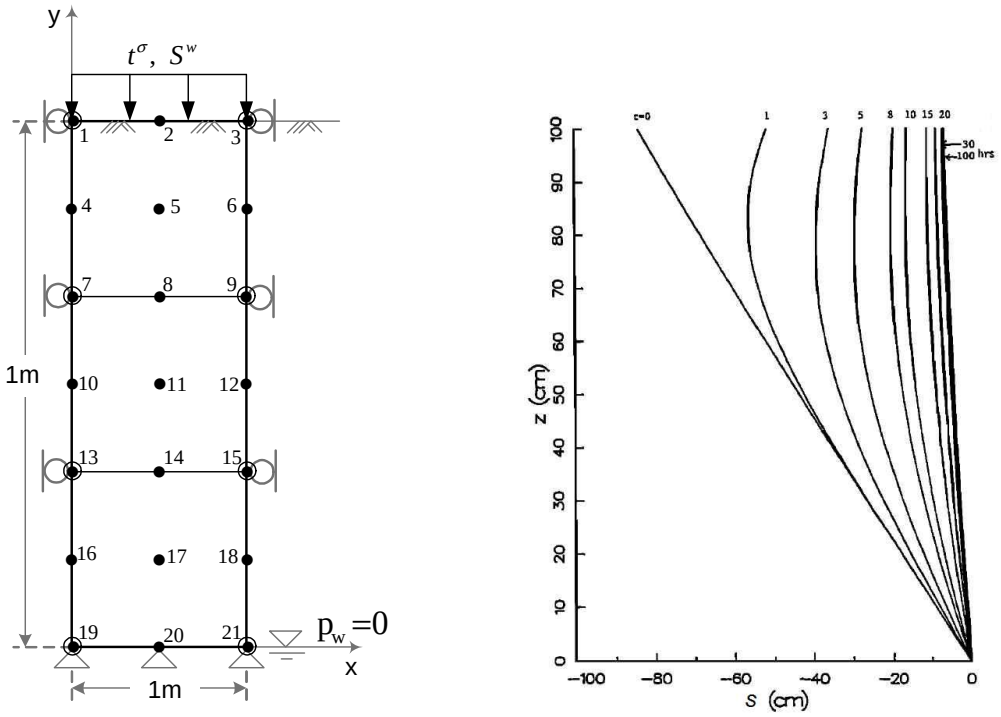

Figure 4.14: Mesh for numerical analysis(left) and analytical solution of partially saturated flow in vadose zone(right; Fig. 1 of Srivastava and Yeh, 1991)

Table 4.4: Soil parameters for semi- and fully-implicit implementation

Soil parameters	Value
K_s	2.8×10^{-6} m/s
α	1/m
Θ_s	0.45
Θ_r	0.2
S_0^w $(t = 0,\ initial)$	2.8×10^{-7} m/s
S^w $(t > 0,\ final)$	$9S_0^w$
γ_w	9800 N/m^3
t $(total)$	100 hrs

numerical examples.

The three element mesh with height 1m is shown with boundary condition in the left of Figure 4.14. All simulations are conducted in plane strain condition, but analytical solution, the right of Figure 4.14, is essentially 1 dimensional for the flow problem (and so is the FE solution with BCs prescribed). When a traction is applied in the next example, horizontal stress develops.

The results of the semi-implicit linear and fully-implicit nonlinear finite element solutions are shown in Figure 4.15, respectively for a constant time increment of $\Delta t = 10$hr. The node 1, 7, and 13 refer, respectively, to pore water pressure nodes on the left hand side of the mesh (open circle nodes) from top, middle, to low nodes (Figure 4.14). The bottom pore water pressure nodes have $p_w = 0$ zero because ground water table is assumed to locate at the bottom of geometry mesh. The results compare well with the analytical solution[81]. The analytical solution is not replicate exactly in closed form in this paper, but the negative water pressure head ψ values from the right of Figure 4.14 $p_w = \psi\gamma_w$, and plotted against the finite element solution here. Beginnings of an oscillation are apparent for the semi-implicit linear method in the left of Figure 4.15, but it remains stable in the steady-state. For fully-implicit nonlinear, the right of Figure 4.15, the solution is smoother. Comparing CPU times, for $\Delta t = 10$hr, it took 9.3 seconds to run the fully implicit nonlinear solution and 6.6 seconds to run the semi-implicit linear solution in Matlab.

To compare the two solution methods, the time increment is decreased to $\Delta t = 1$hr in Figure 4.16. The fully-implicit nonlinear solution is slightly more accurate for $t < 5 \times 10^4$ than the semi-implicit linear solution in Figure 4.15. The difference becomes unnoticeable as the time increment is made smaller $\Delta t \to 0$.

Figure 4.17 shows suction profiles at different time steps for transient flow problem. Semi-implicit time integration scheme needs small time step $\Delta t = 0.1hr$ to get accurate solution comparing analytical solution of Srivastava and Yeh[81]. Fully-implicit time integration scheme shows more stable solution in larger time step $\Delta t = 1hr$. The numerical flow problem is simulated in non-deformable soil column of 8 elements mesh for 100 hrs of total time.

In general, for smaller time steps, like those needed to resolve a sharp ramp in traction (next

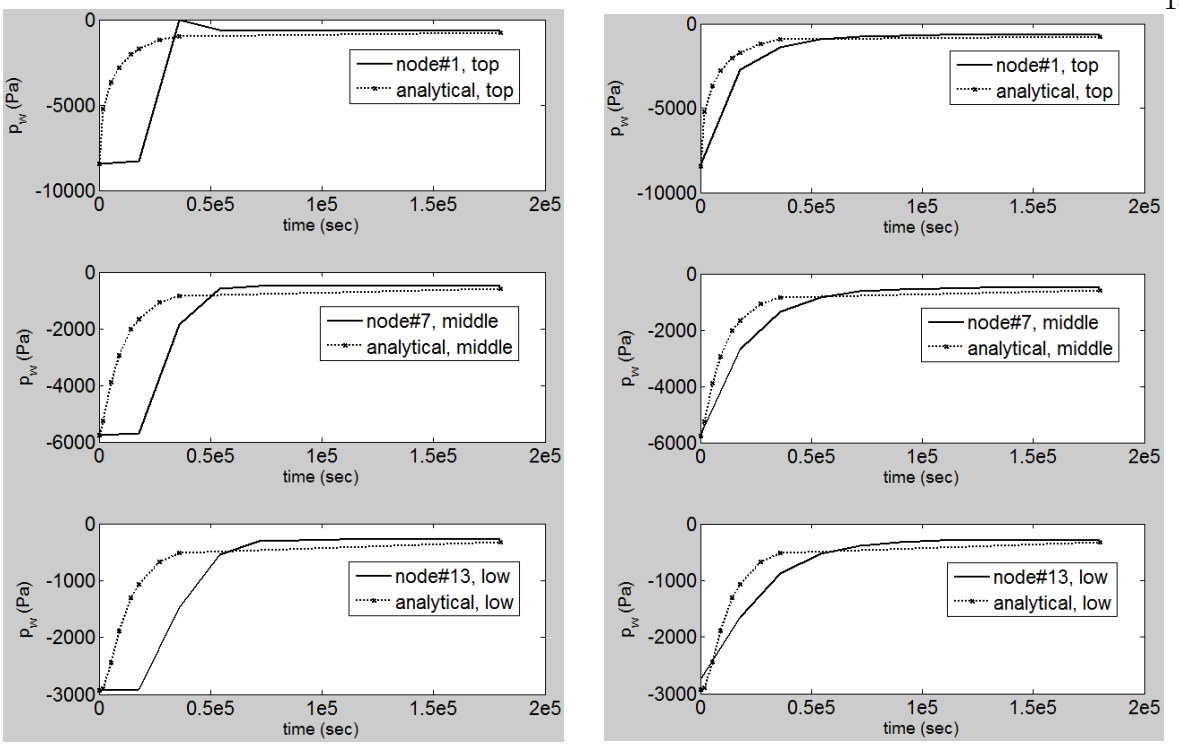

Figure 4.15: Semi-implicit linear(left) and fully-implicit nonlinear(right) solution with $\Delta t = 10hr$

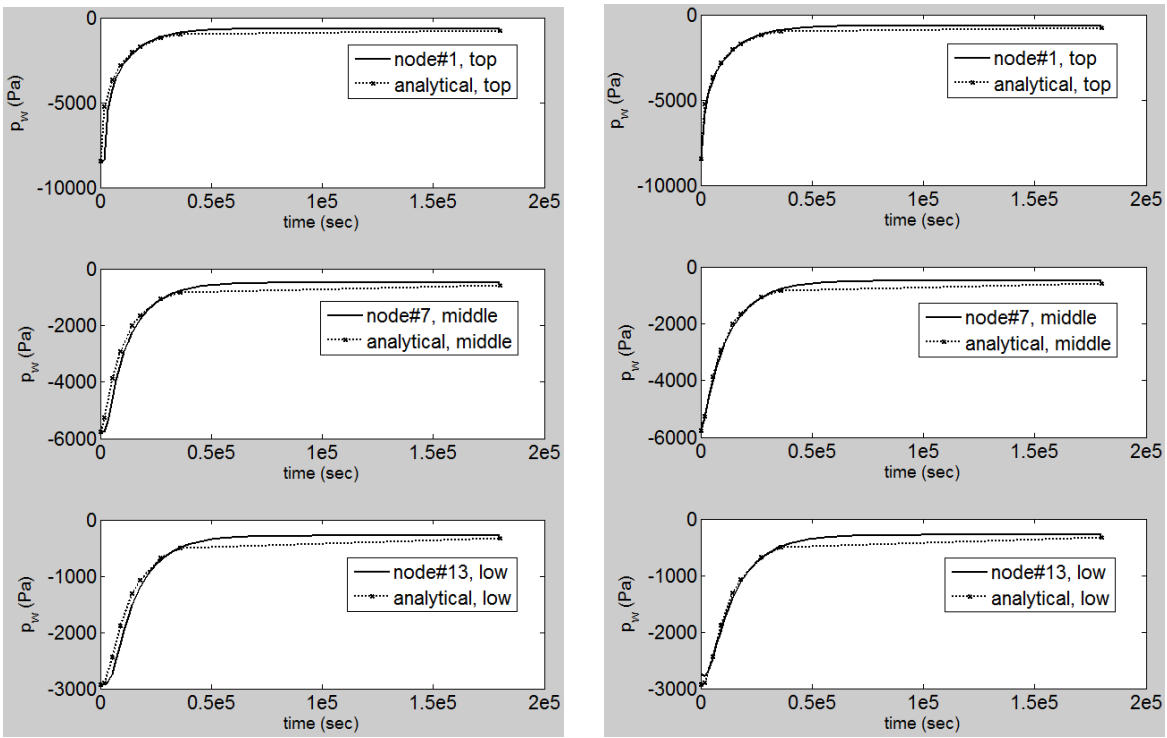

Figure 4.16: Semi-implicit linear(left) and fully-implicit nonlinear(right) solution with $\Delta t = 1hr$

example), the semi-implicit linear method is just as accurate as the fully-implicit nonlinear method, but approximately three times as fast. When accounting for elasto-plasticity through the effective stress $\boldsymbol{\sigma}'(\boldsymbol{d}^e, \boldsymbol{\theta}^e, \boldsymbol{\zeta}^e)$, a nonlinear solution will be required, and I compare in Section 4.4 whether a semi-implicit nonlinear solution method will be more efficient computationally than a fully-implicit nonlinear solution.

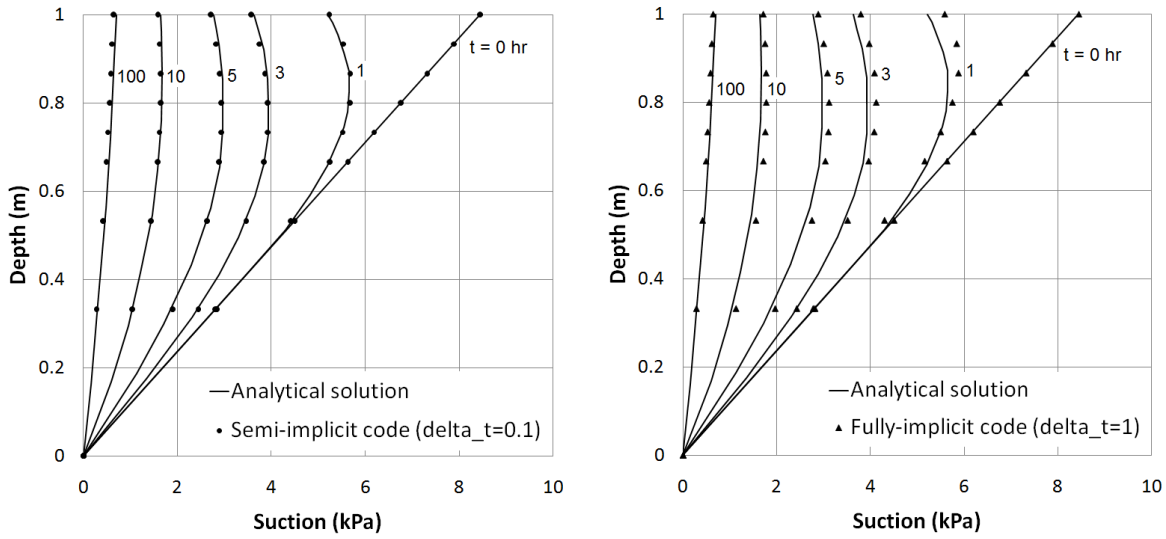

Figure 4.17: Suction variation at different time steps for Semi-implicit linear (left; $\Delta t = 0.1hr$) and fully-implicit nonlinear(right; $\Delta t = 1hr$) solution

The next example considers an application of traction t^σ, as depicted in Figure 4.14 using the relative permeability and degree of saturation in equation (4.18), linear isotropic elasticity is assumed to govern the effective stress $\boldsymbol{\sigma}'$, and we use $\chi = S$ in the definition of the effective stress (equation (2.24)). The additional parameters needed are shown in Table 4.5.

Figure 4.18(left) shows that the traction is ramped up over 6min, with total simulation time of 10hrs. Because the time step must be equal to or smaller than 6min to resolve the ramp up of t^σ, there is little difference in results between semi-implicit liner and fully-implicit nonlinear solution. Thus, the semi-implicit linear scheme is used because it is faster. The various p_w with and without traction applied is shown in Figure 4.18. This figure(left) shows that p_w increases upon application

Table 4.5: Parameters of monolithic coupled deformation-flow for partially saturated analysis

Soil parameters	Value
λ	2.9×10^7 Pa
μ	7×10^6 Pa
t^σ	1×10^6 Pa
n_0	0.42
S^w	$5S_0^w$

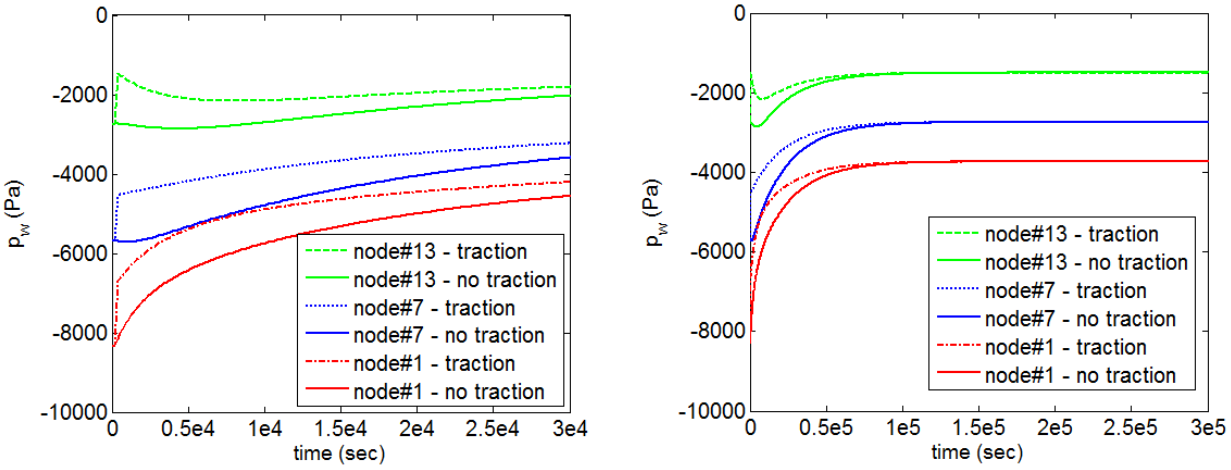

Figure 4.18: Effect of traction of p_w for short term, 10hrs(left) and long term, 100hrs(right), $\Delta t = 0.05hr$

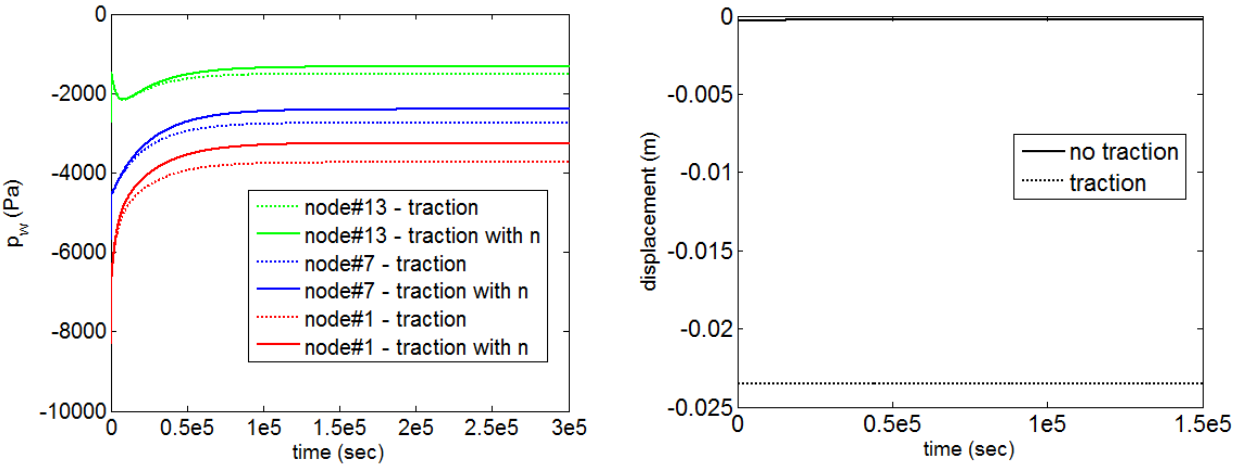

Figure 4.19: Effect of porosity of p_w and displacement due to traction

of t^{σ}, then decreases as the infiltration water seepage S^{w} continues to increase the volume fraction of water n^{w}. This figure(right) shows that each level result obtained from p_w with and without traction merges into the same value through the simulation time of 100hrs (steady state).

Figure 4.19(left) shows the difference when including the porosity dependence of permeability. When considering the porosity dependent permeability, the deformable soil by seepage and flow processes saturates faster than the case using the permeability without porosity factor. The reason is why pore size shrunk due to traction makes a deformable soil saturated at the same volume fraction of water.

The displacement in Figure 4.19(right) shows that without traction there is a small displacement as a result of gravity, while with it there is no noticeable 'consolidation' of the displacement, although it does increase slightly, and becomes more negative as the excess p_w is dissipated. This analysis currently assumed that $p_a = 0$. But, there could be a build up and dissipation of excess pore air pressure p_a during application of the ground surface traction t^{σ} (Section 4.2.4). Hence, the formulation can be extended to solve for p_a as a separate nodal degree of freedom with results in Section 4.2.4. The triphasic mixture approach considering the pore air pressure(p_a) may lead to provide more information and include the real physical behavior at the specific condition, for example, an air storage problem in an aquifer[70] and CO_2 geo-sequestration problems[56].

The evolution of relative and saturated permeability plotted in Figures 4.20 and 4.21 shows the effect of porosity on partially saturated consolidation simulation. When considering the porosity of soil, the relative permeability k_{rw} increases due to increment of water part in soil porosity, as the increase of saturation in Figure 4.20(right). While the saturated permeability k_s decreases due to the compression of porosity caused by a traction when considering the porosity due to a traction. The saturated permeability is the intrinsic permeability $\varkappa$ divided by water viscosity η_w, $k_s = \dfrac{\varkappa}{\eta_w}$. And then, the intrinsic permeability is $\varkappa = l^2\delta(n)$. The expression of $\delta(n)$ is given as $\delta(n) = \dfrac{n^3}{(1-n^2)}$ by Kozeny-Carman's formula. Consequently the saturated permeability k_s decreases as the value of $\delta(n)$ decreases. In this example, the total permeability k_w with consideration of porosity is decreased because the reduction of saturated permeability is larger than the increment of relative

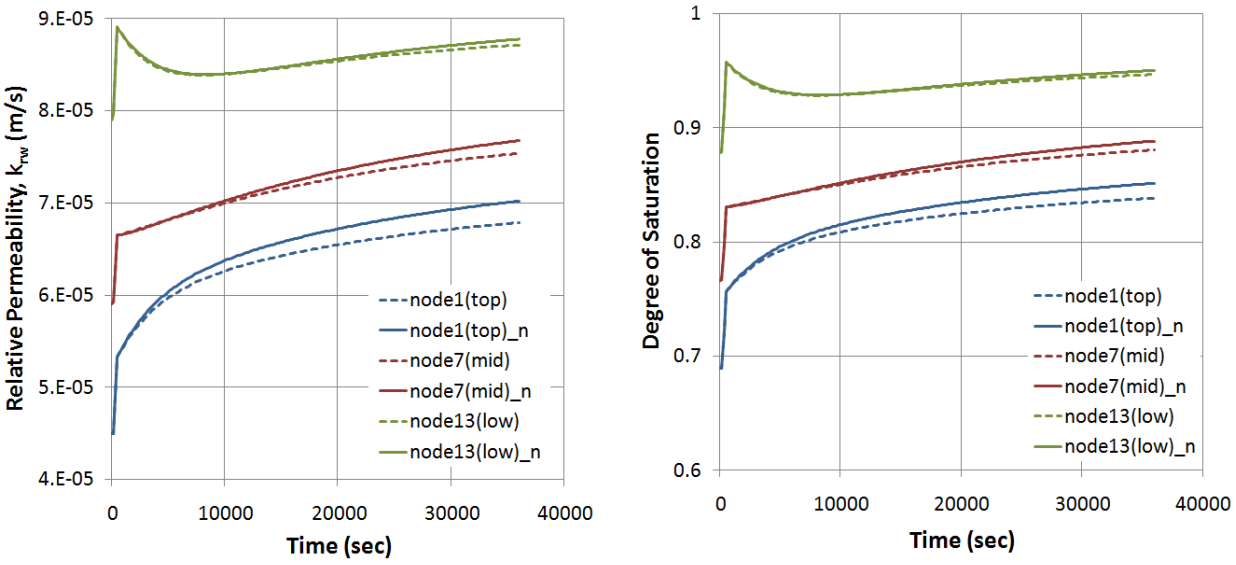

Figure 4.20: Comparison of relative permeability k_{rw}(left) and saturation S(right)

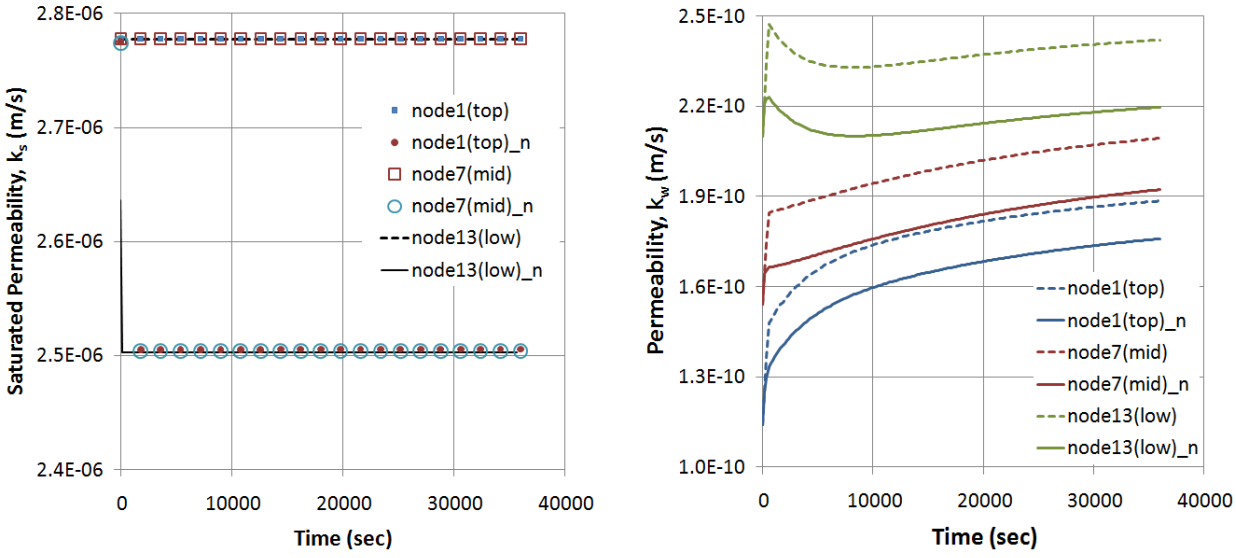

Figure 4.21: Comparison of saturated permeability k_s(left) and permeability k_w(right)

permeability.

4.2.3 Two-field coupling analysis of flow and deformation for linear elastic soil solid skeleton

The flow and deformation coupled analysis of a partially saturated soil is simulated with both staggered and monolithic numerical codes, SEEP/W–SIGMA/W and Matlab. The simulation of infiltration and total displacement during an external load(traction) using 3, 8 and 30 element meshes for both programs is performed. In order to compare the negative pore water pressures (or matric suction) in both codes, the silty soil that numerical results of seepage profile were similar each other is used. The partially saturated hydraulic conductivities applied to the codes is van Genuchten relationships[90] (equation (4.9)). The size of soil column is H:3m × W:1m and the pore water pressures at top(node 1), mid(node 7), and low(node 13) point with the same initial and boundary conditions as shown in Figure 4.14 are plotted. The geometry of simulation composes of 3 nine-node isoparametric Lagrangian elements, a two-dimensional plain strain with nine integration Gauss points has been used, and a backward semi-implicit scheme was used for time integration.

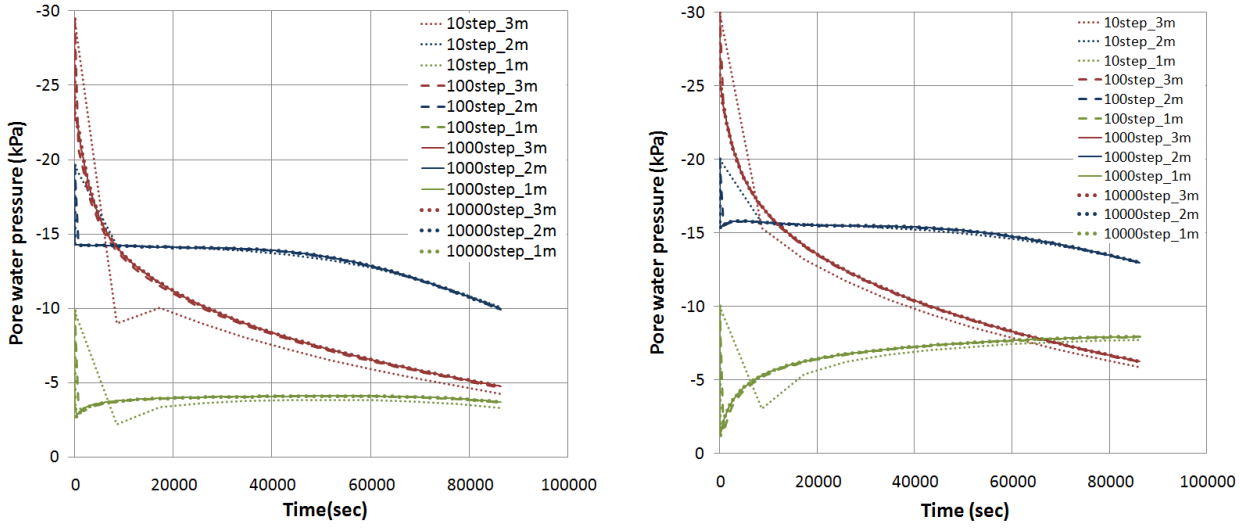

Figure 4.22: Time-step refinement study with SEEP/W–SIGMA/W(left) and Matlab(right)

SIGMA/W is used together with SEEP/W to perform the staggered coupled analysis. Although SIGMA/W calculates the deformations resulting from pore water pressure changes while SEEP/W calculates transient pore water pressure changes, the stress-deformation and seepage dissipation equations are solved by a fixed way regardless of various time-steps. Figure 4.22 shows the time-step refinement study with SEEP/W–SIGMA/W and Matlab codes. The total time period is 1 day (= 86400 sec) and the results are plotted by 4 kinds of time-steps (Δt), such as 8.64, 86.4, 864 and 8640 sec. The traction (1000 kPa) is applied at the initial time-step of each simulation in 8 elements. The staggered coupled analysis is unrelated to small time step for better accurate solution as shown in time-step refinement study. Predicted pore water pressure estimated in SEEP/W for total time is used for stress-strain analysis in SIGMA/W.

Monolithic coupled analysis used in Matlab code can describe that negative pore water pressure change due to seepage leads to changes in stresses and to deformation of a soil. Similarly, stress changes modify the seepage process since soil hydraulic properties such as porosity, permeability and water storage capacity are affected by the changes in stresses. While the analysis of coupled SEEP/W and SIGMA/W is performed in a staggered manner separately. When traction is applied at the first time step, water flow causes a compacted soil obtained from Sigma/W to be saturated quickly, and their hydraulic relationship calculates that soil skeleton behavior by external loading influences partially saturated permeability in each time step. Two manners of coupled analysis produce a difference of negative pore water pressure with the passage of time as shown in Figure 4.23 and 4.24(left). The comparisons of suction profiles describe the behavior resulting from both programs used the same elements, such as 3, 8 and 30 elements, to carry out more accurate results as well as sufficient conditions for stability in finite element analysis. The effect of porosity that performed by Matlab code shows a small difference between dotted and solid lines because of one time loading at the first time step and the variation of pore water pressure due to porosity consideration is larger at top level than low level of the soil column. Figure 4.24(right) shows that displacements on ground surface of both coupled analyses are similar due to the same elastic moduli.

Staggered coupled analysis estimates individually for seepage and stress analysis. Namely,

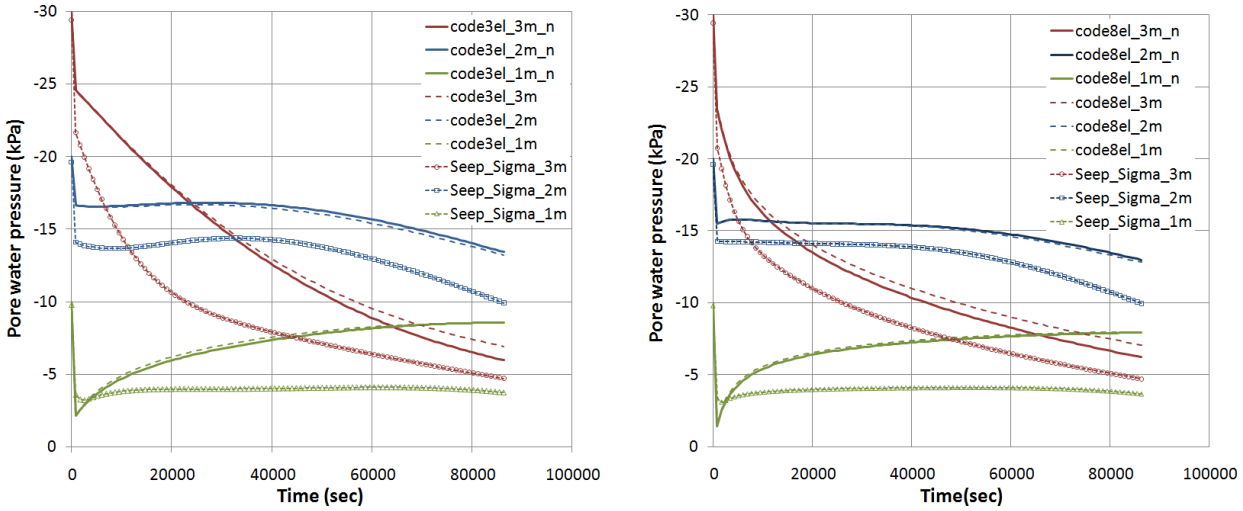

Figure 4.23: Comparison of SEEP/W–SIGMA/W and Matlab in coupled analysis; pwp by 3 elements(left) and pwp by 8 elements(right)

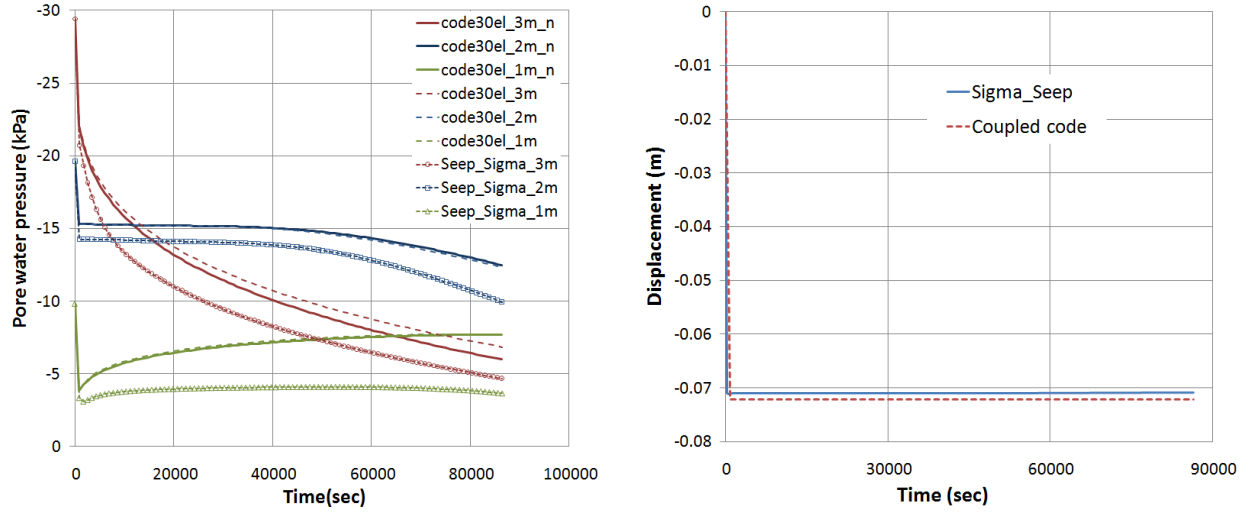

Figure 4.24: Comparison of SEEP/W–SIGMA/W and Matlab in coupled analysis; pwp by 30 elements(left) and displacement(right)

after completing seepage and flow process in rigid soil body in Seep/W, Sigma/W is computed for soil deformation using results obtained from Seep/W. Although these results obtained from the simulation with the same initial and boundary conditions should be verified by field data or experimental test, two different formulations of coupled analysis represent a different mechanism that couples solid deformation with fluid pressure in a partially saturated soil as shown in Figure 4.23 and 4.24(left). The monolithic coupled hydromechanical model would be preferred to estimate the behavior and stability of a partially saturated soil subjected to external loads, especially rainfall because the seepage and stress-deformation problems occurred in the site are linked each other simultaneously.

4.2.4 Two- & three-field coupling analysis for linear elastic soil

Numerical models of partially saturated soil developed by many authors are based on a common assumption that the air phase remains constantly at atmospheric pressure in the partially saturated zone. This means that air pressure is equal to zero which can be ignored in a soil. Morel-Seytoux and Billica[72] presented that the two-phase flow theory for water and air is more realistic than one-phase flow model for water with a one-dimensional mode of a rigid porous medium (semi-infinite soil column). Schrefler and Zhan[76] proposed a fully coupled model to simulate the slow transient phenomena, like consolidation, involving flow of water and air in deforming porous media, and Schrefler and Scotta[75] applied the numerical solution for two-phase fluid flow to an air storage problem in an aquifer.

The numerical simulation for the effect of pore air pressure is performed by comparing Srivastava and Yeh[81]'s analytical solution. As a first approach, the air pressure in triphasic mixture is considered by adding the air permeability of Coussy[23] based on initial, boundary conditions and permeability equations of Srivastava and Yeh.

The pore water pressure($s = 0 - p_w$) in biphasic mixture due to $p_a \approx 0$ means soil suction, but the soil suction in triphasic mixture is significantly subjected to the pore air pressure due to $p_a \neq 0$. The occurrence of pore air pressure within a soil is working for value of suction in

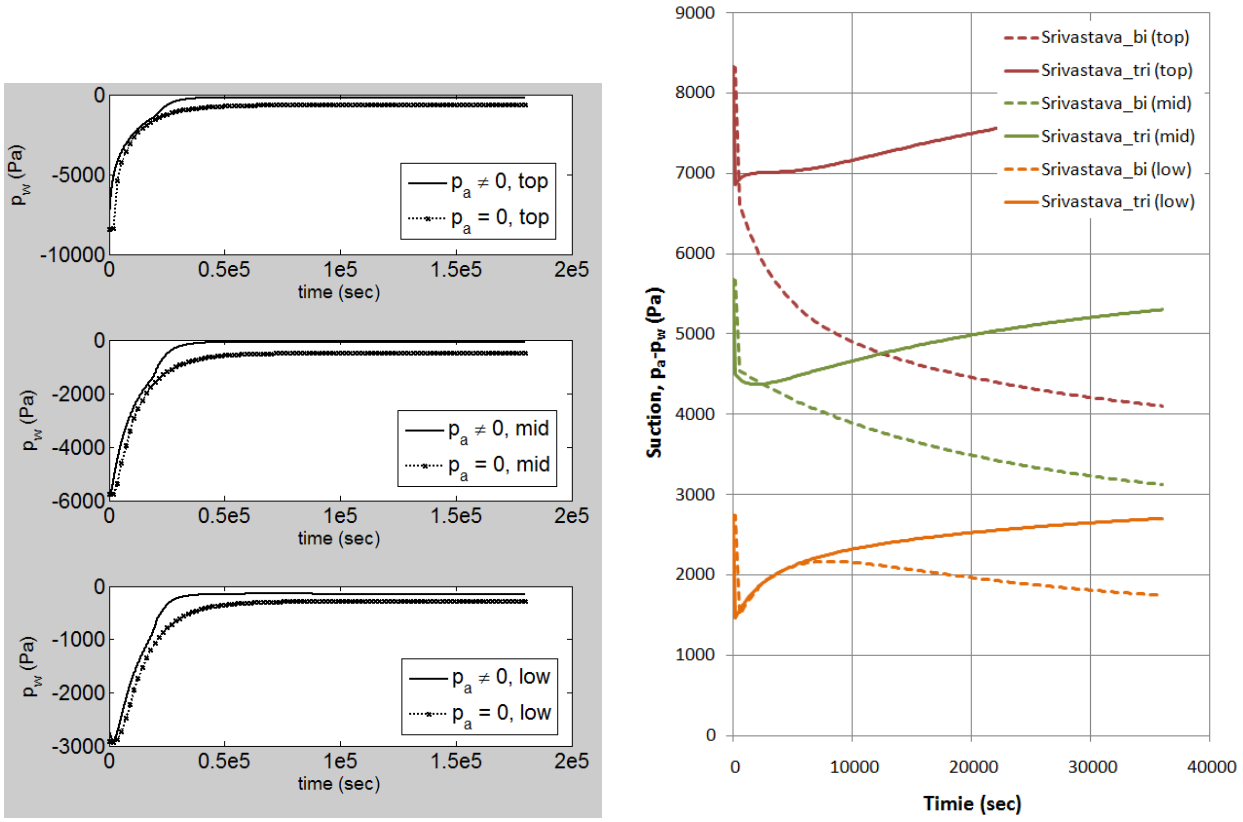

Figure 4.25: Application of ($p_a \neq 0$) to Srivastava and Yeh example

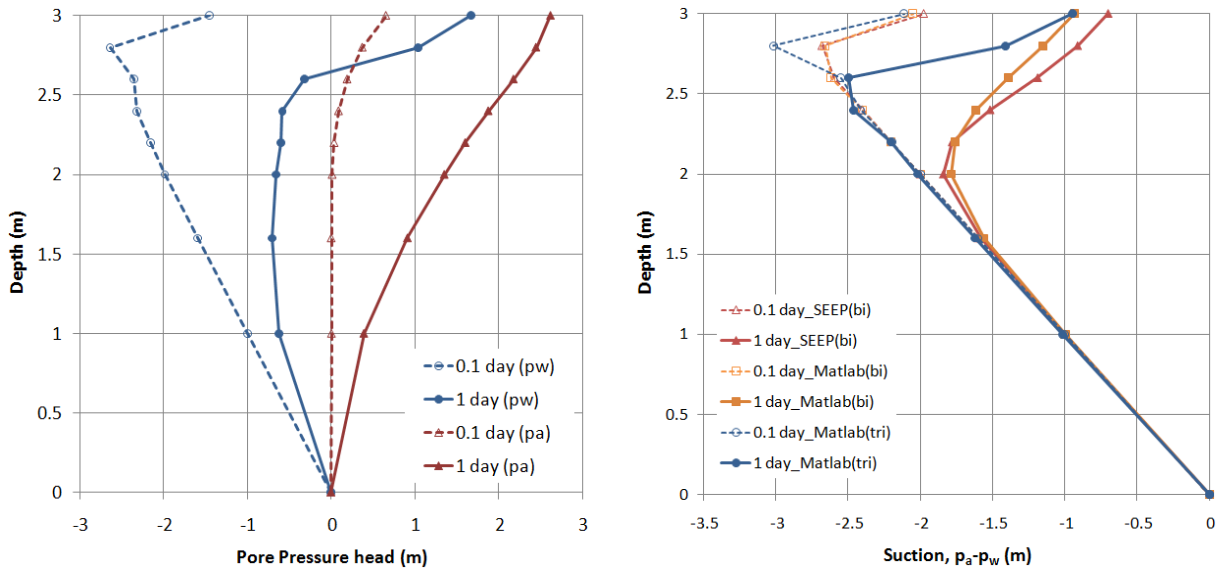

Figure 4.26: Application of pore air pressure p_a in silt

positive. Soil suction increases much by action of pore air pressure at the flow-deformation coupled analysis rather than partially saturated flow analysis. In Figure 4.25(left), the pore water pressure in triphasic mixture closer approaches zero (saturated condition) than that of biphasic mixture, but triphasic mixture has larger suction due to action of pore air pressure in consolidation test with a traction as shown in Figure 4.25(right). Generally the biphasic formulation matches the experimental results better than the triphasic formulation in the geotechnical problems such as a vadose zone, and then considering pore air pressure should be applied to the specific condition such as an air storage problem in an aquifer or CO_2 geo-sequestration to reduce greenhouse gas emission from fossil fuels.

The effect of pore air pressure in triphasic mixture is estimated to observe the profile of suction in the soil as shown in Figure 4.6. By using the same initial and boundary conditions, the profile of suction in silt soil is compared with that of suction in triphasic silt condition. The left of Figure 4.26 shows the distribution of pore air and water pressure, and the right shows difference of suction profile between triphasic and biphasic silt conditions. The result also shows that the soil has the bigger magnitude of suction when considering the pore air pressure in the soil. The bouncing point occurs at the first node beneath the ground surface such that the mesh around the surface is needed to discretize more.

As previously said, since there is no exact solution of a problem of water and air flow in deformable partially saturated soils, numerical modeling of experimental results on the drainage of a sand column is performed. For validation and application of coupling model of solid, water, and air in partially saturated soils, based on the water drainage experiment from a sand column conducted by Liakopoulos[60], the numerical solutions given by Schrefler and Scotta[75] and Gawin et al.[38] are compared to various results obtained from Matlab code. The mesh of this example composed of a column of 20 nine-node isoparametric Lagrangian elements of equal size were employed for all numerical simulations. Numerical integration was semi-implicit and triphasic model associated to linear elasticity has been used with a 2D plain strain of nine integration Gauss points.

The physical experiment consisted of a soil column in 1m high, and a constant flow through

Table 4.6: Soil parameters for triphasic mixture implementation

Soil parameters	Value
Young's modulus, E	1.3 MPa
Poisson ratio, ν	0.4
Solid real density, ρ^{sR}	2000 kg/m^3
Bulk modulus of air, K_a	0.1 MPa
Water real density, ρ^{wR}	1000 kg/m^3
Air real density, ρ^{aR}	1.2 kg/m^3
Initial porosity, n	0.2975
Intrinsic permeability, $\varkappa$	4.5×10^{-13} m^2
Water viscosity, η_w	1.0×10^{-3} Pa s
Air viscosity, η_a	1.8×10^{-5} Pa s

the soil column corresponding to a water pressure gradient is equal to zero initially. Starting time steps, water inflow is cut at top of the soil column and water is flowed out at the bottom. Air pressure is equal to atmospheric pressure at both for top and bottom of the column with zero vertical load at the top, and no deformation is at the bottom and on lateral walls of the column. The gravity-governed changes in constituent volume fractions only depend on soil and water parameters. In numerical test, in the same way as Schrefler and Scotta[75], Matlab code also uses the relationship of Brooks and Corey[18] for the relative permeability of gas pressure, and the experimental function of Schrefler and Scotta[75] for hydraulic properties of the soil as shown in equation (4.19). The material properties used for the numerical test are summarized in Table 4.6.

$$
\begin{aligned}
k_{ra} &= (1 - S_e)^2\Big(1 - S_e^{(2+3\lambda)/\lambda}\Big), && S_e = \frac{S - S_r}{1 - S_r} \\
k_{rw} &= 1 - 2.207(1 - S_e)^{1.0121}, && S = 1 - 1.9722 \times 10^{-11} \cdot s^{2.4279} \\
k_{\alpha} &= \frac{\varkappa}{\eta_\alpha}\, k_{r\alpha}, && \alpha = w, a
\end{aligned}
\tag{4.19}
$$

where η_α the dynamic viscosity and $k_{r\alpha}$ is the relative permeability of the α phase which depends on the relative saturation S_α through suitable experimental relationship $k_{r\alpha} = k_{r\alpha}(S_\alpha)$, $\varkappa$ is the intrinsic permeability, and the respective degrees of saturation S_w and S_a sum to one, $S_w + S_a = 1$. Even if the data for the mechanical behavior and parameters of the Del Monte sand used by

Liakopoulos were missing and unpublished, they have been obtained numerically their solutions by trial and error techniques. Thus, λ is 0.1 and the residual saturation S_r is 0.06689 for sand[75, 38].

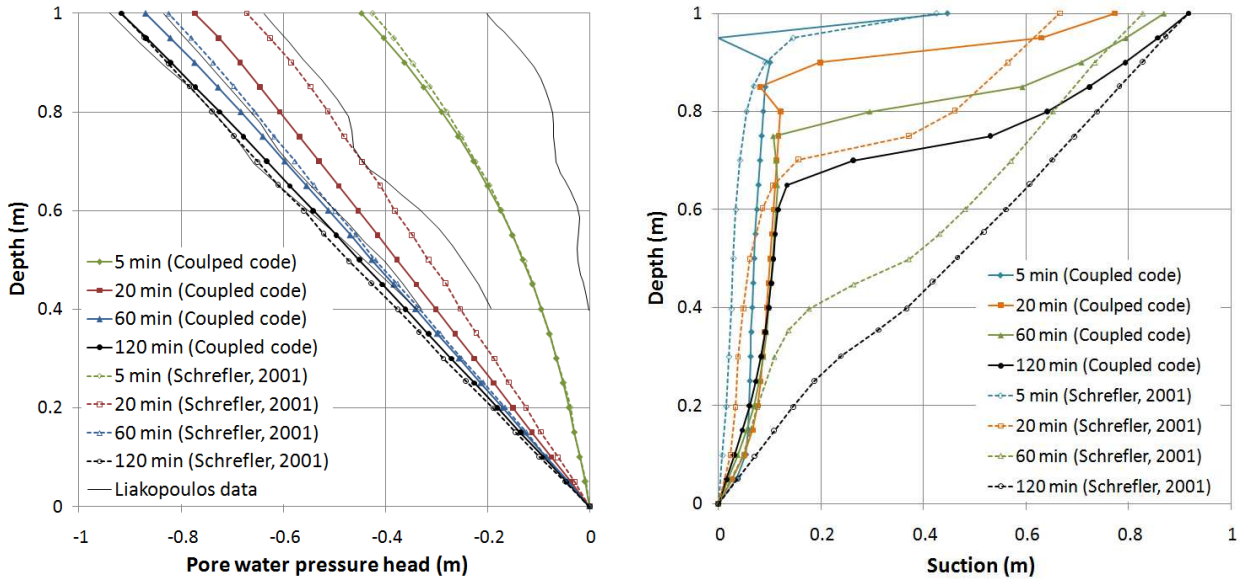

Figure 4.27: Numerical results and experimental measurements from Liakopoulos' test in pore water pressure and suction

The numerical solutions of triphasic mixture analysis obtained from Schrefler and Scotta[75] based on the Liakopoulos' experimental test are compared to that of Coupled code as shown in Figures 4.27-4.29. As no measurement of pore air pressure was made by Liakopoulos, numerical results are plotted and also compared to Schrefler & Scotta[75] and Gawin et al.[38]. The evolution of air pressure is more sensitive to the analysis method than that of water pressure. The comparison of pore water pressure in Figure 4.27(left) is similar to that of Schrefler and Scotta[75], but the results (right figure) of Coupled code have obtained suction increases slower than that found by Schrefler and Scotta since air pressure response from methods applied has sensitive characteristic as shown in suction evolution of Figure 4.28.

Comparing with Gawin et al.[38] and Schrefler and Scotta[75], the air pressure profiles from Matlab code fit closer to that of Gawin et al. than that of Schrefler and Scotta. These differences

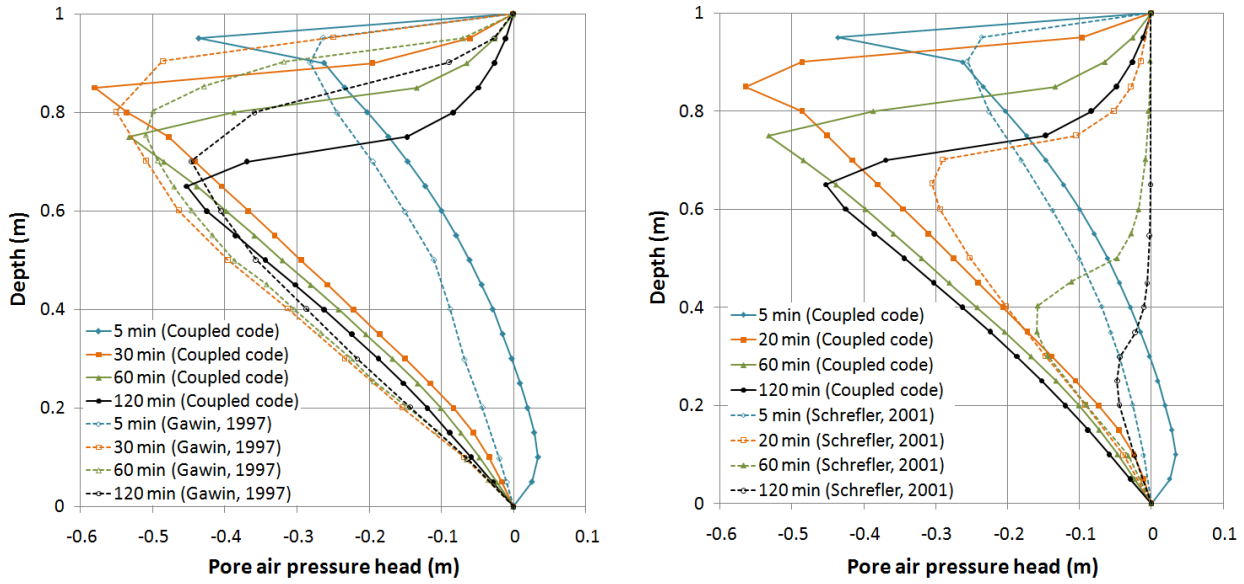

Figure 4.28: Numerical results of p_a compared to Gawin et al.(1997) and Schrefler & Scotta(2001)

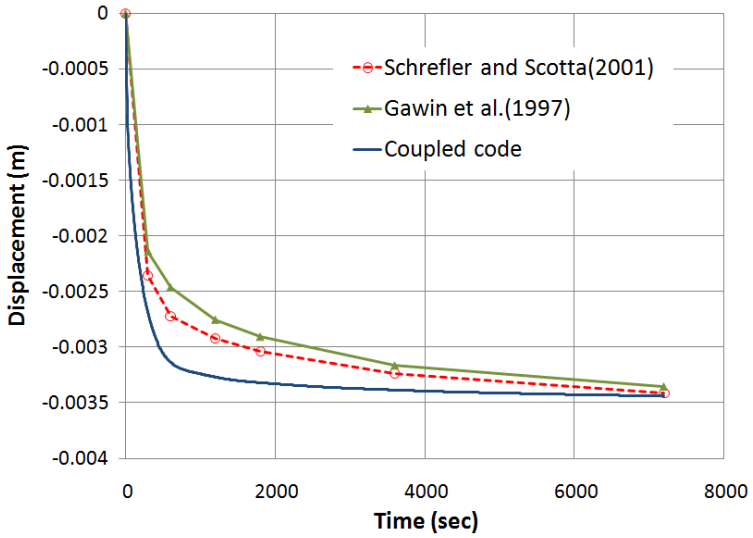

Figure 4.29: Displacement of top surface in drainage test of triphasic mixture

are produced by choosing different sets of governing equations and numerical algorithms between Schrefler and Scotta, and Gawin et al.. Particularly, the averaged density of the mixture $\rho = (1-n)\rho^{sR} + nS\rho^{wR} + (1-n)(1-S)\rho^{aR}$ and bulk modulus of solid grains (10^6 MPa) and water (2×10^3 MPa) used by Schrefler and Scotta are different from those used by Gawin et al. and my own Matlab code. Gawin et al. and Matlab code derived the mass balance equation assuming the bulk moduli (K_s and K_w) are infinite due to large values and the averaged density of the mixture is $\rho = (1-n)\rho^{sR} + nS\rho^{wR} + n(1-S)\rho^{aR}$.

In Figure 4.29, the vertical displacements at the top surface of soil sample shows a little difference during the intermediate progress, but the final vertical displacement coincides with those of Schrefler and Scotta[75], and Gawin et al.[38] using identical initial conditions.

4.2.5 Application of various effective stress equations for linear elastic soil

The effective stress plays an important part in the deformable soil because the deformation and constitutive response of soil mainly depends on the principle of effective stress. Recently, Khalili et al.,[49] and Lu et al.[63] proposed effective stress parameter χ and suction stress using S_e respectively in a partially saturated soil referred in the previous Section 3.3.2. For Khalili et al.'s concept, in order to apply the effective stress parameter χ, the air entry value of soil-water characteristic curve is necessary to implement in partially saturated soil. In the study, it is assumed that the air entry value of each soil obtained from the literature[32, 65], for example loam=5, silt=10, clay=100 (kPa). Suction stress of Lu et al. uses the effective degree of saturation S_e for the effective stress parameter.

By using the same boundary and initial conditions (but, soil column height=3m) in Figure 4.14, the typical effective stress parameter with degree of saturation S (Lewis & Schrefler et al.[58] and Borja[12]) is compared to that with the effective stress parameter χ of the function of suction and air entry value (Khalili et al.[49]) and that with suction stress using effective degree of saturation S_e (Lu et al.[63]). Figure 4.30 shows the comparison of pore water pressure p_w and displacement at top surface under traction(1000 kPa). Even though negative pore water pressure at each node (top,

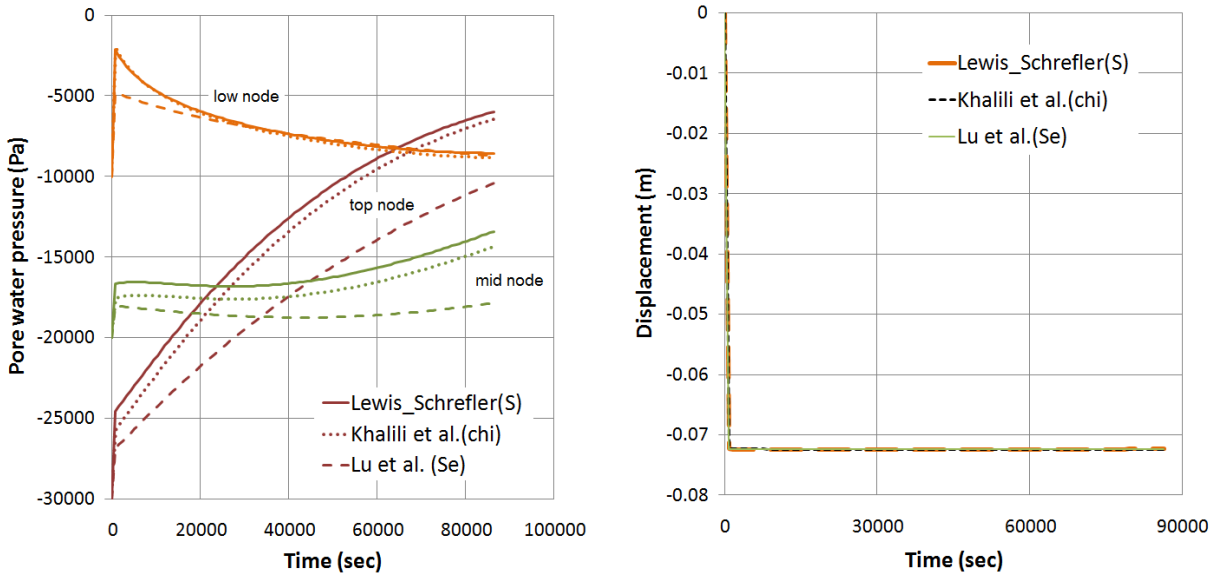

Figure 4.30: Comparison of effective stresses with S, χ and S_e

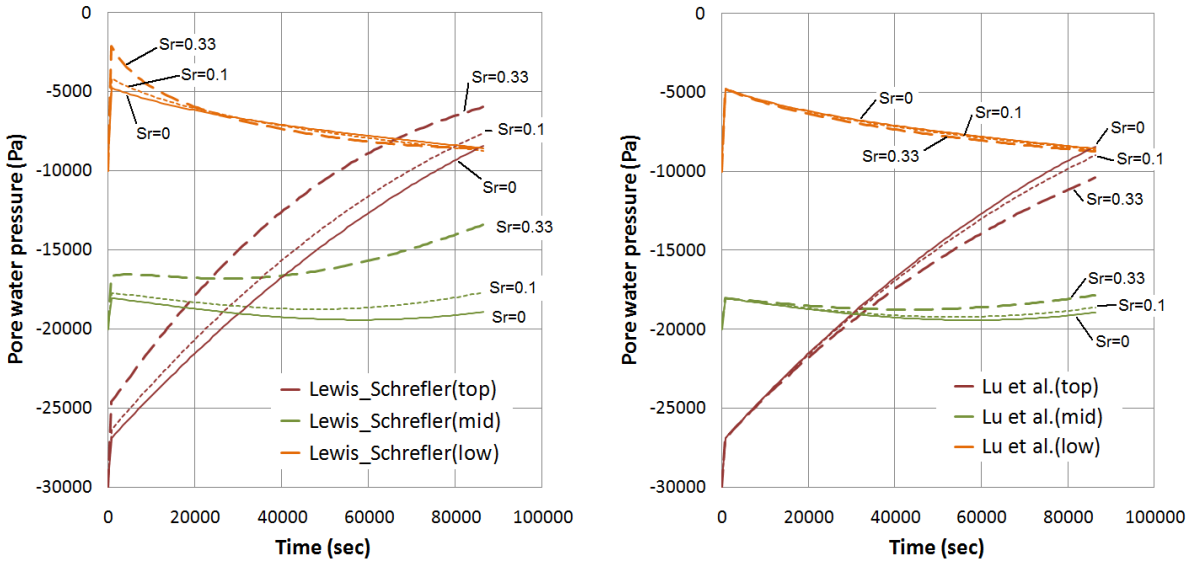

Figure 4.31: Difference between Lewis & Schrefler and Lu et al.'s curves at $S_r = 0.33$, 0.1 and 0

middle, low node) obtained from Khalili el al.'s parameter (χ) is slightly smaller than the result of Lewis and Schrefler's parameter (S), both results have the process with a same pattern because the parameter χ is defined by the average saturation rate according to various suction values as shown in Figure 3.3.

There is some differences between the effective stress concept of Lewis and Schrefler (or Borja[12]) and that of Lu and Likos in Figure 4.30. The reason is difference between degree of saturation S and effective degree of saturation S_e.

$$S = S_r + S_e(1 - S_r) \tag{4.20}$$

$$S_e = \frac{1}{\left[1 + (\alpha s)^{\mathrm{n}}\right]^{\mathrm{m}}} = \frac{S - S_r}{1 - S_r} \tag{4.21}$$

The numerical simulations (Figure 4.30) of three effective stress concepts are estimated by applying 0.33 of residual degree of saturation S_r to the same material parameters of silty soil used in previous simulations(Table 4.1). If S_r approaches zero, both of Lewis & Schrefler and Lu et al.'s plot will agree on the same curve as shown in Figure 4.31. The final displacements obtained from three equations show the same results (Figure 4.30(right)). Khalili et al.'s effective stress equation will also be similar to the pattern of Lewis and Schrefler's curve variation. Basically clayey soils have higher residual degree of saturation than those of silty or sandy soils, and so clayey soils would retain larger matric suction with pass the time during this simulation. The variation of pore water pressure calculated by Lu et al.'s effective stress (Figure 4.31(right)) show a solution appropriate for the response of soil types. The displacement solution in Figure 4.30(left) is expected to be different when an elastoplasticity model as a function of suction s is included.

If the elastic bulk moduli ratio $(1 - K/K_s)$ which Borja and White[17] present is used, a certain material may have different displacements on the top surface. In this study, however, the deformation of elastic soils is rarely affected by effective stress parameters because the elastic moduli are the same and it is assumed $K_s \approx \infty$ for all cases, but for elastoplasticity their should be a difference. All effective stress concepts are the function of matric suction and then these are related to the hydraulic properties of a soil such as pore water pressure, water storage and

soil-water characteristic curve. The variation of matric suction in a partially saturated soil may be significant factor to estimate the effective stress response for constituent modeling of the solid matrix for elastoplasticity.

4.3 Numerical Simulation of Hyperelasto-Plastic Model for Saturated Soil

The behavior predicted by the hyperelasto-plastic model is compared to those predicted by the conventional modified Cam-clay model[15] and coupling plasticity and energy conserving elasticity Cam-clay model[16]. The plasticity problem of the conventional Cam-clay model, hypoelasto-plastic model, is solved by integrating of the rate-constitutive equation.

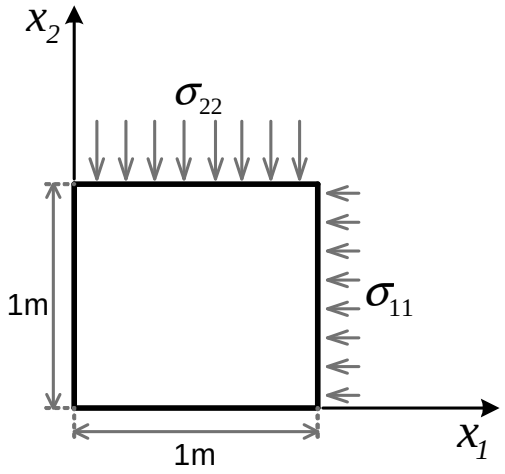

Figure 4.32: Diagram for plane strain example

$$\begin{aligned} \dot{\sigma}_{ij} &= c^e_{ijkl}\dot{\epsilon}^e_{kl}; \qquad \dot{\epsilon}^e_{kl} = \dot{\epsilon}_{kl} - \dot{\epsilon}^p_{kl} \\ K &= \left(\frac{1+e}{\kappa}\right) p' \,, \qquad \mu = \frac{3K(1-2\nu)}{2(1+\nu)} \end{aligned} \tag{4.22}$$

where σ_{ij} is effective Cauchy stress tensor, ϵ_{kl} is small strain tensor, c^e_{ijkl} is elastic stress-strain tensor, and overdots imply a time differentiation. The linear elasticity c^e_{ijkl} can be expressed in

Table 4.7: Soil parameters for Cam-clay simulations

Material parameters	Hyperelastic	Hypoelastic
Initial shear modulus, μ_0	5400 kPa	5400 kPa
Constant coefficient regarding μ, $\bar{\alpha}$	60	-
Initial Young's modulus, E	11880 kPa	11880 kPa
Poisson ratio, ν	-	0.103
Initial porosity, n_0	0.7	-
Initial void ratio, e_0	-	4.28
Elastic compressibility index, $\tilde{\kappa}$	0.018	-
$\kappa(= v_0\tilde{\kappa})$	-	0.060
Virgin compressibility soil index, $\tilde{\lambda}$	0.130	-
$\lambda(= v_0\tilde{\lambda})$	-	0.433
Slope of critical state line, M	1.05	1.05

terms of the elastic bulk modulus K and shear modulus μ, and the elastic moduli depend on the effective confining stress. But the formulation of hyperelasticity has the nonlinear elasticity based on a stored energy function $\psi(\epsilon^e_{ij})$ expressed in terms of elastic component of the small strain tensor ϵ^e_{ij} as referred in the previous Section 3.1.

$$\begin{aligned} \psi(\epsilon^e_{ij}) &= \psi(\epsilon^e_v, \epsilon^e_s) = \tilde{\psi}(\epsilon^e_v) + \frac{3}{2}\mu(\epsilon^e_s)^2 \\ \sigma'_{ij} &= \frac{\partial \psi}{\partial \epsilon^e_{ij}}\,, \qquad c^e_{ijkl} = \frac{\partial \sigma'_{ij}}{\partial \epsilon^e_{kl}} = \frac{\partial^2 \psi}{\partial \epsilon^e_{ij} \partial \epsilon^e_{kl}} \end{aligned} \tag{4.23}$$

Figure 4.32 shows diagram for soil sample test with unit dimensions in 2D plane strain in Borja et al.[16]. The soil specimen is assumed to be normally consolidated and confined by an initial stress of $\sigma_{11} = 90$ kPa. Three kinds of simulation are compared to show the difference between hyperelasto-plastic and hypoelasto-plastic model. The elastic shear modulus of hyperelasto-plastic material varies with mean normal stress p' and the hypoelasto-plastic material has a constant Poisson's ratio. The parameters used for this comparison are summarized in Table 4.7. Note that the compression indices λ and κ of hypoelasto-plastic material are related to the compression indices $\tilde{\lambda}$ and $\tilde{\kappa}$ of hyperelasto-plastic material by the initial specific volume v_0. The parameters of each material have been selected in order to provide the same initial values of elastic shear moduli

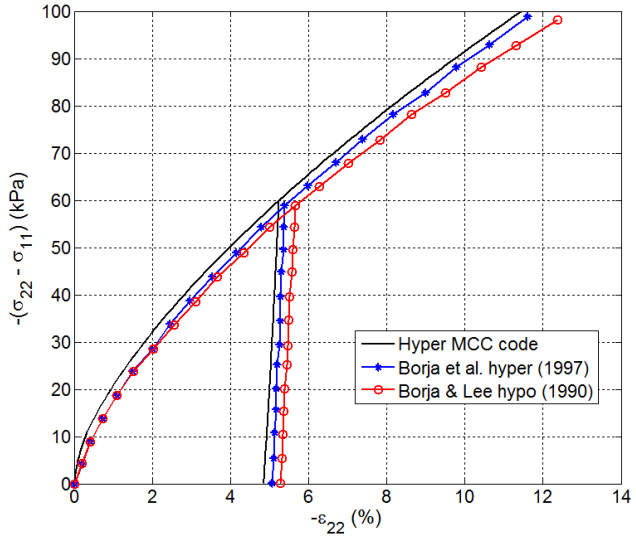

Figure 4.33: Stress-strain curves in 2D plane strain test

Table 4.8: Stress path for triaxial test simulations

State	p (kPa)	q (kPa)	Description
A	90	0	Initial condition
B	90	45	Deviatoric loading
C	180	45	Isotropic loading
D	180	90	Deviatoric loading
E	180	0	Deviatoric unloading

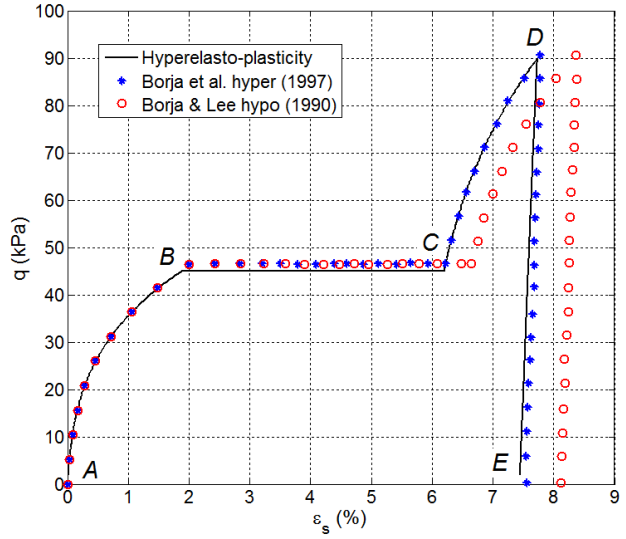

Figure 4.34: Deviatoric Stress-deviatoric strain curves through 3D triaxial loading

at the beginning of shearing.

Figure 4.33 shows a plot of the deviator stress ($\sigma_{22} - \sigma_{11}$) versus nominal axial strain ϵ_{22} as the soil is compressed vertically on the 2D plane strain test. A confining stress equal to σ_{11} is applied and then deviator stress is applied, which causes shearing of the sample, under a stress-controlled condition. The sample is unloaded at a stress difference of $\sigma_{22} - \sigma_{11} = 60$ kPa and then reloaded following the same paths. Although both models have the pressure-dependent nature of the elastic shear modulus, hyperelasto-plastic material used an energy-conserving model behave slightly stiffening for the elastic response with increasing vertical stress. The difference between blue and black lines is become the blue line is plotted by pulling off values from the figure in Borja et al.[16].

Figure 4.34 shows a sequential isotropic and deviatoric loading and unloading triaxial soil test as described in Table 4.8. It shows a plot of the deviatoric stress q versus deviatoric strain ϵ_s with the same material models subjected to initial all-around confining stress of $p_0 = 90$ kPa (state A). During the first deviatoric loading (state A-B), the response of all three curves are almost the same since all three codes uses the same elastic shear modulus. But at the end of the isotropic loading phase (state B-C), the deformation of hyper-model is different from that of hypo-model. The hypo-model has larger deviatoric strain than hyper-model at the end of the isotropic compression phase. The deviatoric strain differentials from isotropic loading are carried over by deviatoric loading (C-D). Finally, the slopes of the deviatoric unloading curve is nearly parallel each other (D-E), but there is an offset between hyperelastic and hypoelastic models.

The comparison between hyperelasto-plastic code and Borja et al.[16]'s curve shows good agreement as shown in Figure 4.33 and 4.34. As a result, the simulations demonstrate that the effective mean normal stress affects the elastoplastic soil behavior and the predicted significant behavior of soil specimen by an isotropic loading shows that the appropriate model for this soil should be applied to many geotechnical applications.

As another example of Cam-clay model, consolidation test(2D plane strain) is performed using hyperelasto-plastic, hyperelastic and linear elastic model under saturated condition. In order

Table 4.9: Soil parameters for consolidation test of Cam-clay model under saturated condition

Initial stresses, $\sigma_{0(11)}, \sigma_{0(22)}$	-84.13, -100 kPa
Initial shear modulus, μ_0	5400 kPa
Constant coefficient regarding μ, $\bar{\alpha}$	60
Initial Young's modulus, E	11880 kPa
Poisson ratio, ν	0.103
Initial porosity, n_0	0.7
Saturated permeability, k_s	1 $\times 10^{-7}$ m/s
Initial elastic strain, ϵ^e_{v0}	2.0446 $\times 10^{-4}$
Elastic compressibility index, $\tilde{\kappa}$	0.018
Initial traction, t^σ_0	-100 kPa
Final traction, t^σ	-200 kPa
Initial preconsolidation pressure, p_c	-91.975 kPa
Virgin compressibility soil index, $\tilde{\lambda}$	0.130
Slope of critical state line, M	1.05

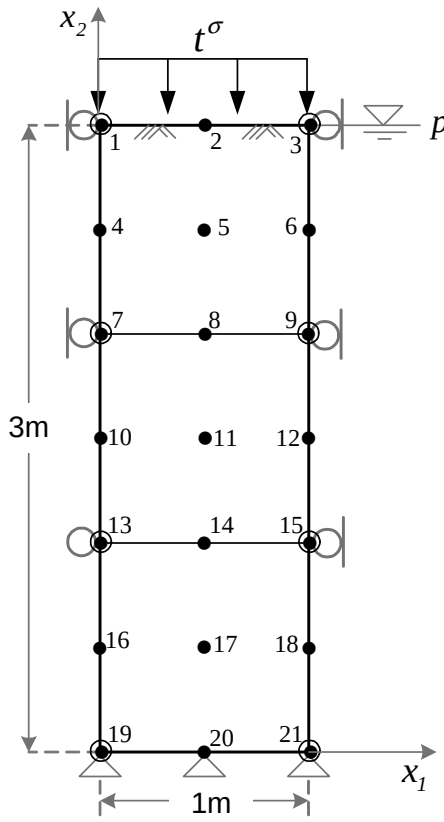

Figure 4.35: 3 element mesh for consolidation test of Cam-clay model

to maintain the same initial conditions of three types of model, a traction on the top surface is loaded to carry out by plastic behavior of a soil. The soil behaviors of hyperelastic and linear elastic model due to the traction shows different responses. The parameters used for the material is summarized in Table 4.9, and 3 element mesh for consolidation test is described in Figure 4.35.

Figure 4.36 shows the plots of three models. The left figure shows the results of excess pore water pressure at the bottom node 19 and the right figure shows the vertical displacement at the top node 1. Excess pore water pressure quickly increases at the first time step, and then it is dissipated to zero with passing time, but the dissipation of excess pore water pressure of hyperelasto-plastic model will take a long time because of volumetric compacting state by plastic behavior. Hyperelastic model which has stiffer response than linear elastic model due to pressure-dependent elastic shear modulus shows smaller increment excess pore water pressure than that of linear elastic model.

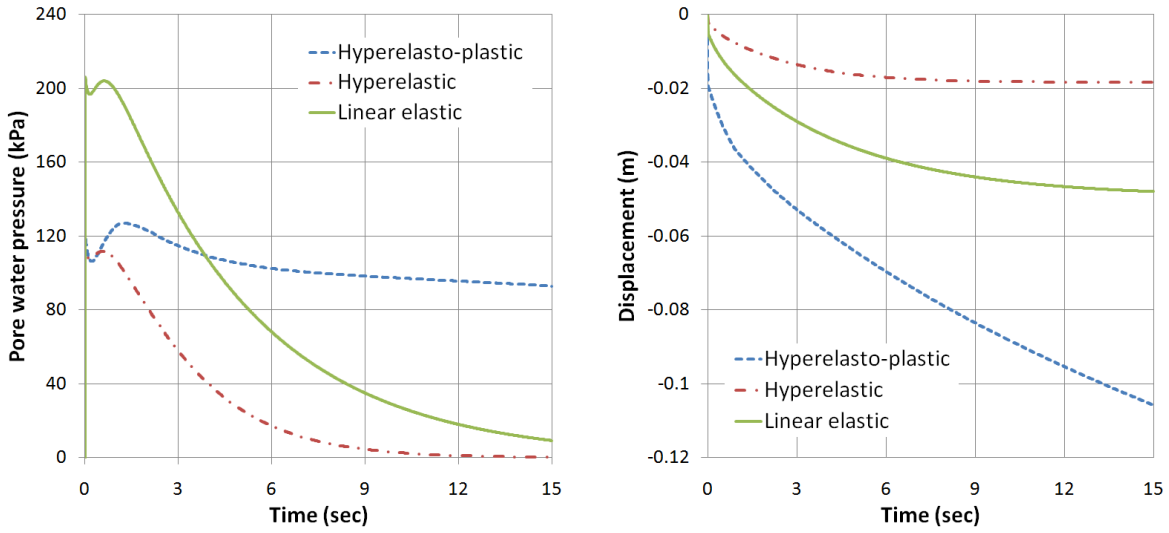

Figure 4.36: Pore water pressure and displacement of Cam-clay model at saturated condition

The displacement of hyperelasto-plastic model also need a lot of time to complete entire consolidation because NC (normally consolidation) soil is still compacting within plastic behavior. Hyperelastic model which shows stiff response has smaller vertical displacement than that of linear

Table 4.10: Parameters for hyperelastic Cam-clay plasticity under partially saturated condition

Constant coefficient regarding μ, $\bar{\alpha}$	60
Initial Young's modulus, E	11880 kPa
Poisson ratio, ν	0.103
Elastic compressibility index, $\tilde{\kappa}$	0.018
Confined and Axial stress	-90, -190 kPa
Initial preconsolidation pressure, p_c	-90 kPa
Virgin compressibility soil index, $\tilde{\lambda}$	0.130
Slope of critical state line, M	1.05
Plastic parameters	
N=2.76, k=0.6, β'=1, c_1=0.185, c_2=1.42	
van Genuchten parameters	
a=50 kPa, n=2.5, m=0.6, S=1, S_r=0.25	

elastic model.

4.4 Numerical Simulation of Hyperelasto-Plastic Model for Partially Saturated Soil

The numerical simulation of hyperelasto-plastic Cam-clay model for partially saturated soil is compared to Borja[16, 12]'s results. Based on hyperelastic Cam-clay plasticity at saturated condition[16], the assumed hyperelastic model and plasticity model parameters for partially saturated condition[12] are summarized in Table 4.10. The assumed hydraulic relations are used as van Genuchten function parameters.

In order to satisfy the saturated condition, $c(\pi) = 1$, $p_a(\pi) = 0$, $p_b(\pi) = 1$, and thus $\bar{p}'_c = p_c$. $p_c < 0$ is the saturated preconsolidation stress and then, $\bar{p}'_c$ is varied within the limit of full saturation. Suction stress and $\bar{p}'_c$ are used for plastic deformation at partially saturated condition, but at saturated condition, the evolution of preconsolidation stress p_c which can be obtained from bilogarithmic compressibility law (saturated soil) varies with the plastic deformation alone.

At 100 kPa of suction value, the stress-strain curve in 2D plane strain test shows stiffer behavior than that of Cam-clay model in saturated condition as shown in Figure 4.37. The growth

of $\bar{p}'_c$ as the suction is increased from saturated condition allow for a material to raise soil strength. The plot of partially saturated Cam-clay model is almost same with behavior of Cam-clay model at saturated condition.

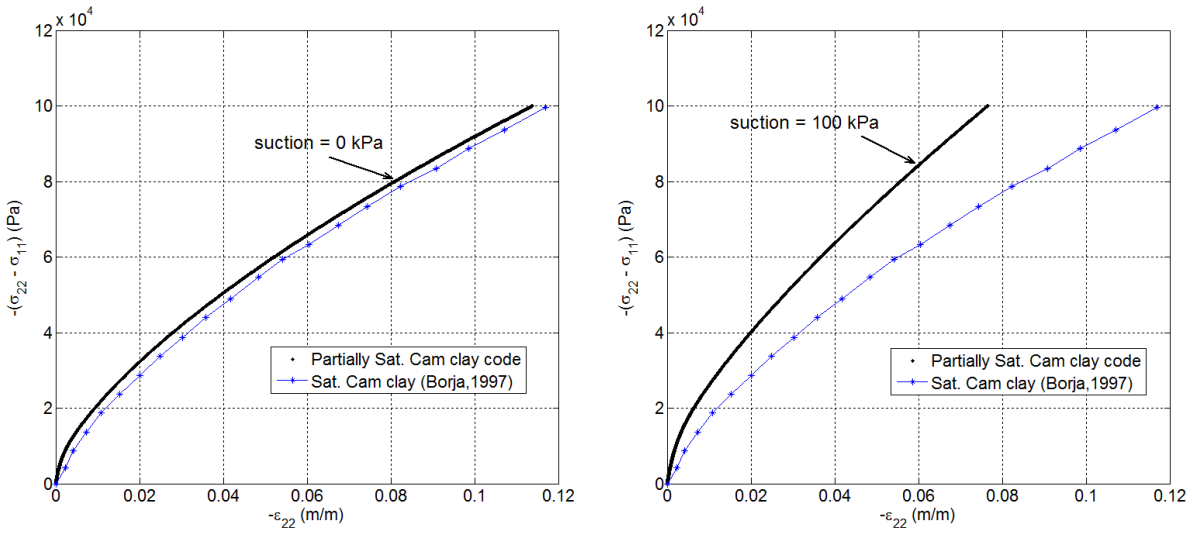

Figure 4.37: Stress-strain curves at different suction applied to Cam-clay model of partially saturated condition

4.5 Simulation of Rainfall Infiltration into Partially Saturated Slope with Gravity Loading

The process of infiltration into a soil slope due to rainfall and its effect on soil slope behavior are simulated using a two-dimensional finite element formulation for flow-deformation coupled analysis. Linear isotropic elasticity is assumed for the solid phase constitutive response for now, and will be extended for an elasto-plastic constitutive model with implementation at small strain. Conventional method of slope stability analysis, like SEEP/W–SIGMA/W, based on the concept of limit equilibrium has been widely adopted mainly due to their simplicity. These methods assume no deformation prior to failure and just give a global safety factor for a specified slip surface, but the finite element formulation can take into account the history of slope with soil deformation.

Table 4.11: Soil parameters for simulation of soil slope due to rainfall

Saturated hydraulic conductivity, k_s	5×10^{-6}, 5×10^{-5} m/s
Rainfall intensity	5.556×10^{-6} m/s
Residual degree of saturation, S_r	0.08
Hydraulic parameters, α, n	0.045 (1/kPa), 2.25
Initial porosity, n_0	0.42
Solid density, ρ_s	2.7 Mg/m^3
Shear modulus, μ	7 MPa
Young's modulus, E	20 MPa
Initial porosity, n	0.545
Gravity, g	9.8 m/s^2

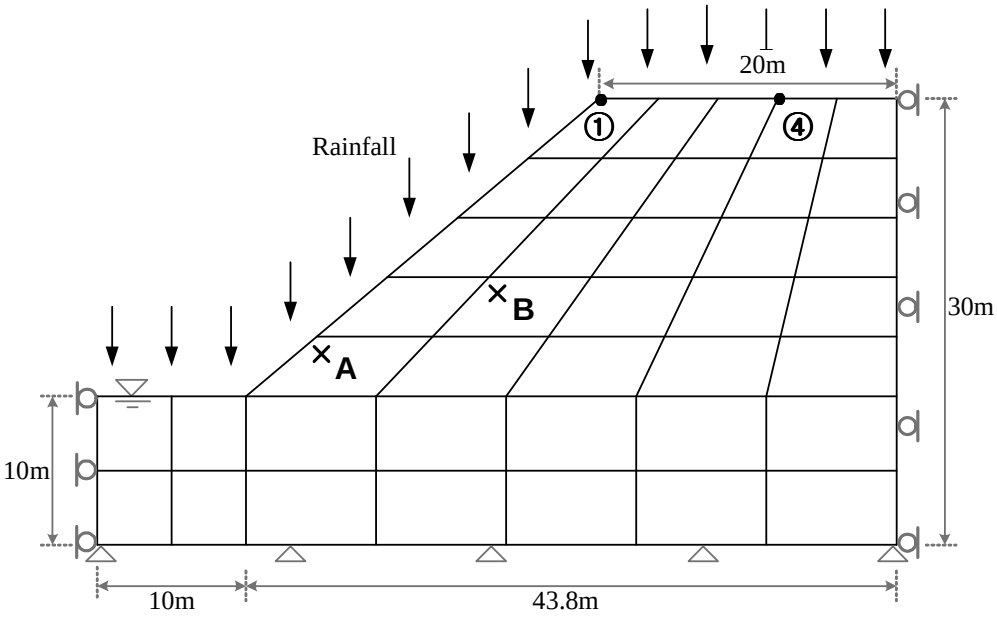

Figure 4.38: Domain of numerical analysis for slope stability

The behavior of a partially saturated soil slope is dependent on the distribution of pore water pressure as well as the deformation of soil skeleton. The flow-deformation coupled analysis is performed for future estimation of slope stability, comparing with results obtained from coupled finite element analysis in the literature by Cho and Lee[21].

The initial and boundary conditions of slope stability analysis, based on the numerical simulation employed by Cho and Lee[21], have been adopted and conducted as shown in Figure 4.38. The slope geometry has a height of 30m and an inclination angle of 40^{o} to the horizontal plane. The initial water table is assumed to be horizontal at the bottom of slope. The pore water pressure varies hydrostatically with distance above and below the water table. Above the water table, maximum negative pore water pressure is -6m (-60 kPa) and the pore water pressure increase hydrostatically with depth by 10m (100 kPa) below the water table. The soil behavior depends on only gravity as body force and rainfall (5.556×10^{-6} m/s) as external force during long duration of 66 hours (237600 sec). The slope is assumed to be homogeneous and isotropic and solved by semi-implicit scheme.

The amount of rainfall which infiltrates the ground surface depends on the saturated hydraulic conductivity k_s. If rainfall intensity which occur in a partially saturated soil is higher than k_s, the positive pore water pressures will be indicated on the ground surface. In other words, water would pond on the surface. If the rainfall intensity is less than k_s, a partially saturated zone would exist within the ground above the water table. Consequently, the infiltration capacity of the ground surface does not exceed the saturated hydraulic conductivity k_s. The simulations use two saturated hydraulic conductivities which are 5×10^{-5} and 5×10^{-6} m/s magnitudes greater and smaller than the rainfall intensity respectively, in order to study the effect of infiltration in the partially saturated soil corresponding to the rainfall intensity. Hydraulic properties, such as relative permeability and degree of saturation, are assumed according to the relationship of van Genuchten[90], and the material data used for the numerical test are summarized in Table 4.11.

Numerical simulations for rainfall-induced seepage problem on soil slope are estimated for two kinds of situation. One is that rainfall and consolidation due to gravity load are together applied

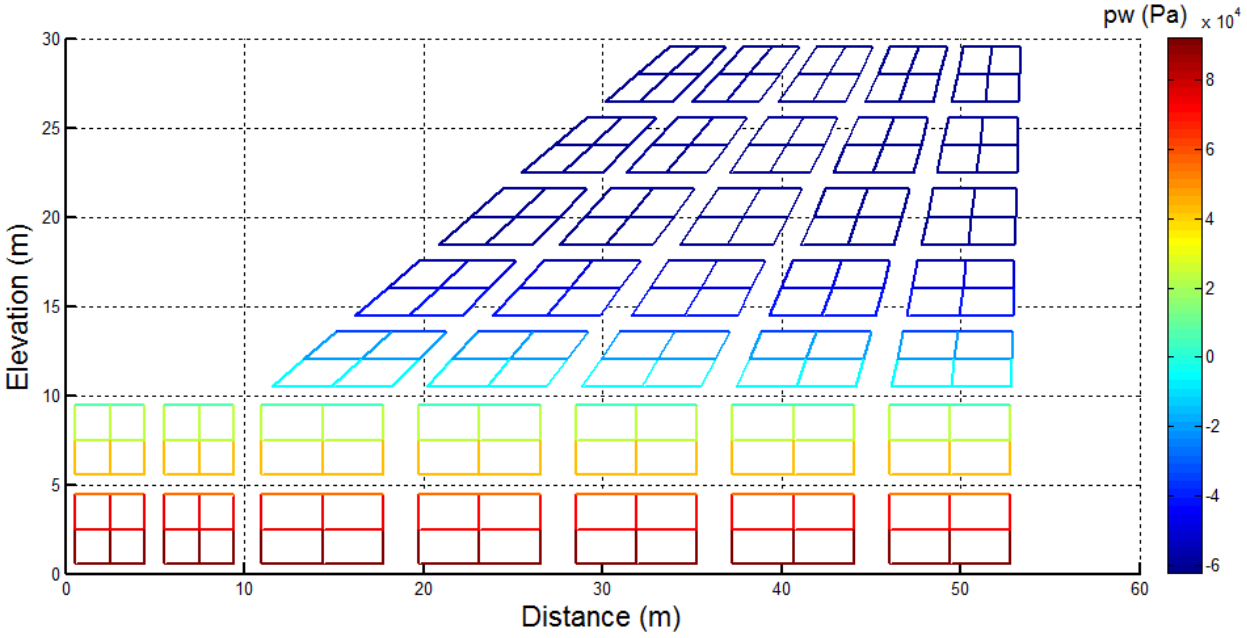

Figure 4.39: Distribution of pore water pressure at initial state

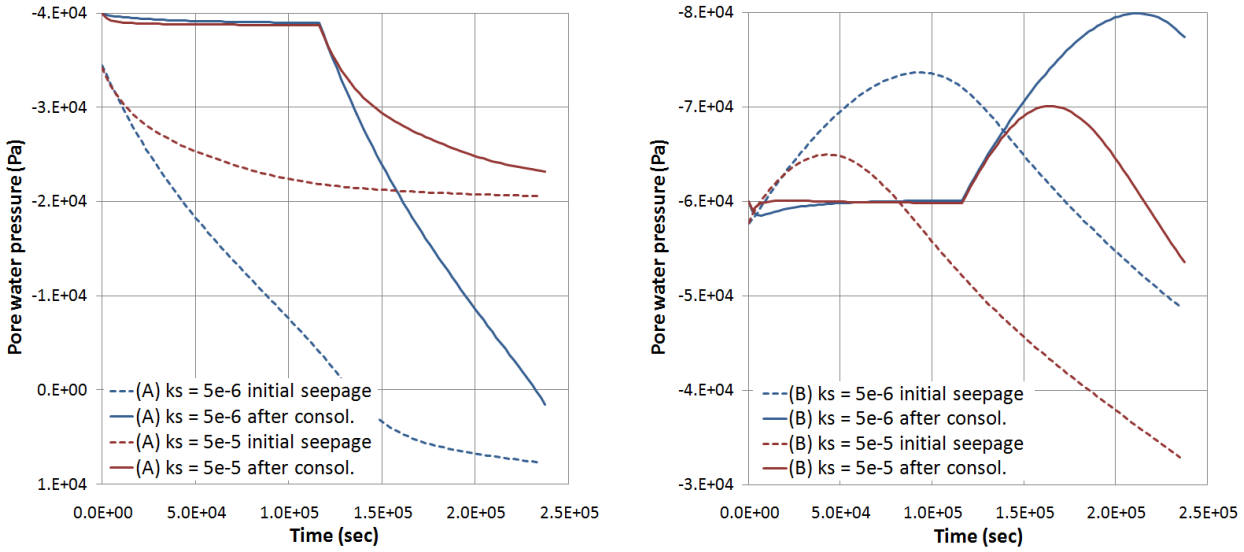

Figure 4.40: Time histories of pore water pressure at A and B points

to soil slope. The other is that rainfall is applied to the slope after completing consolidation due to gravity load. It takes around 32 hours to complete consolidation by gravity load in this simulation.

Figure 4.40 shows the time histories of pore water pressure at Gauss point A and B denoted in Figure 4.38. The point A is located near the ground surface, but the point B is the place which has some distances from the surface. When the distance of infiltration from slope surface is short, the smaller the hydraulic conductivity, the faster the negative pore water pressure reduces as shown in Figure4.40(left). When the infiltration rate is higher than the hydraulic conductivity, the excess pore water pressure occurs in the ground surface. Then, the negative pore water pressure of $k_s = 5 \times 10^{-6}$ case quickly decreases at the point A near the surface. While the negative pore water pressure of the case ($k_s = 5 \times 10^{-6}$) at the point B decreases slower than that of $k_s = 5 \times 10^{-5}$ due to the small partially saturated permeability. It takes long time for water flow to approach to the point B[21]. At the case of point B, suction increases initially and then decreases by lapse of time during the rainfall event. We should use a finer mesh to solve this problem.

Figure 4.39 shows the distribution of pore water pressure of the slope with maximum matric suction of -60 kPa at the initial state. At the end of rainfall (after 66 hrs), the excess pore water pressure(0∼5 kPa) occurs in the ground surface of slope(k_s =5×10^{-6} m/s), and the surface of slope(k_s =5×10^{-5} m/s) still keeps reduced magnitude(≈ -20 kPa) of negative pore water pressure due to rainfall as shown in Figure 4.41 and 4.42. These two contours of pore water pressure distribution are the results obtained from rainfall applied after finishing consolidation.

The vertical displacements at the nodal point of element 1 and element 4 as shown in Figure 4.38 are estimated. Figure 4.43 shows the difference between the edge and middle area on the crest of soil slope due to gravity. The displacement at the middle area on crest of slope larger than that at the edge area because of acting bigger body force in the middle area. The displacement by rainfall after consolidation due to gravity load is slightly smaller than that of both applied.

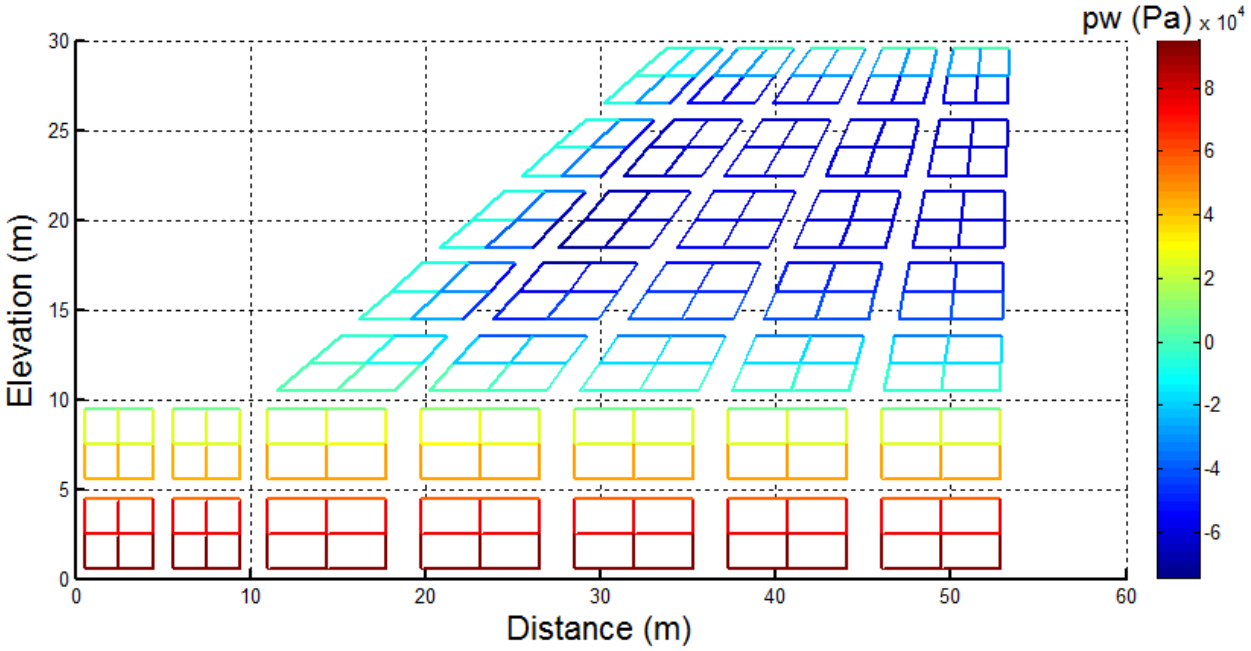

Figure 4.41: Distribution of pore water pressure after 66 hrs(k_s =5×10^{-6} m/s)

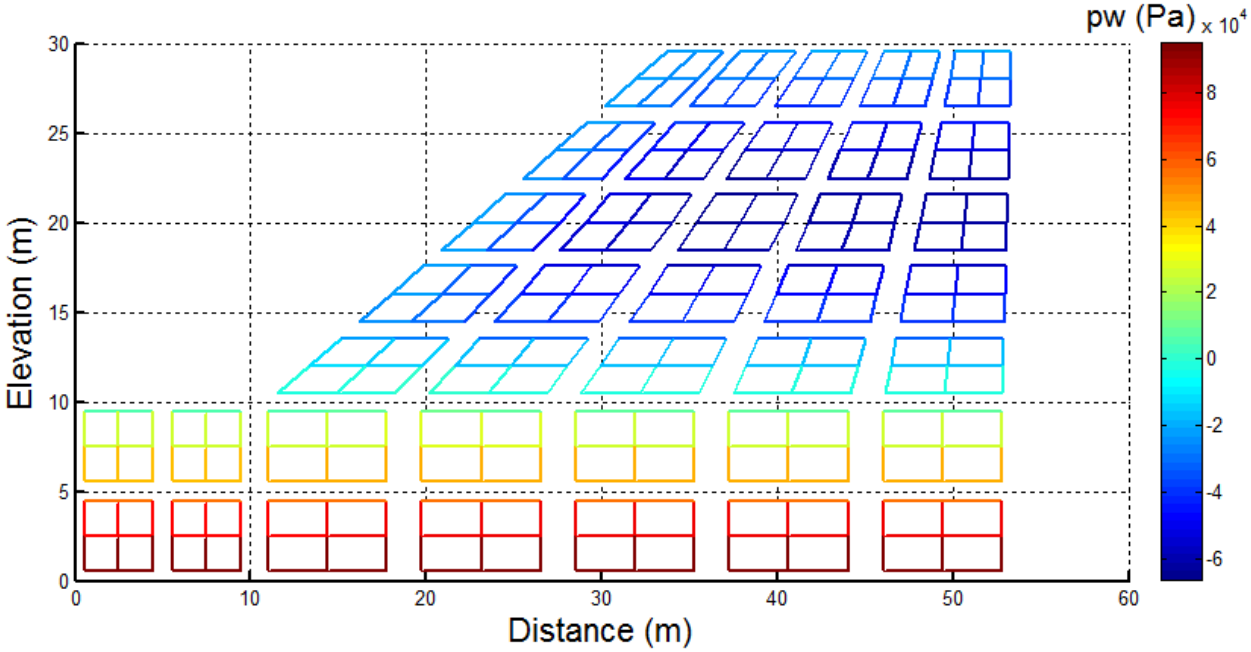

Figure 4.42: Distribution of pore water pressure after 66 hrs(k_s =5×10^{-5} m/s)

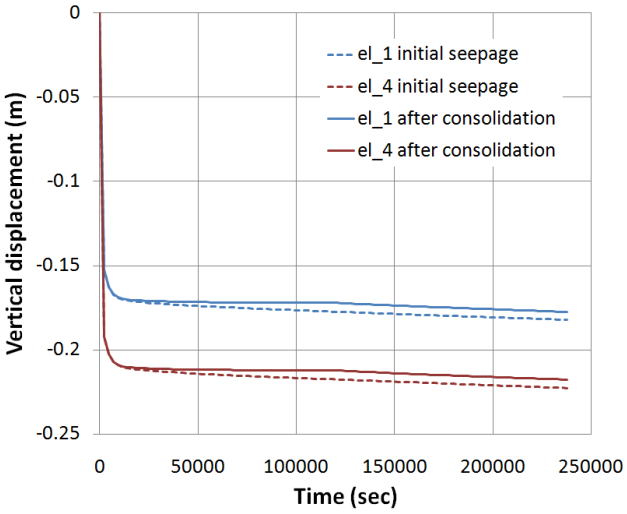

Figure 4.43: Vertical displacement at the crest of the slope(5×10^{-6} m/s)

Chapter 5

Summary and Recommendation for Future Research

5.1 Summary

The objectives of this research have been the following,

(1) formulating and implementing a small strain nonlinear triphasic mixture finite element in a Matlab code to better understand the coupling of deformation and pore air/water flow, and the difference for various effective stress equations.

(2) formulating and implementing the hyperelasto Cam-clay plasticity model for the partially saturated soil.

(3) verifying the triphasic mixture element in Matlab code to partially saturated water flow simulated by commercial codes and analytical solutions.

(4) Obtaining constitutive parameters for flow and plasticity from experimental data available in the literature.

(5) Conducting coupled finite element analysis in plain strain regarding rainfall infiltration with soil weight loading in slope.

The features of the research are as follows:

(1) Semi-implicit linear finite element solution and fully-implicit nonlinear finite element solution as time integration schemes are used for seepage and deformation problems by rainfall

and external loading, and verified by analytical solution of Srivastava and Yeh[81] for transient flow analysis of a partially saturated soil.

(2) For ignoring the pore air pressure in geotechnical engineering problems, the role of the air phase among solid skeleton and water phases is reviewed to implement three-phasic deformable mixture. During infiltration and surface loading on soil column, two-phasic mixture and three-phasic mixture are compared with experimental results and numerical solution in the literature.

(3) Staggered coupled model based on estimating solid deformation after completing seepage analysis, i.e., SEEP/W–SIGMA/W and PlaxFlow-Plaxis, is compared with Matlab code based on monolithic coupled model analyzing both events each time step simultaneously. Difference of both codes influences the calculation of hydraulic conductivity and pore water pressure each step.

(4) The Matlab code applies the porosity-dependent partially hydraulic conductivity. The effect of the function of porosity in permeability gradually causes the difference of results for the pore water pressure and matric suction along passing time.

(5) The implementation of various effective stress, such as Bishop[9], Lewis and Schrefler[58], Borja[12], Borja and White[17], Khalili et al.[49], and Lu et al.[63] in the coupled FE implementation presents the merit and shortcoming of each implementation, and is reviewed.

(6) The constitutive model applies a hyperelasto Cam-clay plasticity model to enhance the elastic behavior of soils[16, 12]. The pressure-dependent elastic shear modulus in a soil needs to be energy-conserving model and is nonlinear elastic. The model provides a fundamentally correct description of elastic material behavior even in the regime of plastic responses.

For lessons learned when running UNSAT-H (flow problem), SEEP/W–SIGMA/W (staggered coupled program), PlaxFlow–Plaxis (staggered coupled program), and ABAQUS (monolithic

coupled program), although PlaxFlow–Plaxis and ABAQUS programs is tried to work for the partially saturated flow analysis coupled to soil solid skeleton deformation and stress, PlaxFlow and Plaxis programs held in computer lab (Bechtel lab) of Civil Department at CU Boulder do not allow for fully coupled flow-deformation analysis. ABAQUS program also works monolithic coupled analysis for partially saturated flow-deformation problems, but it is necessary to get a lot of experimental data and hydraulic information regarding partially saturated conditions, and thus those expert knowledge should be needed to run the program. UNSAT-H program for partially saturated flow problem was developed at Pacific Northwest National laboratory (PNNL) and it can easily be downloaded at http://hydrology.pnl.gov/resources/unsath/unsath.asp. SIGMA/W coupled with SEEP/W could be modeled flow-deformation analysis for partially saturated conditions as staggered coupled finite element analysis.

5.2 Future Work

I need the numerical simulation for partially saturated soil slope stability due to rainfall using hyperelastic Cam-clay plasticity model. Also, I need application of triphasic mixture analysis to air storage problem in an aquifer and $C0_2$ geo-sequestration problem.

Bibliography

[1] ABAQUS. Version 6.9. Manuals, Hibbitt, Karlsson and Sorensen Inc., 2010.

[2] G.D. Aitchison. Relationship of moisture and effective stress function in unsaturated soils. In Pore Pressure and Suction in Soils Conference, London, England, pages 47–52, 1961.

[3] G.D. Aitchison and R. Martin. A membrane oedometer for complex stress-path studies in expansive clays. In in Proceeding the 3th International Conference on Expansive Soils, Haifa, Israel, volume 2, pages 79–82, 1973.

[4] E.E. Alonso. Constitutive modeling of unsaturated soils. Unsaturated soils: Recent Developments and Applications, Civil Engineering European Courses, Barcelona, Spain, 1993.

[5] E.E. Alonso, A. Gens, and D.W. Hight. Special problem soils. general report. In Proceeding 9th European Conference Soil Mechanics and Foundation Engineering Dublin., volume 3, pages 1087–1146, 1987.

[6] E.E. Alonso, A. Gens, and A. Josa. A constitutive model for partially saturated soils. Géotechnique, 40(3):405–430, 1990.

[7] J. Bear. Dynamic of Fluids in Porous Media. Dover Publications, Inc., New York, NY, 1972.

[8] A.W. Bishop. The principle of effective stress. Teknisk Ukeblad I Samarbeide Med Teknikk, 106(39):859–863, 1959.

[9] A.W. Bishop and G.E. Blight. Some aspects of effective stress in saturated and partly saturated soils. Géotechnique, 13(3):177–197, 1963.

[10] A.W. Bishop and I.B. Donald. The experimental study of partly saturated soils in the triaxial apparatus. In in Proceedings of the 5th International Conference on Soil Mechanics and Foundation Engineering, Paris, volume 1, pages 13–21, 1961.

[11] J.A. Blatz and J. Graham. Elastic-plastic modelling of unsaturated soil using results from a new triaxial test with controlled suction. Géotechnique, 53(1):113–122, 2003.

[12] R.I. Borja. Cam-Clay Plasticity. Part V: A mathematical framework for three-phase deformation and strain localization analyses of partially saturated porous media. Computer Methods in Applied Mechanics and Engineering, 193:5301–5338, 2004.

[13] R.I. Borja. On the mechanical energy and effective stress in saturated and unsaturated porous continua. International Journal of Solids and Structures, 43:1764–1786, 2006.

[14] R.I. Borja and A. Koliji. On the effective stress in unsaturated porous continua with double porosity. Journal of the Mechanics and Physics of Solids, 57:1182–1193, 2009.

[15] R.I. Borja and S.R. Lee. Cam-Clay Plasticity, Part I: Implicit integration of elasto-plastic constitutive relations. Computer Methods in Applied Mechanics and Engineering, 78:49–72, 1990.

[16] R.I. Borja, C. Tamagnini, and A. Amorosi. Coupling plasticity and energy-conserving elasticity models for clays. Journal of Geotechnical and Geoenvironmental Engineering, 123(10):948–957, October 1997.

[17] R.I. Borja and J.A. White. Continuum deformation and stability analyses of a steep hillside slope under rainfall infiltration. Acta Geotechnica, 5:1–14, 2010.

[18] R.N. Brooks and A.T. Corey. Properties of porous media affecting fluid flow. J. Irrigation Draining Div., ASCE, 92:61–68, 1966.

[19] R. Butterfield. A natural compression law for soils. Géotechnique, 29:469–480, 1979.

[20] C.F. Chiu and C.W.W. Ng. A state-dependent elasto-plastic model for saturated and unsaturated soils. Géotechnique, 53(9):809–829, 2003.

[21] S.E. Cho and S.R. Lee. Instability of unsaturated soil slopes due to infiltration. Computers and Geotechnics, 28(3):185–208, 2001.

[22] J.D. Coleman. Stress strain relations for partly saturated soil. Correspondence to Géotechnique, 12(4):348–350, 1962.

[23] O. Coussy. Poromechanics. Wiley, Chichester, Hoboken, NJ, 2004.

[24] R.F. Craig. Craig's Soil Mechanics, page 235. Spon Press, New York, NY, 7th edition, 2004.

[25] D. Croney, D.J. Coleman, and W.P.M Black. Movement and distribution fo water in soil in relation to highway design and performance. Special report 40, Water and Its Conduction in Soils Highway Res. Board, Washington, DC, 1958.

[26] C.W. Cryer. A comparison of three dimensional theories of Biot and Terzeghi. Quarterly Journal of Mechanics and Applied Mathematics, 16:72–81, 1963.

[27] R. de Boer. Trends in Continuum Mechanics of Porous Media. Springer, 2005.

[28] P. Delage and J. Graham. Understanding the behaviour of unsaturated soils requires reliable conceptual models. In In Proceedings of the 1st International Conference on Unsaturated Soils, Paris, volume 3, pages 1223–1256, 1995.

[29] W. Ehlers, T. Graf, and M. Ammann. Deformation and localization analysis of partially saturated soil. Computer methods in applied mechanics and engineering, 193:2885–2910, 2004.

[30] A.R. Estabragh, A.A. Javadi, and J.C. Boot. Effect of compaction pressure on consolidation behaviour of unsaturated silty soil. Canadian Geotechnical Journal, 41(3):540–550, 2004.

[31] D.G. Fredlund and N.R. Morgenstern. Stress state variables for unsaturated soils. Journal of Geotech. Engng Div. ASCE, 103(GT5):447–466, 1977.

[32] D.G. Fredlund and H. Rahardjo. Soil Mechanics for Unsaturated Soils. John Wiley and Sons, INC, 1993.

[33] D.G. Fredlund, A. Xing, and S. Huang. Predicting the permeability function for unsaturated soil using the soil-water characteristic curve. Canadian Geotechnical Journal, 31:533–546, 1994.

[34] M.M. Futai, M.S.S. Almeida, W. Conciani, and Filho F.C. Silva. In In Proceeding of the 3th International Conference on Unsaturated Soils, Recife, Brazil, Swets and Zeitlinger, Lisse, pages 721–726, March 2002.

[35] D. Gallipoli, A. Gens, R. Sharma, and J. Vaunat. An elasto-plastic model for unsaturated soil incorporating the effects of suction and degree of saturation on mechanical behaviour. Géotechnique, 53(1):123–135, 2003b.

[36] D. Gallipoli, S.J. Wheeler, and M. Karstunen. Modelling the variation of degree of saturation in a deformable unsaturated soil. Géotechnique, 53(1):105–112, 2003a.

[37] W.R. Gardner. Some steady-state solutions of the unsaturated moisture flow equation with applications to evaporation from a water table. Soil Science, 85:228–232, 1958.

[38] D. Gawin, L. Simoni, and B.A. Schrefler. Numerical model for hydro-mechanical behaviour in deformable porous media: a benchmark problem. In Proceedings of the 9st International Conference on Computer Methods and Advances in Geomechanics, Balkema, Rotterdam, pages 1143–1148, 1997.

[39] A. Gens and E.E. Alonso. A framework for the behaviour of unsaturated expansive clays. Canadian Geotechnical Journal, 29:1013–1032, 1992.

[40] GEO-SLOPE. Version 7.13. User's guide, International Ltd., Calgery, Canada, 2007.

[41] W.G. Gray and B.A. Schrefler. Thermodynamic approach to effective stress in partially saturated porous media. European Journal of Mechanics A/Solids, 20:521–538, 2001.

[42] W.G. Gray and B.A. Schrefler. Analysis of the solid phase stress tensor in multiphase porous media. International Journal for Numerical and Analytical Methods in Geomechanics, 31:541–581, 2007.

[43] D.V. Griffiths and N. Lu. Unsaturated slope stability analysis with steady infiltration or evaporation using elasto-plastic finite elements. International Journal for Numerical and Analytical Methods in Geomechanics, 29:249–267, 2005.

[44] B.B.K. Huat, F.H. Ali, and F.H. Choong. Effect of loading rate on the volume change behavior of unsaturated residual soil. Geotechnical and Geological Engineering, 24:1527–1544, 2006.

[45] Thomas. J.R. Hughes. The Finite Element Method. Dover Publications, Inc., Mineola, NY, 1st edition edition, 2000.

[46] J.E.B. Jennings and J.B. Burland. Limitations to the use of effective stresses in partly saturated soils. Géotechnique, 12(2):125–144, 1962.

[47] C. Jommi. Remarks on the constitutive modelling of unsaturated soils. In In Proceeding of Experimental Evident and Theoretical Approaches in Unsaturated soils, Taratino and Mancuso, Balkema, Rotterdam, ISBN 90 5809 186 4, pages 139–153, 2000.

[48] D.E. Jones and W.G. Holtz. Expansive soils–the hidden disaster. Civil Eng., ASCE, New York, NY, pages 87–89, August 1973.

[49] N. Khalili, F. Geiser, and G.E. Blight. Effective stress in unsaturated soils: Review with new evidence. International Journal of Geomechanics, 4(2):115–126, 2004.

[50] N. Khalili, M.A. Habte, and S. Zargarbashi. A fully coupled flow deformation model for cyclic analysis of unsaturated soils including hydraulic and mechanical hystereses. Computers and Geotechnics, 35:872–889, 2008.

[51] N. Khalili and S. Valliappan. Unified theory of flow and deformation in double porous media. European Journal of Mechanics A/Solids, 15:321–336, 1996.

[52] N. Khalili, R. Witt, L. Laloui, L. Vulliet, and A. Koliji. Effective stress in double porous media with two immiscible fluids. Geophysical Research Letters, 32:L15309, 2005.

[53] Y. Kohgo, M. Nakano, and T. Miyazaki. Theoretical aspects of constitutive modelling for unsaturated soils. Soils and Foundations, 33(4):49–63, 1993a.

[54] Y. Kohgo, M. Nakano, and T. Miyazaki. Verification of the generalized elastoplastic model for unsaturated soils. Soils and Foundations, 33(4):64–73, 1993b.

[55] J.P. Krohn and J.E. Slosson. Assessment of expansive soils in the United States. In in Proceeding the 4th International Conference on Expansive Soils, Denver, CO, volume 1, pages 596–608, 1980.

[56] S. Lacasse and F. Nadim. Reliability issues and future challenges in geotechnical engineering for offshore structures. Norges Geotekniske Institutt, (191):1–30, 1994.

[57] L. Laloui, G. Klubertanz, and L. Vulliet. Solid-liquid-air coupling in multiphase porous media. International Journal for Numerical and Analytical Methods in Geomechanics, 27(3):183–206, 2003.

[58] R.W. Lewis and B.A. Schrefler. The finite element method in the deformation and consolidation of porous media, chapter 2, pages 6–20. John Wiley and Sons Inc., New York, NY, 1987.

[59] R.W. Lewis and B.A. Schrefler. The Finite Element Method in the Static and Dynamic Deformation and Consolidation of Porous Media. John Wiley and Sons, 1998.

[60] A.C. Liakopoulos. Transient Flow through Unsaturated Porous Media. PhD thesis, University of California, Berkeley, 1965.

[61] A. Lloret, M.V. Villar, M. Sanchez, A. Gens, X. Pintado, and E.E. Alonso. Mechanical behaviour of heavily compacted bentonite under high suction changes. Géotechnique, 53(1):27–40, 2003.

[62] B. Loret and N. Khalili. An effective stress elastic-plastic model for unsaturated porous media. Mechanics of Materials, 34:97–116, 2002.

[63] N. Lu, J.W. Godt, and D.T. Wu. A closed-form equation for effective stress in unsaturated soil. Water Resources Research, 46:W05515, 2010.

[64] N. Lu, T. Kim, S. Sture, and W. Likos. Tensile strength of unsaturated sand. Journal of Engineering Mechanics, 135(12):1410–1419, 2009.

[65] N. Lu and W. Likos. Unsaturated Soil Mechanics. John Wiley and Sons, Inc., Hoboken, New Jersey, 2004.

[66] N. Lu and W. Likos. Suction stress characteristic curve for unsaturated soil. Journal of Geotechnical and Geoenvironmental Engineering, 132(2):131–142, 2006.

[67] L.E. Malvern. Introduction to the Mechanics of a Continuous Medium, chapter 6, pages 295–304. Prentice-Hall, Inc., Englewood Cliffs, NJ, 1969.

[68] J. Mandel. Consolidation des sols(in french). Géotechnique, 3(7):287–299, 1953.

[69] E.L. Matyas and H.S. Radhakrishna. Volume change characteristics of partially saturated soils. Géotechnique, 18(4):432–448, 1968.

[70] D. Meiri and G. Karadi. Simulation of air storage aquifer by finite element model. International Journal for Numerical and Analytical Methods in Geomechanics, 6:339–351, 1982.

[71] R.E. Moore. Water conduction for shallow water tables. Hilgardia, 12:383–426, 1939.

[72] H.L. Morel-Seytoux and J.A. Billica. A two-phase numerical model for prediction of infiltration: Applications to a semi-infinite soil column. Water Resources Research, 21(4):607–615, 1985.

[73] PlaxFlow. Version 1.4. Manuals, Delft, Netherlands, 2006.

[74] PLAXIS. Version 8. Manuals, Delft, Netherlands, 2006.

[75] B. Schrefler and R. Scotta. A fully coupled dynamic model for two-phase fluid flow in deformable porous media. Computer methods in applied mechanics and engineering, 190:3223–3246, 2001.

[76] B. Schrefler and X. Zhan. A fully coupled model for water flow and airflow in deformable porous media. Water Resources Research, 29:155–167, 1993.

[77] D. Sheng, S.W. Sloan, A. Gens, and D.W. Smith. Finite element formulation and algorithms for unsaturated soils. Part i: Theory. International Journal for Numerical and Analytical Methods in Geomechanics, 27:745–765, 2003.

[78] D. Sheng, D.W. Smith, S.W. Sloan, and A. Gens. Finite element formulation and algorithms for unsaturated soils. Part ii: Verification and appllication. International Journal for Numerical and Analytical Methods in Geomechanics, 27:767–790, 2003.

[79] F.F.C. Silva, M.S.S. Almeida, and M.M. Futai. Critical state modelling of unsaturated soils. In In Proceeding of the 3th International Conference on Unsaturated Soil, Recife, Brazil, pages 133–137, March 2002.

[80] A.W. Skempton. Effective stress in soils, concrete and rocks. In Conference: Pore Pressure and Suction in Soils, volume 4-16, pages 4–16, 1961.

[81] R. Srivastava and J. Yeh. Analytical solutions for one-dimensional, transient infiltration toward the water table in homogeneous and layered soils. Water Resources Research, 27:753–762, 1991.

[82] D.A. Sun, H. Matsuoka, Y.P. Yao, and W. Ichihara. An elastoplastic model for unsaturated soil in three-dimensional stresses. Soils and Foundations, 40(3):17–28, 2000.

[83] R. Tamagnini. An extended cam-clay model for unsaturated soils with hydraulic hysteresis. Géotechnique, 54(3):223–228, 2004.

[84] G.X. Tang and J. Graham. A possible elasto-plastic framework for unsaturated soils with high plasticity. Canadian Geotechnical Journal, 39:894–907, 2002.

[85] S.M. Tariq. Evaluation of flow characteristics of perforations including nonlinear effects with the finite element method. SPE Production Engineering, 2(2):104–112, 1987.

[86] K. Terzaghi. The shearing resistance of saturated soils and the angle between the planes of shear. In In Proceedings of the 1st Conference on Soil Mechanics, volume 1, pages 54–56, 1936.

[87] K. Terzaghi. Theoretical Soil Mechanics. John Wiley and Sons, New York, NY, 1943.

[88] T.M. Thu, H. Rahardjo, and E.C. Leong. Soil-water characteristic curve and consolidation behavior for a compacted silt. Canadian Geotechnical Journal, 44(3):266–275, 2007.

[89] UNSAT-H. Version 3.0. M.J. Fayer, Pacific Northwest National Laboratory, Richland, Washington, 2000.

[90] M.T. van Genuchten. A closed form equation for predicting the hydraulic conductivity of unsaturated soils. Soil Science Society of America Journal, 44:892–898, 1980.

[91] J. Vaunat, J.C. Cante, A. Ledesma, and A. Gens. Stress point algorithm for an elastoplastic model in unsaturated soils. International Journal of Plasticity, 16(2):121–141, 2000.

[92] H.Q. Vu and D.G. Fredlund. Challenges to modelling heave in expansive soils. Canadian Geotechnical Journal, 43(12):1249–1272, 2006.

[93] S.J. Wheeler, D. Gallipoli, and M. Karstunen. Comments on use of the barcelona basic model for unsaturated soils. International Journal for Numerical and Analytical Methods in Geomechanics, 26:1561–1571, 2002.

[94] S.J. Wheeler, R.J. Sharma, and M.S.R. Buisson. Coupling of hydraulic hysteresis and stress-strain behaviour in unsaturated soils. Géotechnique, 53(1):41–54, 2003.

[95] S.J. Wheeler and V. Sivakumar. An elasto-plastic critical state framework for unsaturated soil. Géotechnique, 45(1):35–53, 1995.

[96] D.M. Wood. Soil Behaviour and Critical State Soil Mechanics. Cambridge University Press, 1990.

[97] L.L. Zhang, L.M. Zhang, and W.H. Tang. Rainfall-induced slope failure considering variability of soil properties. Géotechnique, 55(2):183–188, 2005.

Appendix A

Notation

Greek

α	phases of soil, such as air, water, solid
	or, van Genuchten curve fitting parameter in SWCC(= 1/a)
	or, parameter in trapezoidal rule procedure
$\bar{\alpha}$	constant coefficient of elastic shear modulus
β	parameter controlling the rate of increase of soil stiffness with suction
β'	constant regarding direction of plastic strain rate
Γ	boundary condition in finite element field
$\Delta\gamma,\ \dot{\gamma}$	plastic multiplier
π	bonding variable
$\boldsymbol{\epsilon}$	total solid strain
ϵ_s^e	elastic deviatoric strain
ϵ_v^e	elastic volumetric strain
ϵ_s^p	plastic deviatoric strain
ϵ_v^p	plastic volumetric strain
ϵ_v	volumetric strain
$\boldsymbol{\zeta}^e$	nodal air pressure vector for element
η	weighting function of water pressure
$\eta_a,\ \eta_w$	dynamic air, water viscosity
$\theta_s,\ \theta_r$	saturated, residual volumetric water content
$\boldsymbol{\theta}^e$	nodal water pressure vector for element
κ	slope of the unloading − reloading line
$\tilde{\kappa}$	elastic compressibility index in hyperelastic model
λ	slope of the normal consolidation line, or Lame constant
$\tilde{\lambda}$	virgin compression index of a soil in hyperelastic model
μ^e	elastic shear modulus
ν	specific volume(= $1 + e$)
ξ	coordinate variable in finite element field
δ_{ij}	Kronecker delta
ρ	total mass density of the mixture
ρ^α	partial mass density of the α phase(= $n^\alpha \rho^{\alpha R}$)

$\rho^{aR},\ \rho^{wR},\ \rho^{sR}$	real air, water, solid density
$\hat{\sigma}_{ij}$	Bishop′s effective stress
σ^{*}_{ij}	Jommi′s stress tensor
$\boldsymbol{\sigma}$	Cauchy stress tensor
ϕ_p	negative pore water pressure head
χ	effective stress parameter
χ^{ep}	continuum elastoplastic tangent
Ψ	free energy function
$\psi,\ \tilde{\psi}$	stored energy function
$\psi^a,\ \psi^w$	air, water volume ratio($\psi^w = S,\ \psi^a = 1 - S$)
ω	$= -(\epsilon^e_v - \epsilon^e_{v0})/\tilde{\kappa}$ in hyperelastic model

Alphabet

a	curve fitting parameter in SWCC
a_e	material parameter of a soil
$\mathbf{A}_{e=1}^{n_{\text{el}}}$	element assembly operator
$B,\ B^h_a,\ B^h_w$	discretization domain and spaces in Galerkin Form
B	Biot′s coefficient
$\boldsymbol{B}^{e,u}$	strain − displacement matrix for element
$\boldsymbol{C}$	combination of damping and stiffness matrix
$C(s)$	Fredlund et al.′s correcting function
$\boldsymbol{c}^e$	weighting function variation of displacement for element
$\mathbf{D}, \mathbf{c}^e$	elastic modulus matrix
$\boldsymbol{d}^e$	nodal displacement vector for element
e	void ratio, or element in finite element field
$\boldsymbol{F},\ \boldsymbol{f}$	forcing vector
f	yield locus
$G,\ g$	plastic potential function
$\boldsymbol{g}$	vector of gravity acceleration
h	discretization parameter
$\mathbf{h}$	resultant body force per unit current volume
i	interval between the range of j to N
j	the least negative pore water pressure in Fredlund et al.′s equation
$K,\ K_s$	elastic bulk modulus(solid bulk modulus)
$K_a,\ K_w$	air, water bulk modulus
$\boldsymbol{K},\ \boldsymbol{k}$	stiffness matrix
k	material parameter regarding partially saturated soil
$k_a,\ k_w$	air, water permeability
$\boldsymbol{k}^w,\ \boldsymbol{k}^a$	$= k_w\mathbf{1},\ k_a\mathbf{1}$
k_{ra}	relative permeability of air
k_{rw}	relative permeability of water
k_s	measured saturated conductivity

l^2	unique length for characterizing the porous network geometry
M	slope of the critical state line
m	total mass
m_v	coefficient of volume compressibility
m^α	net mass flux
m	curve fitting parameter in SWCC
$N(s)$	initial specific volume in Alonso′s graph
$\boldsymbol{N}^e$	shape function for element
n	porosity
n	curve fitting parameter in SWCC
$\hat{\boldsymbol{n}}$	direction of deviatoric stress
$n^s,\ n^w,\ n^a$	solid, water, air volume fraction
p	mean total stress
p'	effective mean total stress
p_a	pore air pressure
p'_c	preconsolidation pressure
p_w	pore water pressure
Q	Neumann boundary condition$(= S^w)$
q	deviatoric stress, or infiltration rate
$\mathbf{R}(\mathbf{x})$	residual matrix for Newton − Raphson method
r	parameter defining the maximum soil stiffness
S	degree of saturation
$S^a,\ S^w$	seepage air, water flow force in boundary of finite element
S_e	effective degree of saturation
S_r	residual degree of saturation
s	suction
s^*	function of porosity and suction of a soil
s_c	critical soil suction in elastic regime
$s_{ae},\ s_e$	air entry value
t	time(second)
$\mathbf{t},\ t^\sigma$	traction vector, traction
$\boldsymbol{u}$	displacement vector
v	specific volume$(= 1 + e)$, or total volume
$\boldsymbol{v}$	solid velocity
$\tilde{\boldsymbol{v}}_a,\ \tilde{\boldsymbol{v}}_w$	air, water velocity relative to the solid velocity$(\tilde{\boldsymbol{v}}_\alpha = \boldsymbol{v}_\alpha - \boldsymbol{v})$
$\tilde{\boldsymbol{v}}^w$	superficial Darcy velocity$(= n^w \tilde{\boldsymbol{v}}_w)$
$\boldsymbol{w}$	weighting function of displacement
$\boldsymbol{x}$	location vector
y	elevation coordinate
z	depth under ground surface

Appendix B

Tutorials

B.1 ABAQUS

ABAQUS is a finite element software that can be used to perform monolithically flow and deformation analyses of geotechnical problems. Numerical simulation for consolidation test is transient analysis at saturated condition.

(1) under the CAE pull-down menu Module, select Part

- select Create, and type column for name
  -2D Planar, -Type: Deformable, -Base Feature: Shell, -Approximate size: 10m
- Click Create Lines: Rectangle
  0,0 → 1,3m → Esc → Done

(2) under Module, select Property

- Click Create Material (stress-strain curve symbol) and call porous
  -General, Density, 1566 kg/m^3, -Mechanical, Elasticity, Elastic, Isotropic, $E = 19.64e6$ Pa, $\nu = 0.4$, -Other, Pore fluid, permeability, isotropic, specific weight of wetting fluid=9810 N/m^3, $k = 9.8e$-3 m/s, void ratio $e_0 = n^{f0}/n^{s0} = 0.72$
- Click Create Section
  -Name: column section, -Solid, Homogeneous, -click OK
- Click Assign Section
  -click part and assign section appropriately

(3) under Module, select Assembly

- Click Instance Part
  -instance part

(4) under Module, select Step

- Click Create Step
  -leave default name or create your own, -select Soils, -click Continue to popup Edit Step window, -unselect creep/swelling option, -time period 1s, -initial time step 0.01s, -max pore pressure change 1e8 Pa

(5) under Module, select Load

- Click Create Load
  -name top pressure, -click Pressure, -click Continue, and select top edge, -in Magnitude, enter 4e4 Pa
- Click Create Boundary Condition
  -name fix bottom, -click Displacement/Rotation, -click Continue, and select bottom edge, -in Magnitude, enter 0 for U2
- Click Create Boundary Condition
  -name fix sides, -click Displacement/Rotation, -click Continue, and select left and right edges, -in Magnitude, enter 0 for U1
- Click Create Boundary Condition
  -name top pore press, -click Pore pressure, -click Continue, and select top edge, -in Magnitude, enter 0 Pa
- Click Create Predefined Field
  -name initial void ratio, -click Step, Initial, -Other, Temperature, -Continue, select column part, -in Magnitude, enter 0.72, -under top menu: Model-Edit Keyword-9. Model-1
  you're now looking at the input file; change Temperature to Ratio, -OK

(6) under Module, select Mesh

- Click Assign Mesh Controls
  -select Structured and Quad
- Click Seed Part Instance, and select part
  -Approximate global size: 1m
- Click Assign Element Type
  -Pore Fluid/Stress, Quadratic, -unselect Reduced Integration
- Click Mesh Part

(7) under Module, select Job

- Click Create Job
- Click Job Manager and Submit, and wait until completed successfully; ignore History output warning, if there is one
  -click Results

(8) under Module, select Visualization

- Click Result Options
  -unselect Average element output at nodes
- pull-down Result, Field output, and choose data to view and Plot pore pressure
- select Create XY Data, Path, to view displacement of top node versus time
  you could turn on Nlgeom to see nonlinear geometric effects, but since load is so small, there is little difference between the two solutions

Figure B.1 shows the result of consolidation simulation at saturated condition. It describes contour of excess pore water pressure due to top pressure in ABAQUS program.

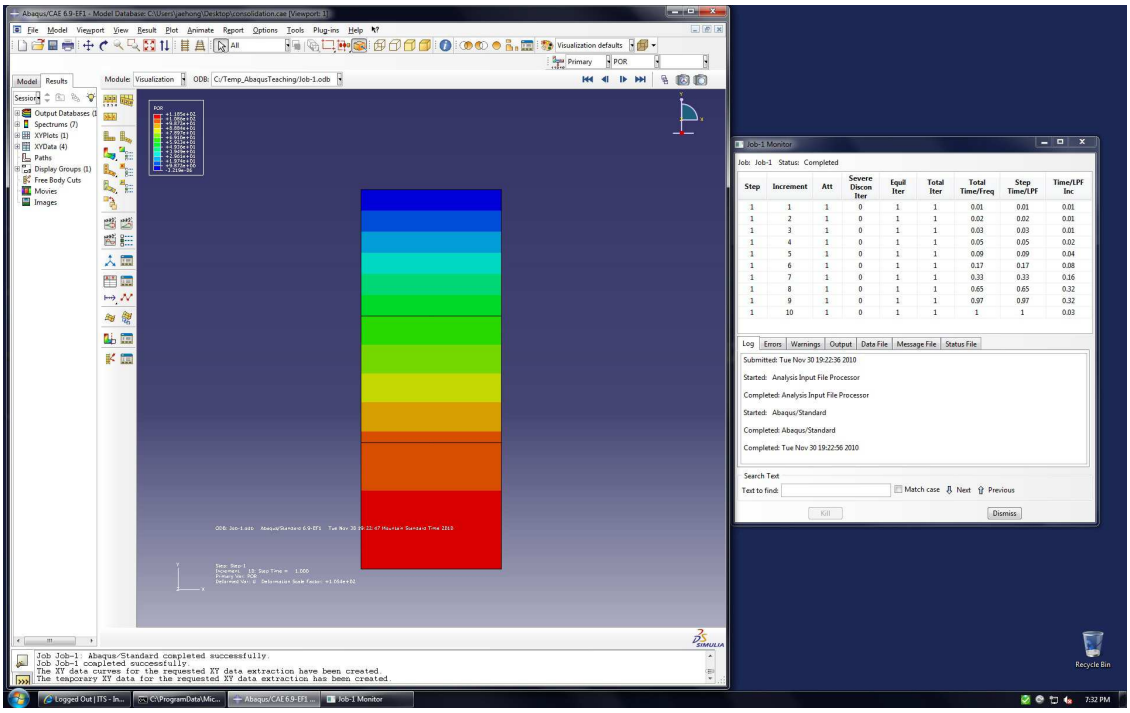

Figure B.1: Contour of excess pore water pressure in ABAQUS

B.2 SEEP/W–SIGMA/W

SIGMA/W is a finite element software that can be used to perform stress and deformation analyses of geotechnical problems. Also SIGMA/W can be used together with SEEP/W to perform a coupled consolidation analysis. SIGMA/W calculates the deformations results from pore water pressure changes while SEEP/W calculates transient pore water pressure changes. This procedure is used to simulate the consolidation process in partially saturated soils.

(1) In Set–Page option, default size is Width:266.7, Height:203.2, and Units is mm.

(2) In Draw option, draw (3m x 1m) size of soil column as shown in Figure B.2

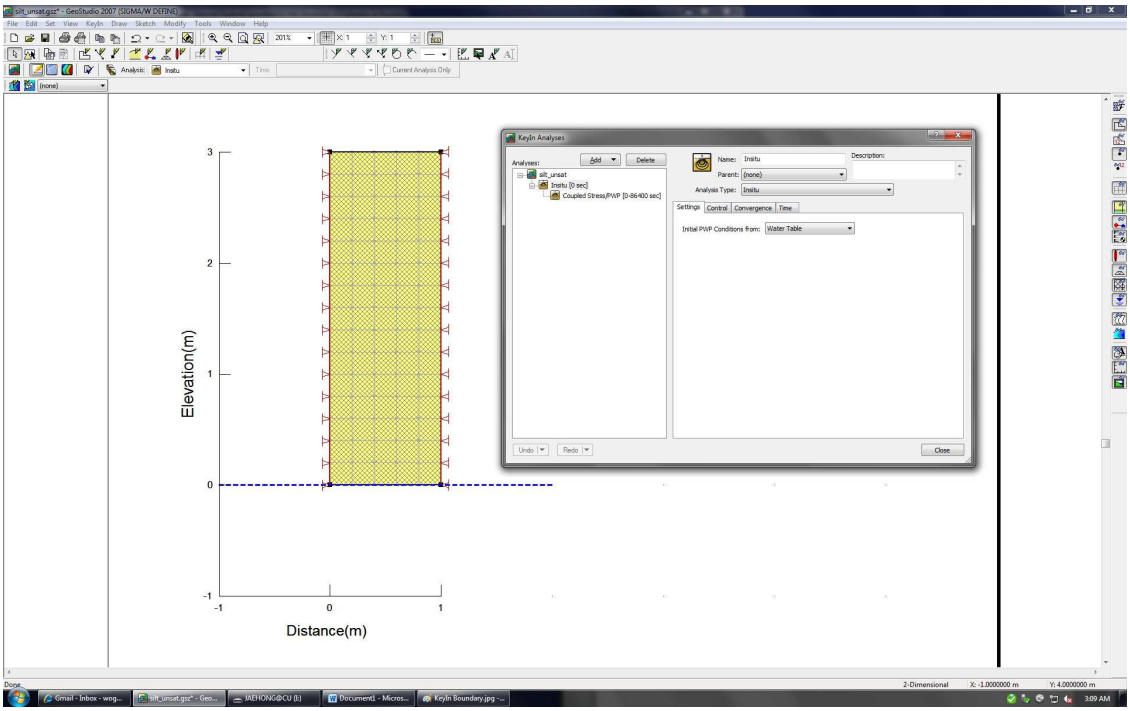

Figure B.2: Insitu

(3) In KeyIn Analyses–settings option, Analysis Type: Insitu, and Initial PWP Conditions from: Water Table.

(4) Change KeyIn Analyses into Analysis Type: Coupled Stress/PWP and Parent: Insitu.

(5) In this option, decide Time: Duration and Time Steps, for example 86400sec (1day) and 100 time steps.

(6) In KeyIn Materials option, decide Vol. Water Content Fn and Hyd. Conductivity Fn using Hydraulic Properties section as shown in Figure B.3.

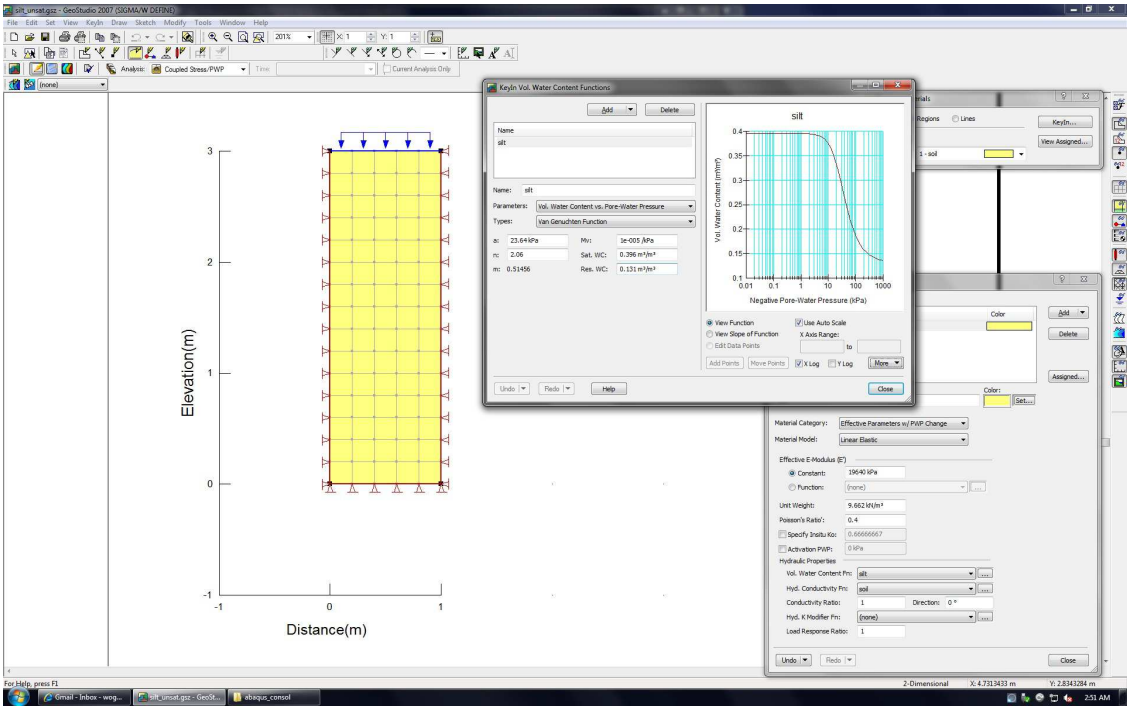

Figure B.3: KeyIn Materials

(7) in KeyIn Vol.Water Content Functions option, input van Genuchten parameters and then input other parameters based on Vol.Water Content Functions in Hydraulic Conductivity Functions option.

(8) in KeyIn Boundary Conditions option, fix both sides of soil column and bottom as shown in Figure B.4.

(9) in KeyIn Hydraulic Boundary Functions option, input seepage force (5.83e-7 m/s) and input traction (1000 kPa) in KeyIn Stress Boundary Functions as shown in Figure B.5.

(10) in Draw Mesh Properties option, decide element size as shown in Figure B.6.

(11) After input is completed, run this problem using Tools–Solve Analyses option.

(12) Click Contour, and then check the distribution of pore water pressure and displacement as select Set Locations option.

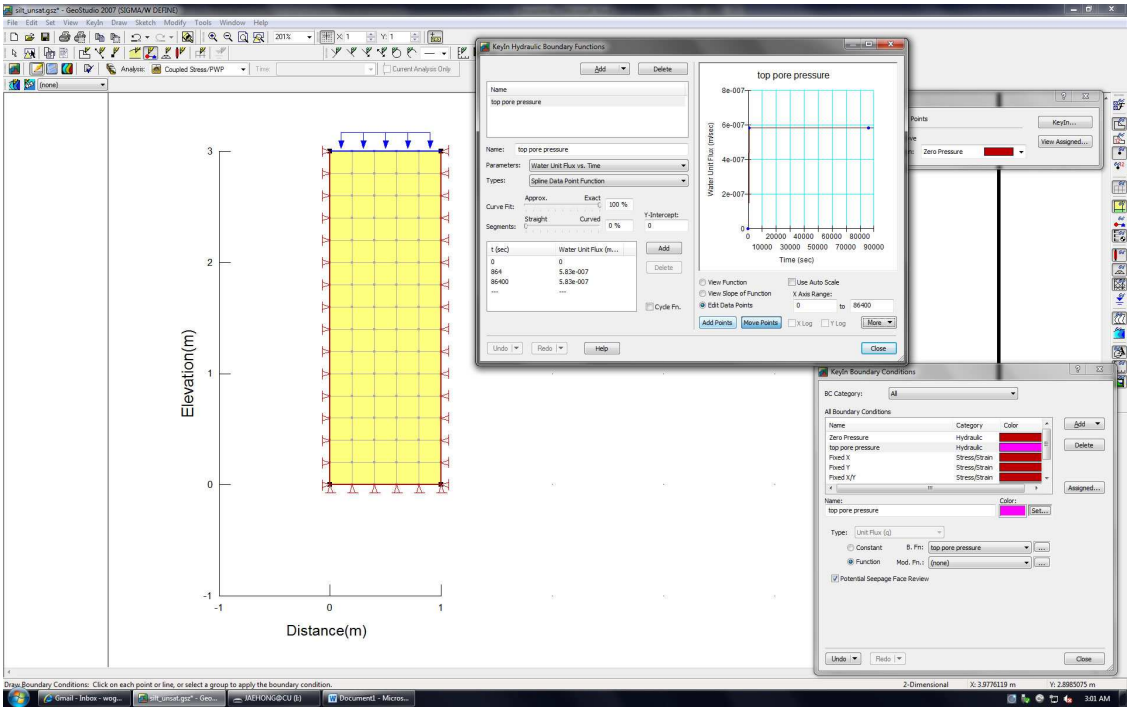

Figure B.4: KeyIn Boundary

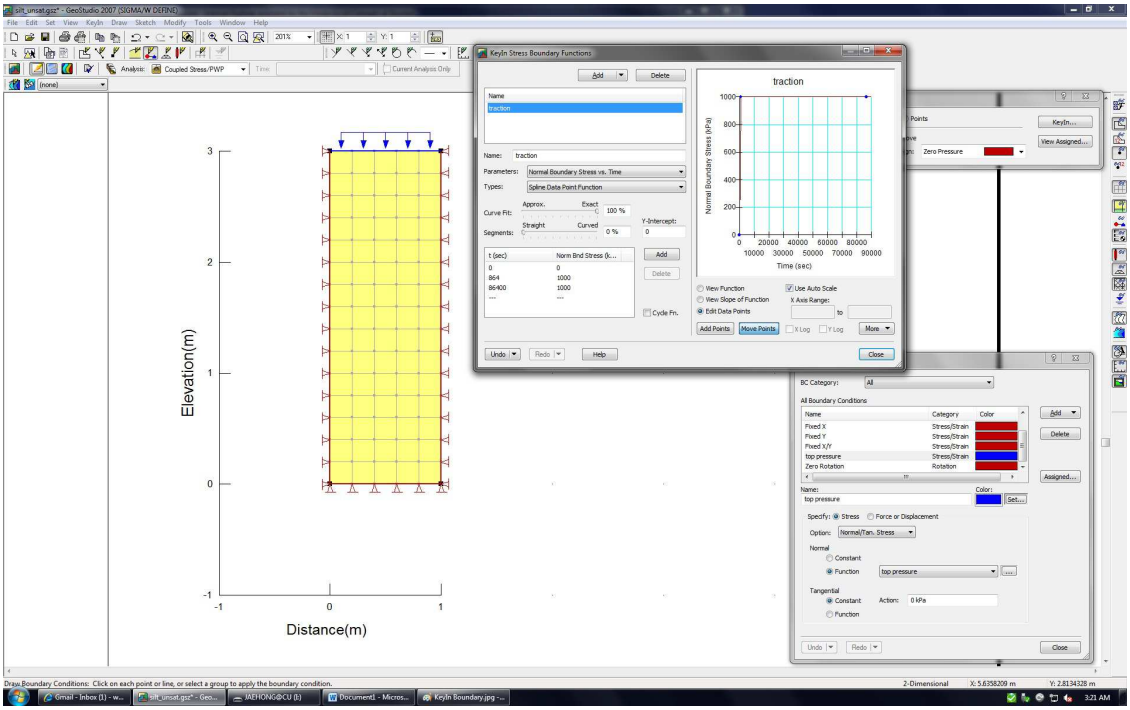

Figure B.5: KeyIn Stress Boundary Functions

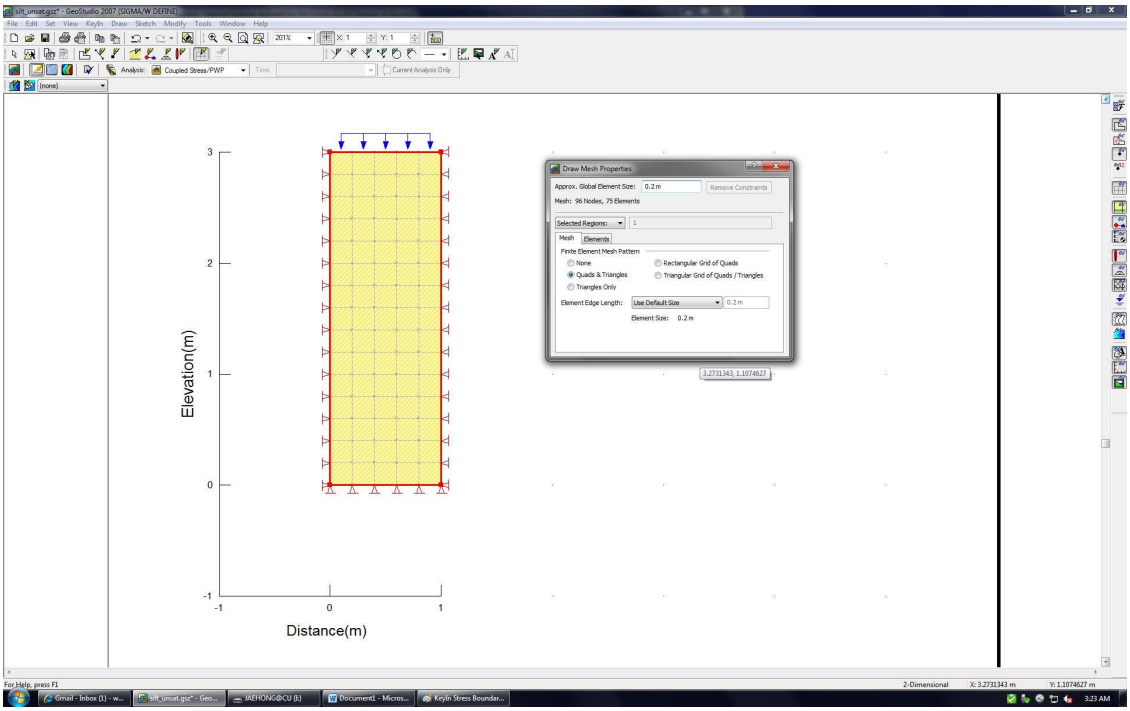

Figure B.6: Draw Mesh Properties

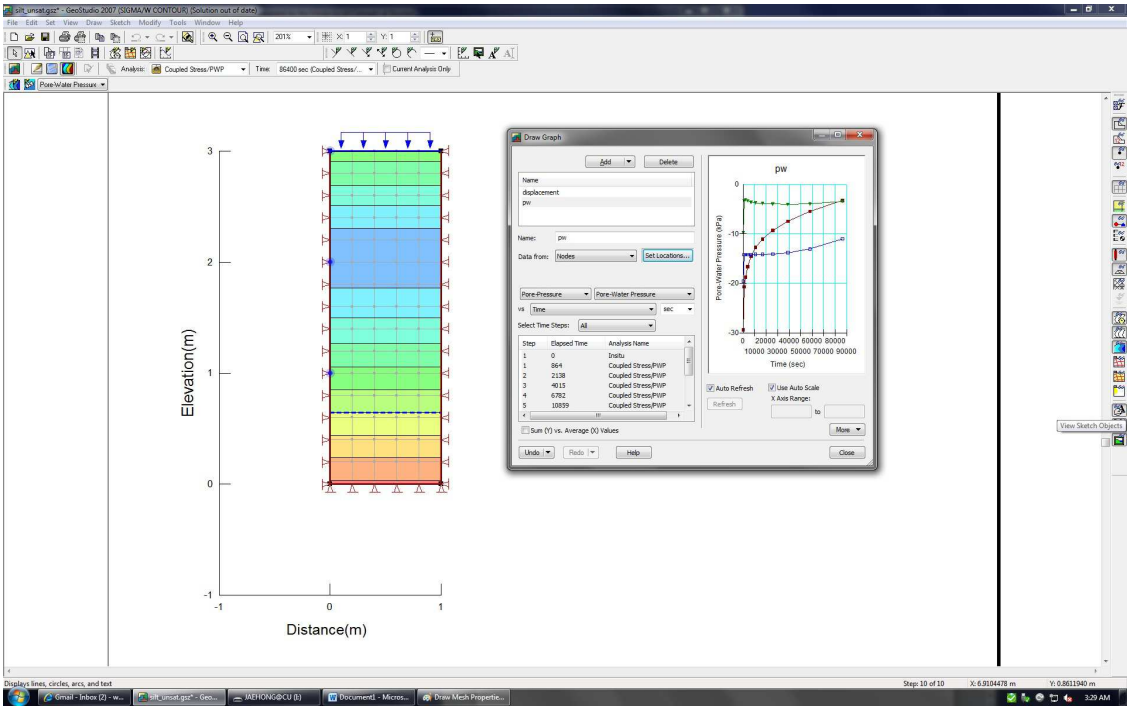

Figure B.7: Contour Draw Graph

B.3 UNSAT-H

UNSAT-H model was developed at Pacific Northwest National Laboratory (PNNL) to assess the water dynamics of arid sites and, in particular, estimate recharge fluxes for scenarios pertinent to waste disposal facilities at the Hanford Site. The UNSAT-H model accomplishes this goal by simulating soil water infiltration, redistribution, evaporation, plant transpiration, deep drainage, and soil heat flow.

The UNSAT-H code is designed to simulate water and heat flow processes in one dimension (typically vertical). UNSAT-H can simulate the isothermal flow of liquid water and water vapor, the thermal flow of water vapor, the flow of heat, the surface energy balance, soil-water extraction by plants, and deep drainage. Information about where to find the code, updates, and lessons learned can be found at http://hydrology.pnl.gov/.

UNSAT-H code composes of three *.exe files, such as din301, uns301, dout301. Start to work din301.ext with input file, and then execute uns301 and dout301 in due order. In Window OS, the code can be worked with 'Command Prompt' as shown in Figure B.8. Figure B.8 shows Command Prompt window and input file which has all information to simulate a flow problem of partially saturated soil. User makes *.inp based on UNSAT-H Input Manual. The manual is organized into five sections:

(1) Options, Constants, and Limits

(2) Soil Property Information

(3) Initial Conditions

(4) Plant Information (optional)

(5) Boundary Conditions

For example, input file (*.inp) in Figure B.8 shows information for flow problem in silt in this study. Figure B.9 shows the output file obtained from executing dout301.exe.

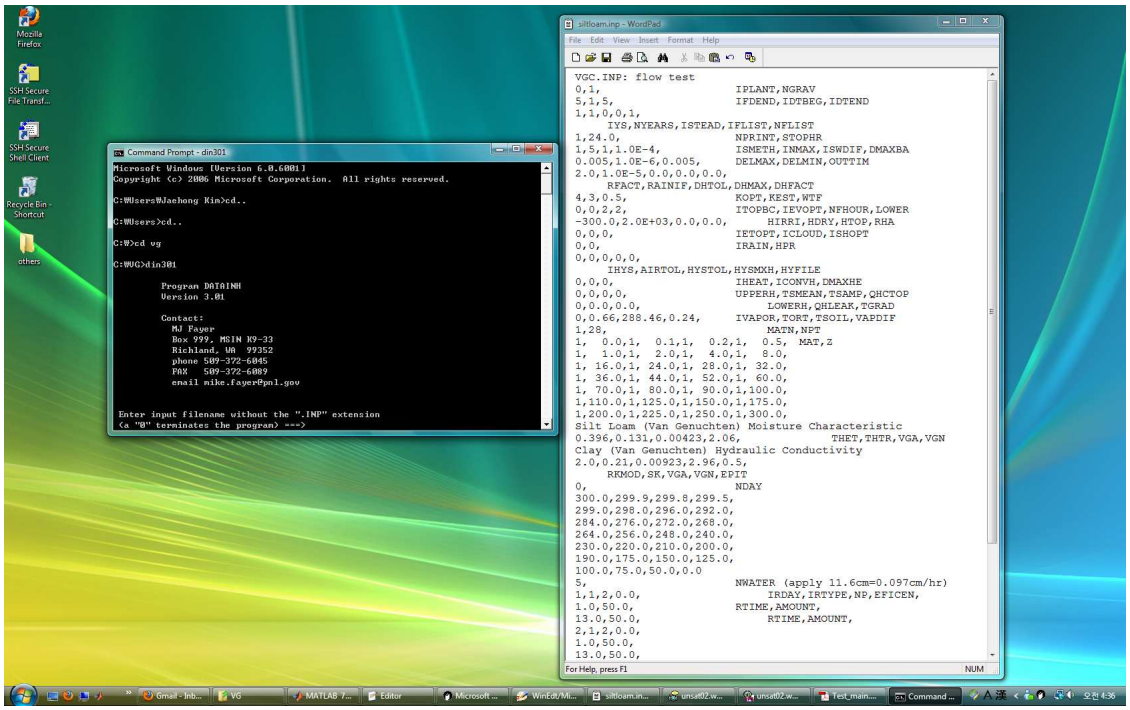

Figure B.8: Start of UNSAT-H code

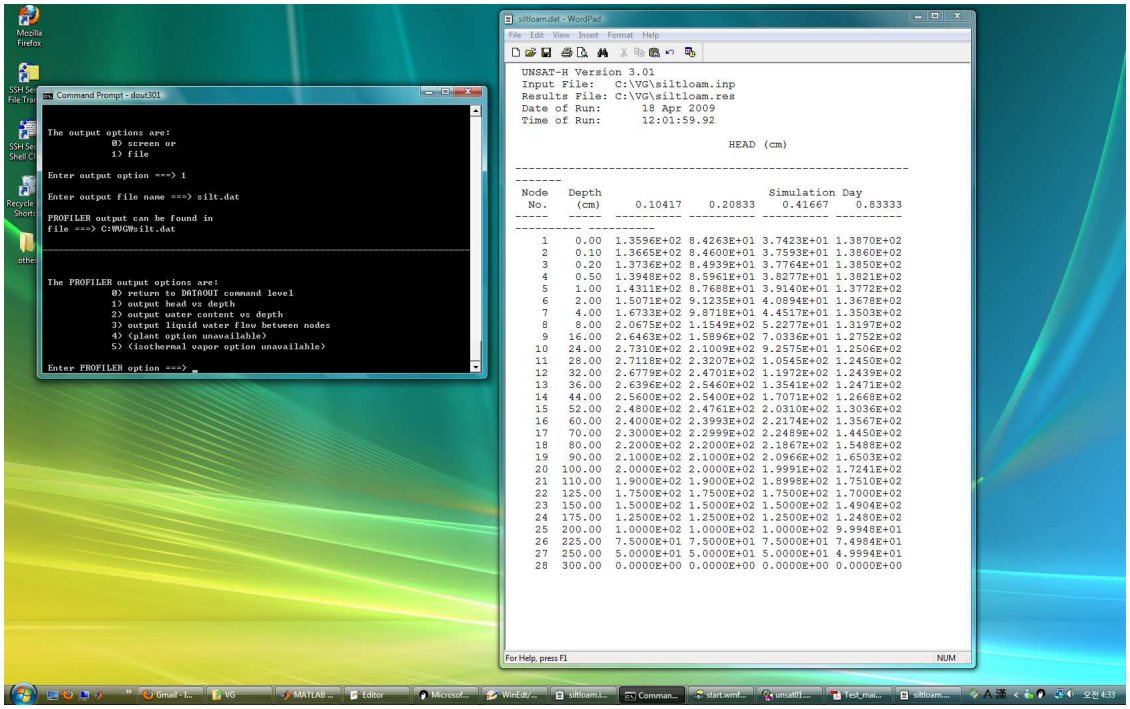

Figure B.9: Output file of UNSAT-H code